

High-Rate, Short-Pulse Sources:
Jitter and Pedestal Level in
Optical Time-Division Multiplexing

A Thesis

Presented to

The Academic Faculty

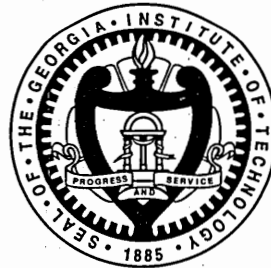
by

Michael Charles Gross

In Partial Fulfillment

of the Requirements for the Degree of

Doctor of Philosophy in Electrical Engineering



School of Electrical and Computer Engineering

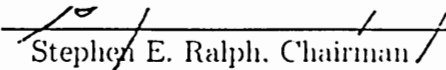
Georgia Institute of Technology


July 2003

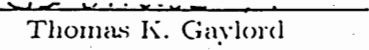
Copyright © 2003 by Michael Charles Gross

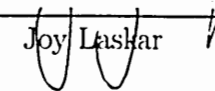
High-Rate, Short-Pulse Sources:
Jitter and Pedestal Level
in Optical Time-Division Multiplexing

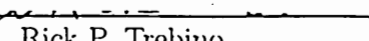
Approved:


Stephen E. Ralph, Chairman


John A. Buck


Thomas K. Gaylord


Joy Laskar


Rick P. Trebino

Date approved by Chairman

30 July 2003

Acknowledgments

This dissertation would not have been possible without the assistance of all the members of the Ultrafast Optical Communications Laboratory and several members of other optics groups at Georgia Tech. In particular, four colleagues provided invaluable, material contributions

Dr. Marc Hanna helped derive the analytical expressions related to temporal-multiplexing-induced amplitude jitter as well as the spectrum of a noisy pulse train. Dr. Hanna also contributed to the coding of the MATLAB routine to simulate gain-switching.

Ketan M. Patel contributed to the design of laser-diode-drive setups and assisted in the derivation of the spectrum of a noisy pulse train. Mr. Patel also assisted in coding the MATLAB jitter-simulation and jitter-characterization programs as well as the LabVIEW data-acquisition routine.

Dr. Stephen E. Ralph provided encouragement, guidance, and, like the patrons of Renaissance Europe, financial support. In addition, Dr. Ralph spent multiple hours editing and fine-tuning publications, presentations, and this very document.

Michael D. Shell designed the bias circuitry used in the board employed to gain-switch the butterfly-packaged laser diode. Mr. Shell also provided several \LaTeX formatting routines and related advise.

Michael Charles Gross

Contents

Contents	iv
List of Tables	viii
List of Figures	ix
Summary	xxxii
1 Introduction	1
1.1 Roadmap	1
1.2 Motivation	1
1.3 Nomenclature	3
1.4 Optical Communications	5
1.5 Jitter Tutorial	15
1.6 Commentary	22
2 Picosecond-Pulse Source	25
2.1 Roadmap	25
2.2 The Problem	25
2.3 Previous Work	26
2.4 Present Contribution	31
2.5 Commentary	44

3	Pulse-Train Gain-Switching	47
3.1	Roadmap	47
3.2	The Problem	47
3.3	Previous Work	48
3.4	Present Contribution	51
3.5	Commentary	56
4	Temporal-Multiplexing Amplitude Jitter	58
4.1	Roadmap	58
4.2	The Problem	58
4.3	Previous Work	59
4.4	Present Contribution	66
4.5	Commentary	81
5	Direct Jitter-Characterization Method	83
5.1	Roadmap	83
5.2	The Problem	83
5.3	Previous Work	85
5.4	Present Contribution	91
5.5	Commentary	142
6	Mixing-Based Jitter-Characterization Method	144
6.1	Roadmap	144
6.2	The Problem	144

6.3	Previous Work	145
6.4	Present Contribution	149
6.5	Commentary	174
7	Conclusions	178
7.1	Introduction	178
7.2	Picosecond-Pulse Source	179
7.3	Pulse-Train Gain-Switching	179
7.4	Temporal-Multiplexing Amplitude Jitter	179
7.5	Direct Jitter Characterization	180
7.6	Mixing-Based Jitter Characterization	180
7.7	Commentary	181
A	Root-Mean-Squared and Peak-to-Peak Jitter	182
B	Simulation Results: Uncompensated Direct Method	183
B.1	Amplitude Jitter	183
B.2	Timing Jitter	198
B.3	Correlation Time	213
C	Simulation Results: Compensated Direct Method	218
C.1	Amplitude Jitter	218
C.2	Timing Jitter	233
C.3	Correlation Time	241

D Simulation Results: Uncompensated Mixing Method	242
D.1 Amplitude Jitter	242
D.2 Timing Jitter	253
D.3 Correlation Time	259
E Simulation Results: Compensated Mixing Method	263
E.1 Amplitude Jitter	263
E.2 Timing Jitter	274
E.3 Correlation Time	280
Bibliography	281
Vita	297

List of Tables

1.1	Origins of jitter contributions in various pulsed lasers.	24
2.1	The performance and goals of the Picosecond-Pulse Source.	32
5.1	Jitter-measurement resolutions when using an Agilent 856X.	135
5.2	Minimum measurable jitters when using an Agilent 856X.	136
5.3	Jitter measured with the oscilloscope method.	141
5.4	Jitter measured with the direct spectral method.	141

List of Figures

1.1	A wavelength-division-multiplexed link.	5
1.2	A multi-source optically time-division-multiplexed link.	6
1.3	A single-source optically time-division-multiplexed link.	7
1.4	A modulating temporal multiplexer.	8
1.5	Several important parameters of a pulse train. (Timing and amplitude jitter are illustrated in Fig. 1.6.) This pulse train has not yet been multiplexed so its repetition frequency, f_{rep} , equals the channel rate. P —power. A —mean peak power. \hat{A}_{ped} —normalized pedestal power. t —time. T —period. Δt —temporal full width at half of maximum power.	10
1.6	An eye diagram of a non-return-to-zero data stream. T_{sys} —mean system period. T_{thr} —threshold time. A —mean amplitude of ONES. A_{thr} —threshold amplitude. $\sigma_{\Delta T}$ —standard deviation of timing jitter. $\sigma_{\Delta A_1}$ —standard deviation of amplitude jitter of ONES. $\sigma_{\Delta A_1}$ —standard deviation of amplitude jitter of ZEROS.	11
1.7	Bit-error rate due solely to either timing or amplitude jitter, $\text{BER}_{\Delta J}$ as a function of the normalized standard deviation of timing or amplitude jitter, $\sigma_{\Delta J}/J$	13
1.8	Types of jitter. This document is concerned only with random jitter (noise), with special emphasis on uncorrelated and correlated jitter. .	15

1.9	Time-domain representations of random sequences. (a) An uncorrelated random sequence, ΔJ_u . (b) A correlated random sequence, ΔJ_c . (c) A super-mode random sequence, ΔJ_p	18
1.10	Autocorrelations of the random sequences shown in Fig. 1.9. (a) The autocorrelation of an uncorrelated random sequence, $\phi_{\Delta J_u}$. (a) The autocorrelation of a correlated random sequence, $\phi_{\Delta J_c}$. (a) The autocorrelation of a super-mode random sequence, $\phi_{\Delta J_p}$	19
1.11	Spectra of the random sequences shown in Fig. 1.9. (a) The spectrum of an uncorrelated random sequence, $\Phi_{\Delta J_u}$. (a) The spectrum of a correlated random sequence, $\Phi_{\Delta J_c}$. (a) The spectrum of a super-mode random sequence, $\Phi_{\Delta J_p}$	20
2.1	The Picosecond-Pulse Source. Points A, B, C, and D are measurement locations. RF—radio-frequency. EDFA—erbium-doped fiber amplifier. DCF—dispersion-compensating fiber. DDF—dispersion-decreasing fiber. DSF—dispersion-shifted fiber.	31
2.2	Simulated gain-switching of a laser diode by a 2.5-GHz sinusoidal current. i_{tot} —total current. p —output optical power. $\delta\lambda$ —deviation from center wavelength. t —time.	33
2.3	Stage 1 of the Picosecond-Pulse Source.	35
2.4	Autocorrelations measured at Points A, B, C, and D of the Picosecond-Pulse Source.	36
2.5	Optical spectra measured at Points A, B, C, and D of the Picosecond-Pulse Source.	36
2.6	Three autocorrelations: the output of the Picosecond-Pulse Source (Point D), a Gaussian pulse with full width at half maximum of 1.04 ps, and an hyperbolic secant pulse with full width of 0.96 ps.	43

3.1	Diagram of experimental setup for pulse-train drive. The impulse generator is omitted for sinusoidal drive. Point A is the fiber-coupled output of the laser. RF—radio-frequency. Match. Net.—matching network. SRD—step-recovery diode. LD—laser diode.	52
3.2	Photograph of experimental setup for pulse-train drive.	53
3.3	Electrical pulse used to drive the chip-carrier-mounted laser.	54
3.4	Measured values plotted against bias current for three gain-switching scenarios: (a) timing jitter, (b) normalized amplitude jitter, and (c) temporal full width at half of maximum.	55
4.1	The ideal nonlinear optical loop mirror.	61
4.2	The transmission of the nonlinear optical loop mirror for four values of the power-splitting ratio, α	62
4.3	The ideal nonlinear amplifying loop mirror.	64
4.4	The nonlinear transmission of the nonlinear amplifying loop mirror.	65
4.5	The electric field of a pedestal-free pulse. E —electric field. t —time. κ —normalization constant. A_0 —power amplitude of pedestal-free pulse. E_0 —time-dependent electric-field envelope of pedestal-free pulse. u_o —unitless, unit-amplitude field-shape function of pedestal-free pulse.	67
4.6	Temporal multiplexing of a finite-pedestal pulse train. E —electric field. t —time. κ —normalization constant. A —power amplitude of finite-pedestal pulse. \hat{E}_{ped} —normalized field amplitude of pedestal. $\hat{E}_0 \equiv 1 - \hat{E}_{\text{ped}}$ —normalized field amplitude of pedestal-free component. E —time-dependent electric-field envelope of finite-pedestal pulse. E_{mux} —time-dependent electric-field envelope after multiplexing. T_{sys} —bit period after multiplexing. u_o —unitless, unit-amplitude field-shape function of pedestal-free component.	68

4.7	Normalized pedestal-induced amplitude jitter, plotted against normalized pedestal power.	71
4.8	The BER, due to pedestal-induced amplitude jitter, of a temporally multiplexed pulse train, plotted against normalized pedestal level.	72
4.9	A diagram of the nonlinear amplifying loop mirror employed in the experiments. DSF—dispersion-shifted fiber.	76
4.10	A photograph of the nonlinear amplifying loop mirror employed in the experiments.	77
4.11	Experimental setup for measuring multiplexing-induced amplitude jitter using a power meter.	78
4.12	Experimental setup for measuring multiplexing-induced amplitude jitter using a persistence autocorrelation.	78
4.13	Multiplexing induced amplitude jitter plotted against pedestal level. Results from theory and two sets of experiments are included. MSE—mean-squared error.	79
4.14	Autocorrelation traces, with persistence, of 4-bit multiplexed pulse trains without (a) and with (b) pedestal suppression by a nonlinear amplifying loop mirror.	80
5.1	The experimental setup employed with the oscilloscope-based jitter-measurement method. RF—radio frequency.	85
5.2	The experimental setup of the jitter-measurement method based on crosscorrelation. In practice a long fiber delay is also often employed.	86
5.3	The experimental setup of the jitter-measurement method based on phase-encoded optical sampling.	87
5.4	The experimental setup of the direct spectral jitter-measurement method. RFSA—radio-frequency spectrum analyzer.	89

5.5	The spectrum of a train of <i>impulses</i> (infinitely narrow pulses) with <i>no</i> jitter.	98
5.6	The spectrum of a train of finite-width <i>pulses</i> train with no jitter. The root-mean-squared duration of the pulse is 5 % of the period.	98
5.7	The spectrum of an impulse pulse train with only <i>uncorrelated amplitude</i> jitter equal to 1 % of the mean amplitude.	98
5.8	The spectrum of an impulse pulse train with only <i>uncorrelated timing</i> jitter equal to 1 % of the mean period.	99
5.9	The spectrum of an impulse train with only <i>correlated amplitude</i> jitter equal to 1 % of the mean amplitude.	99
5.10	The spectrum of an impulse train with only <i>correlated timing</i> jitter equal to 1 % of the mean period.	99
5.11	The spectrum of a <i>pulse</i> train with all four jitter contributions. Each contribution is equal to 1 % of the mean amplitude or period.	100
5.12	Envelope fit of a spectrum containing all four jitter contributions. MSE—mean-squared error.	102
5.13	The spectrum shown in Fig. 5.12 normalized to its envelope.	102
5.14	The spectrum shown in Fig. 5.13 with the harmonic peaks removed and probe points encircled.	103
5.15	Parabolic fit of integrated noise-band power, employed to compute total jitter. MSE—mean-squared error.	104
5.16	Parabolic fit of probe points, employed to compute uncorrelated jitter. MSE—mean-squared error.	105
5.17	Parabolic fit of correlated-noiseband widths, employed to compute correlation times. MSE—mean-squared error.	107

5.18	Extraction errors for (a) total amplitude jitter, $\epsilon_{\Delta A}$, (b) uncorrelated amplitude jitter, $\epsilon_{\Delta A_u}$, and (c) correlated amplitude jitter, $\epsilon_{\Delta A_c}$, obtained with the uncompensated direct method. σ_A/A —normalized total amplitude jitter. σ_T/T —normalized total timing jitter. σ_s/T —normalized root-mean-squared pulse width.	119
5.19	The contours of the plots shown in 5.18	120
5.20	Extraction errors for (a) total timing jitter, $\epsilon_{\Delta T}$, (b) uncorrelated timing jitter, $\epsilon_{\Delta T_u}$, and (c) correlated timing jitter, $\epsilon_{\Delta T_c}$, obtained with the uncompensated direct method. σ_A/A —normalized total amplitude jitter. σ_T/T —normalized total timing jitter. σ_s/T —normalized root-mean-squared pulse width.	122
5.21	The contours of the plots shown in 5.20	123
5.22	Extraction errors for the correlation times of the (a) correlated amplitude jitter, $\epsilon_{\Delta A_c}$ and (b) timing jitter, $\epsilon_{\Delta T_c}$, obtained with the uncompensated direct method. σ_A/A —normalized total amplitude jitter. σ_T/T —normalized total timing jitter. σ_s/T —normalized root-mean-squared pulse width.	125
5.23	Compensation of the uncorrelated-amplitude-jitter extraction.	127
5.24	Extraction errors for (a) total amplitude jitter, $\epsilon_{\Delta A}$, (b) uncorrelated amplitude jitter, $\epsilon_{\Delta A_u}$, and (c) correlated amplitude jitter, $\epsilon_{\Delta A_c}$, obtained with the compensated direct method. σ_A/A —normalized total amplitude jitter. σ_T/T —normalized total timing jitter. σ_s/T —normalized root-mean-squared pulse width.	129
5.25	The contours of the plots shown in 5.24	130
5.26	Compensation of the total-timing-jitter extraction.	131

5.27	Extraction errors for (a) total timing jitter, $\epsilon_{\Delta T}$, (b) uncorrelated timing jitter, $\epsilon_{\Delta T_u}$, and (c) correlated timing jitter, $\epsilon_{\Delta T_c}$, obtained with the compensated direct method. σ_A/A —normalized total amplitude jitter. σ_T/T —normalized total timing jitter. σ_s/T —normalized root-mean-squared pulse width.	132
5.28	The front panel of the LabVIEW data-acquisition routine. White-on-black boxes are controls (inputs); black-on-white boxes are indicators (outputs). The spectra are displayed by a subroutine (not shown) as they are measured and then recorded.	137
5.29	The figure-eight laser.	138
5.30	The seventh harmonic of the gain-switched laser diode's power spectrum. This spectrum was recorded with a 10-Hz step size and 10-Hz resolution bandwidth.	139
5.31	The seventh harmonic of the figure-eight laser's power spectrum. This spectrum was recorded with a 10-Hz step size and 10-Hz resolution bandwidth.	140
6.1	The experimental setup of the mixing-based jitter-characterization method. RF—radio-frequency. RFSA—radio-frequency spectrum analyzer. LFSA—low-frequency RFSA. VDL—variable delay line.	145
6.2	(a) A noisy pulse train with the ideal in-phase and quadrature-phase local-oscillator signals: square and sawtooth waves, respectively. (b) The resulting mixing products. LO—local oscillator. t —time. T —period.	147
6.3	(a) A noisy pulse train with the in-phase and quadrature-phase sine waves used as local-oscillator signals in real-world experiments. (b) The resulting mixing products. LO—local oscillator. t —time. T —period.	148

6.4	The mixing-product spectra of a train of <i>impulses</i> (infinitely narrow pulses) with <i>no</i> jitter. Only the spike of the in-phase spectrum is visible.	153
6.5	The mixing-product spectra of a train of finite-width <i>pulses</i> with no jitter. The root-mean-squared duration of the pulse is 5 % of the period. These spectra appear identical to those in the previous figure.	153
6.6	The mixing-product spectra of an impulse pulse train with only <i>uncorrelated amplitude</i> jitter equal to 1 % of the mean amplitude. The quadrature-phase spectrum is not apparent.	154
6.7	The mixing-product spectra of an impulse pulse train with only <i>uncorrelated timing</i> jitter equal to 1 % of the mean period.	154
6.8	The mixing-product spectra of an impulse train with only <i>correlated amplitude</i> jitter equal to 1 % of the mean amplitude. The quadrature-phase spectrum is not apparent.	155
6.9	The mixing-product spectra of an impulse train with only <i>correlated timing</i> jitter equal to 1 % of the mean amplitude.	155
6.10	The mixing-product spectra of a <i>pulse</i> train with all four jitter contributions. Each contribution is equal to 1 % of the mean amplitude or period.	156
6.11	Illustration of the measurement procedure. Both spectra are normalized to the peak of the in-phase spectrum. The noisebands are integrated to compute the total jitter, and the probe points are used to extract the uncorrelated jitter.	158

6.12	Extraction errors for (a) total amplitude jitter, $\epsilon_{\Delta A}$, (b) uncorrelated amplitude jitter, $\epsilon_{\Delta A_u}$, and (c) correlated amplitude jitter, $\epsilon_{\Delta A_c}$, obtained with the uncompensated mixing method. σ_A/A —normalized total amplitude jitter. σ_T/T —normalized total timing jitter. σ_s/T —normalized root-mean-squared pulse width.	164
6.13	The contours of the plots shown in 6.12	165
6.14	Extraction errors for (a) total timing jitter, $\epsilon_{\Delta T}$, (b) uncorrelated timing jitter, $\epsilon_{\Delta T_u}$, and (c) correlated timing jitter, $\epsilon_{\Delta T_c}$, obtained with the uncompensated mixing method. σ_A/A —normalized total amplitude jitter. σ_T/T —normalized total timing jitter. σ_s/T —normalized root-mean-squared pulse width.	167
6.15	Extraction errors for the correlation times of the (a) correlated amplitude jitter, $\epsilon_{\Delta A_c}$ and (b) timing jitter, $\epsilon_{\Delta T_c}$, obtained with the uncompensated mixing method. σ_A/A —normalized total amplitude jitter. σ_T/T —normalized total timing jitter. σ_s/T —normalized root-mean-squared pulse width.	168
6.16	Extraction errors for (a) total amplitude jitter, $\epsilon_{\Delta A}$, (b) uncorrelated amplitude jitter, $\epsilon_{\Delta A_u}$, and (c) correlated amplitude jitter, $\epsilon_{\Delta A_c}$, obtained with the compensated mixing method. σ_A/A —normalized total amplitude jitter. σ_T/T —normalized total timing jitter. σ_s/T —normalized root-mean-squared pulse width.	170
6.17	The contours of the plots shown in 6.16	171
6.18	Extraction errors for (a) total timing jitter, $\epsilon_{\Delta T}$, (b) uncorrelated timing jitter, $\epsilon_{\Delta T_u}$, and (c) correlated timing jitter, $\epsilon_{\Delta T_c}$, obtained with the compensated mixing method. σ_A/A —normalized total amplitude jitter. σ_T/T —normalized total timing jitter. σ_s/T —normalized root-mean-squared pulse width.	173

A.1	A random variable, X , with a uniform probability distribution function, p_X . μ_X —the mean of X . a —a constant.	182
B.1	Extraction errors for (a) total amplitude jitter, $\epsilon_{\Delta A}$, (b) uncorrelated amplitude jitter, $\epsilon_{\Delta A_u}$, and (c) correlated amplitude jitter, $\epsilon_{\Delta A_c}$, obtained with the uncompensated direct method. σ_A/A —normalized total amplitude jitter. σ_T/T —normalized total timing jitter. σ_s/T —normalized root-mean-squared pulse width.	184
B.2	The contours of the plots shown in B.1	185
B.3	Extraction errors for (a) total amplitude jitter, $\epsilon_{\Delta A}$, (b) uncorrelated amplitude jitter, $\epsilon_{\Delta A_u}$, and (c) correlated amplitude jitter, $\epsilon_{\Delta A_c}$, obtained with the uncompensated direct method. σ_A/A —normalized total amplitude jitter. σ_T/T —normalized total timing jitter. σ_s/T —normalized root-mean-squared pulse width.	186
B.4	The contours of the plots shown in B.3	187
B.5	Extraction errors for (a) total amplitude jitter, $\epsilon_{\Delta A}$, (b) uncorrelated amplitude jitter, $\epsilon_{\Delta A_u}$, and (c) correlated amplitude jitter, $\epsilon_{\Delta A_c}$, obtained with the uncompensated direct method. σ_A/A —normalized total amplitude jitter. σ_T/T —normalized total timing jitter. σ_s/T —normalized root-mean-squared pulse width.	188
B.6	The contours of the plots shown in B.5	189
B.7	Extraction errors for (a) total amplitude jitter, $\epsilon_{\Delta A}$, (b) uncorrelated amplitude jitter, $\epsilon_{\Delta A_u}$, and (c) correlated amplitude jitter, $\epsilon_{\Delta A_c}$, obtained with the uncompensated direct method. σ_A/A —normalized total amplitude jitter. σ_T/T —normalized total timing jitter. σ_s/T —normalized root-mean-squared pulse width.	190
B.8	The contours of the plots shown in B.7	191

B.9	Extraction errors for (a) total amplitude jitter, $\epsilon_{\Delta A}$, (b) uncorrelated amplitude jitter, $\epsilon_{\Delta A_u}$, and (c) correlated amplitude jitter, $\epsilon_{\Delta A_c}$, obtained with the uncompensated direct method. σ_A/A —normalized total amplitude jitter. σ_T/T —normalized total timing jitter. σ_s/T —normalized root-mean-squared pulse width.	192
B.10	The contours of the plots shown in B.9	193
B.11	Extraction errors for (a) total amplitude jitter, $\epsilon_{\Delta A}$, (b) uncorrelated amplitude jitter, $\epsilon_{\Delta A_u}$, and (c) correlated amplitude jitter, $\epsilon_{\Delta A_c}$, obtained with the uncompensated direct method. σ_A/A —normalized total amplitude jitter. σ_T/T —normalized total timing jitter. σ_s/T —normalized root-mean-squared pulse width.	194
B.12	The contours of the plots shown in B.11	195
B.13	Extraction errors for (a) total amplitude jitter, $\epsilon_{\Delta A}$, (b) uncorrelated amplitude jitter, $\epsilon_{\Delta A_u}$, and (c) correlated amplitude jitter, $\epsilon_{\Delta A_c}$, obtained with the uncompensated direct method. σ_A/A —normalized total amplitude jitter. σ_T/T —normalized total timing jitter. σ_s/T —normalized root-mean-squared pulse width.	196
B.14	The contours of the plots shown in B.13	197
B.15	Extraction errors for (a) total timing jitter, $\epsilon_{\Delta T}$, (b) uncorrelated timing jitter, $\epsilon_{\Delta T_u}$, and (c) correlated timing jitter, $\epsilon_{\Delta T_c}$, obtained with the uncompensated direct method. σ_A/A —normalized total amplitude jitter. σ_T/T —normalized total timing jitter. σ_s/T —normalized root-mean-squared pulse width.	199
B.16	The contours of the plots shown in B.15	200

B.17	Extraction errors for (a) total timing jitter, $\epsilon_{\Delta T}$, (b) uncorrelated timing jitter, $\epsilon_{\Delta T_u}$, and (c) correlated timing jitter, $\epsilon_{\Delta T_c}$, obtained with the uncompensated direct method. σ_A/A —normalized total amplitude jitter. σ_T/T —normalized total timing jitter. σ_s/T —normalized root-mean-squared pulse width.	201
B.18	The contours of the plots shown in B.17	202
B.19	Extraction errors for (a) total timing jitter, $\epsilon_{\Delta T}$, (b) uncorrelated timing jitter, $\epsilon_{\Delta T_u}$, and (c) correlated timing jitter, $\epsilon_{\Delta T_c}$, obtained with the uncompensated direct method. σ_A/A —normalized total amplitude jitter. σ_T/T —normalized total timing jitter. σ_s/T —normalized root-mean-squared pulse width.	203
B.20	The contours of the plots shown in B.19	204
B.21	Extraction errors for (a) total timing jitter, $\epsilon_{\Delta T}$, (b) uncorrelated timing jitter, $\epsilon_{\Delta T_u}$, and (c) correlated timing jitter, $\epsilon_{\Delta T_c}$, obtained with the uncompensated direct method. σ_A/A —normalized total amplitude jitter. σ_T/T —normalized total timing jitter. σ_s/T —normalized root-mean-squared pulse width.	205
B.22	The contours of the plots shown in B.21	206
B.23	Extraction errors for (a) total timing jitter, $\epsilon_{\Delta T}$, (b) uncorrelated timing jitter, $\epsilon_{\Delta T_u}$, and (c) correlated timing jitter, $\epsilon_{\Delta T_c}$, obtained with the uncompensated direct method. σ_A/A —normalized total amplitude jitter. σ_T/T —normalized total timing jitter. σ_s/T —normalized root-mean-squared pulse width.	207
B.24	The contours of the plots shown in B.23	208

B.25	Extraction errors for (a) total timing jitter, $\epsilon_{\Delta T}$, (b) uncorrelated timing jitter, $\epsilon_{\Delta T_u}$, and (c) correlated timing jitter, $\epsilon_{\Delta T_c}$, obtained with the uncompensated direct method. σ_A/A —normalized total amplitude jitter. σ_T/T —normalized total timing jitter. σ_s/T —normalized root-mean-squared pulse width.	209
B.26	The contours of the plots shown in B.25	210
B.27	Extraction errors for (a) total timing jitter, $\epsilon_{\Delta T}$, (b) uncorrelated timing jitter, $\epsilon_{\Delta T_u}$, and (c) correlated timing jitter, $\epsilon_{\Delta T_c}$, obtained with the uncompensated direct method. σ_A/A —normalized total amplitude jitter. σ_T/T —normalized total timing jitter. σ_s/T —normalized root-mean-squared pulse width.	211
B.28	The contours of the plots shown in B.27	212
B.29	Extraction errors for the correlation times of the (a) correlated amplitude jitter, $\epsilon_{\Delta A_c}$ and (b) timing jitter, $\epsilon_{\Delta T_c}$, obtained with the uncompensated direct method. σ_A/A —normalized total amplitude jitter. σ_T/T —normalized total timing jitter. σ_s/T —normalized root-mean-squared pulse width.	214
B.30	Extraction errors for the correlation times of the (a) correlated amplitude jitter, $\epsilon_{\Delta A_c}$ and (b) timing jitter, $\epsilon_{\Delta T_c}$, obtained with the uncompensated direct method. σ_A/A —normalized total amplitude jitter. σ_T/T —normalized total timing jitter. σ_s/T —normalized root-mean-squared pulse width.	214
B.31	Extraction errors for the correlation times of the (a) correlated amplitude jitter, $\epsilon_{\Delta A_c}$ and (b) timing jitter, $\epsilon_{\Delta T_c}$, obtained with the uncompensated direct method. σ_A/A —normalized total amplitude jitter. σ_T/T —normalized total timing jitter. σ_s/T —normalized root-mean-squared pulse width.	215

B.32	Extraction errors for the correlation times of the (a) correlated amplitude jitter, $\epsilon_{\Delta A_c}$ and (b) timing jitter, $\epsilon_{\Delta T_c}$, obtained with the uncompensated direct method. σ_A/A —normalized total amplitude jitter. σ_T/T —normalized total timing jitter. σ_s/T —normalized root-mean-squared pulse width.	215
B.33	Extraction errors for the correlation times of the (a) correlated amplitude jitter, $\epsilon_{\Delta A_c}$ and (b) timing jitter, $\epsilon_{\Delta T_c}$, obtained with the uncompensated direct method. σ_A/A —normalized total amplitude jitter. σ_T/T —normalized total timing jitter. σ_s/T —normalized root-mean-squared pulse width.	216
B.34	Extraction errors for the correlation times of the (a) correlated amplitude jitter, $\epsilon_{\Delta A_c}$ and (b) timing jitter, $\epsilon_{\Delta T_c}$, obtained with the uncompensated direct method. σ_A/A —normalized total amplitude jitter. σ_T/T —normalized total timing jitter. σ_s/T —normalized root-mean-squared pulse width.	216
B.35	Extraction errors for the correlation times of the (a) correlated amplitude jitter, $\epsilon_{\Delta A_c}$ and (b) timing jitter, $\epsilon_{\Delta T_c}$, obtained with the uncompensated direct method. σ_A/A —normalized total amplitude jitter. σ_T/T —normalized total timing jitter. σ_s/T —normalized root-mean-squared pulse width.	217
C.1	Extraction errors for (a) total amplitude jitter, $\epsilon_{\Delta A}$, (b) uncorrelated amplitude jitter, $\epsilon_{\Delta A_u}$, and (c) correlated amplitude jitter, $\epsilon_{\Delta A_c}$, obtained with the compensated direct method. σ_A/A —normalized total amplitude jitter. σ_T/T —normalized total timing jitter. σ_s/T —normalized root-mean-squared pulse width.	219
C.2	The contours of the plots shown in C.1	220

C.3	Extraction errors for (a) total amplitude jitter, $\epsilon_{\Delta A}$, (b) uncorrelated amplitude jitter, $\epsilon_{\Delta A_u}$, and (c) correlated amplitude jitter, $\epsilon_{\Delta A_c}$, obtained with the compensated direct method. σ_A/A —normalized total amplitude jitter. σ_T/T —normalized total timing jitter. σ_s/T —normalized root-mean-squared pulse width.	221
C.4	The contours of the plots shown in C.3	222
C.5	Extraction errors for (a) total amplitude jitter, $\epsilon_{\Delta A}$, (b) uncorrelated amplitude jitter, $\epsilon_{\Delta A_u}$, and (c) correlated amplitude jitter, $\epsilon_{\Delta A_c}$, obtained with the compensated direct method. σ_A/A —normalized total amplitude jitter. σ_T/T —normalized total timing jitter. σ_s/T —normalized root-mean-squared pulse width.	223
C.6	The contours of the plots shown in C.5	224
C.7	Extraction errors for (a) total amplitude jitter, $\epsilon_{\Delta A}$, (b) uncorrelated amplitude jitter, $\epsilon_{\Delta A_u}$, and (c) correlated amplitude jitter, $\epsilon_{\Delta A_c}$, obtained with the compensated direct method. σ_A/A —normalized total amplitude jitter. σ_T/T —normalized total timing jitter. σ_s/T —normalized root-mean-squared pulse width.	225
C.8	The contours of the plots shown in C.7	226
C.9	Extraction errors for (a) total amplitude jitter, $\epsilon_{\Delta A}$, (b) uncorrelated amplitude jitter, $\epsilon_{\Delta A_u}$, and (c) correlated amplitude jitter, $\epsilon_{\Delta A_c}$, obtained with the compensated direct method. σ_A/A —normalized total amplitude jitter. σ_T/T —normalized total timing jitter. σ_s/T —normalized root-mean-squared pulse width.	227
C.10	The contours of the plots shown in C.9	228

C.11 Extraction errors for (a) total amplitude jitter, $\epsilon_{\Delta A}$, (b) uncorrelated amplitude jitter, $\epsilon_{\Delta A_u}$, and (c) correlated amplitude jitter, $\epsilon_{\Delta A_c}$, obtained with the compensated direct method. σ_A/A —normalized total amplitude jitter. σ_T/T —normalized total timing jitter. σ_s/T —normalized root-mean-squared pulse width.	229
C.12 The contours of the plots shown in C.11	230
C.13 Extraction errors for (a) total amplitude jitter, $\epsilon_{\Delta A}$, (b) uncorrelated amplitude jitter, $\epsilon_{\Delta A_u}$, and (c) correlated amplitude jitter, $\epsilon_{\Delta A_c}$, obtained with the compensated direct method. σ_A/A —normalized total amplitude jitter. σ_T/T —normalized total timing jitter. σ_s/T —normalized root-mean-squared pulse width.	231
C.14 The contours of the plots shown in C.13	232
C.15 Extraction errors for (a) total timing jitter, $\epsilon_{\Delta T}$, (b) uncorrelated timing jitter, $\epsilon_{\Delta T_u}$, and (c) correlated timing jitter, $\epsilon_{\Delta T_c}$, obtained with the compensated direct method. σ_A/A —normalized total amplitude jitter. σ_T/T —normalized total timing jitter. σ_s/T —normalized root-mean-squared pulse width.	234
C.16 Extraction errors for (a) total timing jitter, $\epsilon_{\Delta T}$, (b) uncorrelated timing jitter, $\epsilon_{\Delta T_u}$, and (c) correlated timing jitter, $\epsilon_{\Delta T_c}$, obtained with the compensated direct method. σ_A/A —normalized total amplitude jitter. σ_T/T —normalized total timing jitter. σ_s/T —normalized root-mean-squared pulse width.	235
C.17 Extraction errors for (a) total timing jitter, $\epsilon_{\Delta T}$, (b) uncorrelated timing jitter, $\epsilon_{\Delta T_u}$, and (c) correlated timing jitter, $\epsilon_{\Delta T_c}$, obtained with the compensated direct method. σ_A/A —normalized total amplitude jitter. σ_T/T —normalized total timing jitter. σ_s/T —normalized root-mean-squared pulse width.	236

C.18	Extraction errors for (a) total timing jitter, $\epsilon_{\Delta T}$, (b) uncorrelated timing jitter, $\epsilon_{\Delta T_u}$, and (c) correlated timing jitter, $\epsilon_{\Delta T_c}$, obtained with the compensated direct method. σ_A/A —normalized total amplitude jitter. σ_T/T —normalized total timing jitter. σ_s/T —normalized root-mean-squared pulse width.	237
C.19	Extraction errors for (a) total timing jitter, $\epsilon_{\Delta T}$, (b) uncorrelated timing jitter, $\epsilon_{\Delta T_u}$, and (c) correlated timing jitter, $\epsilon_{\Delta T_c}$, obtained with the compensated direct method. σ_A/A —normalized total amplitude jitter. σ_T/T —normalized total timing jitter. σ_s/T —normalized root-mean-squared pulse width.	238
C.20	Extraction errors for (a) total timing jitter, $\epsilon_{\Delta T}$, (b) uncorrelated timing jitter, $\epsilon_{\Delta T_u}$, and (c) correlated timing jitter, $\epsilon_{\Delta T_c}$, obtained with the compensated direct method. σ_A/A —normalized total amplitude jitter. σ_T/T —normalized total timing jitter. σ_s/T —normalized root-mean-squared pulse width.	239
C.21	Extraction errors for (a) total timing jitter, $\epsilon_{\Delta T}$, (b) uncorrelated timing jitter, $\epsilon_{\Delta T_u}$, and (c) correlated timing jitter, $\epsilon_{\Delta T_c}$, obtained with the compensated direct method. σ_A/A —normalized total amplitude jitter. σ_T/T —normalized total timing jitter. σ_s/T —normalized root-mean-squared pulse width.	240
D.1	Extraction errors for (a) total amplitude jitter, $\epsilon_{\Delta A}$, (b) uncorrelated amplitude jitter, $\epsilon_{\Delta A_u}$, and (c) correlated amplitude jitter, $\epsilon_{\Delta A_c}$, obtained with the uncompensated mixing method. σ_A/A —normalized total amplitude jitter. σ_T/T —normalized total timing jitter. σ_s/T —normalized root-mean-squared pulse width.	243
D.2	The contours of the plots shown in D.1	244

D.3	Extraction errors for (a) total amplitude jitter, $\epsilon_{\Delta A}$, (b) uncorrelated amplitude jitter, $\epsilon_{\Delta A_u}$, and (c) correlated amplitude jitter, $\epsilon_{\Delta A_c}$, obtained with the uncompensated mixing method. σ_A/A —normalized total amplitude jitter. σ_T/T —normalized total timing jitter. σ_s/T —normalized root-mean-squared pulse width.	245
D.4	The contours of the plots shown in D.3	246
D.5	Extraction errors for (a) total amplitude jitter, $\epsilon_{\Delta A}$, (b) uncorrelated amplitude jitter, $\epsilon_{\Delta A_u}$, and (c) correlated amplitude jitter, $\epsilon_{\Delta A_c}$, obtained with the uncompensated mixing method. σ_A/A —normalized total amplitude jitter. σ_T/T —normalized total timing jitter. σ_s/T —normalized root-mean-squared pulse width.	247
D.6	The contours of the plots shown in D.5	248
D.7	Extraction errors for (a) total amplitude jitter, $\epsilon_{\Delta A}$, (b) uncorrelated amplitude jitter, $\epsilon_{\Delta A_u}$, and (c) correlated amplitude jitter, $\epsilon_{\Delta A_c}$, obtained with the uncompensated mixing method. σ_A/A —normalized total amplitude jitter. σ_T/T —normalized total timing jitter. σ_s/T —normalized root-mean-squared pulse width.	249
D.8	The contours of the plots shown in D.7	250
D.9	Extraction errors for (a) total amplitude jitter, $\epsilon_{\Delta A}$, (b) uncorrelated amplitude jitter, $\epsilon_{\Delta A_u}$, and (c) correlated amplitude jitter, $\epsilon_{\Delta A_c}$, obtained with the uncompensated mixing method. σ_A/A —normalized total amplitude jitter. σ_T/T —normalized total timing jitter. σ_s/T —normalized root-mean-squared pulse width.	251
D.10	The contours of the plots shown in D.9	252

D.11 Extraction errors for (a) total timing jitter, $\epsilon_{\Delta T}$, (b) uncorrelated timing jitter, $\epsilon_{\Delta T_u}$, and (c) correlated timing jitter, $\epsilon_{\Delta T_c}$, obtained with the uncompensated mixing method. σ_A/A —normalized total amplitude jitter. σ_T/T —normalized total timing jitter. σ_s/T —normalized root-mean-squared pulse width.	254
D.12 Extraction errors for (a) total timing jitter, $\epsilon_{\Delta T}$, (b) uncorrelated timing jitter, $\epsilon_{\Delta T_u}$, and (c) correlated timing jitter, $\epsilon_{\Delta T_c}$, obtained with the uncompensated mixing method. σ_A/A —normalized total amplitude jitter. σ_T/T —normalized total timing jitter. σ_s/T —normalized root-mean-squared pulse width.	255
D.13 Extraction errors for (a) total timing jitter, $\epsilon_{\Delta T}$, (b) uncorrelated timing jitter, $\epsilon_{\Delta T_u}$, and (c) correlated timing jitter, $\epsilon_{\Delta T_c}$, obtained with the uncompensated mixing method. σ_A/A —normalized total amplitude jitter. σ_T/T —normalized total timing jitter. σ_s/T —normalized root-mean-squared pulse width.	256
D.14 Extraction errors for (a) total timing jitter, $\epsilon_{\Delta T}$, (b) uncorrelated timing jitter, $\epsilon_{\Delta T_u}$, and (c) correlated timing jitter, $\epsilon_{\Delta T_c}$, obtained with the uncompensated mixing method. σ_A/A —normalized total amplitude jitter. σ_T/T —normalized total timing jitter. σ_s/T —normalized root-mean-squared pulse width.	257
D.15 Extraction errors for (a) total timing jitter, $\epsilon_{\Delta T}$, (b) uncorrelated timing jitter, $\epsilon_{\Delta T_u}$, and (c) correlated timing jitter, $\epsilon_{\Delta T_c}$, obtained with the uncompensated mixing method. σ_A/A —normalized total amplitude jitter. σ_T/T —normalized total timing jitter. σ_s/T —normalized root-mean-squared pulse width.	258

D.16 Extraction errors for the correlation times of the (a) correlated amplitude jitter, $\epsilon_{\Delta A_c}$ and (b) timing jitter, $\epsilon_{\Delta T_c}$, obtained with the uncompensated mixing method. σ_A/A —normalized total amplitude jitter. σ_T/T —normalized total timing jitter. σ_s/T —normalized root-mean-squared pulse width.	260
D.17 Extraction errors for the correlation times of the (a) correlated amplitude jitter, $\epsilon_{\Delta A_c}$ and (b) timing jitter, $\epsilon_{\Delta T_c}$, obtained with the uncompensated mixing method. σ_A/A —normalized total amplitude jitter. σ_T/T —normalized total timing jitter. σ_s/T —normalized root-mean-squared pulse width.	260
D.18 Extraction errors for the correlation times of the (a) correlated amplitude jitter, $\epsilon_{\Delta A_c}$ and (b) timing jitter, $\epsilon_{\Delta T_c}$, obtained with the uncompensated mixing method. σ_A/A —normalized total amplitude jitter. σ_T/T —normalized total timing jitter. σ_s/T —normalized root-mean-squared pulse width.	261
D.19 Extraction errors for the correlation times of the (a) correlated amplitude jitter, $\epsilon_{\Delta A_c}$ and (b) timing jitter, $\epsilon_{\Delta T_c}$, obtained with the uncompensated mixing method. σ_A/A —normalized total amplitude jitter. σ_T/T —normalized total timing jitter. σ_s/T —normalized root-mean-squared pulse width.	261
D.20 Extraction errors for the correlation times of the (a) correlated amplitude jitter, $\epsilon_{\Delta A_c}$ and (b) timing jitter, $\epsilon_{\Delta T_c}$, obtained with the uncompensated mixing method. σ_A/A —normalized total amplitude jitter. σ_T/T —normalized total timing jitter. σ_s/T —normalized root-mean-squared pulse width.	262

E.1	Extraction errors for (a) total amplitude jitter, $\epsilon_{\Delta A}$, (b) uncorrelated amplitude jitter, $\epsilon_{\Delta A_u}$, and (c) correlated amplitude jitter, $\epsilon_{\Delta A_c}$, obtained with the compensated mixing method. σ_A/A —normalized total amplitude jitter. σ_T/T —normalized total timing jitter. σ_s/T —normalized root-mean-squared pulse width.	264
E.2	The contours of the plots shown in E.1	265
E.3	Extraction errors for (a) total amplitude jitter, $\epsilon_{\Delta A}$, (b) uncorrelated amplitude jitter, $\epsilon_{\Delta A_u}$, and (c) correlated amplitude jitter, $\epsilon_{\Delta A_c}$, obtained with the compensated mixing method. σ_A/A —normalized total amplitude jitter. σ_T/T —normalized total timing jitter. σ_s/T —normalized root-mean-squared pulse width.	266
E.4	The contours of the plots shown in E.3	267
E.5	Extraction errors for (a) total amplitude jitter, $\epsilon_{\Delta A}$, (b) uncorrelated amplitude jitter, $\epsilon_{\Delta A_u}$, and (c) correlated amplitude jitter, $\epsilon_{\Delta A_c}$, obtained with the compensated mixing method. σ_A/A —normalized total amplitude jitter. σ_T/T —normalized total timing jitter. σ_s/T —normalized root-mean-squared pulse width.	268
E.6	The contours of the plots shown in E.5	269
E.7	Extraction errors for (a) total amplitude jitter, $\epsilon_{\Delta A}$, (b) uncorrelated amplitude jitter, $\epsilon_{\Delta A_u}$, and (c) correlated amplitude jitter, $\epsilon_{\Delta A_c}$, obtained with the compensated mixing method. σ_A/A —normalized total amplitude jitter. σ_T/T —normalized total timing jitter. σ_s/T —normalized root-mean-squared pulse width.	270
E.8	The contours of the plots shown in E.7	271

E.9	Extraction errors for (a) total amplitude jitter, $\epsilon_{\Delta A}$, (b) uncorrelated amplitude jitter, $\epsilon_{\Delta A_u}$, and (c) correlated amplitude jitter, $\epsilon_{\Delta A_c}$, obtained with the compensated mixing method. σ_A/A —normalized total amplitude jitter. σ_T/T —normalized total timing jitter. σ_s/T —normalized root-mean-squared pulse width.	272
E.10	The contours of the plots shown in E.9	273
E.11	Extraction errors for (a) total timing jitter, $\epsilon_{\Delta T}$, (b) uncorrelated timing jitter, $\epsilon_{\Delta T_u}$, and (c) correlated timing jitter, $\epsilon_{\Delta T_c}$, obtained with the compensated mixing method. σ_A/A —normalized total amplitude jitter. σ_T/T —normalized total timing jitter. σ_s/T —normalized root-mean-squared pulse width.	275
E.12	Extraction errors for (a) total timing jitter, $\epsilon_{\Delta T}$, (b) uncorrelated timing jitter, $\epsilon_{\Delta T_u}$, and (c) correlated timing jitter, $\epsilon_{\Delta T_c}$, obtained with the compensated mixing method. σ_A/A —normalized total amplitude jitter. σ_T/T —normalized total timing jitter. σ_s/T —normalized root-mean-squared pulse width.	276
E.13	Extraction errors for (a) total timing jitter, $\epsilon_{\Delta T}$, (b) uncorrelated timing jitter, $\epsilon_{\Delta T_u}$, and (c) correlated timing jitter, $\epsilon_{\Delta T_c}$, obtained with the compensated mixing method. σ_A/A —normalized total amplitude jitter. σ_T/T —normalized total timing jitter. σ_s/T —normalized root-mean-squared pulse width.	277
E.14	Extraction errors for (a) total timing jitter, $\epsilon_{\Delta T}$, (b) uncorrelated timing jitter, $\epsilon_{\Delta T_u}$, and (c) correlated timing jitter, $\epsilon_{\Delta T_c}$, obtained with the compensated mixing method. σ_A/A —normalized total amplitude jitter. σ_T/T —normalized total timing jitter. σ_s/T —normalized root-mean-squared pulse width.	278

E.15 Extraction errors for (a) total timing jitter, $\epsilon_{\Delta T}$, (b) uncorrelated timing jitter, $\epsilon_{\Delta T_u}$, and (c) correlated timing jitter, $\epsilon_{\Delta T_c}$, obtained with the compensated mixing method. σ_A/A —normalized total amplitude jitter. σ_T/T —normalized total timing jitter. σ_s/T —normalized root-mean-squared pulse width. 279

Summary

In this document, we consider the performance required of an optical-pulse source for use in ultrafast optically time-division-multiplexed communications systems. For such a source, the jitter is a critical parameter for achieving a desired bit-error rate.

We describe a pulse source, consisting of a gain-switched laser diode, a linear pulse compressor, an adiabatic soliton pulse compressor, and a pedestal suppressor. This source meets most of the established criteria. We also examine a means of reducing the jitter of a gain-switched laser diode, the phenomenon of temporal-multiplexing-induced amplitude jitter, and two techniques for characterizing any pulse train's jitter.

We experimentally compare gain-switching of a laser diode by an electrical pulse train (created by driving an impulse generator with a sinusoid) or directly by the sine wave. When the power of the *waveform driving the laser* is equal in both cases, pulse-train drive yields lower pulse width, timing jitter, and amplitude jitter. In contrast, when the power of the *sinusoid* is held constant, no advantages are found to result from pulse-train gain-switching.

We derive an expression for the power fluctuations of a temporally multiplexed pulse train in terms of its pedestal level; this expression quantifies how temporal multiplexing couples pedestal level to slow, correlated amplitude jitter. Experimental results (obtained with two pedestal-suppression devices) confirming the theory are presented.

Finally, we derive two methods of simultaneously extracting the uncorrelated and correlated contributions of the amplitude and timing jitter (and the correlation times of the correlated components) of a pulse train from radio-frequency spectra.

The first technique extracts these contributions directly from the detected train's spectrum. The second extracts the jitter from two spectra obtained from mixing the detected train with sinusoids that are in phase and in quadrature phase. Simulations detailing the conditions under which these methods are accurate are provided. Since the methods' errors are systematic, we can compensate for them, enlarging the high-accuracy domain. Experiments confirming the accuracy of the first scheme are also included.

CHAPTER 1

Introduction

1.1 Roadmap

Chapter 1 serves as an introduction to the work presented in this dissertation. Section 1.2 provides motivation for the work. Section 1.3 is a short note concerning the nomenclature employed. Section 1.4 is an overview of optical communications. Section 1.5 examines the behavior and origin of the various types of jitter. Like all chapters in this document, Chapter 1 ends with a commentary (Section 1.6).

1.2 Motivation

1.2.1 Applications of Short-Pulse Sources

Sources of low-jitter, ultrahigh-rate trains of ultrashort optical pulses have numerous applications, including the following:

- Optical sampling [1]–[7].
- Optical time and frequency metrology [8]–[22].
- Optical pump-probe measurements [23].
- Light detection and ranging (LIDAR) [24].

- Optical telecommunications.

In this dissertation, we are principally concerned with the optical-communications application.

1.2.2 Optical Communications

Typically, one of two optical multiplexing strategies is employed to exploit the enormous bandwidth available in optical fiber: wavelength-division multiplexing¹ (WDM) or optical time-division multiplexing² (OTDM). In addition, progress has recently been made in code-division multiplexing (CDM), though CDM systems are not yet commonly deployed. OTDM communications systems offer several advantages, particularly if a return-to-zero (RZ), or pulsed, format is employed. In this document, we focus on the particular requirements placed on a pulse source in OTDM systems.

1.2.3 Jitter and Pedestal Level

The performance requirements placed on an OTDM pulse source are manifold³:

- A specific repetition rate.
- Low timing jitter.
- Low amplitude jitter.
- A specific pulse shape.
- Low pedestal level.

¹ See Subsection 1.4.1.

² See Subsection 1.4.2.

³ These requirements will be explained and quantified in Subsection 1.4.4

- A narrow pulse width.
- A specific duration-bandwidth product.

In most modern communication systems, both OTDM and WDM, the timing and amplitude jitter ultimately limit error-free performance [25]. As will be shown⁴, OTDM systems require that additional attention be paid to pulse-source jitter [26] and that special care is also taken with the pedestal level [27], [28]. This manuscript is concerned with reducing and characterizing the jitter and pedestal level of the OTDM pulse source. We will show that the process of OTDM multiplexing couples the pedestal level to amplitude jitter⁵. The pedestal level is therefore essentially a jitter issue. Hence, this dissertation can truly be said to focus on jitter related to OTDM pulse sources.

1.3 Nomenclature

Before swimming off into the deep sea of jitter, we present a few notes on our nomenclature.

First, a few standard symbols: as in most optics documents, we use t , τ , f , ω , z , and λ for time, delay (used with autocorrelations), frequency measured in Hz, frequency measured in rad/s, distance in the propagation direction, and wavelength, respectively. We will use T with various subscripts to denote various periods. Additionally, f_{rep} will be the repetition rate of a laser or pulse train, measured in Hz, and ω_{rep} will be same quantity, measured in rad/s.

We will use A to represent the mean (power) amplitude of a pulse train and T to represent the mean period. The mathematics related to amplitude jitter, ΔA , and

⁴ See Subsection 1.4.4.

⁵ See Chapter 4.

timing jitter, ΔT , are often quite parallel. We therefore find it convenient to use ΔJ to stand for either amplitude or timing jitter. Via the process of back-formation, we will use J to stand in for either A or T .

Throughout this document, we use σ_x to signify the root-mean-squared (RMS) width (or standard deviation) of any variable x . Similarly, ϕ_x will represent the autocorrelation of any variable x . We will use Φ_x to stand for the Fourier transform [29] of ϕ_x and thus the power spectral density of x . We will use ε_x to refer to the error with which σ_x is extracted. Of central interest will be $\sigma_{\Delta J}$, RMS amplitude or timing jitter.

Also throughout this manuscript, we use a hat ($\hat{}$) to denote normalized variables. Thus, the normalized form of any variable x is \hat{x} . In each case, the quantity *to which* the variable is normalized will be not only apparent from context but also given. Of particular importance is the normalized RMS amplitude or timing jitter, $\hat{\sigma}_{\Delta J} \equiv \sigma_{\Delta J}/J$.

Now a word about the delimiters used in equations: we use (parentheses) to denote continuous functions and [brackets] to denote discrete functions; {braces} are therefore employed for grouping of terms.

In this document, we use “temporal multiplexing” as a synonym for “optical time-division multiplexing.” Signals can, of course, be temporally multiplexed electronically, but we consider only *optical* multiplexing schemes. Further, we will use “ultrafast” specifically to describe a link with a system rate greater than or equal to 100 Gb/s.

Finally, thought not, strictly speaking, a matter of nomenclature, an aspect of our plotting style should be pointed out. The units for each quantity in each plot are given (in parentheses) on the corresponding axis label. An exception is made for unitless quantities, in which case *no units are given*.

1.4 Optical Communications

The global demand for telecommunications services is increasing at an exponential rate [30]. Optical communication systems represent the best solution to this ever-increasing demand, since just one single-mode optical fiber offers a usable bandwidth on the order of 10 THz [31]. WDM and OTDM are the two multiplexing schemes most frequently employed to make fullest use of this bandwidth; CDM is a less mature technology. The following subsections will describe WDM and OTDM links.

1.4.1 Wavelength-Division Multiplexing

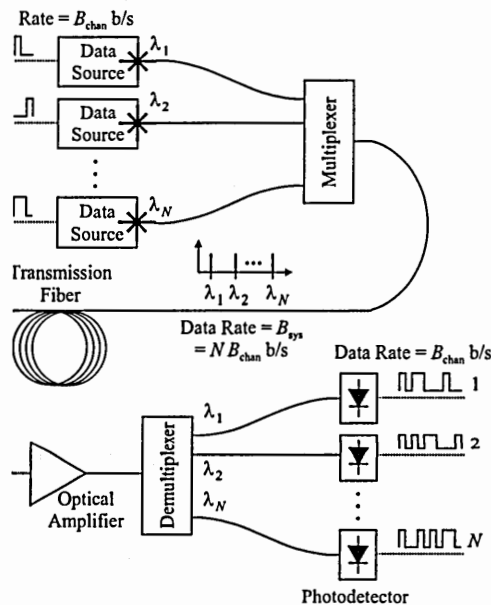


Figure 1.1: A wavelength-division-multiplexed link.

In a simple WDM link (Fig. 1.1) [32]–[34], each channel is assigned a particular wavelength. Typically, N lasers, operating at N distinct wavelengths, are independently driven to produce optical bits at the single-channel bit rate, B_{chan} . These bit streams are combined by a wavelength multiplexer onto a single fiber. This process results in a system data rate, B_{sys} , equal to $N B_{\text{chan}}$. The channels travel together

across the link to the wavelength demultiplexer, where they are separated out onto individual fibers. A photodetector associated with each channel converts the optical signal into an electrical one. It is important to note that all the electronics in the system operate at the channel rate. It should also be pointed out that a WDM *network* can be assembled by combining multiple links with switches, add/drop multiplexers, and other hardware.

1.4.2 Optical Time-Division Multiplexing

In temporally multiplexed systems, each channel is assigned a particular time slot. OTDM links can be assembled with multiple sources, like the a WDM system, or with a single source. As in the WDM case, an OTDM network can be built by combining multiple links, switches, add/drop multiplexers, and other hardware.

1.4.2.1 Multiple-Source Link

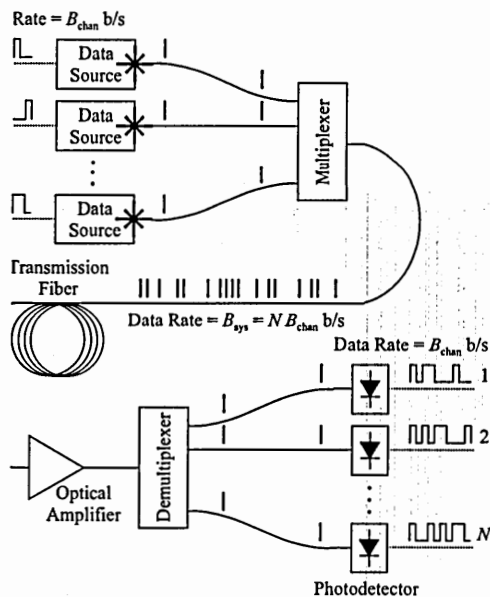


Figure 1.2: A multi-source optically time-division-multiplexed link.

The direct temporal equivalent of the WDM system is the multi-source OTDM link shown in Fig. 1.2. In this system, N lasers, each at the same wavelength, are modulated at the single-channel bit rate, B_{chan} . The channel bit period, T_{chan} , is $1/B_{\text{chan}}$. A passive (non-modulating) temporal multiplexer combines the data streams onto one fiber, placing each pulse in its appropriate time slot to form a single-color data stream at the system bit rate, $B_{\text{sys}} = NB_{\text{chan}}$. The system bit period, T_{sys} , is $1/B_{\text{sys}} = T_{\text{chan}}/N$. At the far end of the link, a demultiplexer splits the channels onto individual fibers. The optical pulses on each fiber are then detected. Note that the relative delay between channels to be multiplexed is critical; either the data sources must be synchronized, taking into account the differing propagation delays, or the multiplexer must re-time the incoming data. This additional difficulty (with respect to a single-source OTDM link) may be justified, however, if the transmitters must be physically separated from one another.

1.4.2.2 Single-Source Link

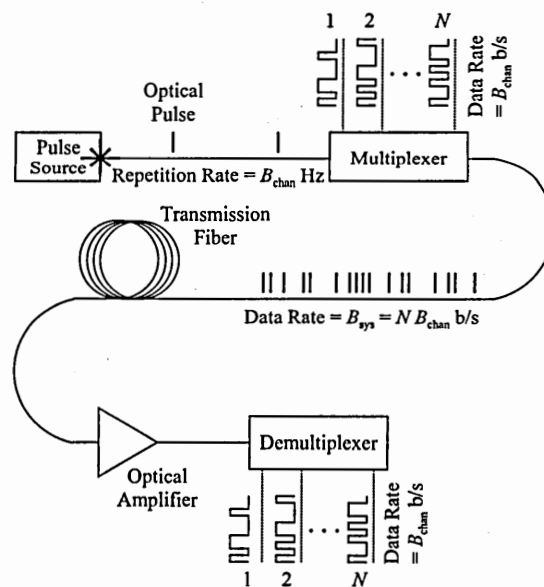


Figure 1.3: A single-source optically time-division-multiplexed link.

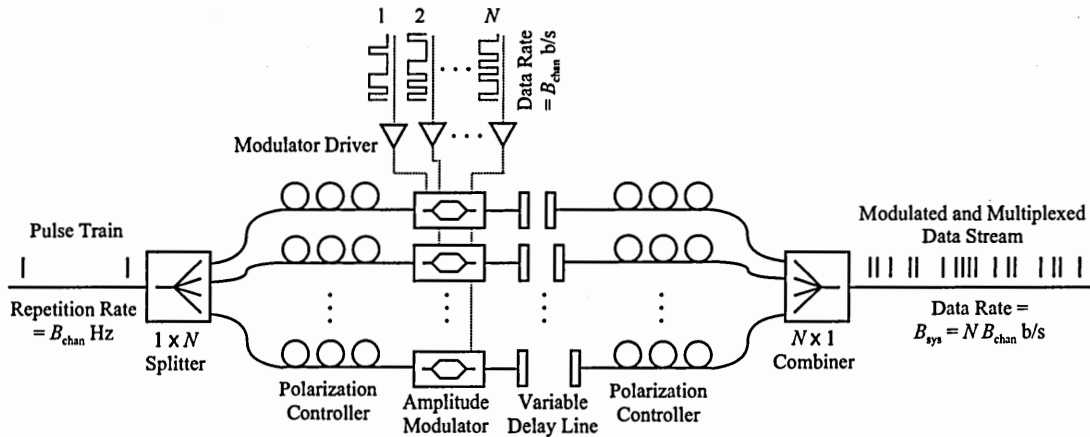


Figure 1.4: A modulating temporal multiplexer.

In practice, most OTDM links rely only on a single pulse source (Fig. 1.3) [35], [36]. In this variant, one laser is driven to produce an unmodulated pulse train⁶ with a repetition frequency, f_{rep} , equal to B_{chan} . An active (modulating) temporal multiplexer (Fig. 1.4) splits the pulse train into N paths, which are each modulated at B_{chan} , differentially delayed, and recombined to form a data stream at the system bit rate, $B_{\text{sys}} = NB_{\text{chan}}$. At the far end of the link, a temporal demultiplexer separates the channels, which are each detected. This type of OTDM system does not require careful timing of multiple sources or clock recovery. Only the differential delays within the multiplexer, which are fixed, require fine timing. Thus, the single-source OTDM link is considerably simpler to operate than the multiple-source variant.

The temporal demultiplexers shown in Figs. 1.2 and 1.3 are full serial-to-parallel converters; they each extract all N channels [35], [37], [38]. In either OTDM scheme a single-channel demultiplexer, such as an ultrafast nonlinear interferometer [39]–[42], a nonlinear-optical-loop-mirror demultiplexer [43]–[46], a terahertz optical asymmetric demultiplexer [47]–[50], or a four-wave-mixing demultiplexer [51]–[53] can be used.

⁶ OTDM is typically performed with RZ data, thus the laser employed is pulsed.

1.4.3 Remarks

It should be pointed out that these two multiplexing paradigms are not antithetical; OTDM can be combined with WDM, though the spacing of the wavelength channels will necessarily be coarser, due to the greater spectral width associated with the short pulses of OTDM. That being said, OTDM links have two significant advantages over their WDM counterparts. First, WDM systems incorporate guard bands between the channels to eliminate crosstalk. OTDM operation obviates these bands, so temporally multiplexed links offer greater spectral efficiency [54]. Second, the number of pulsed lasers required (one for pure OTDM, a few if OTDM is combined with coarse WDM) in an OTDM system is lower than that of a comparable-rate WDM system, simplifying system design and error monitoring [54]. Unfortunately, because OTDM systems operate with shorter pulses, they are more sensitive to dispersion and nonlinear effects. This sensitivity can be reduced by employing solitons [55], thus *exploiting* nonlinear propagation. Return-to-zero systems allow easier nonlinearity optimization and therefore longer spans. Thus, significant effort has been devoted to developing the multi-GHz, picosecond-pulse sources required for ultrafast RZ OTDM links. It is on these sources this dissertation is focused.

1.4.4 Pulse-Source Criteria

An RZ OTDM pulse source must meet a number of strict criteria, as described below and illustrated in Figs. 1.5 and 1.6.

1.4.4.1 Repetition Rate

The pulse repetition rate (Fig. 1.5) must be identically equal to the channel rate, or the system will not function at all.

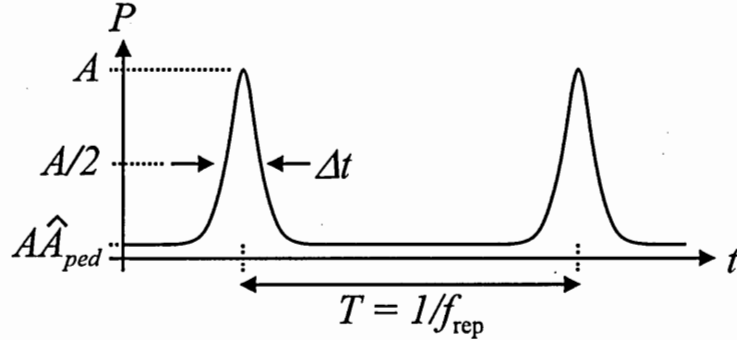


Figure 1.5: Several important parameters of a pulse train. (Timing and amplitude jitter are illustrated in Fig. 1.6.) This pulse train has not yet been multiplexed so its repetition frequency, f_{rep} , equals the channel rate. P —power. A —mean peak power. \hat{A}_{ped} —normalized pedestal power. t —time. T —period. Δt —temporal full width at half of maximum power.

1.4.4.2 Timing Jitter

The root-mean-squared (RMS) timing jitter, $\sigma_{\Delta T}$, must be much less than the system period T_{sys} or crosstalk between OTDM channels will occur. Consider the eye diagram of an non-return-to-zero (NRZ) data stream that is presented in Fig. 1.6 (The result is unchanged for an RZ data stream.), and assume the following:

- The timing jitter has Gaussian statistics.
- The timing threshold is $T_{\text{sys}}/2$.
- Probability of error is 0 between time 0 and T_{sys} and 50 % elsewhere.
- There is no amplitude jitter.

With these assumptions we can calculate the bit-error rate (BER) due solely to timing jitter, $\text{BER}_{\Delta T}$:

$$\text{BER}_{\Delta T} = \frac{1}{2} \text{erfc} \left(\frac{1}{2\sqrt{2}\hat{\sigma}_{\Delta T}} \right) . \quad (1.1)$$

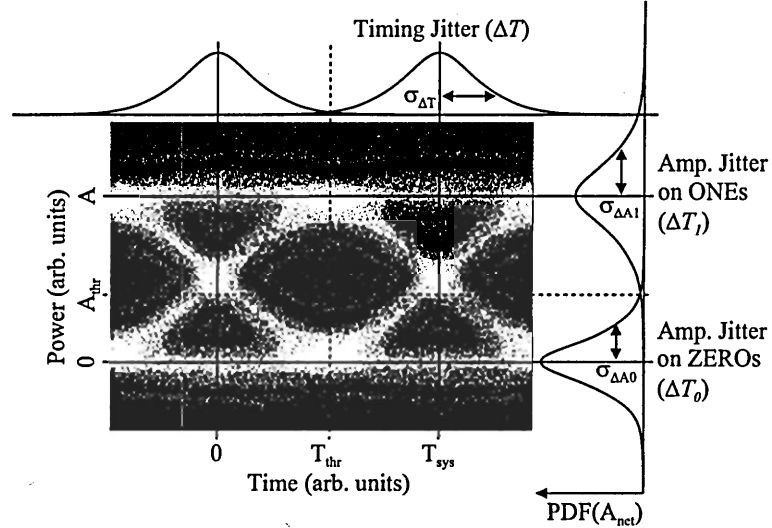


Figure 1.6: An eye diagram of a non-return-to-zero data stream. T_{sys} —mean system period. T_{thr} —threshold time. A —mean amplitude of ONES. A_{thr} —threshold amplitude. $\sigma_{\Delta T}$ —standard deviation of timing jitter. $\sigma_{\Delta A_1}$ —standard deviation of amplitude jitter of ONES. $\sigma_{\Delta A_0}$ —standard deviation of amplitude jitter of ZEROS.

Here, $\hat{\sigma}_{\Delta T} \equiv \sigma_{\Delta T}/T_{\text{sys}}$ is the normalized standard deviation of the timing jitter and erfc is the complementary error function. From Eq. 1.1, we see that, to achieve a bit-error rate less than or equal to 10^{-9} , the standard deviation of the timing jitter must be no more than 8.4 % of the system period. To reach a $\text{BER} \leq 10^{-12}$, $\sigma_{\Delta T}$ must be $\leq 0.071T_{\text{sys}}$. This analysis is only valid if there are no other sources of errors, but it does provide some insight into the impact of timing jitter. The timing-jitter requirement is the same, relative to the system bit period, for both WDM and OTDM but, because of the higher single-color rates of temporally multiplexed links, the timing criterion is more stringent in absolute terms.

1.4.4.3 Amplitude Jitter

The RMS amplitude jitter must be much less than the mean pulse amplitude, A , or a ONE could be interpreted as a ZERO. Again, consider Fig. 1.6 and assume the following

- The amplitude jitter has Gaussian statistics.
- The amplitude jitter on the ZEROS equals that on the ONES, which implies the amplitude threshold is $A/2$, where A is the mean amplitude.
- There is no timing jitter.

With these assumptions, we can compute the BER due solely to amplitude jitter:

$$\text{BER}_{\Delta A} = \frac{1}{2} \text{erfc} \left(\frac{1}{2\sqrt{2}\hat{\sigma}_{\Delta A}} \right). \quad (1.2)$$

Here, $\hat{\sigma}_{\Delta A} \equiv \sigma_{\Delta A}/A$ is the normalized standard deviation of the timing jitter. Note that this result has the same form as Eq. 1.1, and, likewise, is valid only as long as there are no other error sources. Thus, to achieve a BER less than 10^{-9} (10^{-12}), $\hat{\sigma}_{\Delta A}$ must be below 0.084 (0.071). Both Eqs. 1.1 and 1.2 are plotted as one curve in Fig. 1.7. (Recall that J represents either A or T_{sys} and $\sigma_{\Delta J}$ stands for either ΔT or ΔT , correspondingly.)

The amplitude-jitter limit for *linear* OTDM systems (the one described in this document) is the same as that for linear WDM systems. By contrast, in OTDM communications systems employing *nonlinear* transmission, the criterion will be more strict. In nonlinear systems, the peak power of the pulses is chosen very carefully to balance the dispersion of the fiber; pulses with the incorrect peak power will be distorted during propagation. Consequently, for nonlinear systems, the BER's sensitivity to amplitude jitter will increase beyond that described by Eq. 1.2.

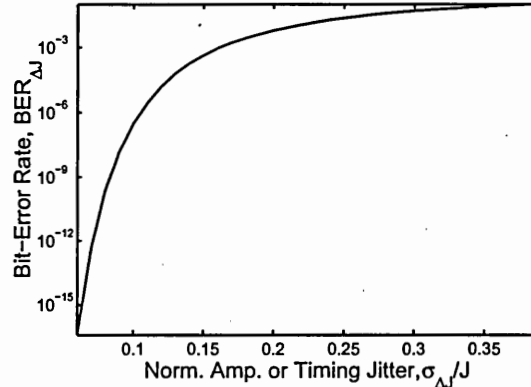


Figure 1.7: Bit-error rate due solely to either timing or amplitude jitter, $\text{BER}_{\Delta J}$ as a function of the normalized standard deviation of timing or amplitude jitter, $\sigma_{\Delta J}/J$.

1.4.4.4 Pedestal Level

The pedestal level, A_{ped} , is the instantaneous power of the pulse far from the peak (Fig. 1.5). Typically, the pedestal power normalized by the peak power, $\hat{A}_{\text{ped}} \equiv A_{\text{ped}}/A$, is discussed, and “far from the peak” is taken to mean one system period. Though the pedestal level might be deemed part of the pulse shape, we will consider it separately. For a WDM communications link, the pedestal must only be low enough to avoid intersymbol interference (ISI). For an OTDM system, the criterion is *qualitatively* different and much more stringent; the pedestal must be low enough that interpulse interference does not result in slow power fluctuations in the temporally multiplexed train⁷. These fluctuations, which amount to correlated amplitude jitter with a long correlation time, must be below the limits described above for amplitude jitter, in order to achieve the given bit-error rates⁸. We will show that, for multiplexing-induced power fluctuations no more than 8.4 % (and thus $\text{BER} \leq 10^{-9}$), the normalized pedestal level must be at least 22.7 dB below the peak. Similarly, for power fluctuations no more than 7.1 % (and $\text{BER} \leq 10^{-12}$), we will show that \hat{A}_{ped}

⁷ See Chapter 4.

⁸ Note that it is the *total* amplitude variation, given by the sum-of-squares addition of the RMS amplitude jitter inherent in the source and the RMS pedestal-induced fluctuations, that must remain under the stated limits. We will, however, examine these two effects separately.

must be at most -24.1 dB. Once again, this analysis assumes there are no other sources of errors.

1.4.4.5 Pulse Shape

In linear WDM or OTDM links, the exact shape of the pulse is noncritical. For optimal propagation in a nonlinear OTDM system, however, a fundamental soliton [55] is required. The pulse generated by the source must therefore have a sech^2 power profile.

1.4.4.6 Temporal Width

In a WDM system, Δt , the temporal full width at half maximum (FWHM), must be less than the system period (Fig. 1.5), or ISI will occur. In an OTDM system, the width of the pulse must be low enough that the wing of even a pedestal-free pulse will be below the maximum we imposed to limit power fluctuations. Thus, a hyperbolic-secant pulse, which has broader wings than a Gaussian, must have width at most 0.39 times the system period for BER to be no greater than 10^{-9} , and it must have $\Delta T \leq 0.37T_{\text{sys}}$ for BER $\leq 10^{-12}$. (Again, we assume no other error sources.)

1.4.4.7 Time-Bandwidth Product

The laser's output must be close to transform-limited (no excess spectral content), or even nonlinear propagation will not prevent dispersion-induced broadening. The time-bandwidth product (TBP) of a transform-limited hyperbolic secant is 0.315, so the TBP of the laser must be below approximately 0.40. Note that, for a linear WDM system, a hyperbolic secant pulse is not required, yielding a more relaxed TBP limit.

1.4.4.8 Remarks

While several of these conditions listed above apply to WDM sources, it is clear that jitter and pedestal level are particularly critical parameters in OTDM systems.

1.5 Jitter Tutorial

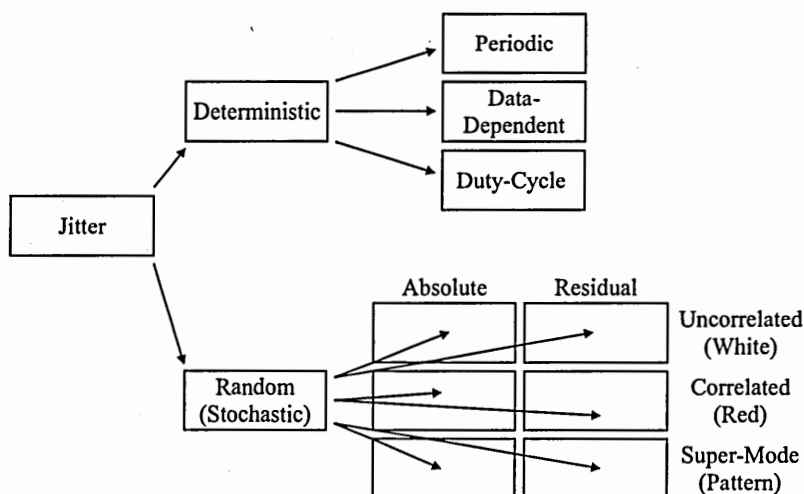


Figure 1.8: Types of jitter. This document is concerned only with random jitter (noise), with special emphasis on uncorrelated and correlated jitter.

At this point, it is helpful to explain the distinctions between the various types of jitter. As illustrated by Fig. 1.8, jitter can be categorized as either deterministic or random, and both of these types can be subcategorized.

1.5.1 Random and Deterministic

Deterministic jitter consists of *predictable, non-random* deviations, from the ideal, of the amplitude, period, or other parameter of a pulse train or data stream. Examples of deterministic jitter include data-dependent, periodic, and duty-cycle.

Data-dependent (pattern-dependent) jitter [56] can result from electronic, electro-optic, and optical processes. Different sequences of ONEs and ZEROs have different frequency content and thus propagate through the frequency-dependent system components with different group delays. This description is applicable whether the pattern appears in the electrical domain (where the frequencies in question are radio-frequency [RF] and the the frequency-dependent elements are electronic and electro-optic components, such as amplifier/drivers, modulators, detectors, and receivers) or in the optical domain (where the frequencies in question are optical and the the frequency-dependent element is dispersive fiber) [57]. Note, however, that electrical-domain pattern dependence can affect even a back-to-back (zero-distance) experiment.

Periodic jitter [56] is any jitter that repeats periodically. (This periodicity clearly places periodic jitter within the bounds of deterministic jitter.) Periodic jitter is typically caused by leakage into the system of external, periodic signals from, for example, a power supply or RF synthesizer.

Duty-cycle (edge-dependent) jitter [56] is *timing* jitter that is predicted by whether the associated edge is rising or falling. This type of jitter is therefore encountered only in NRZ systems, since, in RZ systems, every ONE bit has both a rising and falling edge. Duty-cycle jitter can come about for two reasons: (a) the rise time differs from the fall time, or (b) the decision threshold is chosen incorrectly. In either case, the histogram of the edge crossing consists of two groups, leading to increased BER.

Random jitter is just that: stochastic, nondeterministic, unpredictable. This type of jitter, often called noise because of its random nature, can be can be partitioned into two orthogonal subsets, which are illustrated by Fig. 1.8 and described in the remainder of this section. The remainder of this dissertation is concerned only with *random* jitter; it does not address deterministic jitter. We will therefore use

“noise” as a synonym for “jitter”. Accordingly, will use the phrase “total jitter” to indicate the total random jitter.

1.5.2 Absolute and Residual

The absolute jitter of a device is the jitter of the device’s output, measured relative to some ideal (constant-period, constant-amplitude) clock signal. Residual jitter [58]–[61] is the noise added to the signal, measured relative to the input. Typically, the device in question is a laser, and the radio-frequency signal employed to drive it, if any, is the reference against which the residual noise is measured. However, we could also speak of the residual jitter of a fiber link (downstream of a laser), for example, where the laser’s output is the reference clock. Note that a laser must be driven or triggered by some signal in order for the concept of residual noise to have meaning.

1.5.3 Total, Uncorrelated, Correlated, and Pattern

The total noise includes uncorrelated (white), correlated (red or drift), and pattern (super-mode) contributions, which originate from distinct mechanisms in each system component. The total timing or amplitude jitter, ΔJ , will be given by the sum of these contributions, which are denoted by a subscript u , c , or p , respectively:

$$\Delta J = \Delta J_u + \Delta J_c + \Delta J_p . \quad (1.3)$$

If the three contributions are assumed to be independent, the variance of the total jitter will be the sum of the variances of the contributions:

$$\sigma_{\Delta J}^2 = \sigma_{\Delta J_u}^2 + \sigma_{\Delta J_c}^2 + \sigma_{\Delta J_p}^2 . \quad (1.4)$$

1.5.3.1 Behavior

Let us consider the behavior of the uncorrelated, correlated, and pattern contributions. Example realizations of ΔJ_u , ΔJ_c , and ΔJ_p are plotted in Fig. 1.9. The

autocorrelations and power spectra of these sequences are shown in Figs. 1.10 and 1.11, respectively.

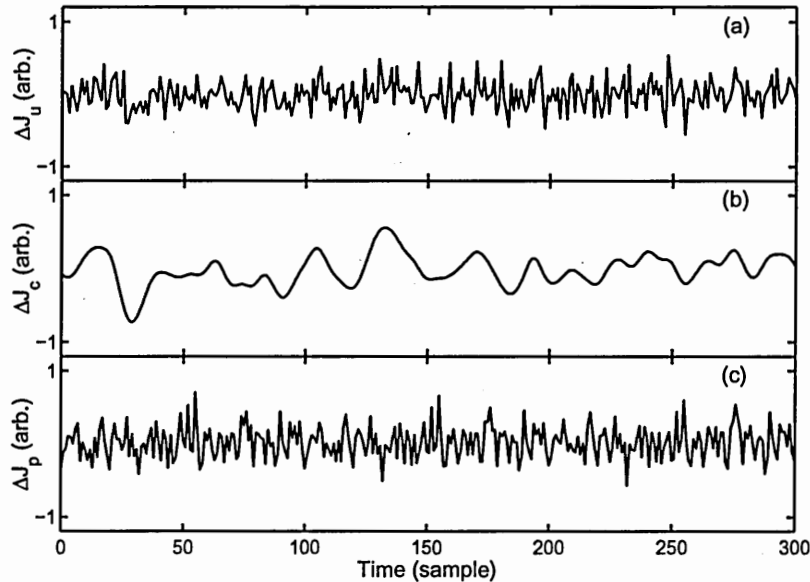


Figure 1.9: Time-domain representations of random sequences. (a) An uncorrelated random sequence, ΔJ_u . (b) A correlated random sequence, ΔJ_c . (c) A super-mode random sequence, ΔJ_p .

Consider Fig. 1.9. Each value of ΔJ_u is independent of any of the previous samples and does not affect the value of any following samples; an uncorrelated random process has no memory. In contrast, each value of ΔJ_c is affected by and affects those around it; the random sequence has memory, and can be thought of as drift. (The ΔJ_c sequence shown is the correlated version of ΔJ_u , created by convolving the ΔJ_u sequence with a pulse-shaped function.) Contrastingly, each value of ΔJ_p is correlated not with its neighbors, but with values multiples of m samples away. The resulting pattern, or super-mode, does not exactly repeat but approximately repeats every m samples. (For the example sequence shown, $m = 100$; the sequence was created by convolving samples of ΔJ_u separated by 100. The pattern almost-repeats three times in the 300 samples shown.)

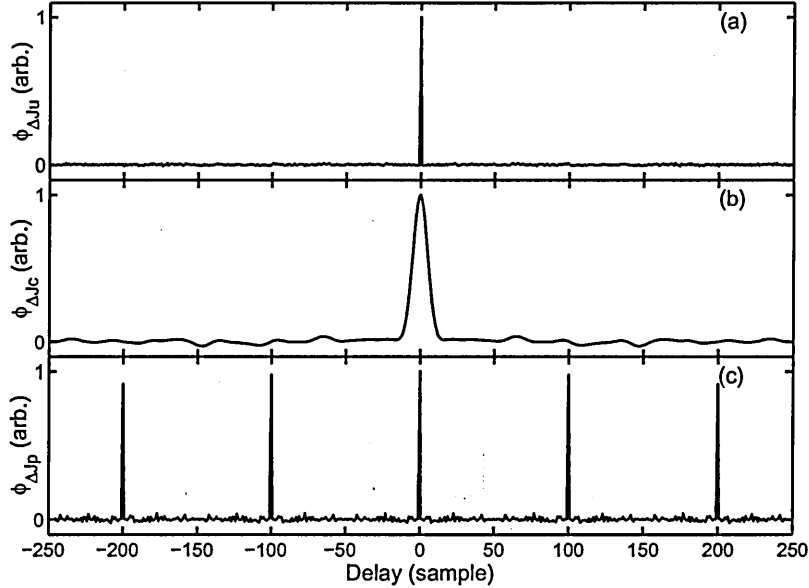


Figure 1.10: Autocorrelations of the random sequences shown in Fig. 1.9. (a) The autocorrelation of an uncorrelated random sequence, $\phi_{\Delta J_u}$. (a) The autocorrelation of a correlated random sequence, $\phi_{\Delta J_c}$. (a) The autocorrelation of a super-mode random sequence, $\phi_{\Delta J_p}$.

Now let us turn our attention to Fig. 1.10. The autocorrelation $\phi_{\Delta J_u}$ is a delta distribution located at the origin; because the values have no connection, the integral of their product is only nonzero at zero delay. Contrastingly, $\phi_{\Delta J_c}$ has finite width; because of the memory, nearby values are correlated. Meanwhile, $\phi_{\Delta J_p}$ shows spikes at all delays equal to multiples of m . However, since the pattern in ΔJ_p does not exactly repeat, the spike at zero is the tallest.

Finally, let us examine Fig. 1.11. The power spectrum $\Phi_{\Delta J_u}$ is approximately constant; all frequency bins contain equal power; all colors are equally present. For this reason, uncorrelated noise is called white noise. By comparison, $\Phi_{\Delta J_c}$ is concentrated around zero; more power is found at lower frequencies. Correlated noise is accordingly termed red noise. Thus, for some readers, it may be helpful to consider correlated noise as a band-limited version of the uncorrelated noise. Lastly, $\Phi_{\Delta J_p}$

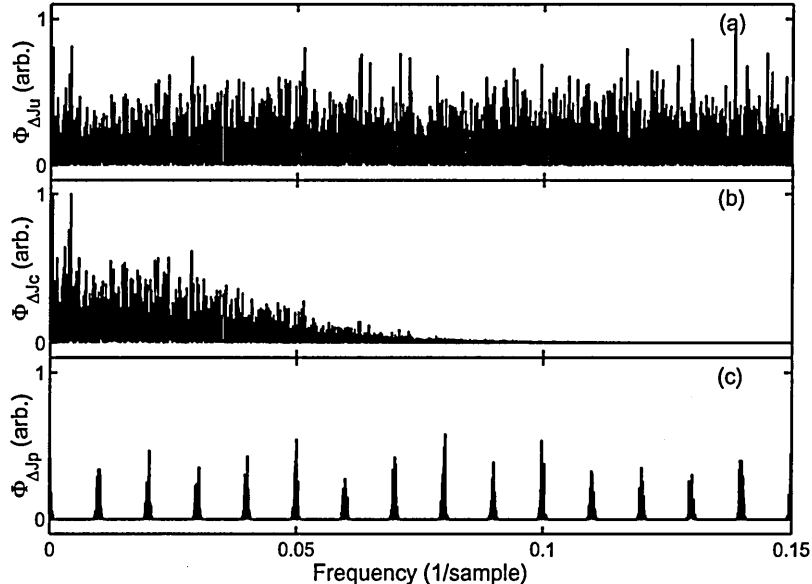


Figure 1.11: Spectra of the random sequences shown in Fig. 1.9. (a) The spectrum of an uncorrelated random sequence, $\Phi_{\Delta J_u}$. (b) The spectrum of a correlated random sequence, $\Phi_{\Delta J_c}$. (c) The spectrum of a super-mode random sequence, $\Phi_{\Delta J_p}$.

consists of spurs at multiples of $1/m$. (In the plotted realization, the spurs appear at multiples of $1/100$.)

1.5.3.2 Origins

Now let us consider the sources of the uncorrelated, correlated, and pattern contributions in real-world lasers. These sources are summarized in Table 1.1.

In directly modulated (e.g. loss-switched or gain-switched) lasers, each pulse is produced independently, beginning with a spontaneously emitted photon [62]. Consequently, the timing and peak power of the pulses are uncorrelated; each pulse has no memory of previous pulses and no impact on following ones.

A similar phenomenon affects externally modulated or mode-locked lasers. The gain medium in the laser introduces amplified spontaneous emission (ASE) into the laser's output. Each spontaneously emitted photon adds its own electric-field ampli-

tude, phase, and polarization to that of the light that is passing. These photons are uncorrelated and yield uncorrelated noise.

In lasers driven with an RF source (directly modulated, externally modulated, actively mode-locked [AML], and hybridly mode-locked [HML] lasers) the RF source's correlated noise (drift) will appear in the optical output. Fortunately, microwave sources with very low noise are readily available; hence the noise of RF-source-driven lasers may be dominated by other contributions. Similarly, any drift in a mode-locked lasers cavity's optical length (from, e.g., thermal variations) will manifest in the laser's output as correlated timing noise.

In lasers mode-locked at the fundamental, each pulse circulates within the cavity and a fraction of it is out-coupled on every revolution. Thus, any uncorrelated or correlated noise in the timing and amplitude of the n^{th} output pulse (arising from ASE, the RF source, cavity-length drift, *et cetera*) is correlated with the $(n + 1)^{\text{th}}$, the $(n + 2)^{\text{th}}$, and so on; the output of a mode-locked laser exhibits correlated noise. This drift is especially prominent in the timing noise of passively mode-locked (PML) lasers, where the pulses are not retimed on each circuit [63]. Indeed, for PML lasers, since the output is not tied to a clock signal, the concept of RMS jitter is often eschewed; instead these lasers are frequently characterized in terms of pulse-to-pulse jitter or pulse-to-pulse "kicks" [23], [64]. In this document, we measured jitter relative to a clock, and therefore characterize the jitter in terms of its standard deviation.

Now consider lasers mode-locked at the m^{th} harmonic, where m pulses circulate within the cavity. In these sources, the noise of the n^{th} pulse is correlated with that of the $(n + m)^{\text{th}}$, the $(n + 2m)^{\text{th}}$, and so on. Thus does super-mode noise appear in the laser's output.

It should be pointed out that, in addition to the jitter present at the laser output, noise can accumulate downstream, depending on the application. In metrological applications, for example, the laser is typically followed by a supercontinuum-

generation stage, where uncorrelated jitter can arise from shot noise [20]. In communications applications, numerous mechanisms exist whereby noise can accumulate during propagation. In single-wavelength links, noise can accrue due to the Gordon-Haus effect [65]–[69], Kerr nonlinearities (cross-phase modulation and four-wave mixing) [70], [71], electrostrictive effects [32], polarization-mode-dispersion [32], and soliton interactions [32], depending on whether nonlinear propagation and/or dispersion management are employed. Wavelength-division-multiplexed links can, in addition, accumulate noise due to more complicated, interchannel soliton collisions [32]. Finally, note that many of these propagation effects can also take place within the cavity of a fiber laser.

1.6 Commentary

In Chapter 1, we have seen that low-jitter, high-rate, short-pulse lasers have many applications, and we have focused not just on the communications application, but on optical-time-division multiplexing in particular. We have found that, for OTDM, the jitter and pedestal level are vital parameters. We will now outline the work at the heart of this dissertation.

1.6.1 Pulse-Source Technologies

Chapters 2 through 4 describe technologies of short-pulse production. Chapter 2 presents a pulse source, based on a gain-switched laser diode, designed for use in OTDM communications. Chapter 3 attempts to determine whether gain-switching with an electrical comb (rather than a sinusoid) can improve the jitter or pulse-width of the resulting pulse train. Chapter 4 closely examines the phenomenon, only hinted at in Subsubsection 1.4.4.4, whereby temporal multiplexing of a pulse train with non-zero pedestal power leads to correlated amplitude jitter.

1.6.2 Diagnostic Tools

Chapters 5 and 6 describe two methods of *characterizing* the jitter of a pulse train. By “characterizing” we mean not simply measuring the total timing or amplitude noise, but extracting the uncorrelated and correlated contributions⁹. Chapter 5 presents a jitter-characterization technique that extracts these jitter parameters directly from the RF spectrum of a detected pulse train, while Chapter 6 presents a technique that extracts these parameters from RF spectra obtained by mixing the detected train with each of two sinusoids.

⁹ We will not attempt to extract the super-mode noise.

Table 1.1: Origins of jitter contributions in various pulsed lasers.

Laser	Uncorrelated	Correlated	Pattern
Directly modulated	Independent production	RF source	
Externally modulated		RF source	
PML at fundamental	ASE	Cavity drift Circulating single pulse	
PML at harmonic	ASE	Cavity drift	Cavity drift Circulating pulse pattern
AML or HML at fundamental	ASE	RF source Cavity drift Circulating single pulse	
AML or HML at harmonic	ASE	RF source Cavity drift	RF source Cavity drift Circulating pulse pattern

AML—Actively mode-locked. ASE—Amplified spontaneous emission. HML—Hybridly mode-locked. PML—Passively mode-locked. RF—radio-frequency.

CHAPTER 2

Picosecond-Pulse Source

2.1 Roadmap

Chapter 2 discusses a pulse source designed to be compatible with ultrafast OTDM. Section 2.2 is a brief summary of the performance required of the source. Section 2.3 reviews previous work in the field. Section 2.4 represents the bulk of the chapter; in this section, we describe the short-pulse source and compare the performance demonstrated by the laser to that required by ultrafast OTDM communications links. Section 2.5 provides some commentary.

2.2 The Problem

We require a 2.50-GHz optical-pulse source, for use in ultrafast optically time-division-multiplexed communications systems. The source must be capable of being temporally multiplexed to 160 Gb/s. Applying $B_{\text{chan}} = 2.5 \times 10^9$ GHz, $B_{\text{sys}} = 1.6 \times 10^{11}$ GHz, and $\text{BER} = 10^{-9}$ to the list of criteria in Subsection 1.4.4 yields the following requirements:

- The repetition rate must = 2.5 GHz.
- The RMS timing jitter must be ≤ 0.53 ps.

- The normalized RMS amplitude jitter must be $\leq 8.4\%$.
- The normalized pedestal level must be ≤ -23 dB.
- The pulse shape must be sech^2 in power.
- The temporal FWHM must be ≤ 2.4 ps.
- The TBP must be ≤ 0.40 .

2.3 Previous Work

A number of pulse sources have been proposed for use in ultrafast OTDM links. Many, but by no means all, of these technologies are discussed in this section.

2.3.1 Passively Mode-Locked Fiber Lasers

Passive mode-locking [72]–[77] of a fiber laser [78]–[86] can easily yield 1-ps, sech^2 pulses with low pedestal level. However, by the very nature of fiber lasers (assembled of optical fiber), the cavities are typically at least few meters long. It is difficult to produce a fiber laser with the 20-cm round-trip cavity length required for the fundamental repetition rate to equal the 1-GHz channel rate sometimes seen in ultrafast OTDM systems. Higher channels rates necessitate even shorter cavities. It is also difficult to make a PML laser mode-lock *harmonically*, that is, with multiple pulses evenly and stably distributed in the cavity. PML lasers produce pulse trains exhibiting correlated jitter, since all output pulses are simply fractions of a single intracavity pulse circulating around the cavity. Typically, the jitter is small, well below 1 ps.

2.3.2 Actively Mode-Locked Fiber Lasers

Active mode-locking of fiber lasers [63], [77], [87]–[96] does not have this problem with the repetition rate. Because AML fiber lasers incorporate a phase or amplitude modulator, they can be driven at a harmonic of the fundamental repetition rate. However, the cavity must be dynamically stabilized to ensure that the length does not fluctuate due to varying environmental conditions. (Fiber lasers are especially sensitive to environmental variations, due to their length.) Further, AML fiber lasers typically produce fairly wide pulses (on the order of 10 ps), unless (a) some form of soliton shaping is incorporated into the cavity or (b) extracavity pulse compression is appended to the laser. Unfortunately, pulse compression often leads to detrimental pedestals, which must be suppressed. The jitter exhibited by AML lasers is correlated. This jitter originates with the radio-frequency source employed to drive the modulator. This jitter is typically small, since RF synthesizers with 100-fs jitter are readily available.

2.3.3 Hybridly Mode-Locked Fiber Lasers

One solution to the shortcomings of the above two laser systems is to combine them, yielding a hybridly mode-locked laser [97]. In such optical sources, active modulation is used to harmonically mode-lock the laser, and a saturable absorber is incorporated to narrow the pulses. HML lasers can produce 10-GHz trains of 1-ps pulses. Not surprisingly, these lasers share the characteristics of PML and AML fiber lasers: HML lasers require dynamic cavity-length control and produce pulse trains exhibiting sub-picosecond correlated timing jitter.

2.3.4 Passively Mode-Locked Laser Diodes

Laser diodes (LDs), like fiber lasers, can be passively mode-locked [64], [98]–[103]. Because of the extremely short cavity, fundamental repetition rates as high as 240 GHz [103] are possible. Further, harmonic mode-locking can raise repetition rates to a dizzying 2.1 THz [103]. PML LDs can produce trains of sub-picosecond pulses with sub-picosecond (correlated) timing jitter [104]. Unfortunately, an “off-the-shelf” LD cannot be made to mode-lock; the diode must be fabricated specifically for passive mode-locking, incorporating gain and saturable-absorption sections.

2.3.5 Actively Mode-Locked Laser Diodes

Actively mode-locked laser diodes [58], [104]–[111] can also operate at extremely high repetition rates, such as 160 GHz [109]. Like their passive siblings, AML LDs can produce trains of sub-picosecond pulses with sub-picosecond, correlated timing jitter [104], [109]. As in the PML case, a laser diode must be fabricated specifically for active mode-locking; it must include gain and modulation sections.

2.3.6 Hybridly Mode-Locked Lasers Diodes

Hybridly mode-locked laser diodes [60], [104], [112], [113], like their fiber counterparts, attempt to combine the best properties of passive and active mode-locking. Thanks to their short cavity lengths (even in external-cavity configurations) fundamental repetition rates on the order of 10 GHz are easily attainable [23]; Because of the hybrid mode-locking, sub-picosecond pulse widths and very low jitter are possible.

2.3.7 Loss-Switched Laser Diodes

Laser diodes can also be loss-switched (Q-switched) [62], [114]–[116] at multiple-GHz rates. Since each pulse is produced from spontaneous emission, with no memory of

the previous pulses [62], [114], the output of loss-switched LDs is usually dominated by uncorrelated jitter. (The RF source used to drive the laser introduces correlated jitter, but this noise is usually much smaller than that of the loss-switching process itself.) This jitter can be less than 1 ps. Indeed, it has been proposed [62], [114], [115] that loss-switched diodes are inherently lower-noise than their gain-switched counterparts. As in gain-switching, the pulses produced by loss-switching are typically multiple picoseconds in length, though they can be compressed through a variety of means. These compression stages often leave unwanted pedestals however, which must be removed. Loss-switched laser diodes, too, must be fabricated explicitly for loss switching, in two partitions: one gain section and one loss section.

2.3.8 Gain-Switched Laser Diodes

2.3.8.1 Description

Gain-switching (GS), which is essentially the opposite of loss-switching, can also be applied to LDs [62], [100], [115], [117]–[120] to produce RZ sources for OTDM. Laser diodes can be gain-switched at up to approximately 20 GHz, limited by the resonance frequency of the diode [100]. GS LDs typically produce pulses 10 to 30 ps in width, but these pulses can be compressed to below 1 ps. Indeed, compression to 20-fs widths has been demonstrated [120]. Examples of pulse-compression technologies include linear compression¹), adiabatic soliton compression², higher-order soliton compression [121], and higher-order soliton compression in dispersion-decreasing fiber (a hybrid of the previous two schemes) [122].

¹ See Section 2.4.2.

² See Section 2.4.3.

2.3.8.2 Advantages

Gain-switched laser diodes, when cascaded with compression stages, can produce pulses trains of the required repetition rate and pulse width. Furthermore, they are simple and inexpensive to build, easy to operate, and compact: no dynamic cavity stabilization is required, and the diode need not be designed explicitly for gain-switching³. (Since the LD need only consist of a single gain section, laser diodes designed for non-return-to-zero operation can be gain-switched.)

2.3.8.3 Disadvantages

The first disadvantage associated with gain-switched and compressed laser diodes is jitter. As with loss-switched LDs, GS LDs generate each pulse from spontaneous emission [62], so their output is dominated by uncorrelated noise. (Again, the RF source adds correlated noise.) Under ideal conditions, the timing jitter can be well below 1 ps [62], [116], [119], [123]–[125]. However, if care is not taken, the timing noise can be several picoseconds, and the amplitude noise can be similarly high.

The second difficulty is pedestal level (though this shortcoming comes about because of the pulse duration). The compression stages often employed to reduce the temporal width of the GS LD's output to an acceptable value frequently leave a substantial pedestal of uncompressed energy [120]–[122], [126]–[129]. However, it has been shown that the pedestal can be reduced using a nonlinear intensity filter [121], [122], [127]–[130], though spectral broadening often results.

2.3.8.4 Remarks

Note that the two principal disadvantages of GS LDs, are the very parameters most critical in OTDM sources. Still, the advantages make this technology attractive. In

³ However, as we will see in Section 3.3, there are advantages to be reaped if the laser is designed specifically for gain-switching.

the next section, we will focus our attention on producing, from a gain-switched laser diode, pulse trains with the required parameters.

2.4 Present Contribution

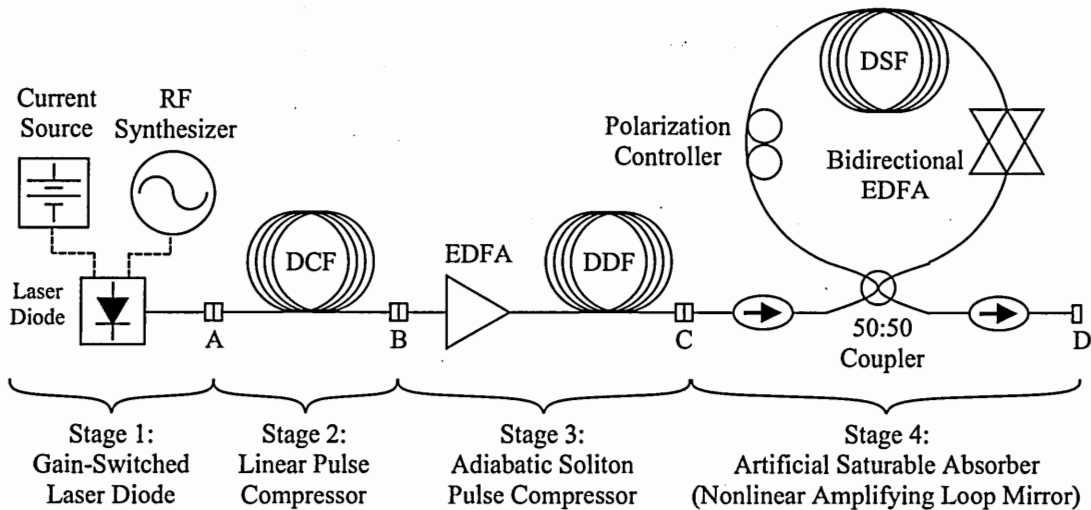


Figure 2.1: The Picosecond-Pulse Source. Points A, B, C, and D are measurement locations. RF—radio-frequency. EDFA—erbium-doped fiber amplifier. DCF—dispersion-compensating fiber. DDF—dispersion-decreasing fiber. DSF—dispersion-shifted fiber.

This section details the pulse source we developed with the intention of meeting the requirements of ultrafast OTDM, one based on a gain-switched laser diode. As explained in Subsubsection 2.3.8.2, this technology is attractive, because GS LDs are simple (Inexpensive LDs can be used, and no phase-locked loop is required.), and this simplicity confers robustness.

We call the laser under investigation the Picosecond-Pulse Source (psPS). The psPS consists of four stages, as diagrammed in Fig. 2.1:

- A gain-switched, distributed-feedback laser diode.

- A linear pulse compressor.
- An adiabatic soliton pulse compressor.
- An artificial saturable absorber for pedestal suppression.

The performance of each stage in the system, and the performance goals, are summarized in Table 2.1.

Table 2.1: The performance and goals of the Picosecond-Pulse Source.

	Point A	Point B	Point C	Point D	Goal
f_{rep} (GHz)	2.50	2.50	2.50	2.50	2.50
$\sigma_{\Delta T}$ (ps)	5.0	—	—	—	≤ 0.53
$\hat{\sigma}_{\Delta A}$	0.19	—	—	—	≤ 0.084
\hat{A}_{ped} (dB)	—	—	-19.2	-37.1	≤ -23
Pulse shape	Gaussian	Gaussian	sech ²	sech ²	sech ²
Δt (ps)	16.7	6.8	1.5	0.96	≤ 2.4
TBP	0.70	0.37	0.42	0.66	≤ 0.40

Points A, B, C, and D are the outputs of Stages 1, 2, 3, and 4, respectively, as indicated in Fig. 2.1. f_{rep} —repetition frequency. $\sigma_{\Delta T}$ —standard deviation of total timing jitter. $\hat{\sigma}_{\Delta A}$ —normalized standard deviation of total amplitude jitter. \hat{A}_{ped} —normalized pedestal power. Δt —temporal full width at half of maximum. TBP—time-bandwidth product.

2.4.1 Stage 1: Gain-Switched Laser Diode

The first stage of the psPS is a gain-switched laser diode [62], [100], [115], [117]–[120]. The purpose of this stage is to generate the a pulse train at the desired repetition rate. Each pulse in the train will be shaped by the following stages of the laser system.

2.4.1.1 Theory

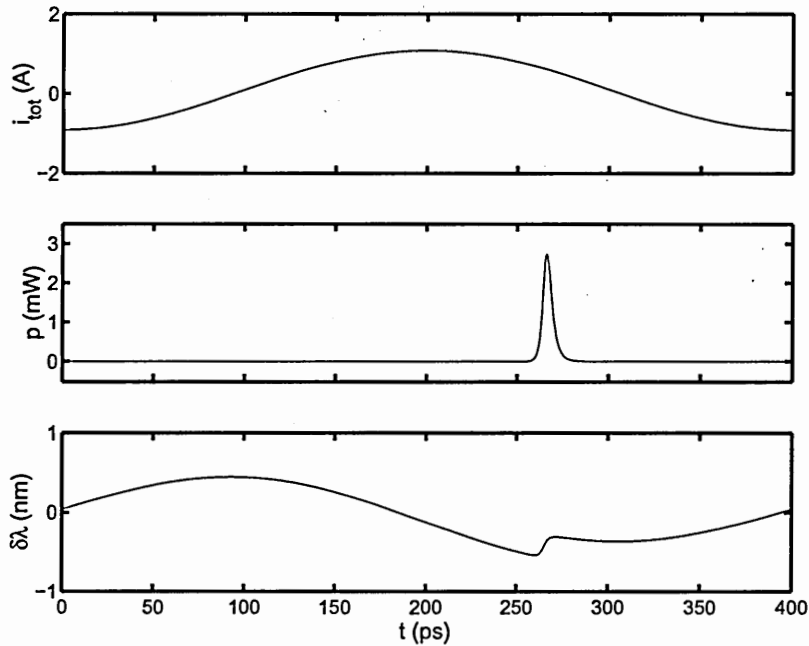


Figure 2.2: Simulated gain-switching of a laser diode by a 2.5-GHz sinusoidal current. i_{tot} —total current. p —output optical power. $\delta\lambda$ —deviation from center wavelength. t —time.

The laser diode is gain-switched by a combination of direct-current (DC) bias and a high-power, RF sine wave⁴. The gain-switching process, which is illustrated in Fig. 2.2, relies on the nonlinear behavior of the diode (the strong coupling between the population inversion and the photon number). During the trough of the RF signal, the two currents combine to set the laser below threshold. The peak of the sinusoid briefly brings the diode far above threshold. This process initiates a series of relaxation oscillations in the LD output. The next trough of the RF, arriving after the first oscillation, brings the laser back below threshold before the second oscillation begins. The resulting single-peak pulse is much narrower than the RF period. The

⁴ A laser diode can also be gain-switched by an electrical pulse train. For more information on pulse-train gain-switching, see Chapter 3.

precise shape and duration of the optical pulse will be determined by how quickly charge carriers can be moved into and out of laser diode [100]. Thus the capacitance of the diode (determined by the areas of the electrical contacts, the distance between them, and the dielectric constant of the cavity) is a critical parameter.

During the production of each pulse, the variation in the net current yields changes in the carrier density in the laser cavity. Because the refractive index in the active region is dependent on the carrier density, the cavity index varies during the production of each pulse. Thus, the resonant wavelength of the cavity (and the output wavelength) changes during the production of each pulse. In particular, the resulting pulse has a strong, nearly linear, negative chirp⁵.

Note that, since the net current is below threshold between each pulse (because a high extinction ratio is required), a new pulse is produced from spontaneously emitted photons [62] during each RF period. Therefore the turn-on delays of the pulses constitute an uncorrelated random sequence, and uncorrelated timing jitter appears in the output of the LD. Similarly, the stochastic nature of the pulse production also means that the peak powers are an uncorrelated random sequence, and uncorrelated amplitude jitter is also present in the laser's output.

2.4.1.2 Experiment

The laser employed for Stage 1 is a 2.50-GHz InGaAsP multiple-quantum-well laser diode sealed in a butterfly package (Nortel Networks model LC155W0000-20A). The laser's center wavelength is specified to be 1547.7 nm, though, in practice, it can be tuned a nanometer or so in either direction by adjusting the laser's temperature. The butterfly package is, in turn, embedded in a driver board (Fig. 2.3).

⁵ "Negative" chirp means that the higher frequencies (shorter wavelengths) appear at the front of the pulse, while the lower frequencies (longer wavelengths) appear at the rear.

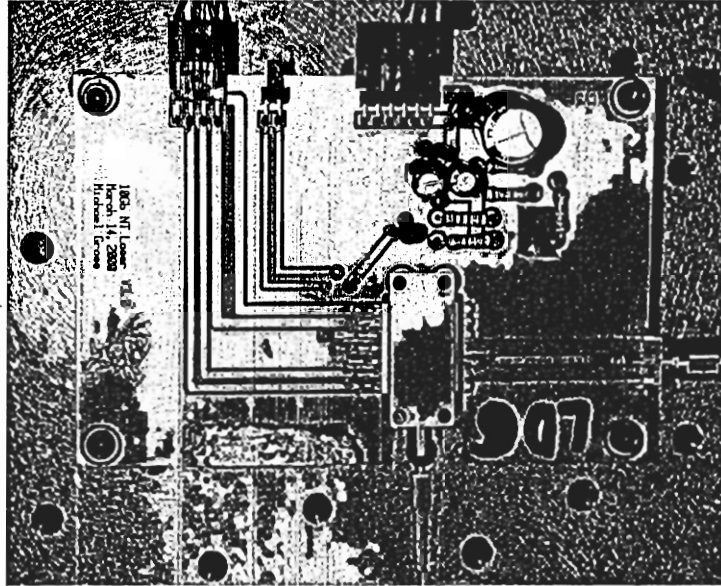


Figure 2.3: Stage 1 of the Picosecond-Pulse Source.

The driver board contains circuitry for maintaining the diode's temperature, biasing the laser, and driving the laser with the RF signal. The temperature-control circuitry consists of a connector and a few simple traces to link the off-board temperature controller (ILX Lightwave model LDT-5412) to the thermister and thermo-electric cooler in the butterfly package. The bias circuitry consists of connections to an off-board power supply (Tektronix model CPS250), a voltage regulator, a few capacitors for despiking, and a voltage divider with potentiometer for tuning. The RF circuitry consists of a short microstrip waveguide and an SMA connector for linking the off-board RF source to the laser's package. The length of the waveguide is designed to be one half of the wavelength of a 2.5-GHz current sinusoid, given the impedance of the waveguide. This length is chosen so that any reflections, due to impedance mismatch, at the waveguide/butterfly interface add in phase, when reflected (again) from the connector/waveguide interface [119], [123]. This arrangement is called resonant drive⁶. The off-board RF source consists of an RF synthesizer (Ag-

⁶ See Subsection 3.3.6.

ilent model 83640L) and an RF amplifier (Anritsu model A3H2206), which is biased by a power supply (Hewlett-Packard model 6237B) and bias tee (Hewlett-Packard model 33150A).

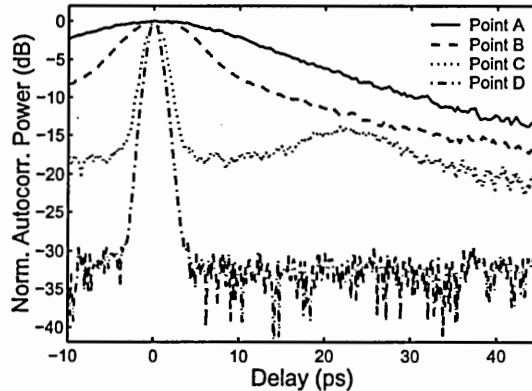


Figure 2.4: Autocorrelations measured at Points A, B, C, and D of the Picosecond-Pulse Source.

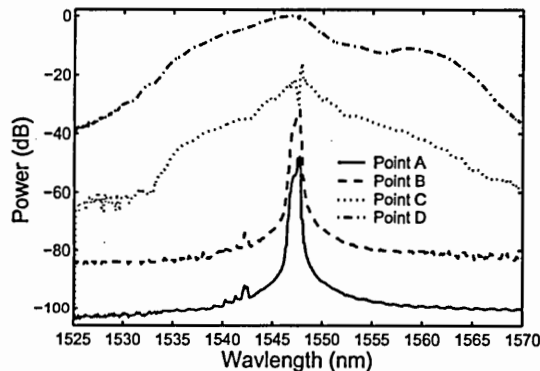


Figure 2.5: Optical spectra measured at Points A, B, C, and D of the Picosecond-Pulse Source.

Driving this setup with a 2.50-GHz, 18.0-dBm RF sinusoid produces, at Point A of Fig. 2.1, a pulse with temporal FWHM of 16.7 ps (Fig. 2.4). (We have assumed a Gaussian pulse shape in order to compute the temporal width from the autocorrelation width.) The pulse is centered at 1547.7 nm and exhibits a strong, nearly linear negative chirp⁷, with a spectral full width of 0.33 nm (Fig 2.5) and a TBP of 0.70.

⁷ The sign and linearity of the LD's chirp is deduced from the sign of the dispersion used in the linear compressor and the degree of compression that results; see Subsection 2.4.2.

These temporal and spectral widths are far greater than the performance criteria we have established. However, we may be able to use the excess spectrum to shorten the pulse, thus “killing two birds with one stone.” This “double aviacide” is the motivation for Stage 2. But before we consider the linear compressor, we must investigate the jitter of the laser.

We characterize the noise of the pulse train at Point A using the oscilloscope (histogram) technique and with the direct RF-spectral technique⁸. These measurements suggest that RMS total timing jitter is 5.0 ps and that the normalized RMS total amplitude jitter is 19 %. We have found that the following stages do not add measurable jitter to that of Stage 1 through the Gordon-Haus effect or any other propagation-induced-noise effects⁹. Thus, jitter values for the Stages 2 through 3 do not appear in Table 2.1.

2.4.2 Stage 2: Linear Pulse Compressor

The second stage of the psPS is a linear pulse compressor [120], [131]–[134], consisting entirely of a length of positive-dispersion (normal-dispersion) fiber. The purpose of this stage is to reduce the temporal width and duration-bandwidth product of pulse produced by Stage 1.

2.4.2.1 Theory

Consider the electric-field envelope of the pulse, E , as it enters the fiber [135]:

$$E(0, t_{loc}) = \kappa \sqrt{A(0)} u(0, t_{loc}) , \quad (2.1)$$

⁸ See Chapter 5.

⁹ See Subsubsection 1.5.3.2.

where the 0 argument indicates that this variable is evaluated at the input of the positive-dispersion fiber ($z = 0$), and the t_{loc} argument,

$$t_{\text{loc}} \equiv t - \frac{z}{v_g} , \quad (2.2)$$

is the “local” time in a frame moving at v_g , the group velocity of the pulse. The parameter κ is a normalization constant (with units) and u is a unitless field-shape function which, initially, has unit amplitude. The significance of the \sqrt{A} factor becomes apparent when we compute the power of the pulse, P :

$$\begin{aligned} P(0, t_{\text{loc}}) &= \frac{A_{\text{eff}}}{\eta} |E(0, t_{\text{loc}})|^2 \\ &= \frac{A_{\text{eff}}}{\eta} \kappa^2 A(0) s(0, t_{\text{loc}}) , \end{aligned} \quad (2.3)$$

where η is the impedance of the medium, A_{eff} is the effective area of the fiber, and

$$s \equiv |u|^2 \quad (2.4)$$

is a unitless *power*-shape function. If we choose

$$\kappa \equiv \sqrt{\frac{\eta}{A_{\text{eff}}}} , \quad (2.5)$$

then

$$P(0, t_{\text{loc}}) = A(0) s(0, t_{\text{loc}}) , \quad (2.6)$$

and $A(0)$ becomes the initial power amplitude (peak power) of the pulse. Its units are W.

Let us assume that the pulse, as it enters the positive-dispersion fiber, has a Gaussian profile. If it were not chirped, we would have

$$u(0, t_{\text{loc}}) = \exp \left(-\frac{1}{2} \left\{ \frac{t_{\text{loc}}}{\Delta t_{\text{HW}1e}(0)} \right\}^2 \right) . \quad (2.7)$$

Here, $\Delta t_{\text{HW}1e}$ is the temporal half width at 1/e of the pulse power, which, for a Gaussian, is related to the FWHM by [135]

$$\begin{aligned} \Delta t &= 2\sqrt{\ln(2)} \Delta t_{\text{HW}1e} \\ &\simeq 1.665 \Delta t_{\text{HW}1e} . \end{aligned} \quad (2.8)$$

In our case, the pulse *is* chirped, so

$$u(0, t_{\text{loc}}) = \exp\left(-\frac{1 + iC(0)}{2} \left\{ \frac{t_{\text{loc}}}{\Delta t_{\text{HW1e}}(0)^2} \right\}^2\right). \quad (2.9)$$

Here, C is the (unitless) chirp parameter. For positively chirped pulses (higher frequencies in back), $C > 0$; for negatively chirped (higher frequencies in front, like our pulse), $C < 0$.

Now let the pulse propagate through dispersive fiber. All the parameters with zero arguments above, become functions of z . Of particular interest to us is $\Delta t_{\text{HW1e}}(z)$. If we ignore higher-order dispersion, then we can represent the dispersion of the fiber with D , the dispersion parameter, or β_2 , the GVD parameter. The two are related through

$$D = \frac{2\pi c}{\lambda^2} \beta_2, \quad (2.10)$$

where c is, as usual, the speed of light in a vacuum, and λ is the operating wavelength. The evolution of $\Delta t_{\text{HW1e}}(z)$, due to dispersion, can then be quantified by

$$\frac{\Delta t_{\text{HW1e}}(z, t_{\text{loc}})}{\Delta t_{\text{HW1e}}(0)} = \sqrt{\left\{ 1 + \frac{C\beta_2 z}{\Delta t_{\text{HW1e}}^2(0)} \right\}^2 + \left\{ \frac{\beta_2 z}{\Delta t_{\text{HW1e}}^2(0)} \right\}^2}. \quad (2.11)$$

If C and β_2 have the same sign, the pulse will only elongate as it propagates. Contrastingly, if C and β_2 are of opposite sign, the pulse will go through a compression phase first, then an expansion phase. Thus, by appropriate choice of the dispersion parameter and length of the fiber, the *linear component* of the pulse's negative chirp can be compensated. Higher-order chirp, however, remains uncompensated. At some optimum distance, z_{opt} , the minimum pulse width will occur. The optimum distance is

$$z_{\text{opt}} = \frac{C}{1 + C^2} \frac{\Delta t_{\text{HW1e}}^2(0)}{|\beta_2|}, \quad (2.12)$$

and the corresponding pulse duration is

$$\Delta t_{\text{HW1e}}(z_{\text{opt}}) = \frac{\Delta t_{\text{HW1e}}(0)}{\sqrt{1 + C^2}}. \quad (2.13)$$

Because our pulse has negative chirp, we choose a pulse with positive (normal) dispersion ($\beta_2 > 0$ and $D < 0$). In particular, we employ 200 m of Corning dispersion-compensating fiber (DCF) as this positive-dispersion fiber. The dispersion parameter, D , and dispersion slope, $dD/d\lambda$ are specified to be -92.23 ps/[nm-km] and -0.12 ps/[nm²-km], respectively, at 1545 nm.

2.4.2.2 Experiment

At Point B, the pulse width is reduced to 6.8 ps, assuming a Gaussian shape (Fig. 2.4), and the spectrum is slightly broadened to 0.43 nm (Fig. 2.5). We would expect the spectrum to remain unchanged, since the linear compressor is designed to be *linear*. It is possible that a small amount of self-phase modulation occurs in Stage 2, but this explanation is unlikely to be correct, given the few-milliwatt peak power and the short propagation length. It is more likely that the compression and *reshaping* that take place in the DCF are the source of the “broadening.” It may be that the pulse measured at Point B simply corresponds to a broader power spectrum than the pulse measured at point A. In other words, perhaps no new colors have been added; the peak has just been reduced.

Using this new spectral width, the TBP is calculated to be 0.37, indicating the pulse is close to transform-limited. This result means that that the compression was nearly optimal. This TBP (and the indicated near-optimal linear compression) is the basis for our claim that the chirp at Point A is nearly linear.

2.4.3 Stage 3: Adiabatic Soliton Pulse Compressor

The third stage of the psPS is an adiabatic soliton pulse compressor [66], [120], [122], [127], [128], [136]. The purpose of this stage is to further reduce the temporal pulse width.

2.4.3.1 Theory

Our adiabatic soliton pulse compressor is composed of an erbium-doped fiber amplifier (EDFA) followed by a length of dispersion-decreasing fiber (DDF). The DDF exhibits negative (anomalous) dispersion that decreases in magnitude along its length.

A soliton [55] is pulse in which the nonlinearity (self-phase modulation) balances the dispersion, and it therefore resists dispersion-induced broadening. A (bright) soliton can only exist in media with negative (anomalous) dispersion, it must be transform-limited (chirp-free), and the field-shape function must be a hyperbolic secant. Thus, as the pulse enters the DDF ($z = 0$), the electric-field envelope is

$$E(0, t_{\text{loc}}) = \sqrt{\frac{\eta}{A_{\text{eff}}}} \sqrt{A(0)} u(0, t_{\text{loc}}), \quad (2.14)$$

with

$$u(0, t_{\text{loc}}) = \text{sech}\left(\frac{t_{\text{loc}}}{\Delta t_{\text{char}}(0)}\right), \quad (2.15)$$

where Δt_{char} is a characteristic temporal width (*not* the same as Δt or Δt_{HW1e}).

A soliton is often characterized by its order, N_{sol} , given by

$$N_{\text{sol}}^2 = \frac{\gamma A \Delta t_{\text{char}}^2}{|\beta_2|}, \quad (2.16)$$

where γ is the nonlinearity parameter of the fiber. Because the pulse experiences decreasing dispersion as it propagates along this fiber, it must temporally shorten (thus increasing peak power) to maintain the balance between dispersion and nonlinearity that constitutes a soliton. This process preserves the soliton order. Thus, the evolution of the pulse duration can be described with

$$\Delta t_{\text{char}}(z) = N_{\text{sol}} \sqrt{\frac{|\beta_2(z)|}{\gamma A(z)}}. \quad (2.17)$$

Our adiabatic compressor uses a Corning DDF with initial dispersion, D_{in} , of 10.5 ps/[nm-km], and final dispersion, D_{out} , of -0.1 ps/[nm-km] (both specified at

1550 nm). The DDF is 11 km long; this length is chosen to ensure that the evolution of the soliton is adiabatic. The EDFA is used amplify each pulse so that it forms a fundamental soliton (soliton order = 1) as it enters the high-dispersion input end of the DDF.

2.4.3.2 Experiment

The gain of the EDFA in Stage 3 is adjusted to optimize the pulse at Point C. The adiabatic compressor relies on fundamental-soliton propagation, so we expect to observe sech^2 pulses at Point C, and, indeed, the measured autocorrelation (Fig. 2.4) is consistent with a hyperbolic secant of full width 1.5 ps. Unfortunately, Stage 3 leaves a large pedestal of uncompressed energy, corresponding to the narrow spike observed in the spectrum (Fig. 2.5) [127], [129]. When we compensate for the distortion of the autocorrelator¹⁰, the pedestal level is found to be -19.2 dB. Because of the spike, $\Delta\lambda$ is not a good measure of the spectral content, and the TBP is also not very meaningful.

2.4.4 Stage 4: Pedestal Suppressor

The fourth stage of the psPS is an artificial saturable absorber or high-pass intensity filter. The purpose of this stage is to suppress the pedestal that results after the linear and nonlinear compression of Stages 2 and 3 and thus to reduce the amplitude jitter that results after OTDM multiplexing¹¹. We have chosen a nonlinear amplifying loop mirror (NALM) [78], [130] as our intensity filter.

We use a NALM rather than another loop-mirror variant, because the higher asymmetry, and thus greater phase difference, between the two paths will yield superior performance. Additionally, the NALM can achieve a 100 % contrast ratio with

¹⁰ The autocorrelation process exaggerates the pedestal level; see Subsubsection 4.4.1.2.

¹¹ See Chapter 4.

finite input power. Furthermore, the amplifier gain provides an additional degree of freedom and allows the NALM to be easily optimized, particularly for varying input-pulse characteristics. (Furthermore, experiments performed with an artificial saturable absorber based on nonlinear polarization rotation [137] were only able to reduce the pedestal level to -21.8 dB.)

2.4.4.1 Theory

The nonlinear amplifying loop mirror is treated theoretically in Chapter 4. That chapter also contains a theoretical treatment of OTDM jitter.

2.4.4.2 Experiment

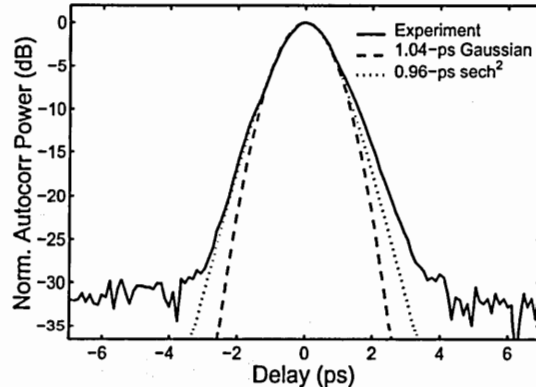


Figure 2.6: Three autocorrelations: the output of the Picosécond-Pulse Source (Point D), a Gaussian pulse with full width at half maximum of 1.04 ps, and an hyperbolic secant pulse with full width of 0.96 ps.

The pedestal reduction of the NALM is controlled by the gain in the loop. Increasing the gain decreases \hat{A}_{ped} but also increases the positive chirp of the output pulses. We find that a minimum gain of 16.8 dB is required to completely eliminate the spectral spike observed at Point C. Further increasing the gain additionally broadens the spectrum without significantly reducing \hat{A}_{ped} . We find that the easiest

method for optimizing the NALM gain and fiber polarization controller is to minimize the spectral spike; the settings yielding the smallest spike also produce the lowest pedestal. The autocorrelation (Fig. 2.4 and 2.6) and spectrum (Fig. 2.5) measured at the NALM output demonstrates that the pedestal is dramatically suppressed (and the corresponding spectral spike is eliminated). Once we correct for the exaggeration of the pedestal by the autocorrelation process, the pedestal level is revealed to be -37.1 dB. This pedestal level represents an improvement of 17.9 dB and should more than suffice to reduce the power fluctuations to a sufficiently small value.

The autocorrelation of the pulse is well fit¹² by an the autocorrelation of a 960-fs hyperbolic secant over the first 25 dB. Thus, the NALM not only suppresses the pedestal, but also reduces the pulse width by about a third and produces the desired hyperbolic secant pulse shape. The spectral width is now 5.5 nm, and the TBP is 0.66, indicating that the NALM imparts considerable chirp. It may be possible to reduce this chirp by propagating the pulse through appropriately dispersive fiber [127] or a bandpass filter, though, as our experiments with this final step indicate, care must be taken due to the high peak power.

2.5 Commentary

The psPS meets the majority of the criteria established for our application¹³:

- The repetition rate (2.50 GHz) is correct.
- The pedestal level (-36.6 dB) is well below the desired maximum (-23 dB).
- The pulse shape (hyperbolic secant) is correct.

¹² The left side of the autocorrelation indicates the shape of the pulse with more fidelity. The right-hand side is less accurate; the integration time of the photo-multiplier tube in the autocorrelator was chosen to be 100 fs in order to yield a usably large signal, but it also slows the falling-edge response of the autocorrelator.

¹³ See Subsection 1.4.4 and Section 2.2.

- The temporal full width (0.96 ps) is less than the required maximum (2.4 ps).

However, the laser fails to meet several critical requirements:

- The RMS timing jitter (5.0 ps) surpasses the maximum allowed (0.53 ps).
- The RMS amplitude jitter (0.19) exceeds the maximum allowed (8.4 %).
- The TBP (0.66) is greater than the desired maximum (0.40).

Thus, the psPS is deficient in terms of noise and time-bandwidth product.

2.5.1 Jitter

The excess jitter results directly from the inherently noisy gain-switching process. However, a number of methods have been shown to reduce the jitter of a GS LD's output¹⁴. Some of the more successful methods involve designing the laser specifically for low-noise operation. For example, lasers with extremely small active regions, such as selectively oxidized, vertical-cavity, surface-emitting lasers¹⁵ [124], [125], [138]. In addition, optical feedback¹⁶ have been shown to produce pulse trains with timing jitter below 100 fs [139]–[144] has been shown to reduce the jitter of of a GS LD's output train. Further, at least two devices have been demonstrated to reduce some aspects of a laser's jitter, when placed *downstream* of laser [145], [146]. Perhaps a different gain-switching technique, a different design of laser diode, or a post-laser jitter-reduction device would suffice to bring the noise of our laser system below the established limits.

¹⁴ See Section 3.3.

¹⁵ See Subsection 3.3.5.

¹⁶ See Subsection 3.3.1.

2.5.2 Time-Bandwidth Product

The excess spectral width, which results in the excess TBP, can be traced back to the surfeit of *temporal* width present at the output of the LD. The pulse width can be reduced by utilizing linear or nonlinear pulse compressors, yielding a lower time-bandwidth product. However, this pulse compression results in a significant pedestal. The pedestal can, in turn, be reduced, but doing so can increase the chirp. Moreover, additional shortening of the pulse is not only unnecessary but also deleterious; shorter pulses will have higher peak powers and greater sensitivity to nonlinear effects. The TBP of the pulse can be directly reduced by propagation through a spectral filter, but filtering high-power pulses often results in significant distortion. Thus, correcting each problem seems to create a new one; the excessive temporal width of the LD's output pulse necessitates up to four additional stages.

2.5.3 Alternatives

Even if the jitter and bandwidth issues could be resolved by the addition of one or two further stages, problems remain. A five- or six-stage pulse source is not only inelegant, but also cumbersome and, because of the large number of degrees of freedom, prone to misadjustment. Further, it may be that the psPS, even with the modifications discussed above, may not be able to meet all the established criteria.

It is more efficient and more elegant to produce narrow-width, low-noise, low-pedestal pulse trains directly from the laser cavity. The sigma laser [87], [89], [91], [92], [94], [95], [147], for example, has demonstrated production of 11.4-GHz trains of pulses with 10-fs timing jitter and amplitude noise $< 0.1\%$ [91]. The 1.4-ps pulses produced have pedestals ≥ 34 dB [95] below the peak. These results were obtained without extracavity pulse compression, pedestal reduction, or active jitter reduction. A variant of the sigma laser has even been made to operate with multiple wavelengths [147], making it a potential source for WDM or WDM-plus-OTDM links.

CHAPTER 3

Pulse-Train Gain-Switching

3.1 Roadmap

Chapter 3 addresses gain-switching by an electrical pulse train as a means of reducing pulse width and jitter. Section 3.2 briefly states the problem at hand. Section 3.3 reviews previous work in the field. Section 3.4 represents the bulk of the chapter; in this section, we experimentally compare the pulse width as well as the timing and amplitude jitter of pulse trains generated by sinusoidal and pulsed gain-switching of a single laser diode. Section 3.5 is a brief commentary.

3.2 The Problem

When a laser diode is gain-switched with complete extinction between pulses, each pulse is produced independently from spontaneous emission. Each pulse has neither memory of previous pulses and no affect on subsequent pulses. Thus, GS LDs typically produce pulse trains exhibiting uncorrelated noise, which can be quite large unless specific steps are taken (as described in the next section). The purpose of this chapter is investigate the efficacy of one of these methods, pulse-train gain-switching.

3.3 Previous Work

Many methods have been employed to produce gain-switched laser diodes exhibiting subpicosecond timing jitter. The very number of these solutions indicates the significance of the problem. These methods include feedback, external seeding, a cavity supporting multiple longitudinal or transverse modes, a very small active region, resonant drive, and pulse-train drive.

3.3.1 Feedback

Optical feedback, also known as self-seeding [139]–[144] can be used to induce production of a pulse by *stimulated* emission. Thus, the principle source of jitter in gain-switching is reduced. Note that adding feedback will not only reduce the jitter, but also *correlate* it to some degree.

3.3.2 External Seeding

If the laser diode is externally seeded [120], [144], [148], [149] with a continuous-wave laser, then, as soon as gain is available in the cavity, an optical pulse is produced from *stimulated* emission [114]. Thus, the timing jitter can be significantly reduced. One drawback for the external-seeding scheme is the requirement of a second laser.

3.3.3 Multiple Longitudinal Modes

If the laser being gain-switched has multiple longitudinal modes, there are many routes through which the system can decay from an unstable state (population inversion) to a more stable state (no population inversion). Thus, the decay is faster. This means that a multiple-longitudinal-mode laser diode, such as a Fabry-Perot (FP) LD will have lower timing jitter than a single-longitudinal-mode diode, such as

a distributed-feedback (DFB) laser diode [114], [125], [150]. Simple FP LDs [142] or tapered-stripe FP LDs [119], [123] have been used to obtain subpicosecond timing jitter. Unfortunately, the lower jitter of FP LDs is offset by the increased dispersion-induced broadening they suffer due to their greater spectral width [150].

3.3.4 Multiple Transverse Modes

The multi-mode/timing-jitter argument made above applies equally to lasers with multiple transverse modes, as most vertical cavity, surface-emitting lasers (VCSELs) [151] are. However, multiple-transverse-mode VCSELs suffer higher *amplitude* jitter than single-transverse-mode lasers [151]. Additionally, multiple-transverse-mode lasers are very difficult to couple into the single-mode fiber used for high-rate communications.

3.3.5 Small Active Region

It has been proposed that the jitter of a laser diode is proportional to the volume of its active region [125]. Thus, if the laser diode is made small enough, very low timing jitter can be obtained, irrespective of the pulsing technology (mode-locking, gain-switching, *et cetera*). Note that this jitter will then originate principally with the RF synthesizer driving the laser, and, as such, the jitter will be correlated-dominated. VCSELs offer extremely small active-region volumes, but typically lase in multiple transverse modes. The number of transverse modes can be reduced to one by decreasing the transverse dimension of the cavity through selective oxidation or other means [152]. Note that doing so also reduces the total active-region volume. When this process is done, timing jitter on the order of 100 fs can be obtained [124], [125], [138].

3.3.6 Resonant Drive

GS-LD driver boards have sometimes been designed so that the distance between the RF input to the board and the laser diode is (or can be adjusted to be) equal to exactly half of the RF wavelength in the [119], [123], [153]. When this is done, any reflections from the board/LD interface “re-reflect” from the input connector and add *in phase* to the drive signal. This arrangement maximizes the drive power delivered to the laser. Since the jitter of a gain-switched laser diode decreases with increasing drive power [114], [115], [125], this resonant-drive condition reduces jitter.

3.3.7 Pulse-Train Drive

The jitter of a GS LD decreases not only with increasing drive-current amplitude [114], [115], [125], but also with decreasing current build-up time [115]. These two patterns can be simultaneously exploited by using a current pulse train to gain-switch the laser diode [119], [123], [124], [138], [142], [154], [155]. Indeed, as the width of the electrical pulse approaches zero (the pulse becomes an impulse), the magnitude of the timing jitter becomes independent of the spontaneous-emission noise [138]. Thus, the noise should become correlated-dominant. As an additional benefit, pulse-train drive also reduces the temporal width of the resulting optical pulses.

Experiments have been performed to demonstrate timing-jitter reduction at up to 1.2 GHz in FP LDs [119], [123], at up to 500 MHz in VCSELs [138] and in DFB LDs at up to 500 MHz [154]. To our knowledge, no experiments have been conducted to compare multi-GHz gain-switching of a distributed-feedback laser diode by a pulse train to that by a sinusoid. Since DFB LDs suffer from inherently higher jitter [125], [150], producing sub-picosecond timing jitter from a DFB is more challenging than in the FP LD or VCSEL cases. Further, no one has studied the impact of pulse drive on the *amplitude* jitter of a laser diode. In this proposal, we will address these two issues.

3.4 Present Contribution

3.4.0.1 Theory

Traditionally, a laser diode is gain-switched by a combination of bias current and a high-power, RF *sinusoid*, as described in Subsubsection 2.4.1.1. Now consider this description, but imagine replacing the sinusoid with a train of current pulses, pulses considerably narrower than the FWHM of the sinusoidal signal. The time during which the net current is above threshold is lowered. Thus, the the resulting optical pulse will be narrower [115], if the properties of the laser diode (carrier lifetime, photon lifetime, capacitance, *et cetera*) allow it. Further, because the window during which amplified spontaneous emission can occur is reduced, the timing and amplitude jitter should also diminish [115]. It has been shown that jitter also decreases with increasing drive-current amplitude [114], [115], [125]; thus, an electrical pulse train should produce lower-jitter optical pulse trains than an equal-power sine wave.

We can derive a simple estimate reduction of the amplitude jitter, timing jitter, and optical pulse width by assuming these values are proportional to the width of the rising edge of the drive signal. We further assume that the width of the rising edge is proportional to the full width at half maximum, Δt , of the drive signal:

$$\frac{\sigma_{\Delta J, \text{pulse}}}{\sigma_{\Delta J, \text{sin}}} \simeq \frac{\Delta t_{\text{pulse}}}{\Delta t_{\text{sin}}}, \quad (3.1)$$

where the “sin” and “pulse” subscripts denote sinusoidal and pulsed drive signals, respectively. Noting that the FWHM of a sine wave is half of the period yields

$$\frac{\sigma_{\Delta J, \text{pulse}}}{\sigma_{\Delta J, \text{sin}}} \simeq 2f_{\text{rep}} \Delta t_{\text{pulse}}. \quad (3.2)$$

3.4.0.2 Experiment

Our experimental setup (Figs. 3.1 and 3.2) is centered around a 10-GHz InGaAs/InGaAsP multiple-quantum-well DFB LD mounted on a chip-carrier (NTT model KELD1551CCA).

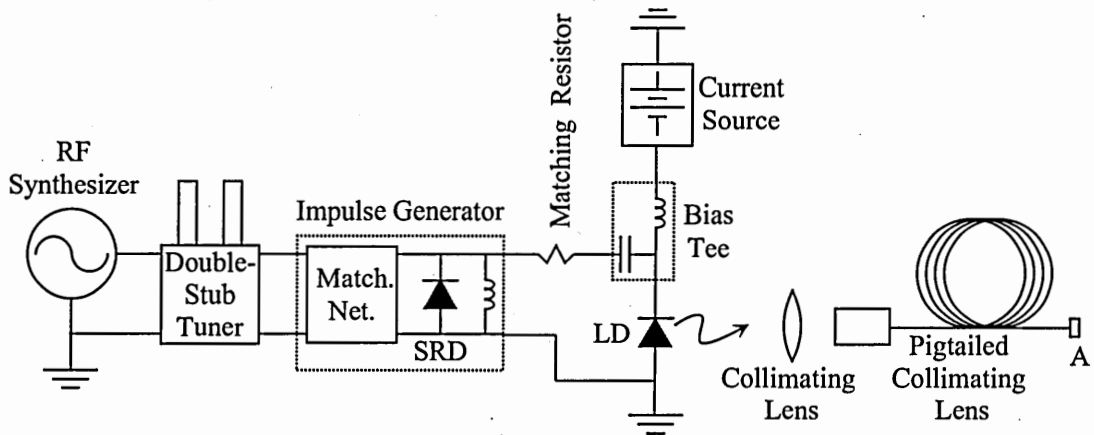


Figure 3.1: Diagram of experimental setup for pulse-train drive. The impulse generator is omitted for sinusoidal drive. Point A is the fiber-coupled output of the laser. RF—radio-frequency. Match. Net.—matching network. SRD—step-recovery diode. LD—laser diode.

The chip carrier is, in turn, mounted in an intricate setup designed for (a) biasing and driving the laser, (b) measuring and maintaining the laser's temperature, and (c) coupling its output into a single-mode fiber. The temperature-maintaining circuitry consists of connections to an external temperature controller (ILX Lightwave model LDT-5412). The bias circuitry consists of connections to an external power supply (Agilent model E36331A). The RF-drive portion of the setup includes a 50- Ω transmission line and a resistor to match the approximately 3- Ω impedance of the diode to that of the transmission line. A double-stub tuner provides finer impedance matching. This setup allows us to directly compare sinusoidal and pulse-train drive, using the same laser chip and the same setup for both drive conditions. The laser can be driven either directly with an RF sine wave or through a 2.5-GHz impulse generator (Herotek model GC2500-329). The RF drive sinusoid is supplied by an RF synthesizer (Agilent model 83640L), and an RF amplifier (Mini-Circuits model ZVE-8G, with a Power-One model HB12-1.7-A power supply). All experiments are performed at 2.5 GHz, the design frequency of the impulse generator.

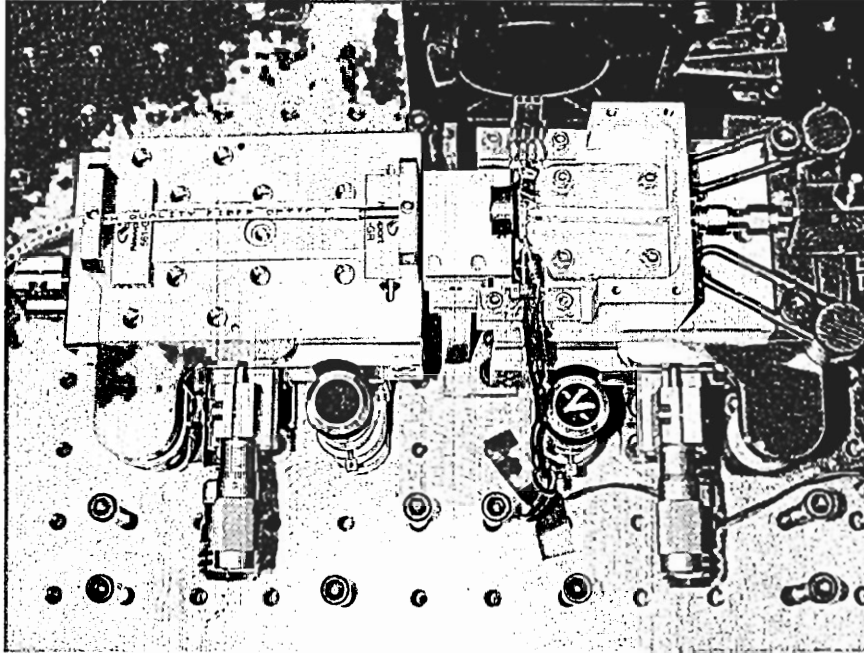


Figure 3.2: Photograph of experimental setup for pulse-train drive.

The electrical pulse employed for the pulse-drive experiments (Fig. 3.3), is measured with a sampling head with a 40-GHz bandwidth and $50\text{-}\Omega$ input impedance (Tektronix model SD-30), which is mounted in a digital oscilloscope (Tektronix model 11801B). The negative-going pulse has a FWHM, Δt_{pulse} , of 35.5 ps and a zero-to-peak amplitude of -3.8 V. By substituting $\Delta t_{\text{pulse}} = 35.5$ ps and $f_{\text{rep}} = 2.50$ GHz into Eq. 3.2, we predict that pulse-train drive should reduced the jitter and duration to approximately 0.20 of that produced by an equal-power sine wave.

We measure the timing and amplitude jitter as well as the temporal pulse width of the laser's optical output using a fast photodetector (Newport model D-15ir) and the same sampling head and oscilloscope. The sampling head and oscilloscope have a measured trigger jitter of 1.7 ps.

The laser diode was gain-switched using three drive conditions:

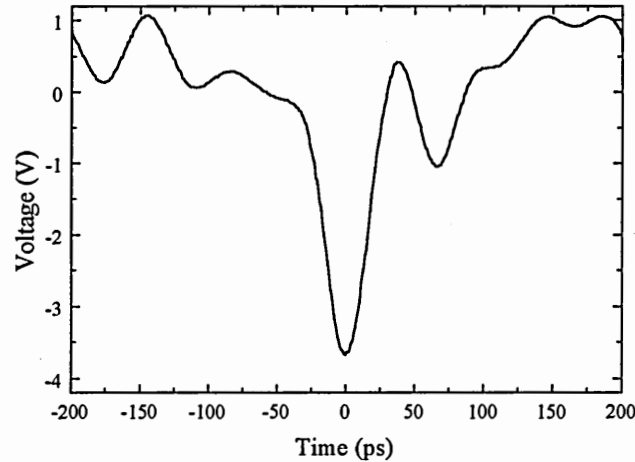


Figure 3.3: Electrical pulse used to drive the chip-carrier-mounted laser.

- Pulse-train drive: The impulse generator is included in the setup and was driven with a 30.0-dBm sinusoid. The electrical pulse train produced contains 14.1 dBm of power.
- Low-power sinusoidal drive: The impulse generator is removed, and the laser is driven directly with a 14.1-dBm sine-wave. This power equals that measured at the output of the impulse generator in the pulse-drive case.
- High-power sinusoidal drive: The impulse generator is removed, and the laser is driven directly with a 30.0-dBm sine-wave. This power equals that measured at the input of the impulse generator in the pulse-drive case.

For each drive condition, the bias is varied from -17 to -26 mA in even steps. The RMS timing noise, RMS amplitude noise, and pulse width measured for each of these twelve conditions are plotted in Fig. 3.4.

From the plots, we see that pulse-train gain-switching does indeed reduce the optical pulse width as well as the timing and amplitude jitter when the power in

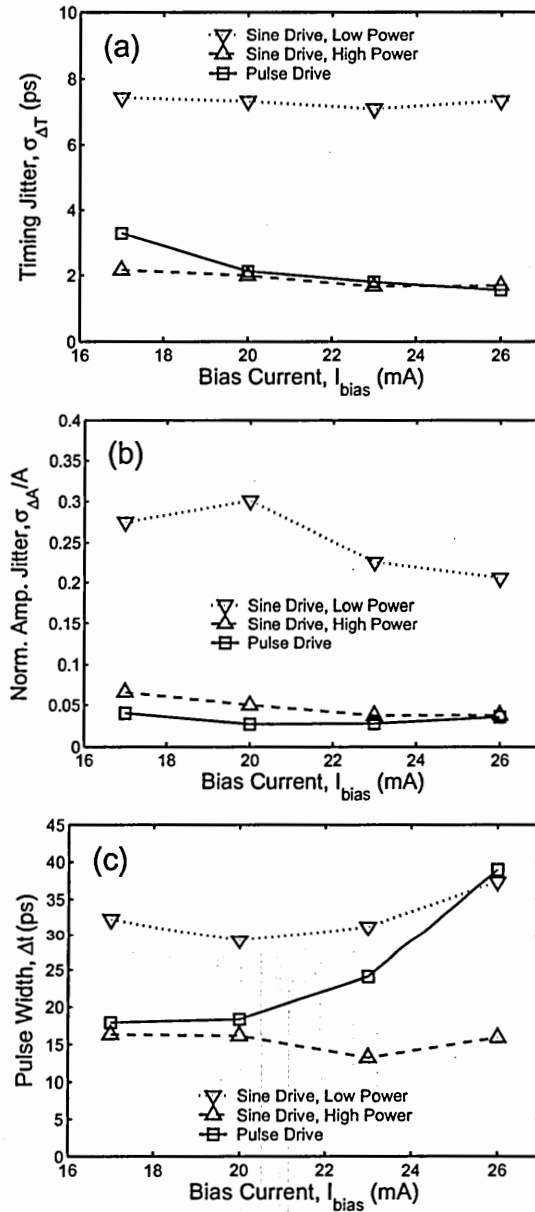


Figure 3.4: Measured values plotted against bias current for three gain-switching scenarios: (a) timing jitter, (b) normalized amplitude jitter, and (c) temporal full width at half of maximum.

the sine wave and pulse train are equal. In particular, the timing jitter is reduced, when we consider an average of all four biases, to 0.30 of that obtained in the low-power-sinusoid case. The amplitude jitter is reduced, on average, to 0.13 of the low-power-sinusoid value. Both of these results agree, approximately with our prediction, indicating that both jitter values are indeed proportional to the FWHM of the drive signal (for equal-power drive signals). In contrast, the optical pulse width is, on average, only reduced to 0.76 of the initial value, indicating that the duration of the optical pulse is limited, in this case, by other factors, perhaps the resonance of the laser diode.

Contrastingly, when the power in the sine wave is equal to that used to drive the impulse generator, we find that the timing and amplitude jitter are nearly the same in both the sinusoidal and pulse-train drive, and the pulse width is *lower* in the sine-drive case (for higher biases). In particular, the timing jitter is reduced, considering an average of all four biases, to 0.26 of that obtained in the low-power-sinusoid case. If we ignore the lowest-bias datum, the timing-jitter-reduction ratio computed for the pulse-drive case drops to the same value obtained, for the remaining three biases, in the sine-drive case. The amplitude jitter is reduced, on average, to 0.13 of the low-power-sinusoid value. These results indicate that it the power, rather than the pulse width, of the electrical drive signal determines the jitter. The optical pulse width is, on average, reduced to 0.47 of the initial value. This ratio superior to that found in that found in the pulse-drive case, but still far different from what is predicted by Eq. 3.2.

3.5 Commentary

Our results indicate that, though some jitter and pulse-width reduction may be obtained by using a pulse train to gain-switch the laser diode, it is just as effective and considerably simpler to use a higher-power sinusoid. This finding suggests that, in

our case, the jitter-reduction associated with increasing drive-signal amplitude (or, equivalently, power) [114], [115], [125] outweighs the reduction of jitter associated with decreasing drive-current rise time [115].

CHAPTER 4

Temporal-Multiplexing Amplitude Jitter

4.1 Roadmap

Chapter 4 discusses the power fluctuation that results from temporally multiplexing a pulse that contains a finite pedestal. Section 4.2 describes this difficulty and the need for a solution. Section 4.3 reviews previous work in the fields of OTDM jitter and pedestal suppression. Section 4.4 is the heart of this chapter; in this section, we present a theoretical analysis of temporal-multiplexing-induced amplitude jitter, and describe experimental (and quantitative) confirmation of this theory. Section 4.5, as usual, is a brief review of the chapter.

4.2 The Problem

In an optical time-division multiplexer (Fig. 1.4), a single, lower-rate pulse train is temporally interleaved and modulated to produce a higher-rate train: each pulse produced by the source is split, differentially delayed, modulated, and recombined. In the recombined pulse train, interference occurs between each pulse and the pedestal of nearby pulses. The net pedestal is composed of energy, from all other pulses, that occurs within the time slot of the given pulse. In the temporal multiplexer, especially a fiber-based embodiment, fluctuations in environmental parameters, such as temperature and strain, result in variations of the pulse-pedestal relative phase

prior to recombination. These phase fluctuations result in a slow (compared to the repetition rate) modulation of the pulse intensity of the multiplexed data stream.

Note that this problem is alleviated *somewhat* if alternating polarization states are used. However, some demultiplexing schemes, such as surface-emitted second-harmonic generation [35], [37], [38] require uniformly polarized data streams. Further, the pedestal often extends over several times T_{sys} , so alternating the polarizations will not ameliorate the problem sufficiently.

These intensity fluctuations are a form of correlated amplitude jitter with a very long (~ 1 s) correlation time. Thus, Eq. 1.2 applies when quantifying the effect of these fluctuations on the BER of an OTDM link.

Many means of short-pulse production, typically those involving pulse compression, result in pulses with a significant fraction of their energy in a pedestal [120]–[122], [126]–[129], [156], [157]. In fact, nearly all pulses produced with some type of non-linear compression exhibit significant pedestals. It is, therefore, imperative to find a means of reducing a pulse’s pedestal.

4.3 Previous Work

4.3.1 Pedestal Suppression

Since the temporal-multiplexing power fluctuation is slow (typically on the order of 1 Hz), it should be possible to reduce them using automatic power control [158], [159]: However, pedestal suppression using a saturable absorber (a high-pass intensity filter) directly addresses the cause of the problem and is a more elegant solution. Several researchers have shown that a saturable absorber (a high-pass intensity filter) can be employed to suppress the pedestal level of a pulse train [121], [122], [127]–[130].

4.3.2 Saturable Absorbers

All saturable absorbers can be classified as either real or artificial. A real saturable absorber is any material with a positively sloped transmission-*versus*-irradiance curve. An artificial saturable absorber (ASA) is a device that converts some nonlinear phenomenon, such as nonlinear phase shifting (NPS) [78], [122], [127], [128], [128]–[130], [160], Kerr lensing [161], or nonlinear polarization rotation (NPR) [35], [121], [137], [162], into a transmission function that increases with increasing irradiance. (Note that real and artificial saturable absorber are often used to initiate passive mode-locking or for pulse-shortening in hybrid mode-locking¹. Saturable absorbers are also categorized as either slow (The response time is long compared to duration of the optical pulse in question.) or fast (The response time is short compared to the pulse width.).

Since our experiments were performed with a nonlinear amplifying loop mirror (Experiments performed with an NPR-based ASA yielded disappointingly high pedestals.), it is prudent to discuss the theory behind the NALM's operation. Before doing so, it is illustrative to consider the NALM's predecessor, the nonlinear optical loop mirror (NOLM).

4.3.2.1 Nonlinear Optical Loop Mirror

The nonlinear optical loop mirror (Fig. 4.1) [78], [122], [128], [130] is an elegant, all-fiber artificial fast saturable absorber based on the Sagnac interferometer. The NOLM is simply a directional coupler whose output ports (Ports 3 and 4) have been connected together. The coupler's power splitting ratio is α ; the power coupled from Port 1 to Port 3 is α , and the power coupled from Port 1 to Port 4 is $1 - \alpha$. The fiber polarization controller (FPC) is included to set the Jones matrix of the loop to

¹ See Section 2.3.

the identity matrix; thus, when the pulse halves meet in the coupler, they will have the same polarization and will therefore interfere.

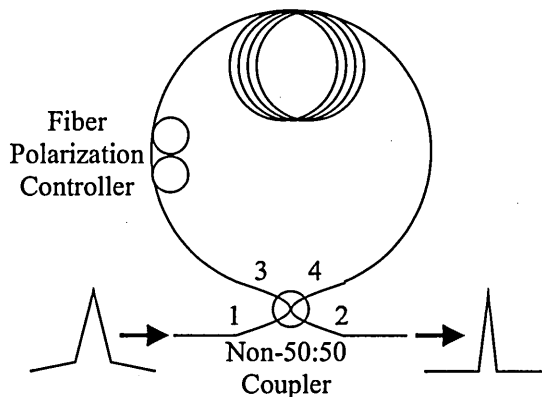


Figure 4.1: The ideal nonlinear optical loop mirror.

Let E_{1i} be the electric-field envelope impinging on the coupler from Port 1. The corresponding power is $P_{1i} \propto E_{1i}^2$, and $I_{1i} = P_{1i}/A_{\text{eff}}$ is the irradiance, where A_{eff} is the effective area of the fiber. The fields departing through Ports 3 and 4 are given, respectively, by

$$E_{3o} = \sqrt{\alpha}E_{1i} ; \quad (4.1)$$

$$E_{4o} = i\sqrt{1-\alpha}E_{1i} . \quad (4.2)$$

(The i in E_{4o} comes about because of the phase shift the field experiences when switching fibers inside the coupler: $i = e^{i\pi/2}$.)

We can calculate the nonlinear phase shift experienced by each of these fields as they propagate around the loop. The result gives us the fields going back into Ports 3 and 4, E_{3i} and E_{4i} , respectively:

$$E_{3i} = E_{4o} \exp[i(1-\alpha)n_2I_{1i}kL_{\text{NOLM}}] ; \quad (4.3)$$

$$E_{4i} = E_{3o} \exp[i\alpha n_2I_{1i}kL_{\text{NOLM}}] . \quad (4.4)$$

In both equations, n_2 is the nonlinear index of the fiber. ($n_2 \simeq 2.2 \cdot 10^{-20}$ to $3.4 \cdot 10^{-20}$ m^2/W for silica fibers [135].), Additionally, $k = 2\pi/\lambda$ is the wavenumber of the optical field, and L_{NOLM} is the length of the NOLM's loop.

The net phase difference between these two fields as they recombine in the coupler, φ_{NOLM} , is given by

$$\varphi_{\text{NOLM}} = (1 - 2\alpha)n_2I_{1i}kL_{\text{NOLM}} . \quad (4.5)$$

(The i from before plays no part, because light in one fiber must cross to the other before interfering, which cancels out the phase shift.)

Finally, we can calculate the irradiance *output* through Port 1, I_{1o} , to be

$$I_{1o} = I_{1i}2\alpha(1 - \alpha)[1 + \cos(\varphi_{\text{NOLM}})] . \quad (4.6)$$

Using $I_{2o} = I_{1i} - I_{1o}$, we can calculate the NOLM's power reflection, $\mathcal{R}_{\text{NOLM}}$, and power transmission, $\mathcal{T}_{\text{NOLM}}$:

$$\begin{aligned} \mathcal{R}_{\text{NOLM}} &\equiv \frac{I_{1o}}{I_{1i}} \\ &= 2\alpha(1 - \alpha)[1 + \cos(\varphi)] ; \end{aligned} \quad (4.7)$$

$$\begin{aligned} \mathcal{T}_{\text{NOLM}} &\equiv \frac{I_{2o}}{I_{1i}} \\ &= 1 - 2\alpha(1 - \alpha)[1 + \cos(\varphi)] . \end{aligned} \quad (4.8)$$

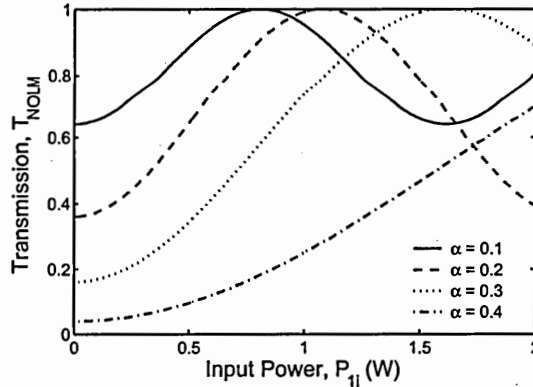


Figure 4.2: The transmission of the nonlinear optical loop mirror for four values of the power-splitting ratio, α .

In Fig. 4.2, $\mathcal{T}_{\text{NOLM}}$ is plotted for four values of α : 0.1, 0.2, 0.3, and 0.4. (The plot assumes $n_2 = 3 \times 10^{-20} \text{ m}^2/\text{W}$, $A_{\text{eff}} = 50 \text{ } \mu\text{m}^2$, $\lambda = 1550 \text{ nm}$, and $L_{\text{NOLM}} = 3$

km.) Note the intensity-dependent switching action of the NOLM. Physically, this switching arises from the unequal splitting of the power. Since the clockwise-travelling and counterclockwise-travelling pulses have different intensities, they see different refractive indices. Hence one pulse is phase-shifted with respect to the other. When the pulses recombine at the coupler, this phase shift forces the optical power to split unequally between Ports 1 and 2. (If there were no nonlinear effects, the coupler would exactly undo the splitting of the power, and all the energy would exit Port 1.) This unequal split varies, depending on the input intensity and the initial splitting ratio.

From the equation and the figure, we see that the contrast ratio increases as the splitting ratio approaches 50:50. Unfortunately, the input irradiance required for switching increases as α tends toward 0.50, becoming infinite there. As the split approaches equality, the difference in power between the counter-propagating pulses, for a given input power, drops. Thus more and more input intensity is required to achieve the same index difference and the same switching behavior. At $\alpha = 0.50$, no amount of input pulse energy will produce an intensity difference or the resulting index difference.

Looking at Fig. 4.2, we see that, over some domain, the NOLM can act as a saturable absorber. As a result, it can be used to mode-lock a laser (when incorporated into the cavity) or suppress unwanted pedestals (when placed downstream of the laser source).

Note that the nonlinear phase shifting of the NOLM relies on the Kerr nonlinearity. The response time of this nonlinearity is approximately 2 to 4 fs [135]. Thus, the NALM is more than fast enough to suppress the pedestals of picosecond pulses. One drawback to the NOLM is that it adds chirp to its optical output, broadening the spectrum beyond the transform limit. [157].

Variations on the on the basic NOLM include the dispersion-imbalanced NOLM [127]–[129], [157] (Here, different dispersion parameters on each side of the loop provide asymmetry, allowing a 50:50 coupler to be employed.), the dispersion-decreasing NOLM [160] (This loop mirror is a “continuous” version of the dispersion-imbalanced NOLM; the loop fiber’s dispersion varies smoothly along its length.), and the nonlinear amplifying loop mirror. IN the next Subsubsection, we look more closely at the NALM.

4.3.2.2 Nonlinear Amplifying Loop Mirror

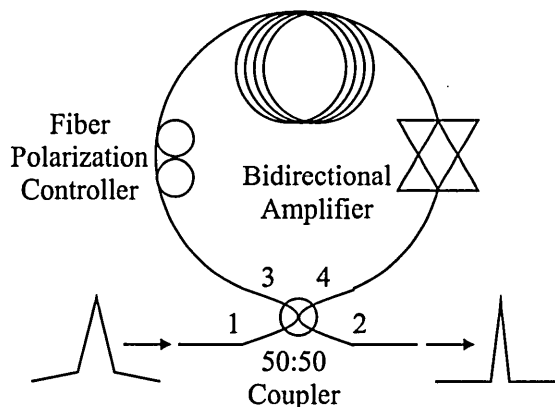


Figure 4.3: The ideal nonlinear amplifying loop mirror.

In the nonlinear amplifying loop mirror [78], [130], also called the amplifying Sagnac switch, an optical amplifier is used to provide the asymmetry, enabling the use of a 50:50 splitter, which yields high contrast with finite power. The ideal NALM is diagrammed in Fig. 4.3.

The amplifier, usually an EDFA, is placed close to one port of the coupler. Because of the 50:50 coupler, the pulses entering the loop have the same power. One of these pulses is immediately boosted to a much higher power. From this point on, the NALM works much like a NOLM. The net phase difference is

$$\varphi_{\text{NALM}} = (G - 1)n_2 I_1 k L_{\text{NALM}} , \quad (4.9)$$

where G is the gain of the amplifier and L_{NALM} is the length of the NALM's loop. Modifying our earlier calculations, we find the following results, which are similar in form to the NOLM results:

$$I_{1o} = I_{1i} G \cos^2(\varphi_{\text{NALM}}) . \quad (4.10)$$

$$I_{2o} = I_{1i} G \sin^2(\varphi_{\text{NALM}}) . \quad (4.11)$$

These equations leads to

$$\begin{aligned} \mathcal{R}_{\text{NALM}} &\equiv \frac{I_{1o}}{I_{1i}} \\ &= G \cos^2(\varphi_{\text{NALM}}) ; \end{aligned} \quad (4.12)$$

$$\begin{aligned} \mathcal{T}_{\text{NALM}} &\equiv \frac{I_{2o}}{I_{1i}} \\ &= G \sin^2(\varphi_{\text{NALM}}) . \end{aligned} \quad (4.13)$$

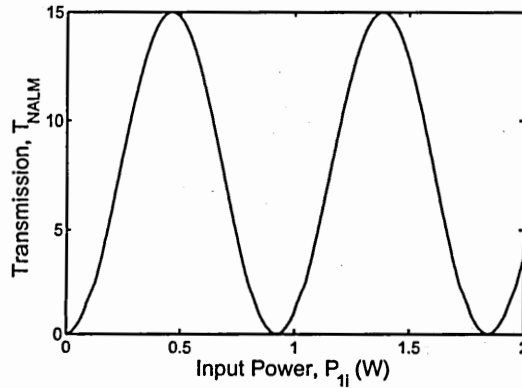


Figure 4.4: The nonlinear transmission of the nonlinear amplifying loop mirror.

We plot Eq. 4.13 in Fig. 4.4. (The plot was made assuming $n_2 = 3 \times 10^{-20} \text{ m}^2/\text{W}$, $A_{\text{eff}} = 50 \text{ } \mu\text{m}^2$, $\lambda = 1550 \text{ nm}$, and $L_{\text{NALM}} = 100 \text{ m}$, and $G = 15$.) Again, we see saturable absorption. This time, however, we can achieve 100 % contrast with finite input power.

Note that the NALM, also works by the Kerr nonlinearity, and is therefore sufficiently fast for our purpose. Also like the NOLM, a NALM adds chirp to its

output. Indeed, the chirp imposed by the NALM is often greater than that imposed by the NOLM, due to higher powers that result from use of the amplifier.

4.3.3 Remarks

To our knowledge, until the author's work [27], [28] no researcher has systematically investigated the effect of pedestal level on interference-induced power fluctuations of the temporally multiplexed data stream. It is this topic we will investigate in this chapter.

4.4 Present Contribution

4.4.1 Theory

Before we begin our analysis, we present a note about the nomenclature employed in this chapter. We will frequently need to discuss the pulse shape, which is a function of

$$t_{\text{loc}} \equiv t - \frac{z}{v_g}, \quad (4.14)$$

the local time in a frame moving at v_g , the group velocity of the pulse. Due to this frequency of use, the parameter t_{loc} becomes somewhat cumbersome. In this chapter, we will, therefore, use t as a shorthand for t_{loc} .

4.4.1.1 Temporal-Multiplexing Jitter

We would like to quantify the impact of pedestal level on temporal-multiplexing jitter. We begin by establishing our notation. Consider a pedestal-free pulse (Fig. 4.5) propagating through an optical fiber. The electric-field envelope of the pulse, E_0 , is given by

$$E_0(t) = \kappa \sqrt{A_0} u_0(t), \quad (4.15)$$

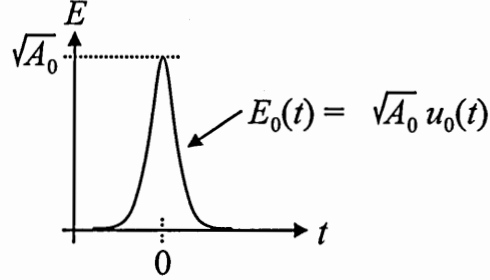


Figure 4.5: The electric field of a pedestal-free pulse. E —electric field. t —time. κ —normalization constant. A_0 —power amplitude of pedestal-free pulse. E_0 —time-dependent electric-field envelope of pedestal-free pulse. u_0 —unitless, unit-amplitude field-shape function of pedestal-free pulse.

where κ is a normalization constant and $u_0(t)$ is a unitless, unit-amplitude *field*-shape function. The significance of the $\sqrt{A_0}$ factor becomes apparent when we compute the power of the pulse, P_0 :

$$\begin{aligned} P_0(t) &= \frac{A_{\text{eff}}}{\eta} |E_0(t)|^2 \\ &= \frac{A_{\text{eff}}}{\eta} \kappa^2 A_0 s_0(t), \end{aligned} \quad (4.16)$$

where η is the impedance of the medium and $s_0(t) \equiv |u_0(t)|^2$ is a unitless, unit-amplitude *power*-shape function. If we choose

$$\kappa \equiv \sqrt{\frac{\eta}{A_{\text{eff}}}}, \quad (4.17)$$

then

$$P_0(t) = A_0 s_0(t), \quad (4.18)$$

and A_0 becomes the power amplitude of the pulse (with units are W).

Now consider a more general pulse, one with a finite pedestal (Fig. 4.6). The electric field envelope of this pulse, E , is

$$E(t) = \sqrt{\frac{\eta}{A_{\text{eff}}}} \sqrt{A} \{ \hat{E}_0 u_0(t) + \hat{E}_{\text{ped}} \}. \quad (4.19)$$

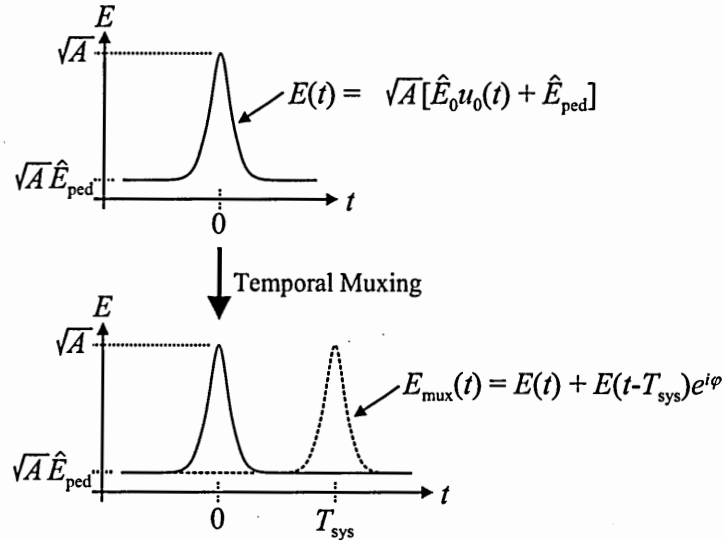


Figure 4.6: Temporal multiplexing of a finite-pedestal pulse train. E —electric field. t —time. κ —normalization constant. A —power amplitude of finite-pedestal pulse. \hat{E}_{ped} —normalized field amplitude of pedestal. $\hat{E}_0 \equiv 1 - \hat{E}_{\text{ped}}$ —normalized field amplitude of pedestal-free component. E —time-dependent electric-field envelope of finite-pedestal pulse. E_{mux} —time-dependent electric-field envelope after multiplexing. T_{sys} —bit period after multiplexing. u_0 —unitless, unit-amplitude field-shape function of pedestal-free component.

Here, A is the power-amplitude of the pulse. $\hat{E}_0 \equiv E_0/\sqrt{A}$ and $\hat{E}_{\text{ped}} \equiv E_{\text{ped}}/\sqrt{A}$ are the normalized, unitless field-amplitudes of the pedestal-free pulse component and the pedestal, respectively; E_0 and E_{ped} are the corresponding non-normalized field amplitudes, the units of which units are V/m. Note that we want

$$E(0) = \sqrt{\frac{\eta}{A_{\text{eff}}}}. \quad (4.20)$$

This requirement implies

$$\hat{E}_0 = 1 - \hat{E}_{\text{ped}}. \quad (4.21)$$

The power of the finite-pedestal pulse is

$$P(t) = \frac{A_{\text{eff}}}{\eta} |E(t)|^2$$

$$= A \{ \hat{A}_0 s_1(t) + \hat{A}_{\text{ped}} \} . \quad (4.22)$$

where

$$s_1(t) \equiv s_0(t) + \hat{E}_0 \hat{E}_{\text{ped}}^* u_0(t) + \hat{E}_0^* \hat{E}_{\text{ped}} u_0^*(t) , \quad (4.23)$$

where the superscript asterisk (*) indicates complex conjugation. Note that, for low small pedestals, $s_1 \simeq s_0$. Further, $\hat{A}_0 \equiv A_0/A$ and $\hat{A}_{\text{ped}} \equiv A_{\text{ped}}/A$ are the normalized, unitless power-amplitudes of the pedestal-free pulse component and the pedestal, respectively; A_0 and A_{ped} are the corresponding non-normalized power amplitudes, whose units are W. It is important to note that \hat{A}_{ped} is the normalized pedestal power. Note that want the pulse amplitude to be A :

$$P(0) = A . \quad (4.24)$$

This requirement is satisfied by Eq. 4.21.

Now let us move on to the temporal multiplexing of two finite-pedestal pulses (Fig. 4.6). If we assume the peak and pedestal of each pulse are coherent and like-polarized, the electric-field envelope of the output of the temporal multiplexer, E_{ped} , is given by

$$\begin{aligned} E_{\text{mux}}(t) &= E(t) + E(t - T_{\text{sys}}) e^{i\pi} \\ &= \sqrt{\frac{\eta}{A_{\text{eff}}}} \sqrt{A} \{ \hat{E}_0 u_0(t) + \hat{E}_{\text{ped}} + \hat{E}_0 u_0(t - T_{\text{sys}}) e^{i\varphi} + \hat{E}_{\text{ped}} e^{i\varphi} \} , \end{aligned} \quad (4.25)$$

where φ is the phase difference between the two pulses, and T_{sys} is the system period.

Although the entire pulse fluctuates, it is useful to consider only the fluctuations at the peak of the pulse. Looking only at the peak simplifies the mathematics but does not change the result. The electric field at the peak is

$$E_{\text{mux}}(0) = \sqrt{\frac{\eta}{A_{\text{eff}}}} \sqrt{A} \{ \hat{E}_0 u_0(0) + \hat{E}_{\text{ped}} + \hat{E}_0 u_0(-T_{\text{sys}}) e^{i\pi} + \hat{E}_{\text{ped}} e^{i\pi} \} . \quad (4.26)$$

Because $u_0(0) = 1$ and $\hat{E}_0 = 1 - \hat{E}_{\text{ped}}$, the first two terms sum to unity. Recall that $T_{\text{sys}} \gg \Delta t$, in accordance with Subsection 1.4.4. Hence, the third term is approxi-

mately zero. Therefore,

$$E_{\text{mux}}(t) \simeq \sqrt{\frac{\eta}{A_{\text{eff}}}} \sqrt{A} \{1 + \hat{E}_{\text{ped}} e^{i\pi}\} . \quad (4.27)$$

In other words, in agreement with intuition, the net electric field at the peak of one pulse can be written as the sum of the fields of the peak of that pulse and of the pedestal of the other.

The power of the peak in question, $P_{\text{mux}}(0)$, is

$$\begin{aligned} P_{\text{mux}}(0) &= \frac{A_{\text{eff}}}{\eta} |E_{\text{mux}}(0)|^2 \\ &\simeq A \left\{ 1 + 2\sqrt{\hat{A}_{\text{ped}}} \cos(\varphi) + A_{\text{ped}} \right\} , \end{aligned} \quad (4.28)$$

if \hat{A}_{ped} is real.

We can now calculate the peak-to-peak deviation of the *peak* power, ΔP_{PP} , due to differential environmental fluctuations in the paths of the multiplexer. If we assume that that the phase difference can vary over $[0, 2\pi)$, then

$$\Delta P_{\text{PP}} \simeq 4A\sqrt{\hat{A}_{\text{ped}}} . \quad (4.29)$$

If we further assume that the probability-distribution function of φ is *uniform* [163], [164], the mean of the peak power, μ_P will be given by

$$\mu_P \simeq A \left\{ 1 + \sqrt{\hat{A}_{\text{ped}}} \right\} . \quad (4.30)$$

Thus, $\widehat{\Delta P}_{\text{PP}}$, the normalized peak-to-peak deviation of the power of the peak of the multiplexed train is

$$\begin{aligned} \widehat{\Delta P}_{\text{PP}} &\equiv \frac{\Delta P_{\text{PP}}}{\mu_P} \\ &\simeq \frac{4\sqrt{\hat{A}_{\text{ped}}}}{1 + \sqrt{\hat{A}_{\text{ped}}}} . \end{aligned} \quad (4.31)$$

This result is plotted in Fig. 4.7. Note that both of the assumptions we've made about distribution of φ are very physically reasonable.

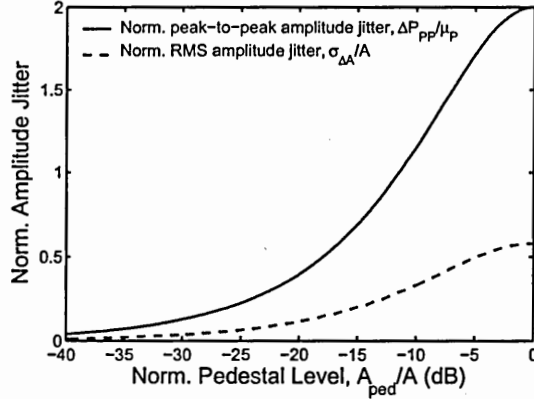


Figure 4.7: Normalized pedestal-induced amplitude jitter, plotted against normalized pedestal power.

Finally, the assumption of uniform distribution allows us to compute the root-mean-squared deviation from the peak-to-peak deviation. Because the peak-power variation we've described in this subsection is equivalent to amplitude jitter, we will denote the RMS deviation (or standard deviation) of the peak power with $\sigma_{\Delta A}$; the normalized version will be denoted by $\hat{\sigma}_{\Delta A}$. According to Appendix A (Eq. A.2),

$$\sigma_{\Delta A} = \frac{\Delta P_{PP}}{2\sqrt{3}}. \quad (4.32)$$

Examining Eq. 4.30, we see that the mean of the peak power is approximately A . Hence,

$$\begin{aligned} \hat{\sigma}_{\Delta A} &\equiv \frac{\sigma_{\Delta A}}{A} \\ &\simeq \frac{2A\sqrt{\hat{A}_{ped}}}{\sqrt{3}\{1 + \sqrt{\hat{A}_{ped}}\}}. \end{aligned} \quad (4.33)$$

This equation is also plotted in Fig. 4.7.

By combining Eqs. 1.2 and 4.33, we can now express the bit-error rate of a temporally multiplexed pulse train as a function of the normalized pedestal level, \hat{A}_{ped} .

This relationship is plotted in Fig. 4.8. (Note that we are not considering other types of amplitude jitter in this analysis. Since the pedestal-induced jitter and the

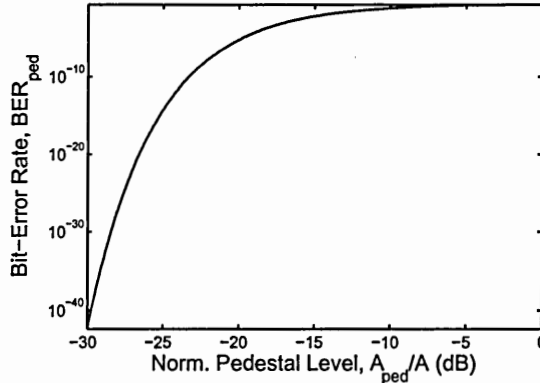


Figure 4.8: The BER, due to pedestal-induced amplitude jitter, of a temporally multiplexed pulse train, plotted against normalized pedestal level.

noise of the source itself are independent, the RMS *total amplitude variation* will be given by the sum-of-squares addition of the RMS OTDM jitter and the source's RMS amplitude jitter, and the BER will be impacted accordingly.) Note also that we are ignoring timing jitter, pulse width, and any other problems with the pulse train, which would also raise the BER. Examining Fig. 4.8, we see that, to achieve a BER of 10^{-9} or 10^{-12} , the pedestal must be at 22.7 dB or 24.1 dB below the peak, respectively. Clearly, practical RZ OTDM sources must exhibit *dramatically* low pedestal levels.

4.4.1.2 Autocorrelation Pedestal Level

As we can only observe the temporal dependence of picosecond pulses (which are much shorter than the impulse response of our fastest photoreceiver) with an autocorrelator, it is useful to be able calculate normalized pedestal level of a pulse from that of the intensity autocorrelation. Recall that the time-dependent power of a finite-pedestal pulse is

$$P(t) \simeq A \{ \hat{A}_0 s_1(t) + \hat{A}_{ped} \} . \quad (4.34)$$

Consider the autocorrelation of the this pulse, $\phi_p(\tau)$:

$$\phi_P(\tau) \equiv \int_{-\infty}^{\infty} P^*(t) P(t + \tau) dt , \quad (4.35)$$

where τ is the temporal delay of the autocorrelation. Note that all integrals in this chapter run from $-\infty$ to ∞ unless otherwise indicated. Evaluating the integral yields

$$\phi_P(\tau) \simeq A^2 \int \left\{ \widehat{A}_0^2 s_1(t) s_1(t + \tau) + \widehat{A}_0 \widehat{A}_{\text{ped}} \{s_1(t) + s_1(t + \tau)\} + \widehat{A}_{\text{ped}}^2 \right\} dt. \quad (4.36)$$

The last term is very small, since \widehat{A}_{ped} is, by assumption, small. Hence,

$$\phi_P(\tau) \simeq A^2 \int \left\{ \widehat{A}_0^2 s_1(t) s_1(t + \tau) + \widehat{A}_0 \widehat{A}_{\text{ped}} \{s_1(t) + s_1(t + \tau)\} \right\} dt. \quad (4.37)$$

Let us examine the autocorrelation at $\tau = 0$, where the peak occurs.

$$\phi_P(0) \simeq A^2 \int \left\{ \widehat{A}_0^2 s_1^2(t) + 2\widehat{A}_0 \widehat{A}_{\text{ped}} s_1(t) \right\} dt. \quad (4.38)$$

The second term is very small compared to the first, so

$$\phi_P(0) \simeq A^2 \widehat{A}_0^2 \int s_1^2(t) dt. \quad (4.39)$$

Now let us examine the autocorrelation at τ_{far} , a delay much greater than Δt , the width of the pulse.

$$\begin{aligned} \phi_P(\tau_{\text{far}}) \simeq A^2 \left\{ \widehat{A}_0^2 \int s_1(t) s_1(t + \tau_{\text{far}}) dt \right. \\ \left. + \widehat{A}_0 \widehat{A}_{\text{ped}} \int s_1(t) dt \right. \\ \left. + \widehat{A}_{\text{ped}}^2 \int s_1(t + \tau_{\text{far}}) dt \right\}. \end{aligned} \quad (4.40)$$

Since $\tau_{\text{far}} \gg \Delta t$, there is very little overlap between $s_1(t)$ and $s_1(t + \tau_{\text{far}})$. Thus, the first integrand is approximately zero for all t . Because the bounds of integration are infinite, the $t + \tau_{\text{far}}$ in the third term can be replaced with t . Therefore,

$$\phi_P(\tau_{\text{far}}) \simeq A^2 \widehat{A}_0 \widehat{A}_{\text{ped}} \int s_1(t) dt. \quad (4.41)$$

Now we want to compute the normalized pedestal level of the autocorrelation, which we denote with \widehat{B}_{ped} :

$$\widehat{B}_{\text{ped}} \equiv \frac{\phi_P(\tau_{\text{far}})}{\phi_P(0)}. \quad (4.42)$$

Computing the ratio of the true and autocorrelation pedestal levels yields

$$\frac{\hat{A}_{\text{ped}}}{\hat{B}_{\text{ped}}} \simeq \frac{1}{\xi}, \quad (4.43)$$

where

$$\xi \equiv \frac{2 \int s_1(t) dt}{\int s_1^2(t) dt}. \quad (4.44)$$

We must know the pulse shape to compute ξ . By assuming Gaussian and hyperbolic secant shapes, we arrive at

$$\xi = \begin{cases} 2\sqrt{2} & \text{Gaussian .} \\ 3 & \text{sech}^2 . \end{cases} \quad (4.45)$$

Thus,

$$\frac{\hat{A}_{\text{ped}}}{\hat{B}_{\text{ped}}} \simeq \begin{cases} \frac{1}{2\sqrt{2}} & \text{Gaussian .} \\ \frac{1}{3} & \text{sech}^2 . \end{cases} \quad (4.46)$$

The result shows that the autocorrelator exaggerates the pedestal level.

4.4.1.3 Autocorrelation Amplitude Jitter

One of our measurements of the pedestal level is made with an intensity autocorrelation recorded by an oscilloscope operating in persistence mode. Thus, we would like to be able to extract the power fluctuation (amplitude jitter, intensity noise) from those of the persistence autocorrelation.

Consider a pulse whose noisy (power) amplitude is given by

$$A' = A + \Delta A, \quad (4.47)$$

where ΔA is zero-mean random variable representing amplitude jitter. (Note that the mean of A' , is A .) The time-dependent power of the pulse will be

$$P(t) \simeq A's(t). \quad (4.48)$$

The autocorrelation of the pulse, ϕ_P , is given by

$$\phi_P(\tau) = A'^2 \phi_s(\tau), \quad (4.49)$$

where ϕ_s is the autocorrelation of the shape function, and τ is the temporal delay. Note that the amplitude of the autocorrelation is proportional to the square of the power amplitude of the pulse.

For convenience, let us define

$$B' \equiv A'^2. \quad (4.50)$$

Further, let us define, for any variable x , x_{\min} as the minimum of x , and x_{\max} as the maximum of x . The peak-to-peak power fluctuation of the pulse, ΔP_{PP} , is simply $A'_{\max} - A'_{\min}$, while the mean of A' , is $\frac{1}{2}(A'_{\max} + A'_{\min})$. Thus the *normalized* peak-to-peak deviation is

$$\begin{aligned} \widehat{\Delta P}_{PP} &= \frac{A'_{\max} - A'_{\min}}{\frac{1}{2} \{A'_{\max} + A'_{\min}\}} \\ &= 2 \frac{\sqrt{B'_{\max}} - \sqrt{B'_{\min}}}{\sqrt{B'_{\max}} + \sqrt{B'_{\min}}}. \end{aligned} \quad (4.51)$$

Note that this analysis ignores any noise in the autocorrelation process.

We can easily account for *thermal* noise. (Shot noise is more difficult.) We measure the thermal noise by examining the autocorrelation power at a delay far from the pulses, denoted by C' . If we let $C'_{\text{dif}} = C'_{\max} - C'_{\min}$, then we can correct Eq. 4.51 for the thermal noise by replacing B'_{\max} with $D'_{\max} \equiv B'_{\max} - \frac{1}{2}C'_{\text{dif}}$ and replacing B'_{\min} with $D'_{\min} \equiv B'_{\min} + \frac{1}{2}C'_{\text{dif}}$. The result is

$$\begin{aligned} \widehat{\Delta P}_{PP} &= 2 \frac{\sqrt{D'_{\max}} - \sqrt{D'_{\min}}}{\sqrt{D'_{\max}} + \sqrt{D'_{\min}}} \\ &= 2 \frac{\sqrt{B'_{\max} - \frac{1}{2}C'_{\text{dif}}} - \sqrt{B'_{\min} + \frac{1}{2}C'_{\text{dif}}}}{\sqrt{B'_{\max} - \frac{1}{2}C'_{\text{dif}}} + \sqrt{B'_{\min} + \frac{1}{2}C'_{\text{dif}}}}. \end{aligned} \quad (4.52)$$

If we assume a uniform PDF, we can use Eq. 4.32 to compute the RMS multiplexing-induced amplitude jitter:

$$\hat{\sigma}_{\Delta A} = \frac{1}{\sqrt{3}} \frac{\sqrt{B'_{\max} - \frac{1}{2}C'_{\text{dif}}} - \sqrt{B'_{\min} + \frac{1}{2}C'_{\text{dif}}}}{\sqrt{B'_{\max} - \frac{1}{2}C'_{\text{dif}}} + \sqrt{B'_{\min} + \frac{1}{2}C'_{\text{dif}}}}. \quad (4.53)$$

4.4.2 Experiment

4.4.2.1 Experimental Setup

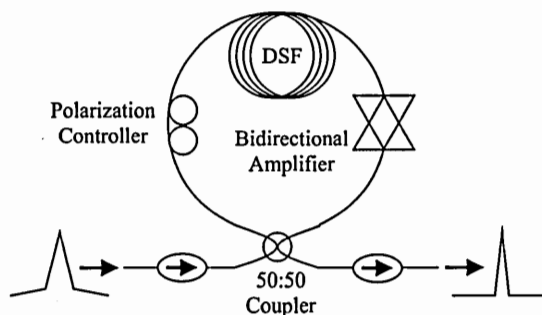


Figure 4.9: A diagram of the nonlinear amplifying loop mirror employed in the experiments. DSF—dispersion-shifted fiber.

We employed the first 3 stages of the psPS² to provide pulses with significant pedestals. We choose a NALM as the saturable absorber, rather than another loop-mirror variant, because the higher asymmetry, and resulting greater phase difference, between the two paths yields superior performance. Furthermore, the NALM can achieve a 100 % contrast ratio with finite input power. In addition, the amplifier gain provides an additional degree of freedom and allows the NALM to be easily optimized.

A diagram and a photograph of the nonlinear amplifying loop mirror we constructed for these experiments are shown in Figs. 4.9, and 4.10, respectively. The NALM employ 300 m of dispersion-shifted fiber (Corning model SMF-DS, $D = 0$ ps/[nm-km] and $dD/D\lambda = 0.0687$ ps/[nm²-km], both measured at 1562.82 nm) and

² See Chapter 2.

a bidirectional, wide-core EDFA of length 2.1 m (Pritel model SPFA-1550). To prevent lasing, we insert isolators at the input and output of the NALM and make all connections by splicing or with angled connectors.

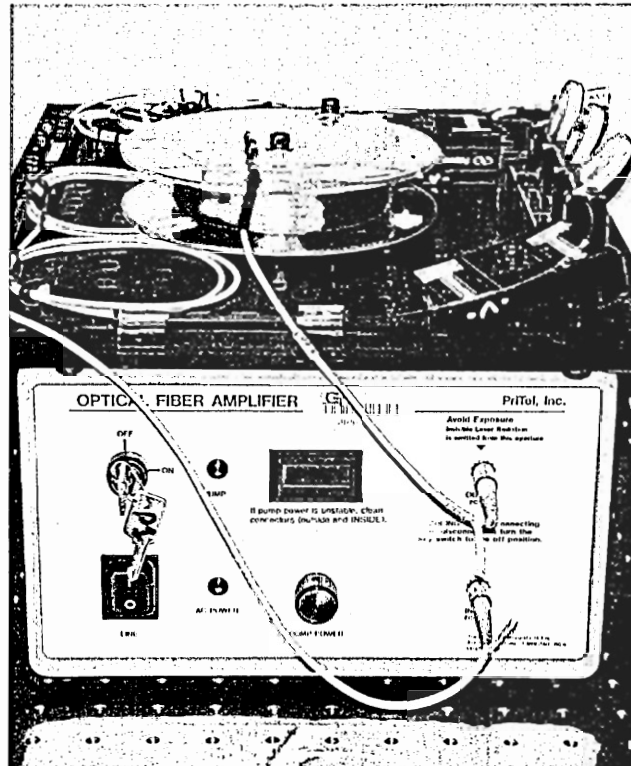


Figure 4.10: A photograph of the nonlinear amplifying loop mirror employed in the experiments.

To evaluate the impact of pedestal reduction on the power variations of an OTDM data stream, we employ a fiber-based temporal multiplexer (a four-channel version of the device shown in Fig. 1.4). The inter-pulse delays are set to 6.25 ps (160 GHz), and the pulse polarizations are set equal. The modulators are biased to produce an all-ONES data stream. This multiplexer can be configured to produce one-, two-, three- or four-bit trains.

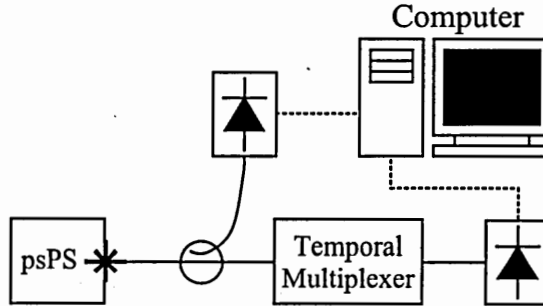


Figure 4.11: Experimental setup for measuring multiplexing-induced amplitude jitter using a power meter.

4.4.2.2 Measurement Techniques

We employ two techniques to measure $\widehat{\Delta P}_{PP}$ and $\widehat{\sigma}_{\Delta A}$ of the multiplexed train: one method employs a power meter, and one employs an autocorrelator.

In the first method (Fig. 4.11), we record the power of two-bit trains over several minutes using an integrating sphere (Newport model 818-IS-1) and power meter (Newport model 2832-C). This measurement assumes the power fluctuations are slower than the 500-kHz sampling rate of the power meter. Note the two-arm setup in the figure; the optical power is measured both before and after the multiplexer, and a computer normalizes the output power to the input power. Thus, any drift of the source power does not affect the measurement.

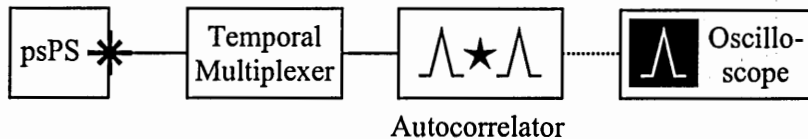


Figure 4.12: Experimental setup for measuring multiplexing-induced amplitude jitter using a persistence autocorrelation.

In the second method (Fig. 4.12), we record the autocorrelations of four-bit trains, using an oscilloscope in persistence mode, over five minutes. (Our autocorrelator is a Femtochrome model FR-103XL.) The persistence traces (Fig. 4.14)

qualitatively illustrate the dramatic reduction in the amplitude variations of these multiplexed pulse trains.

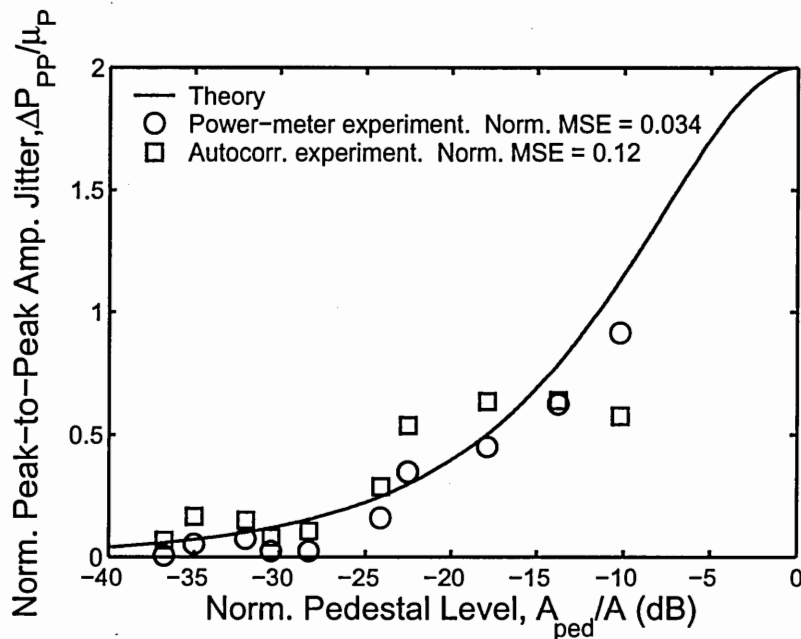


Figure 4.13: Multiplexing induced amplitude jitter plotted against pedestal level. Results from theory and two sets of experiments are included. MSE—mean-squared error.

4.4.2.3 Remarks

Both sets of experimental results are compared with the theoretical power fluctuations predicted by Eq. 4.31 in Fig. 4.13. The figure shows that both data sets are in approximate agreement with the theory.

The power-meter measurement of the multiplexing-induced amplitude jitter agrees more closely with our theory than the persistence-autocorrelation method, indicating that it may be a better technique. (This disparity is principally due to a single, perhaps anomalous point.) In particular, the normalized mean-squared error (MSE), of the power-meter measurement is 0.034. The normalized MSE of the

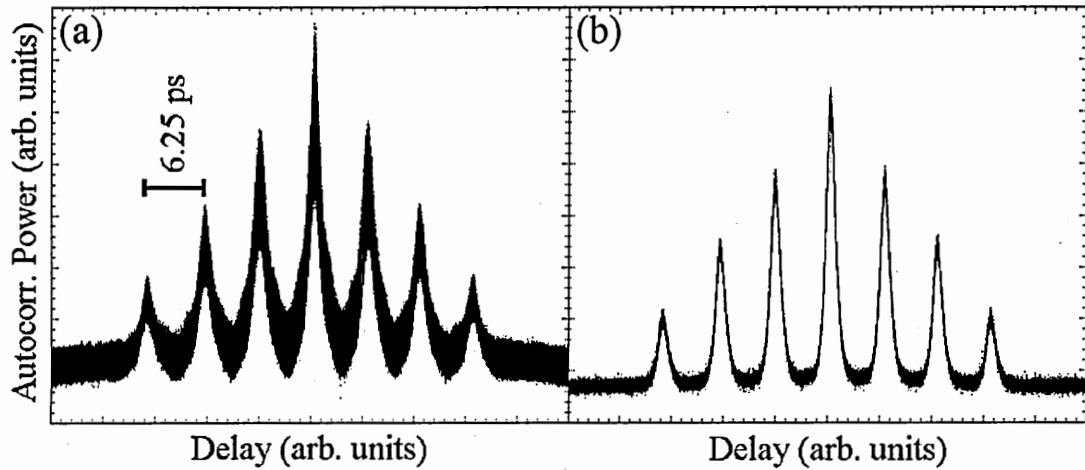


Figure 4.14: Autocorrelation traces, with persistence, of 4-bit multiplexed pulse trains without (a) and with (b) pedestal suppression by a nonlinear amplifying loop mirror.

persistence-autocorrelation data set is 0.12. The autocorrelation technique, however, does provide a more visual indication of reduction of OTDM jitter, as indicated by Fig. 4.14.

This agreement between experiment and theory indicates that, when the pedestal is below the noise limit of the measurement, as is the case in our experiment, the two indirect, multiplexing measurements described here may actually be *better* measures of the pedestal level than the autocorrelation is.

Finally, it is important to note that, as exemplified by Fig. 2.6, the low-pedestal pulses produced by the NALM are essentially hyperbolic secant in shape.

4.5 Commentary

4.5.1 Confirmation of Theory

We have presented theory describing the slow peak-power fluctuation that results from OTDM multiplexing. We have also experimentally confirmed this theory using a NALM.

4.5.2 Suitability of the Loop Mirror

In our experiments, the NALM is capable of reducing the pedestals to as low as 36.8 dB below the peak (Fig. 4.13). This pedestal level is 14.1 dB and 12.7 dB below the levels we established in Subsubsection 4.4.1.1 for BERs of 10^{-9} and 10^{-12} , respectively. Thus, the NALM suffices to reduce the pedestal to acceptable levels.

4.5.3 Excess Spectrum

One drawback to the NALM is the spectral broadening associated with its use. It may be possible to reduce this broadening by fine-tuning the pump power and FPC setting. As we pointed out in Subsection 2.4.4, the TBP of the output pulse can be reduced by propagating the pulse through a fiber with the correct total dispersion [127] or filtering the excess spectrum. Both methods of TBP reduction have their pitfalls, however. Filtering high-power pulses can lead to distortion. Compressing the pulse would reduce the pulse width, but if the pulse output by the NALM is already at the design duration of the link, the compression is not just unnecessary but deleterious; a too-short pulse may suffer from (undesirable) nonlinear effects during propagation.

4.5.4 Pedestal-Level Measurement

Since the pedestal level at the output of the NALM can be below the noise level of the autocorrelation measurement, the two methods of measuring the power fluctuations of the temporally multiplexed train (with a power meter or with a persistence autocorrelation) are *better* methods of determining the true pedestal level when that level is very low.

CHAPTER 5

Direct Jitter-Characterization Method

5.1 Roadmap

In Chapter 5, we describe a method of extracting, from the RF spectrum of a pulse train, the train's total, uncorrelated, and correlated amplitude and timing jitter as well as the correlation times of the two correlated contributions. Section 5.2 briefly states the problem at hand. Section 5.3 reviews previous work in the field. Section 5.4 represents the core of this chapter; in this section, we derive the spectrum of a noisy pulse train, describe a means of extracting all the jitter parameters, and assess the performance of the jitter-characterization technique with simulations and experiments. Section 5.5 consists of a summary and few comments concerning the method.

5.2 The Problem

As quantified in Subsection 1.4.4, the usefulness of a pulse train for OTDM communications systems is often limited by both timing and amplitude jitter. Further, as evident from Section 1.5, the stochastic jitter¹ can be divided into absolute and residual components or into uncorrelated, correlated, and super-mode contributions.

¹ This chapter does not address deterministic jitter.

These three noise components originate from different sources, and knowledge of them facilitates determination and elimination of the source of the noise. Thus, a means of not simply measuring the total jitter of a pulse train, but of *characterizing* the it (extracting the individual contributions) is required.

The direct spectral method is a technique commonly employed to measure *absolute* jitter. This method has been shown to distinguish between amplitude and timing noise, but not to distinguish between the uncorrelated, correlated, and super-mode components. We wish to extend the direct method simultaneously extract the total, uncorrelated, and correlated contributions to the absolute timing and amplitude jitter and to measure the correlation times of the correlated contributions. (We will not attempt to extract the super-mode noise.) In other words, we intend to modify this method to extract the following eight parameters of the *absolute random* jitter:

- Total timing.
- Total amplitude.
- Uncorrelated timing.
- Uncorrelated amplitude.
- Correlated timing.
- Correlated amplitude.
- Correlation time of the correlated timing jitter.
- Correlation time of the correlated amplitude jitter.

5.3 Previous Work

A number of techniques for measuring the jitter of a pulse train have been demonstrated. The advantages, and disadvantages of each are sketched below. These techniques can be divided into temporal and spectral techniques.

5.3.1 Temporal Methods

5.3.1.1 Oscilloscope

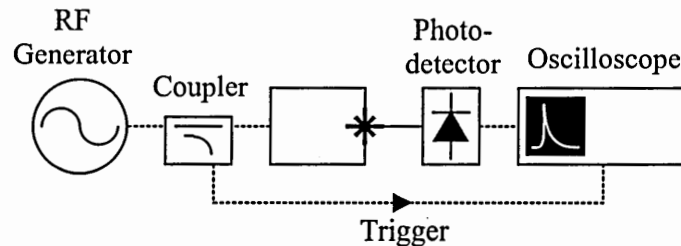


Figure 5.1: The experimental setup employed with the oscilloscope-based jitter-measurement method. RF—radio frequency.

The oscilloscope (histogram) method (Fig. 5.1) of noise measurement is the most intuitive and simplest technique. In this temporal method, the instrument is operated in persistence mode and simply assembles a vertical or horizontal histogram at the appropriate point in the waveform to measure the amplitude or timing noise. Unfortunately, this time-domain method is limited to measuring timing jitters greater than the trigger jitter of the oscilloscope and amplitude jitters greater than the intensity noise of the instrument. Even modern multi-GHz digital sampling oscilloscopes have trigger jitters² on the order of 1 ps. Furthermore, this method can misrepresent intensity noise as phase noise [25].

² The total sampling timing noise of an oscilloscope consists of jitter in the trigger as well as in the digitizing circuit. This noise is often simply called trigger jitter.

5.3.1.2 Crosscorrelation

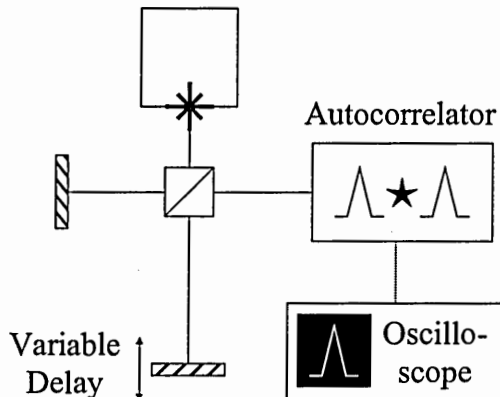


Figure 5.2: The experimental setup of the jitter-measurement method based on cross-correlation. In practice a long fiber delay is also often employed.

The crosscorrelation technique (Fig. 5.2) [23], [59], [64], [66], [112] is also a temporal method. This approach exploits the fact that the RMS width of the cross-correlation, σ_{XC} , is broadened by timing jitter. This measurement must be calibrated by first measuring the RMS width of the *autocorrelation* both before and after propagation through the long and dispersive fiber delay used for crosscorrelating distant pulses. These autocorrelation widths are labelled σ_{AC_1} and σ_{AC_2} , respectively. If we assume a Gaussian pulse shape, the *pulse-to-pulse* RMS timing jitter, σ_{PP} , can then be computed from [23]

$$\sigma_{PP} = \sqrt{\sigma_{XC}^2 - \sigma_{AC}^2}. \quad (5.1)$$

Here, σ_{AC} is defined to be the mean of two *squared* autocorrelation widths:

$$\sigma_{AC}^2 \equiv \frac{\sigma_{AC_1}^2 + \sigma_{AC_2}^2}{2}. \quad (5.2)$$

In this method, the intensity noise averages out and therefore cannot be measured [23], [112]. This fact can be considered a disadvantage (if we are interested in extracting both the timing and amplitude noise) or an advantage (if we are only interested in the timing noise). This technique has other disadvantages and advantages. The first disadvantage is that the method requires additional opto-electronic

equipment and free-space alignment. The second disadvantage: three experiments (one each to record σ_{AC_1} , σ_{AC_2} , and σ_{XC}) are required for each measurement [23], [112]. One advantage: by crosscorrelating pulse pairs of varying delay, the entire *probability density function* of the timing jitter can be mapped [23], a very powerful capability.

5.3.1.3 Phase-Encoded Optical Sampling

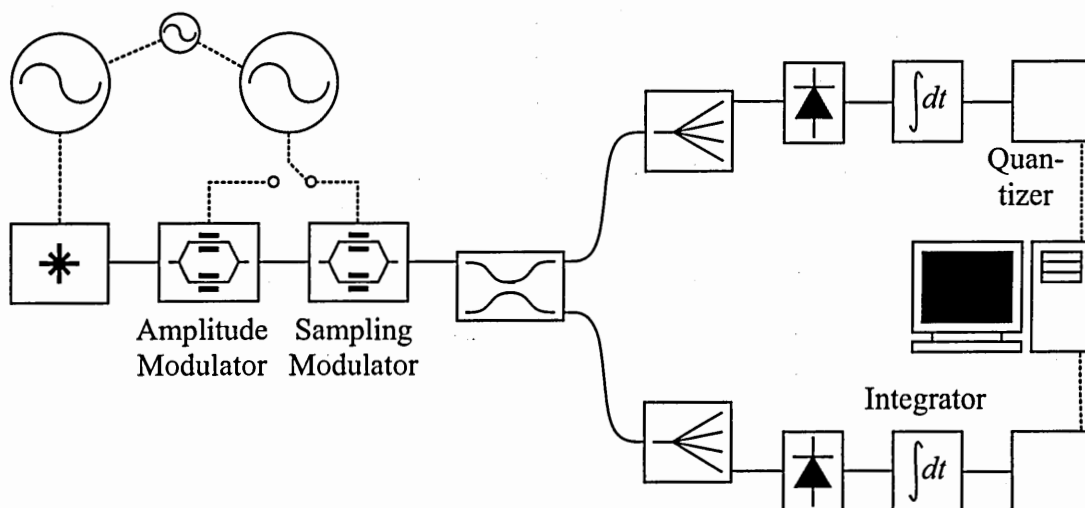


Figure 5.3: The experimental setup of the jitter-measurement method based on phase-encoded optical sampling.

Another temporal jitter-measurement method [2], [6] has been developed by clever extension of a technique for optical analog-to-digital conversion called phase-encoded optical sampling [1]. In the optical-sampling application, a pulsed laser and an electro-optic modulator are used to sample an unknown, analog RF signal (Fig. 5.3). The laser is required to have amplitude and timing noise that is much lower than any “interesting” structure in the RF signal. In the jitter-measurement application the same setup is employed, but the unknown RF signal is replaced by a sinusoid produced by an RF synthesizer. In a sense, the roles of the optical and RF

signals are reversed; it is the sine wave which must have very low noise, in order to measure the noise in the laser.

Like the other temporal methods (other than the oscilloscope method), the jitter-measurement technique based on optical sampling cannot measure amplitude jitter [2], [6]. However, this technique, uniquely, *does* allow pattern noise to be quantified.

5.3.2 Spectral Methods

The two RF-spectral techniques (the direct and mixing-based methods) are the most popular means of measuring subpicosecond timing jitter. The first fact in their favor is that only spectral techniques (and the oscilloscope method) can measure both timing and amplitude noise [2], [6]. Second, these measurement schemes (the direct method especially) require little additional equipment.

Third advantage of the spectral techniques is that they have very fine resolution, and can measure very small jitters, as we will show³. The reason for the improved performance is that the RFSA is not required to have the same broad, flat frequency response that, for example, an oscilloscope is [57]. The spectrum is assembled by combining a number of power measurements, each made over a different *narrow* frequency band. Thus, the frequency response of the instrument need only be flat over each band; any broader variation in the frequency response can be calibrated out. By contrast, temporal measurements are made at all frequencies at once, placing much more stringent demands on the performance of the oscilloscope.

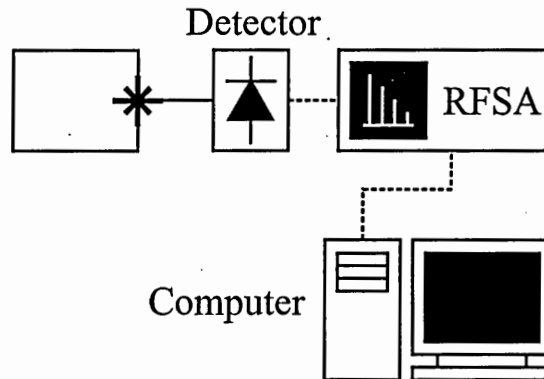


Figure 5.4: The experimental setup of the direct spectral jitter-measurement method. RFSA—radio-frequency spectrum analyzer.

5.3.2.1 Direct Spectral

A radio-frequency spectrum analyzer (RFSA) was first employed to determine the jitter of a pulse train by von der Linde in 1986 [165]. His analysis assumed *correlated* noise (because von der Linde was interested in mode-locked lasers) and revealed that the integrated noise power around harmonic h of the power spectrum was the sum of two terms, one proportional to the amplitude jitter, and one proportional to h^2 times the timing jitter. Thus, by integrating the noise power around two harmonics, the total amplitude and timing noise could be determined. (Note that, since this work was conducted in 1986, it was often not possible to record the spectrum *digitally* or to use a computer to sum the noise power in each frequency bin. Thus, von der Linde simply approximated the integral of the noise power by computing the product of the spectral width of the noise band and the maximum PSD.) Unfortunately, because this analysis assumed the jitter is correlated, yielding a spectrum with discrete noise bands centered on each harmonic of the repetition rate, it was incomplete.

The direct method has been employed many times in the years following the publication of von der Linde's paper [26], [116], [119], [140], [148], [166]–[169], and a number of modifications of the basic two-harmonic approach have arisen. For ex-

³ See Subsubsections 5.4.1.3, 5.4.1.4, 5.4.4.1.2, 5.4.4.1.3, 6.4.1.3, and 6.4.1.4.

ample, some authors [140], [167], [170]–[172] have exploited the fact that *a single harmonic* is sufficient if we only wish to measure the timing noise. Because of the constant nature of the amplitude-noise power and the harmonic-number-squared dependence of the timing-noise power, the integrated noise power around high harmonics is dominated by timing noise.

The modification that is most relevant to this document was made by Leep and Holm in 1992 [26]. Their analysis assumed *uncorrelated* noise (because Leep and Holm were interested in gain-switched lasers) and revealed that the noise *PSD* is proportional to the amplitude noise and the squared frequency times the timing noise. This analysis provides a similar means to distinguish between the amplitude and timing noise. Indeed, if you integrate the noise power around each harmonic, you get the same result for the total jitter. Unfortunately, because the Leep analysis assumed uncorrelated noise, yielding a spectrum with a single continuous noise band, it was also incomplete.

5.3.2.2 Mixing-Based Spectral

The mixing-based method is a development of the direct technique that was intended to measure *residual jitter*⁴. This method can separate the amplitude and timing noise.

5.3.2.3 Remarks

Before this author's work, neither the direct nor the mixing-based spectral method has distinguished between the uncorrelated and correlated contributions of the noise. However, the von der Linde and Leep computations have been applied, *incorrectly*, [172], [173] to extract the uncorrelated and correlated timing and intensity noise. Further, to our knowledge, before the author's work, no one has published a systematic

⁴ See Subsection 1.5.2.

investigation of the accuracy of any jitter-measurement technique. In this chapter, we describe how we have extended the direct technique to discriminate between the uncorrelated and correlated contributions to the noise. In Chapter 6, we describe a similar extension of the mixing method.

5.4 Present Contribution

5.4.1 Theory

5.4.1.1 Spectrum of a Noisy Pulse Train

The goal of this subsection is the computation of the power spectrum of a noisy pulse train. Before we begin, however, it may be helpful to provide the reader with a summary or abstract of the upcoming computation. This summary is, functionally, very much like the dumb show in *Hamlet*, as described by the Player in *Rosencrantz and Guildenstern are Dead* [174]:

Well, it's a device really—it makes the action that follows more or less comprehensible; you understand we are tied down to a language that makes up in obscurity what it lacks in style.

In our case, of course, the obscure language isn't English or even Danish, but mathematics, making the need for an outline perhaps even greater.

In our analysis, we will proceed as follows:

- Analytically describe the detected voltage of a noise-free impulse train.
- Incorporate a finite pulse width as well as amplitude and timing noise.
- Compute the autocorrelation of the resulting noisy pulse train.

- Take the time average to eliminate the temporal dependence.
- Evaluate the Fourier transform to arrive at the spectrum.

A note about our nomenclature before we proceed to the computation: As will be explained⁵, our jitter-characterization technique is not appropriate for data streams, only to unmodulated pulse trains. Thus, it cannot be applied to the output of the temporal multiplexer, but only to the output of the pulse source, which has period equal to the *channel* period, T_{chan} . In this chapter and the next, we will, for compactness, use T to represent the period of the pulse train under examination. (The reciprocal of T is, therefore, the repetition frequency of the laser in Hz, f_{rep} , and $2\pi/T$ is the repetition frequency of the laser in rad/s, ω_{rep} .) It is important to recall that timing-jitter criterion listed in Subsection 1.4.4 is expressed in terms of the *system* period, T_{sys} .

We begin with a noise-free train of *impulses* (infinitely narrow pulses). The detected voltage of this temporal comb v_{IT} , is proportional to the optical power of the train (the definition of square-law detection) and is given by

$$v_{\text{IT}}(t) = \underbrace{\sum_{j=-\infty}^{\infty} A\delta(t - jT)}_{\text{temporal comb}}, \quad (5.3)$$

where δ is the Dirac delta distribution. It is easy to see from this equation, that A and T are the amplitude and period of the impulses train, respectively. All summation in this chapter will run from $-\infty$ to ∞ , so, for compactness, we will omit the limits from future summations. We can create the detected voltage of a noise-free *pulse* train by convolving the impulse train with a unitless, unit-amplitude shape-function of finite width, s . This convolution (indicated by the \otimes operator) is equivalent to simply replacing the δ in Eq. 5.3 with an s .

$$v_{\text{PT}}(t) = \underbrace{s(t)}_{\text{shape}} \otimes \sum_j A\delta(t - jT)$$

⁵ See Subsection 5.5.4.

$$= \sum_j As(t - jT) . \quad (5.4)$$

To assemble the detected voltage of a *noisy* pulse train, v_{NT} , we add jitter terms (each the sum of uncorrelated and correlated contributions) to the amplitude and period⁶:

$$\begin{aligned} v_{\text{NT}}(t) &= \sum_j \{ A + \underbrace{\Delta A[j]}_{\text{amp. jitter}} \} s(t - jT - \underbrace{\Delta T[j]}_{\text{timing jitter}}) ; \\ \Delta J &= \underbrace{\Delta J_u}_{\text{uncorr.}} + \underbrace{\Delta J_c}_{\text{corr.}} . \end{aligned} \quad (5.5)$$

(Recall that we use ΔJ to stand in for ΔA or ΔT .) It is by the inclusion of uncorrelated and correlated timing and amplitude jitter that our analysis differs from others'. The four noise terms are zero-mean, wide-sense stationary (WSS) random sequences [164], which we assume to be independent of each other. Since the random sequences have means of zero, A and T become the *mean* amplitude and period. Further, since the ΔJ_u and ΔJ_c are, by assumption, independent, their variances add:

$$\sigma_J^2 = \sigma_{J_u}^2 + \sigma_{J_c}^2 . \quad (5.6)$$

To simplify the following manipulations, we express the function s as a Taylor series about $t - jT$. We assume the noise is small; hence we can truncate the series after two terms:

$$s(t - jT - \Delta T[j]) \simeq s(t - jT) - \Delta T[j] \dot{s}(t - jT) \quad (5.7)$$

where the dot ($\dot{}$) indicates temporal differentiation. Thus,

$$v_{\text{NT}}(t) \simeq \sum_j As(t - jT) + \Delta A[j]s(t - jT) - A\Delta T[j]\dot{s}(t - jT) , \quad (5.8)$$

Since the noise is small, the four cross terms (containing, for example, $\Delta A_u \Delta T_u$) are very small, and can be neglected.

⁶ We do not specifically account for pulse-width fluctuations, since these contribute little to the spectrum [26].

The PSD of any random process x , is Φ_x , given by [163]

$$\Phi_x(\omega) \equiv \mathcal{F}(\mathcal{E}(\phi_x(t, t + \tau))) . \quad (5.9)$$

Here, ϕ_x , Φ_x , and X are the autocorrelation, PSD, and Fourier transform of x , respectively. The \mathcal{F} and \mathcal{E} operators denote Fourier transformation and expectation, respectively.

So our next task is to calculate $\phi_{v_{\text{NT}}}(t, t + \tau)$ by computing $\mathcal{E}(v_{\text{NT}}(t)v_{\text{NT}}(t + \tau))$, the expected value of $v_{\text{NT}}(t)v_{\text{NT}}(t + \tau)$. Note that two summation indices (j and k), one for each time argument, must be used. Because all noise terms are independent, the cross terms, such as $\mathcal{E}(\Delta A_u[j]\Delta A_c[k])$ or $\mathcal{E}(\Delta T_c[j]\Delta A_c[k])$, vanish. Further, since the jitter terms are WSS, only the *difference* in the index matters, and the “noncross” terms, such as $\mathcal{E}\{\Delta J_u[j]\Delta J_u[k]\} \equiv \phi_{\Delta J_u}[j, k]$, simplify [164] to terms like $\phi_{\Delta J_u}(\ell)$, where $\ell \equiv k - j$. The result is

$$\phi_{v_{\text{NT}}}(t, t + \tau) \simeq \sum_j \sum_\ell \left\{ \begin{array}{l} A^2 s(t - jT) s(t - \{j + \ell\}T + \tau) + \\ \phi_{\Delta A}[\ell] s(t - jT) s(t - \{j + \ell\}T + \tau) + \\ A^2 \phi_{\Delta T}[\ell] \dot{s}(t - jT) \dot{s}(t - \{j + \ell\}T + \tau) \end{array} \right\} . \quad (5.10)$$

Note that $\phi_{v_{\text{NT}}}$ is periodic in t . (Thus v_{NT} is cyclostationary.) The period is T .

To remove the time dependence, we evaluate $\bar{\phi}(\tau)$, the time average of $\phi_{v_{\text{NT}}}$ over one period [164]:

$$\bar{\phi}(\tau) = \int_0^T \phi_{v_{\text{NT}}}(t, t + \tau) dt . \quad (5.11)$$

After interchanging the order of the summations and the integration (because both types of operation are linear) and executing a change of variables ($t - jT \rightarrow t$), we arrive at an infinite sum of finite integrals that *abut* to cover all time:

$$\bar{\phi}_{v_{\text{NT}}}(\tau) \simeq \frac{1}{T} \sum_\ell \sum_j \int_{-jT}^{T-jT} \left\{ \begin{array}{l} A^2 s(t) s(t - \ell T + \tau) + \\ \phi_{\Delta A}[\ell] s(t) s(t - \ell T + \tau) + \\ A^2 \phi_{\Delta T}[\ell] \dot{s}(t) \dot{s}(t - \ell T + \tau) \end{array} \right\} dt . \quad (5.12)$$

Note that the index j does not appear in the integrand. We can replace this infinite sum of integrals with a single infinite integral. We also note [175] that, for any continuous-time functions, f and g , and for any delay, ζ ,

$$\int_{-\infty}^{\infty} f(t)f(t+\zeta)dt \equiv \phi_f(\zeta) , \quad (5.13)$$

and

$$\sum_{\ell} g(t-\zeta) = g(t) \otimes \sum_{\ell} \delta(t-\ell\zeta) . \quad (5.14)$$

Substitution yields

$$\bar{\phi}_{v_{\text{NT}}}(\tau) \simeq \frac{1}{T} \left\{ \begin{array}{l} A^2 \phi_s(\tau) \sum_{\ell} \delta(\tau - \ell T) + \\ \phi_s(\tau) \sum_{\ell} \phi_{\Delta A}[\ell] \delta(\tau - \ell T) + \\ \phi_s(\tau) A^2 \sum_{\ell} \phi_{\Delta T}[\ell] \delta(\tau - \ell T) \end{array} \right\} . \quad (5.15)$$

Let us look more closely at the uncorrelated and correlated contributions. Note that, since (a) ΔJ_u and ΔJ_c are independent and (b) autocorrelation is a linear process,

$$\phi_{\Delta J}[\ell] = \phi_{\Delta J_u}[\ell] + \phi_{\Delta J_c}[\ell] . \quad (5.16)$$

Further, by definition of an uncorrelated random sequence,

$$\phi_{\Delta J_u}[\ell] = \sigma_{\Delta J_u}^2 \delta[\ell] , \quad (5.17)$$

where $\sigma_{\Delta J_u}^2$ is the variance of ΔJ_u . By substituting according to Eqs. 5.16 and 5.17, we see that each of the two noise terms in Eq. 5.15 contains

$$\sum_{\ell} \delta(\tau - \ell T) \{ \underbrace{\sigma_{\Delta J_u} \delta[\ell]}_{\text{uncorrelated}} + \underbrace{\phi_{\Delta J_c}[\ell]}_{\text{correlated}} \} = \sigma_{\Delta J_u} \sum_{\ell} \delta(\tau - \ell T) \delta[\ell] + \sum_{\ell} \delta(\tau - \ell T) \phi_{\Delta J_c}[\ell] . \quad (5.18)$$

The uncorrelated term in the last equation reduces to $\sigma_{\Delta J_u} \delta(\tau)$. The correlated term resembles the sampling of a continuous-time autocorrelation. Let \check{f} be

a continuous-time function. Now let \tilde{f} be the sampled (but still continuous-time) version, as define by

$$\tilde{f}(t) = \check{f}(t) \sum_{\ell} \delta(t - \ell T) . \quad (5.19)$$

Note the the right-hand side can be rewritten:

$$\tilde{f}(t) = \sum_{\ell} \check{f}(\ell T) \delta(t - \ell T) . \quad (5.20)$$

We can easily define a discrete-time version, \hat{f} , by using the value of the sample version at each multiple of T :

$$\hat{f}[\ell] \equiv \check{f}(\ell T) . \quad (5.21)$$

With this definition,

$$\tilde{f}(t) = \sum_{\ell} \hat{f}[\ell] \delta(t - \ell T) . \quad (5.22)$$

In our case, the correlated term in Eq. 5.18 is the same as the right-hand side of Eq. 5.22 with the discrete-time function \hat{f} replaced by $\phi_{\Delta J_c}$. We can therefore replace the correlated term with

$$\check{\phi}_{\Delta J_c}(t) \sum_{\ell} \delta(t - \ell T) , \quad (5.23)$$

where $\check{\phi}_{\Delta J_c}$ is the continuous-time version of $\phi_{\Delta J_c}$.

Finally, we can now compute $\Phi_{\text{NT}}(\omega)$, the PSD of v_{NT} , by calculating the Fourier transform of $\bar{\phi}_{v_{\text{NT}}}$:

$$\Phi_{\text{NT}}(\omega) = \mathcal{F} \left\{ \bar{\phi}_{v_{\text{NT}}} \right\} . \quad (5.24)$$

After a few manipulations, we arrive at the principal result of this subsection:

$$\begin{aligned} \Phi_{\text{NT}}(\omega) &\simeq \frac{1}{T} \underbrace{|S(\omega)|^2}_{\text{pulse shape}} \left\{ \underbrace{A^2 \text{III}(\omega/\omega_{\text{rep}})}_{\text{freq. comb}} + \underbrace{\Phi_{\Delta A}(\omega)}_{\text{amp. jitter}} + \underbrace{A^2 \omega^2 \Phi_{\Delta T}(\omega)}_{\text{timing jitter}} \right\} ; \\ \Phi_{\Delta J}(\omega) &\equiv \underbrace{\sigma_{\Delta J_u}^2}_{\text{uncorr. jitter}} + \underbrace{\frac{1}{T} \sum_k \check{\phi}_{\Delta J_c}(\omega - k\omega_{\text{rep}})}_{\text{corr. jitter}} . \end{aligned} \quad (5.25)$$

In these two equations, S and $\check{\Phi}_{\Delta J_c}$ are the Fourier transforms of s and $\check{\phi}_{\Delta J_c}$, respectively. Also, $\text{III}(\omega/\omega_{\text{rep}})$ is the shah (comb) distribution [175] with period ω_{rep} :

$$\text{III}(\omega/\omega_{\text{rep}}) \equiv \omega_{\text{rep}} \sum_k \delta(\omega - k\omega_{\text{rep}}) . \quad (5.26)$$

We again note that the analysis leading to Eq. 5.25 differs from other treatments [26], [165] by the explicit inclusion of both uncorrelated and correlated noise, which allows comparison of all four contributions. The salient features of Eq. 5.25 are illustrated in Figs. 5.5 through 5.11 by spectra corresponding to several simulated pulse trains. Considering Eq. 5.25 and the aforementioned figures, the first feature to note is that the spectrum is scaled by an envelope due to the pulse shape⁷. The first term within the braces is the spectral comb, corresponding to a jitter-free pulse train. The second term represents amplitude jitter, and the third is timing jitter. In form, the noise terms differ only by the $A^2\omega^2$ factor in the timing noise. This quadratic dependence allows us to distinguish between intensity and timing jitter. The second line of Eq. 5.25 reveals that each noise term is composed of two “subterms”: (a) the variance of the uncorrelated jitter (a constant), corresponding to a single noise band spanning the entire spectrum and (b) a sum of copies of the correlated-jitter spectrum, corresponding to multiple narrow noise bands, each centered at multiples of ω_{rep} . This difference allows us to distinguish between uncorrelated and correlated components.

⁷ In a real-world experiment, the detector and RFSA have finite bandwidth, so the envelope term will be multiplied by $|R(\omega)|^2$, where R is the Fourier transform of the detector/RFSA impulse response. We will ignore this effect; we later normalize the spectrum to its envelope, so $R(\omega)$ is irrelevant.

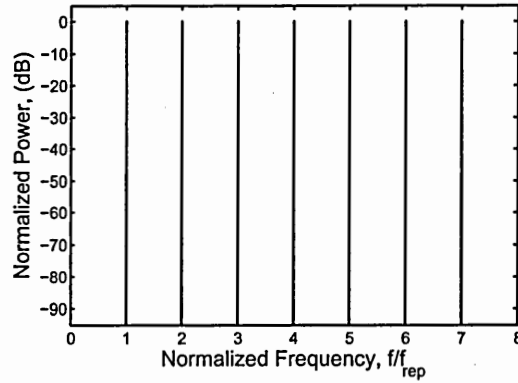


Figure 5.5: The spectrum of a train of *impulses* (infinitely narrow pulses) with *no* jitter.

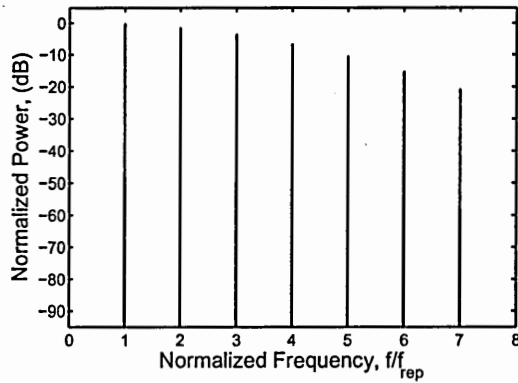


Figure 5.6: The spectrum of a train of finite-width *pulses* train with no jitter. The root-mean-squared duration of the pulse is 5 % of the period.

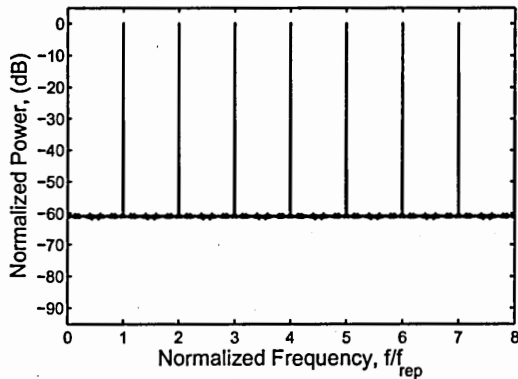


Figure 5.7: The spectrum of an impulse pulse train with only *uncorrelated amplitude* jitter equal to 1 % of the mean amplitude.

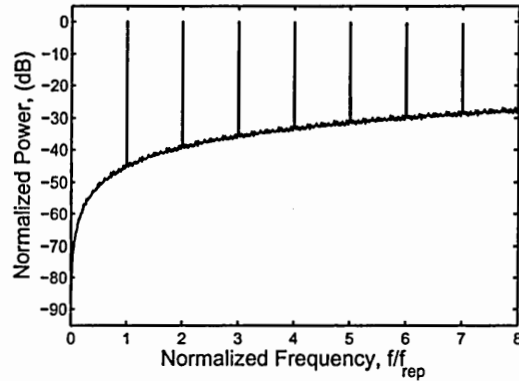


Figure 5.8: The spectrum of an impulse pulse train with only *uncorrelated timing* jitter equal to 1 % of the mean period.

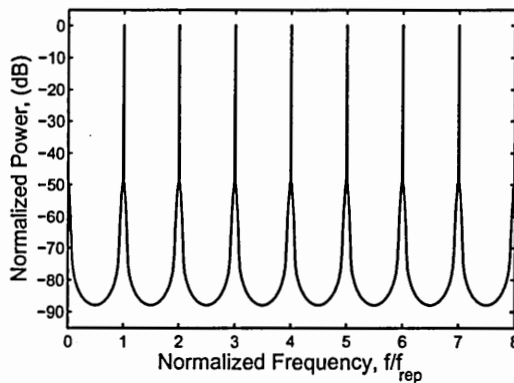


Figure 5.9: The spectrum of an impulse train with only *correlated amplitude* jitter equal to 1 % of the mean amplitude.

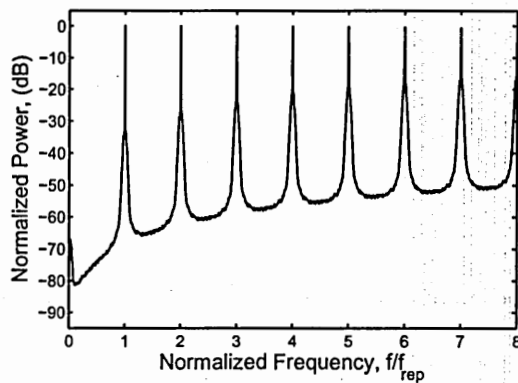


Figure 5.10: The spectrum of an impulse train with only *correlated timing* jitter equal to 1 % of the mean period.

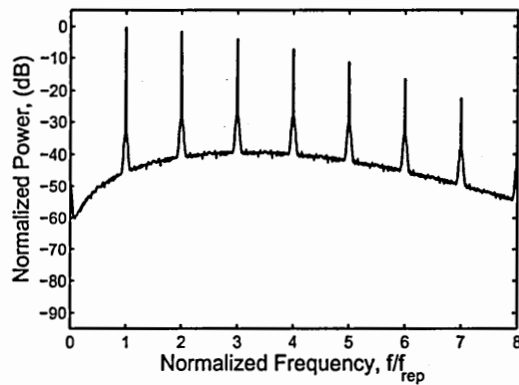


Figure 5.11: The spectrum of a *pulse* train with all four jitter contributions. Each contribution is equal to 1 % of the mean amplitude or period.

5.4.1.2 Measurement Procedure

Now that we understand how the various jitter parameters manifest themselves in the RF spectrum of the pulse train, we can extract them from a simulated or measured spectrum.

5.4.1.2.1 Correction for Theoretical Approximation First, we note an approximation in our theoretical treatment; it does not conserve energy. The power in the noise bands does not come at the expense of power in the comb. To compare the simulated or measured spectrum to the theory, we adjust the spectrum by integrating the total noise power around each harmonic and add that power to the comb. This correction is very small for $\hat{\sigma}_{\Delta J}$ less than about 0.01.

5.4.1.2.2 Noise-Floor Subtraction The noise floor of the measurement setup (the spectrum measured with no input signal) must always be carefully considered, especially when attempting to measure very small jitters [176]. Some authors [140] choose to subtract the noise floor (measured separately) from the signal spectrum. However, this subtraction is dangerous, especially when the jitter of the laser under investigation is very small. An early version of our procedure included noise-floor subtraction, but the most recent version eliminates this step. (The noise floor is still recorded, so that it can be plotted with the signal spectrum, giving an indication of the relationship between the two spectra.)

5.4.1.2.3 Normalization Next, we normalize the spectrum to its envelope. For jitter values appropriate to the theory ($\hat{\sigma}_{\Delta J} \ll 1$), the noise PSD is negligible compared to the comb power, so we approximate the envelope, at $k\omega_{\text{rep}}$, as the measured harmonic peaks (triangles in Fig. 5.12). We then fit to the appropriate pulse shape to determine the value of the envelope *at all frequencies* (dashed curve in Fig. 5.12).

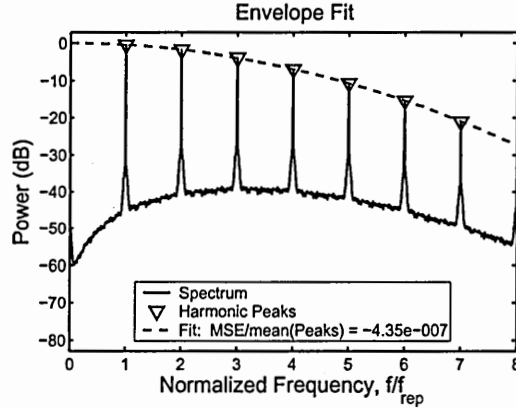


Figure 5.12: Envelope fit of a spectrum containing all four jitter contributions. MSE—mean-squared error.

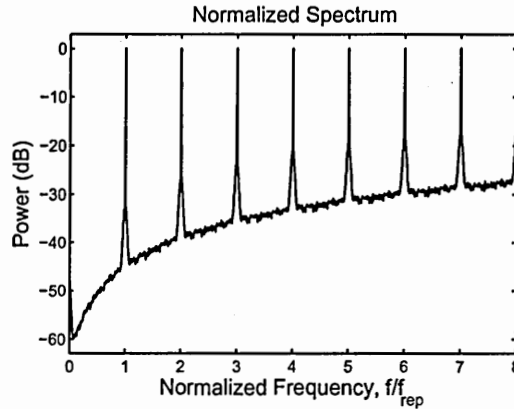


Figure 5.13: The spectrum shown in Fig. 5.12 normalized to its envelope.

Dividing by this curve yields the normalized PSD, $\hat{\Phi}_{\text{NT}}$ (Fig. 5.13):

$$\hat{\Phi}_{\text{NT}}(\omega) \simeq \frac{1}{\omega_{\text{rep}} A^2} \left\{ A^2 \text{III}(\omega/\omega_{\text{rep}}) + \Phi_{\Delta A}(\omega) + A^2 \omega^2 \Phi_{\Delta T}(\omega) \right\}. \quad (5.27)$$

The factor of $1/(\omega_{\text{rep}} A^2)$ is required to make the power in the first harmonic peak equal to unity.

5.4.1.2.4 Total Jitter To extract the total jitter, we compute the total normalized noise-band power around the h^{th} harmonic, $\hat{P}_{\text{noise}}[h]$, by integrating $\hat{\Phi}_{\text{NT}}$, excluding the comb spike, from $(h - 1/2)\omega_{\text{rep}}$ to $(h + 1/2)\omega_{\text{rep}}$. In practice, we carry out the

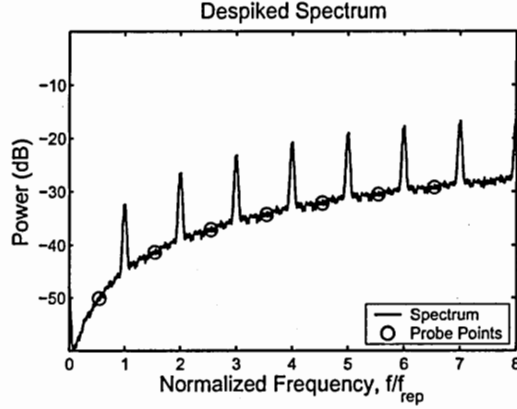


Figure 5.14: The spectrum shown in Fig. 5.13 with the harmonic peaks removed and probe points encircled.

the noise-only integration by first “depsiking” (removing the harmonics peaks from) the spectrum (Fig. 5.13), then integrating the result. Integrating Eq. 5.27 (without the comb spike)) with the approximation $\omega \simeq h\omega_{\text{rep}}$ yields

$$\hat{P}_{\text{noise}}[h] \simeq \hat{\sigma}_{\Delta A}^2 + \{2\pi h\}^2 \hat{\sigma}_{\Delta T}^2. \quad (5.28)$$

We *could* now compute the standard deviations of the amplitude and timing jitter by applying Eq. 5.28 to two harmonics (harmonics m and n):

$$\hat{\sigma}_{\Delta A} \simeq \sqrt{\frac{\hat{P}_{\text{noise}}[n] - \{n/m\}^2 \hat{P}_{\text{noise}}[m]}{1 - \{n/m\}^2}}; \quad (5.29)$$

$$\hat{\sigma}_{\Delta T} \simeq \frac{1}{2\pi} \sqrt{\frac{\hat{P}_{\text{noise}}[n] - \hat{P}_{\text{noise}}[m]}{n^2 - m^2}}. \quad (5.30)$$

We choose, however, to use more than two harmonics to increase the robustness and precision of our measurement, as described in the following paragraph. The most obvious way to make use of > 2 measurements is to compute $\hat{\sigma}_{\Delta A}$ and $\hat{\sigma}_{\Delta T}$ from the average of all the pairwise combinations (obtained from Eqs. 5.29 and 5.30). Instead, we fit the integrated harmonic powers to a parabola, as illustrated in Fig. 5.15, and extract the jitter parameters from Eq. 5.28.

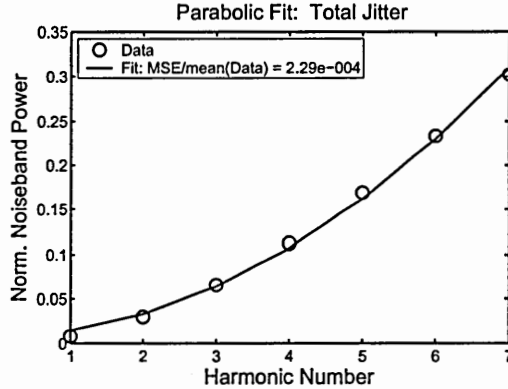


Figure 5.15: Parabolic fit of integrated noise-band power, employed to compute total jitter. MSE—mean-squared error.

We employ > 2 harmonics because, when this jitter-characterization routine is applied experimentally⁸, the integrated noiseband power *does not* always exhibit parabolic dependence on the harmonic number. If seven harmonics are measured, for example, one or two of values of $\hat{P}_{\text{noise}}[h]$ will often lie far from the parabola defined by the other values. Integrating several harmonics allows these anomalous values to be identified and excised from the jitter computation.

5.4.1.2.5 Uncorrelated Jitter In order to extract the uncorrelated jitter, we use a “pointwise” (rather than integrating) method: we measure $\hat{\Phi}_{NT}$ at “probe” frequencies, ω_p far from any peak. Typically, these probe points are chosen such that

$$\omega_p \simeq \omega_{\text{rep}} \{h \pm 1/2\} . \quad (5.31)$$

Since the probe points (circles in Fig. 5.14) are far from any harmonic, the normalized uncorrelated noise spectrum $\hat{\Phi}_u(\omega_p)$ dominates $\hat{\Phi}_{NT}(\omega_p)$:

$$\begin{aligned} \hat{\Phi}_{NT}(\omega_p) &\simeq \hat{\Phi}_u(\omega_p) \\ &\simeq \frac{2\pi}{\omega_{\text{rep}}} \left\{ \hat{\sigma}_{\Delta A_u}^2 + \omega_p^2 T \hat{\sigma}_{\Delta T_u}^2 \right\} . \end{aligned} \quad (5.32)$$

⁸ See Subsection 5.4.4.

As in the total-jitter case, we could compute the uncorrelated timing and amplitude jitter from two probe frequencies (ω_m and ω_n):

$$\begin{aligned}\hat{\sigma}_{\Delta A_u} &\simeq \sqrt{\frac{\hat{\Phi}_p(\omega_n) - (\omega_n/\omega_m)^2 \hat{\Phi}_p(\omega_m)}{T[1 - (\omega_n/\omega_m)^2]}} \\ \hat{\sigma}_{\Delta T_u} &\simeq \frac{1}{T} \sqrt{\frac{\hat{\Phi}_p(\omega_n) - \hat{\Phi}_p(\omega_m)}{T(\omega_n^2 - \omega_m^2)}}.\end{aligned}\quad (5.33)$$

However, as before, probing more than two harmonics and fitting the probe points to a parabola (Fig. 5.16) increases the precision of the jitter extraction and allows us to omit anomalous points (increasing the robustness). It should be pointed out that the use of smoothing (local, frequency-domain averaging) of a few points around the probe points can reduce the sensitivity of the jitter extraction to anomalies. Lastly, it is important to note that, in cases where uncorrelated noise dominates, the uncorrelated-jitter measurement yields a good estimate of the total jitter.

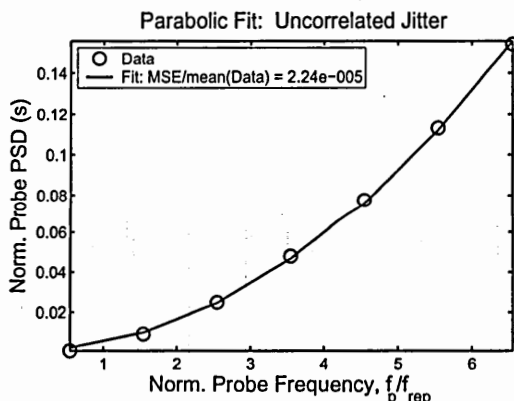


Figure 5.16: Parabolic fit of probe points, employed to compute uncorrelated jitter. MSE—mean-squared error.

5.4.1.2.6 Correlated Jitter At this point, a number of methods of correlated-jitter extraction are available. One *could* apply the integrating technique (described above for measuring the total jitter) with limits corresponding to the width of the

correlated-noise bands. doing so includes some uncorrelated-noise power and excludes some correlated-noise power. Another approach is to (a) estimate the uncorrelated noise PSD with a polynomial fit of the probe points, (b) subtract the estimate from the normalized spectrum, and apply the integrating scheme to measure the *total remaining* jitter, which should be the correlated jitter. Lastly, and most simply, one could estimate the correlated contribution using

$$\sigma_{\Delta J_c} = \sqrt{\sigma_{\Delta J}^2 - \sigma_{\Delta J_u}^2} \quad (5.34)$$

or the equivalent

$$\hat{\sigma}_{\Delta J_c} = \sqrt{\hat{\sigma}_{\Delta J}^2 - \hat{\sigma}_{\Delta J_u}^2} . \quad (5.35)$$

This third approach assumes ΔJ_u and ΔJ_c are independent.

An earlier version of our jitter-characterization routine used the polynomial-fit-subtraction approach. We found that it did not output correlated-jitter values significantly different from those obtained with the simple sum-of-squares calculation. The similarity between the results obtained with these two approaches should come as no surprise. If the polynomial resulting from the fit is a parabola (as it will be, if, as described above, we ignore nonparabolic probe points), then these two schemes are equivalent. Thus, to conserve floating-point operations, we compute the correlated contribution by the third, sum-of-squares method.

5.4.1.2.7 Correlation Time Lastly, to calculate the RMS correlation times of the correlated components, σ_{c_A} and σ_{c_T} , we assume the RMS width of the h^{th} correlated-noise band, $\varpi[h]$ can be approximated by weighted mean of the amplitude and timing correlation bandwidths, ϖ_A and ϖ_T :

$$\varpi[h] \simeq \frac{\varpi_A + h^2 \varpi_T}{1 + h^2} . \quad (5.36)$$

Once again, we could measure exactly two harmonics and extract the two correlation times. By now, the reader is no doubt expecting that we will will measure multiple

correlation bandwidths and fit them to a parabola. The reader will not be disappointed. However, we must first manipulate the last equation into a form that can be parabolically fit. After multiplying each of the measured harmonics by $1 + h^2$, we can fit the result to a parabola (Fig. 5.17) to determine ϖ_J . Finally, if we assume both ΔJ_c have Gaussian statistics, we can compute the correlation times from

$$\sigma_{c,J} = \frac{1}{\varpi_J} . \quad (5.37)$$

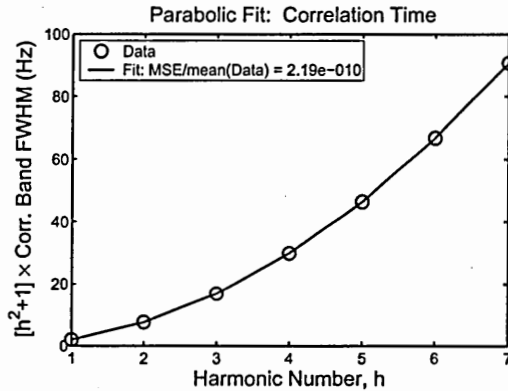


Figure 5.17: Parabolic fit of correlated-noiseband widths, employed to compute correlation times. MSE—mean-squared error.

5.4.1.2.8 Measurement Routine We have coded a suite of MATLAB routines to perform all of the appropriate manipulations of spectra and calculate all the jitter parameters as described above. This measurement routine, which represents a significant fraction of the work described in this chapter, is tested in Subsection 5.4.2.

5.4.1.3 Resolution

It is important to be able to estimate the resolution, or precision, of the direct jitter measurement.

5.4.1.3.1 Total Jitter By starting with Eq. 5.28 and assuming there is no timing noise, we see that

$$\hat{\sigma}_{\Delta A} \sim \sqrt{\hat{P}_{\text{noise}}[h]}, \quad (5.38)$$

where the hat again indicates a normalized jitter. (Assuming no timing jitter will yield the best-case [finest] resolution of the amplitude jitter. We will take a similar approach for calculating the resolutions of all the parameters.)

The power in the h^{th} noiseband can be rewritten:

$$\hat{P}_{\text{noise}}[h] = \frac{P_{\text{noise}}[h]}{P_{\text{pk}}[1]}. \quad (5.39)$$

In the following analysis, we omit the $[h]$ and $[1]$ for simplicity. The *double-sided, additive* resolution of the amplitude-jitter extraction, $\Delta\sigma_A$, will be given by the difference between the maximum and minimum values of $\sigma_{\Delta A}$, which are determined by the *single-sided, additive* power resolution of the RF spectrum analyzer, $\Delta P'$:

$$\frac{\Delta\sigma_{\Delta A}}{A} \sim \sqrt{\frac{P_{\text{noise}} + \Delta P'_{\text{noise}}}{P_{\text{pk}} - \Delta P'_{\text{pk}}}} - \sqrt{\frac{P_{\text{noise}} - \Delta P'_{\text{noise}}}{P_{\text{pk}} + \Delta P'_{\text{pk}}}}, \quad (5.40)$$

where $\Delta P'_{\text{noise}}$ and $\Delta P'_{\text{pk}}$ indicate single-sided, additive resolutions of the noise-power and peak-power measurements, respectively.

The RF spectrum analyzer is typically operated with a logarithmic vertical axis (to measure small powers with greater precision). In this case, the power resolution of the RFSA (usually called the marker resolution) is specified as a double-sided, *multiplicative* resolution, ∂P :

$$\partial P \equiv 1 + \frac{\Delta P}{P}, \quad (5.41)$$

Here, $\Delta P/P$ is the normalized, double-sided, additive resolution of the instrument. Because of the logarithmic scaling, the multiplicative resolution is the same for all powers, so

$$\partial P_{\text{noise}} = \partial P_{\text{pk}} = \partial P. \quad (5.42)$$

In practice, ∂P is typically specified in dB, so the single-sided, multiplicative resolution, $\partial P'$, is computed simply by halving the specified double-sided, multiplicative

resolution in the logarithmic domain. Thus, we can substitute for $1 + \Delta P/P$ in Eq. 5.40. We can also replace $1 - \Delta P/P$. Consider $1/\partial P'$:

$$\begin{aligned}\frac{1}{\partial P'} &= \frac{1}{1 + \frac{\Delta P'}{P}} \\ &= \frac{1 - \frac{\Delta P'}{P}}{1 - \left\{ \frac{\Delta P'}{P} \right\}^2}.\end{aligned}\quad (5.43)$$

For fine resolutions, the second term in the denominator is very small, so

$$1 - \frac{\Delta P'}{P} \simeq \frac{1}{\partial P'}.\quad (5.44)$$

Substitution for $1 + \Delta P'/P$ and $1 - \Delta P'/P$ yields

$$\frac{\Delta\sigma_{\Delta A}}{A} \sim \sqrt{\frac{P_{\text{noise}}}{P_{\text{pk}}}} \left\{ \partial P' - \frac{1}{\partial P'} \right\}.\quad (5.45)$$

Recall, from Eq. 5.38, that the first factor on the right-hand side (the one with the radical) approximates the normalized RMS amplitude jitter. Hence, we can compute the multiplicative resolution of the total-amplitude-jitter measurement,

$$\begin{aligned}\partial\sigma_{\Delta A} &\equiv 1 + \frac{\Delta\sigma_{\Delta A}}{\sigma_{\Delta A}} \\ &\sim 1 + \partial P' - \frac{1}{\partial P'}.\end{aligned}\quad (5.46)$$

Now consider the measurement of total timing jitter. Examining Eq. 5.28 and neglecting the amplitude noise, we see that

$$\hat{\sigma}_{\Delta T} \sim \frac{1}{2\pi h} \sqrt{\hat{P}_{\text{noise}}[h]}.\quad (5.47)$$

By similarity with the amplitude-jitter case, we arrive at

$$\frac{\Delta\sigma_{\Delta T}}{T} \sim \frac{1}{2\pi h} \sqrt{\frac{P_{\text{noise}}}{P_{\text{pk}}}} \left\{ \partial P' - \frac{1}{\partial P'} \right\}\quad (5.48)$$

where $\Delta\sigma_{\Delta T}$ is the double-sided, additive resolution of the total-timing-jitter measurement. We note that the the first two factors of the right-hand side are the normalized

RMS timing jitter. Thus, the factor of $2\pi h$ cancels, and the multiplicative resolution of the total-timing-jitter measurement is given by

$$\partial\sigma_{\Delta T} \sim 1 + \partial P' - \frac{1}{\partial P'} . \quad (5.49)$$

Note that this last result is identical to the one we obtained for the amplitude case, so we can summarize the resolution of both total jitter measurements with a single approximation:

$$\begin{aligned} \partial\sigma_{\Delta J} &\equiv \frac{\Delta\sigma_{\Delta J}}{\sigma_{\Delta J}} \\ &\sim 1 + \partial P' - \frac{1}{\partial P'} . \end{aligned} \quad (5.50)$$

From this approximation, we see that a smaller vertical span yields finer precision. This result makes intuitive sense.

5.4.1.3.2 Uncorrelated Jitter Let us turn our attention to the uncorrelated amplitude jitter. From Eq. 5.32 (and if we neglect timing noise), we see that

$$\begin{aligned} \sigma_{\Delta A_u} &\sim \sqrt{f_{\text{rep}} \widehat{\Phi}_{\text{NT}}(\omega_p)} \\ &\sim \sqrt{\frac{f_{\text{rep}} \Phi_{\text{noise}}(\omega_p)}{P_{\text{pk}}[1]}} . \end{aligned} \quad (5.51)$$

For compactness, we will omit the (ω_p) and $[1]$ below. Recall that, in a real RFSA, the PSD is actually measured as the *power*, P_{bin} , in some bin of width $\Delta\omega_{\text{res}}$. ($\Delta\omega_{\text{res}}$ is said to be the resolution bandwidth of the instrument.) We can therefore replace Φ_{noise} with $P_{\text{bin}}/\Delta\omega_{\text{res}}$. From this point, the analysis is exactly parallel to that from the total-jitter case, so

$$\partial\sigma_{\Delta A_u} \sim 1 + \partial P' - \frac{1}{\partial P'} . \quad (5.52)$$

Now consider the uncorrelated-timing-jitter extraction. We see, from Eq. 5.32 (and if we neglect amplitude noise), that

$$\sigma_{\Delta T_u} \sim \frac{1}{\omega_p} \sqrt{f_{\text{rep}} \widehat{\Phi}_{\text{NT}}(\omega_p)} . \quad (5.53)$$

Much as in the total-timing-jitter case, the factor of $1/\omega_p$ cancels, leaving

$$\partial\sigma_{\Delta T_u} \sim 1 + \partial P' - \frac{1}{\partial P'}. \quad (5.54)$$

Thus, the multiplicative resolutions of the two uncorrelated-jitter measurements are equal not only to each other, but also to the resolution of the total-jitter measurement:

$$\begin{aligned} \partial\sigma_{\Delta J_u} &\sim \partial P \sigma_{\Delta J} \\ &\sim 1 + \partial P' - \frac{1}{\partial P'}. \end{aligned} \quad (5.55)$$

5.4.1.3.3 Correlated Jitter Now consider the resolution of the of the correlated-jitter measurement. Recall that we compute the uncorrelated jitter by assuming the total jitter is the RMS sum of the uncorrelated and correlated contributions:

$$\sigma_{\Delta J_c} = \sqrt{\sigma_{\Delta J}^2 + \sigma_{\Delta J_u}^2}. \quad (5.56)$$

The additive resolution of the measurement of the correlated jitter, $\Delta\sigma_{\Delta J_c}$, is given by the difference between the maximum and minimum that can be measured, based on the single-sided, multiplicative resolutions of the total- and uncorrelated-jitter measurements, $\partial\sigma'_{\Delta J}$ and $\partial\sigma'_{\Delta J_u}$:

$$\Delta\sigma_{\Delta J_c} = \sqrt{\{\sigma_{\Delta J} \partial\sigma'_{\Delta J}\}^2 - \left\{\frac{\sigma_{\Delta J_u}}{\partial\sigma'_{\Delta J_u}}\right\}^2} - \sqrt{\left\{\frac{\sigma_{\Delta J}}{\partial\sigma'_{\Delta J}}\right\}^2 - \{\sigma_{\Delta J_u} \partial\sigma'_{\Delta J_u}\}^2}. \quad (5.57)$$

Noting that $\partial\sigma_{J_u} \sim \partial\sigma_J$ (according to Eqs. 5.50 and 5.55) and squaring both sides yields

$$\begin{aligned} \{\Delta\sigma_{\Delta J_c}\}^2 &\sim \{\sigma_{\Delta J}^2 - \sigma_{\Delta J_u}^2\} \{\partial\sigma'_{\Delta J}{}^2 - \partial\sigma'_{\Delta J}{}^2\} - \\ &2\sqrt{\sigma_{\Delta J}^4 - \partial\sigma'_{\Delta J}{}^2 \sigma_{\Delta J}^2 \sigma_{\Delta J_u}^2 - \frac{\sigma_{\Delta J}^2 \sigma_{\Delta J_u}^2}{\partial\sigma'_{\Delta J}{}^2} + \sigma_{\Delta J_u}^4}. \end{aligned} \quad (5.58)$$

For cases where $\partial\sigma_{\Delta J} \simeq 1$ (fine resolution), the second term on the right-hand side simplifies to

$$-2\sqrt{\sigma_{\Delta J}^4 - 2\sigma_{\Delta J}^2 \sigma_{\Delta J_u}^2 + \sigma_{\Delta J_u}^4} = -2\sqrt{\{\sigma_{\Delta J}^2 - \sigma_{\Delta J_u}^2\}^2}. \quad (5.59)$$

If we incorporate this approximation and note that $\{\sigma_{\Delta J}^2 - \sigma_{\Delta J_u}^2\}^2$ in the first term is the variance of the correlated contribution, we arrive at

$$\{\Delta\sigma_{\Delta J_c}\}^2 \sim \sigma_{\Delta J_u}^2 \left\{ \partial\sigma'_{\Delta J}{}^2 - 2 + \frac{1}{\partial\sigma'_{\Delta J}{}^2} \right\}. \quad (5.60)$$

Taking the square root of both sides and dividing gives $\partial\sigma_{\Delta J_c}$, the multiplicative resolution of the correlated-jitter measurements:

$$\partial\sigma_{\Delta J_c} \sim 1 + \partial\sigma'_{\Delta J} - \frac{1}{\partial\sigma'_{\Delta J}}. \quad (5.61)$$

There are two points that are important to note about Eq. 5.61. The first is the the similarity of form between this equation and Eqs. 5.50 and 5.55. The second is that, for fine RFSA resolutions, the multiplicative resolution of the correlated-jitter measurement will be close to 3 (or 4.77 dB).

5.4.1.4 Minimum Measurable Jitter

We would also like to compute the minimum jitter that can be measured with the direct spectral technique. The analysis that follows assumes that the minimum noise power that can be measured is limited by the dynamic range of the RF spectrum analyzer employed for the measurement. It is also possible that the minimum measurable noise power will be limited by the noise floor of the instrument. In this case, the dynamic range in the following equations would be replaced by the reciprocal of the normalized noise-floor power.

5.4.1.4.1 Total Jitter Consider the total amplitude jitter, approximately given by Eq. 5.38. Clearly the minimum measurable jitter corresponds to the minimum normalized noise power that can be measured:

$$\hat{\sigma}_{\Delta A, \min} \sim \sqrt{\hat{P}_{\text{noise}, \min}}. \quad (5.62)$$

In turn, the minimum \hat{P}_{noise} is given by

$$\hat{P}_{\text{noise,min}} = \frac{P_{\text{bin,min}} \Delta f_{\text{span}}}{P_{\text{pk}[1]} \Delta f_{\text{res}}}, \quad (5.63)$$

where $P_{\text{bin,min}}$ is the minimum power in each bin, and Δf_{span} is the span of the measurement. (We use hertz-frequency, rather than radian-frequency parameters because the PSD is given in W/Hz.) Note that we will ignore the dependence on $h = 1$ in all that follows.

To measure the smallest possible jitter for a given $P_{\text{noise,min}}$, we want the largest resolution bandwidth that does not exceed the step size, Δf_{step} . (We disallow $\Delta f_{\text{res}} > \Delta f_{\text{step}}$ because we do not wish to count any power more than once.) So we set $\Delta f_{\text{res}} = \Delta f_{\text{step}}$. To maximize the step size (and thus the resolution bandwidth) we set the frequency span of the RFSA to f_{rep} . If there are N_{pt} frequency bins in the spectrum, the span is $\{N_{\text{pt}} - 1\} \Delta f_{\text{step}}$. Finally, let us define $\widehat{\Delta P}_{\text{DR}}$ to be the dynamic range of the RFSA. (The normalized dynamic range is defined such that it is greater than unity, so, when expressed in dB, it will be greater than zero.) The minimum measurable noise power is then

$$\hat{P}_{\text{noise,min}} = \frac{P_{\text{pk}[1]} \{N_{\text{pt}} - 1\} \Delta f_{\text{step}}}{\widehat{\Delta P}_{\text{DR}} P_{\text{pk}[1]} \Delta f_{\text{step}}}. \quad (5.64)$$

The minimum measurable normalized total amplitude jitter is, therefore,

$$\hat{\sigma}_{\Delta A,\text{min}} \sim \sqrt{\frac{N_{\text{pt}} - 1}{\widehat{\Delta P}_{\text{DR}}}}. \quad (5.65)$$

Note that a higher dynamic range and a larger number of points yields a smaller minimum jitter.

Now let us examine the total timing jitter, approximated by Eq. 5.47. By similarity with the amplitude-jitter case, we see that

$$\hat{\sigma}_{\Delta T,\text{min}} \sim \frac{1}{2\pi h_{\text{max}}} \sqrt{\frac{N_{\text{pt}} - 1}{\widehat{\Delta P}_{\text{DR}}}}. \quad (5.66)$$

Note that smallest minimum amplitude jitter will result from the largest harmonic h_{max} .

5.4.1.4.2 Uncorrelated Jitter The uncorrelated amplitude jitter is given, approximately, by Eq. 5.51. Recall, from the resolution computation, we can replace Φ_{noise} with $P_{\text{bin}}/\Delta\omega_{\text{res}}$. The reported jitter will be minimized, therefore, not only when the P_{bin} is minimized, but also when the resolution bandwidth is maximized. Since we wish to avoid $\Delta f_{\text{res}} > \Delta f_{\text{step}}$, we again choose $\Delta f_{\text{res}} = \Delta f_{\text{step}}$. If we use the same spectra recorded for the total-jitter measurement, $\Delta f_{\text{step}} = \Delta f_{\text{span}}/\{N_{\text{pt}} - 1\}$. By similarity with our previous work, we arrive at

$$\begin{aligned}\hat{\sigma}_{\Delta A_u, \min} &\sim \hat{\sigma}_{\Delta A, \min} \\ &\sim \sqrt{\frac{N_{\text{pt}} - 1}{P_{\text{DR}}}}.\end{aligned}\quad (5.67)$$

This result equals that obtained in the total-amplitude-noise case.

The uncorrelated timing jitter is approximated by Eq. 5.53. Note that the probe frequency, ω_p , can be expressed with

$$\begin{aligned}\omega_p &= \omega_{\text{rep}} \{h + \Delta h_p\} \\ &= \frac{2\pi}{T} \{h + \Delta h_p\},\end{aligned}\quad (5.68)$$

where Δh_p is the offset frequency of the probe point expressed in terms of the repetition rate. (In order to measure only uncorrelated noise, without ‘‘contamination’’ from correlated noise, the probe point is chosen to be far from any harmonic peak. Thus, Δh_p is typically $\sim \pm 0.5$.) By similarity with the previous work,

$$\hat{\sigma}_{\Delta T_u, \min} \sim \frac{1}{2\pi \{h_{\text{max}} + \Delta h_p\}} \sqrt{\frac{N_{\text{pt}} - 1}{P_{\text{DR}}}}.\quad (5.69)$$

Once again, higher harmonics yield smaller minimum measurable jitters. Note that, for large h_{max} , we can say, within the precision of the computations presented here, $h_{\text{max}} + \Delta h_p \sim h_{\text{max}}$, which gives the same result obtained for the total timing jitter:

$$\begin{aligned}\hat{\sigma}_{\Delta T_u, \min} &\sim \hat{\sigma}_{\Delta T, \min} \\ &\sim \frac{1}{2\pi h_{\text{max}}} \sqrt{\frac{N_{\text{pt}} - 1}{\Delta P_{\text{DR}}}}.\end{aligned}\quad (5.70)$$

Thus, the minimum measurable total and uncorrelated timing jitter are equal.

5.4.1.4.3 Correlated Jitter The RMS correlated noise is computed from the *difference* between the total and uncorrelated noises. Thus, the minimum reportable correlated jitter is 0. This very small minimum of the correlated-jitter measurement is offset, however, by the large resolution of the measurement⁹.

5.4.2 Simulation

We have written a series of MATLAB routines to simulate pulse trains with arbitrary jitter and to compute the corresponding power spectra. The program, which represents a large portion of the work described in this chapter, provides independent control of both uncorrelated jitters, both correlated jitters, both correlation times, and the pulse width, among other parameters. For consistency, we characterize the pulse width by the standard deviation (also called the RMS width) of s , denoted by σ_s . The normalized RMS pulse width is $\hat{\sigma}_s \equiv \sigma_s/T$. For a Gaussian pulse, the temporal FWHM and RMS width are related through

$$\begin{aligned} \frac{\Delta t}{\sigma_s} &= 2\sqrt{2 \ln \{2\}} \\ &\approx 2.35 . \end{aligned} \tag{5.71}$$

For the simulations shown here, the parameters vary as follows:

- $\hat{\sigma}_T$ from 0 to 0.1 in 14 steps.
- $\hat{\sigma}_A$ from 0 to 0.1 in 14 steps.
- $\hat{\sigma}_s$ from 0 to 0.1 in 7 steps.

Thus, 169 jitter combinations are represented for each pulse width, and 1372 jitter/pulse-width combinations are simulated.

⁹ See Paragraph 5.4.1.3.3.

Each spectrum is obtained by averaging the spectra of 128 simulated pulse trains, each train comprising 128 pulses. In order to conserve floating-point operations and reduce the simulation time, the time step, Δt_{step} , is determined adaptively for each jitter/width combination. In particular, the simulation routine chooses

$$\Delta t_{\text{step}} = \frac{1}{4} \min[T/128, \sigma_{T_u}, \sigma_{T_c}, \sigma_{c_T}, \sigma_{c_A}, \sigma_s/8] , \quad (5.72)$$

when each argument of the minimum operator is greater than zero. When an argument is zero, it is not considered when computing the time step. Finally, Δh_p , the probe-point offset normalized to the repetition rate, is chosen to be -0.45, and the nine points at and around each probe frequency are averaged together to reduce sensitivity to anomalies.

In the analysis presented in Subsubsection 5.4.1.1, we computed the spectrum by evaluating the Fourier transform of the autocorrelation of the signal, which was the least difficult route, analytically. The program, by contrast, calculates the spectrum of the train by taking the square modulus of the Fourier transform of the signal. These two computations are equivalent. We have chosen the second approach for the simulation because, for numerical computation, that approach is much, much faster; squaring the elements of a vector is much less computationally intensive than evaluating the autocorrelation, and Fourier transforming a vector of length N_{pt} is much easier than transforming one of length $2N_{\text{pt}} - 1$.

The results described below are couched in terms of the *normalized extraction error*. The relative or normalized error in the extraction of total timing or amplitude jitter, $\varepsilon_{\Delta J}$ is defined by

$$\varepsilon_{\Delta J} \equiv \frac{\sigma_{\Delta J, \text{ext}} - \sigma_{\Delta J}}{\sigma_{\Delta J}} , \quad (5.73)$$

where the “ext” subscript denotes the extracted value. (The quantity without the subscript is the true, simulated quantity.) The errors obtained for the uncorrelated and correlated contributions, $\varepsilon_{\Delta J_u}$ and $\varepsilon_{\Delta J_c}$, as well as those obtained for the correlation

times, $\varepsilon_{\Delta c_A}$ and $\varepsilon_{\Delta c_T}$, are defined likewise. We will use ε alone, without a subscript as a synonym for "error."

5.4.2.1 Amplitude Jitter

For each of the seven pulse widths, we have plotted the extraction error for total, uncorrelated, and correlated amplitude jitter ($\varepsilon_{\Delta A}$, $\varepsilon_{\Delta A_u}$, and $\varepsilon_{\Delta A_c}$) against the normalized total amplitude jitter, and the normalized total timing jitter. These surface plots, and the corresponding contour plots, show only a weak dependence on pulse width. Therefore, for compactness, we show only the plots associated with a single RMS pulse width ($\hat{\sigma}_s = 0.01$) in Figs. 5.18 and 5.19. The plots for all of the pulse widths are included in an appendix (Section B.1).

The first fact to notice is that all three amplitude-jitter-extraction errors (total, uncorrelated, and correlated) have similar dependence on the true timing and amplitude jitter. In other words, for any simulated pulse width, the three surface plots resemble each other. The second important feature of these plots is the extreme overestimation of the amplitude noise for cases where the amplitude noise is small and the timing noise is large (the far corner in the surface plots, and the upper left corner of the contour plots). This overestimate results because of the quadratic frequency dependence of the timing jitter. When the normalized RMS timing jitter is greater than the normalized RMS amplitude jitter, the ω^2 dependence causes the timing-noise PSD (and integrated timing-noise power) in the spectrum to dominate the amplitude-noise contribution. In fact, for large timing jitters, the characterization routine reports an amplitude jitter that depends more strongly on the *timing jitter*, than on the amplitude jitter itself! However, it is important to note that there is still a large region in which the extraction error is small; for every pulse width and for each amplitude-jitter contribution the extraction errors are remain below 0.30 as long as

$$\hat{\sigma}_A^{0.75} \gtrsim 1.5\hat{\sigma}_T . \quad (5.74)$$

We can approximate this relationship by saying the error is less than 30 % as long as the normalized RMS total amplitude jitter is approximately greater than the normalized RMS total timing jitter:

$$\hat{\sigma}_{\Delta A} \gtrsim \hat{\sigma}_T . \quad (5.75)$$

This domain of low error is easy to discern in the contour plots; it appears as the triangular region on the lower right. Note that the extraction of the correlated jitter is the least accurate, perhaps because of the indirect way in which it is computed.

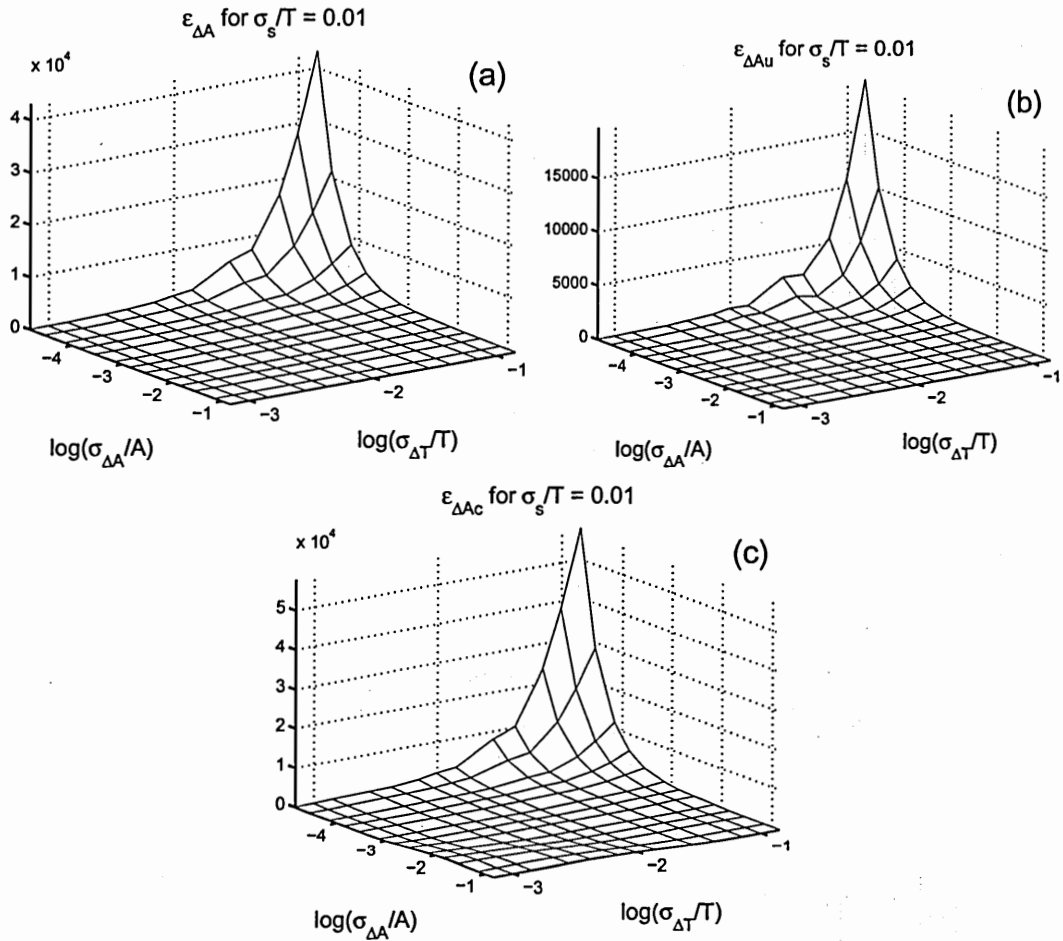


Figure 5.18: Extraction errors for (a) total amplitude jitter, $\epsilon_{\Delta A}$, (b) uncorrelated amplitude jitter, $\epsilon_{\Delta Au}$, and (c) correlated amplitude jitter, $\epsilon_{\Delta Ac}$, obtained with the uncompensated direct method. σ_A/A —normalized total amplitude jitter. σ_T/T —normalized total timing jitter. σ_s/T —normalized root-mean-squared pulse width.

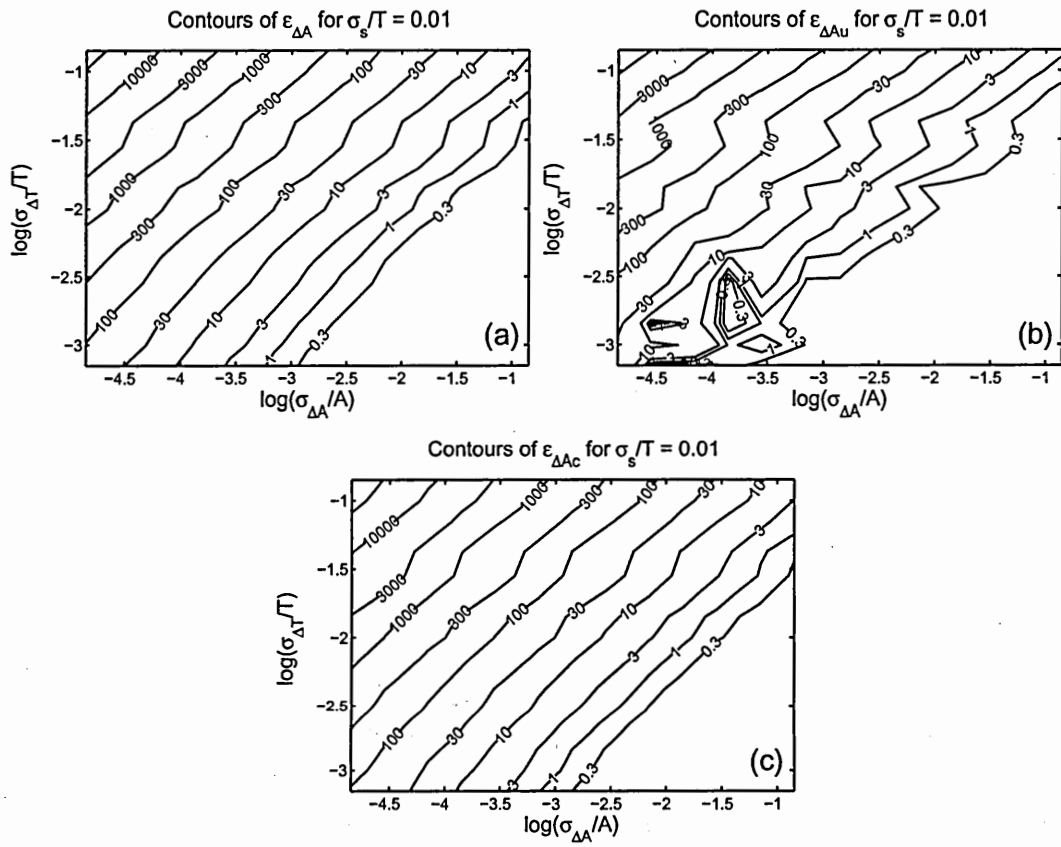


Figure 5.19: The contours of the plots shown in 5.18

5.4.2.2 Timing Jitter

The surface plots the three timing-jitter errors ($\epsilon_{\Delta T}$, $\epsilon_{\Delta T_u}$, and $\epsilon_{\Delta T_c}$) and the corresponding contours, are, as in the amplitude-jitter case, insensitive to pulse width. Thus, we only include the plots associated with the RMS pulse width of 1 % in Figs. 5.20 and 5.21, while all the plots are shown in an appendix (Section B.2). Note that the orientation of the axes of the surface plots differs from that of the amplitude-noise-error surfaces; the axes in each case are arranged to best present the features of the plots.

The first feature we note is that, as in the amplitude case, the error is similar for the three timing-jitters. Second, the error is independent of the true amplitude jitter. Both of these features are good. The third feature of note is that the routine underestimates for large timing jitter. This underestimation results from the small-noise approximation we made in the derivation of the spectrum, and it provides information about the limitations of the measurement that are imposed by this assumption. However, even with this underestimation, the magnitude of the error remains below 30 % for all pulse widths and for all timing-jitter contributions so long as

$$\hat{\sigma}_T \lesssim 0.032 . \quad (5.76)$$

Note that, as in the amplitude-jitter case, the correlated-jitter extraction is the least accurate.

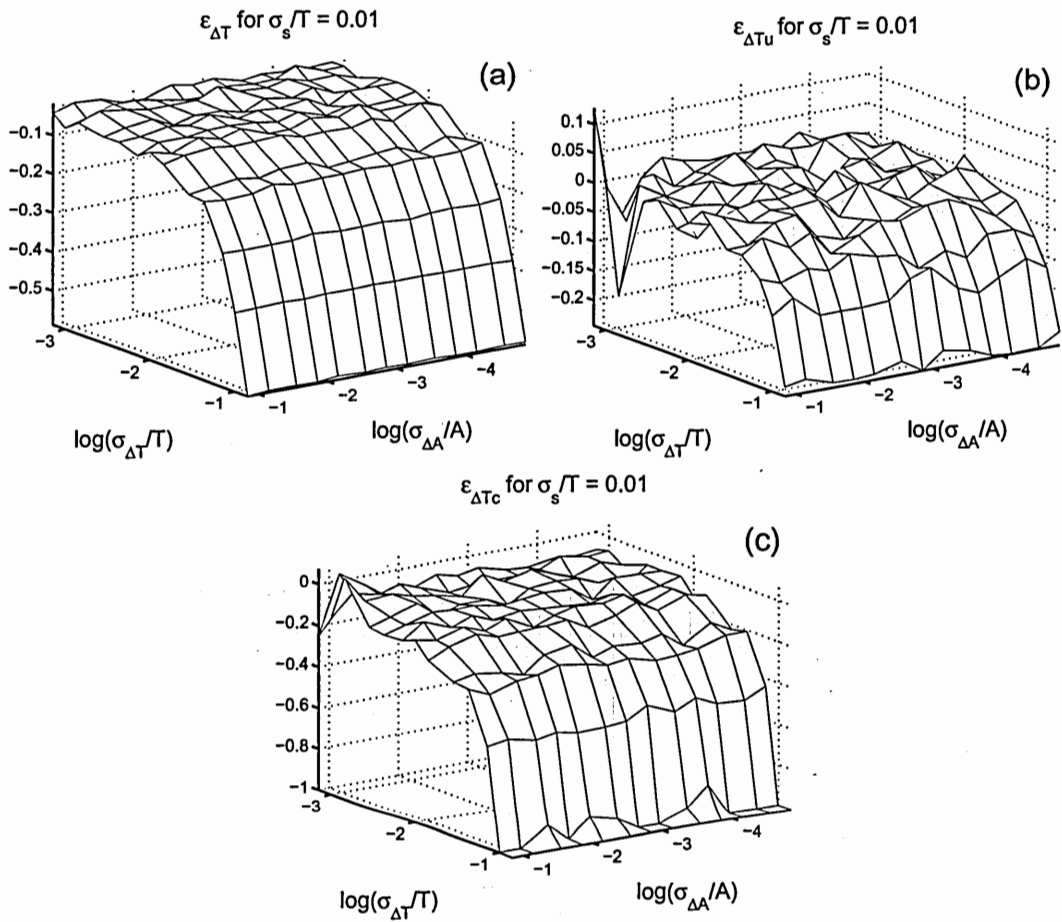


Figure 5.20: Extraction errors for (a) total timing jitter, $\epsilon_{\Delta T}$, (b) uncorrelated timing jitter, $\epsilon_{\Delta T_u}$, and (c) correlated timing jitter, $\epsilon_{\Delta T_c}$, obtained with the uncompensated direct method. σ_A/A —normalized total amplitude jitter. σ_T/T —normalized total timing jitter. σ_s/T —normalized root-mean-squared pulse width.

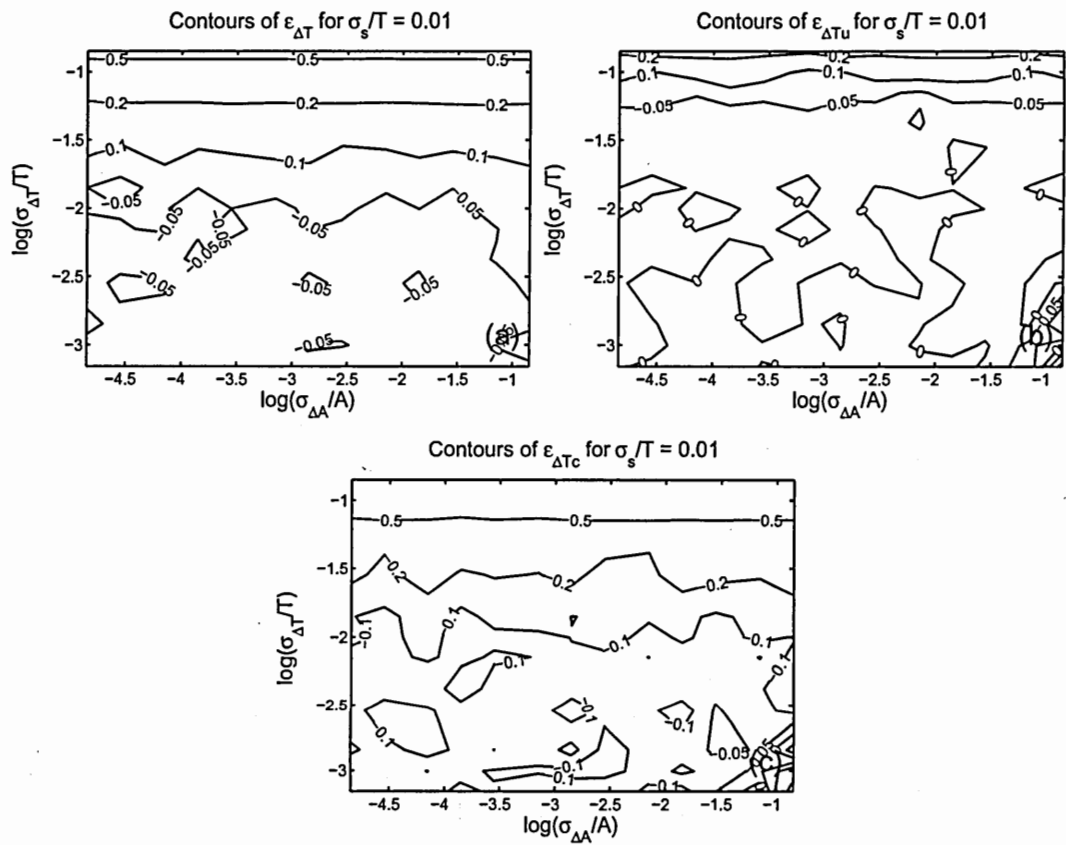


Figure 5.21: The contours of the plots shown in 5.20

5.4.2.3 Correlation Time

The extraction-error surfaces for the two correlation times (σ_{c_A} and σ_{c_A}) are also qualitatively similar for all pulse widths. Thus, only the surface plots corresponding to $\hat{\sigma}_s = 0.01$ are shown in Fig. 5.22. (The contour plots are omitted, because they are not very illustrative.) The surface plots of all pulse widths are included in an appendix (Section B.3).

The correlation-time surface plots exhibit no prominent pattern such as those seen on the amplitude-noise and timing-noise cases. The surface plots are flat *on average*, though very rough; the magnitude of the error is less than 30 % for many simulated timing-noise/amplitude-noise/pulse-width combinations, but there are many combinations with errors beyond this range of $[-0.30 < \varepsilon < 0.30]$. The extraction of the timing-jitter correlation time is much more accurate than the extraction of the amplitude-noise correlation time. It should be noted that the correlation time was fixed at $5T$ during these simulations, so the correlation-time extraction was not fully tested.

Clearly, the correlation-time extraction would benefit from fine tuning. It may be that the problem arises from a too-wide frequency step, giving too-coarse resolution of the widths of the correlated-noise bands around each harmonic. If so, the problem would be solved by reducing the frequency step, which means increasing the temporal span (or equivalently, number of periods) of the simulated pulse train. This solution would increase the time required for the computation of the spectrum,

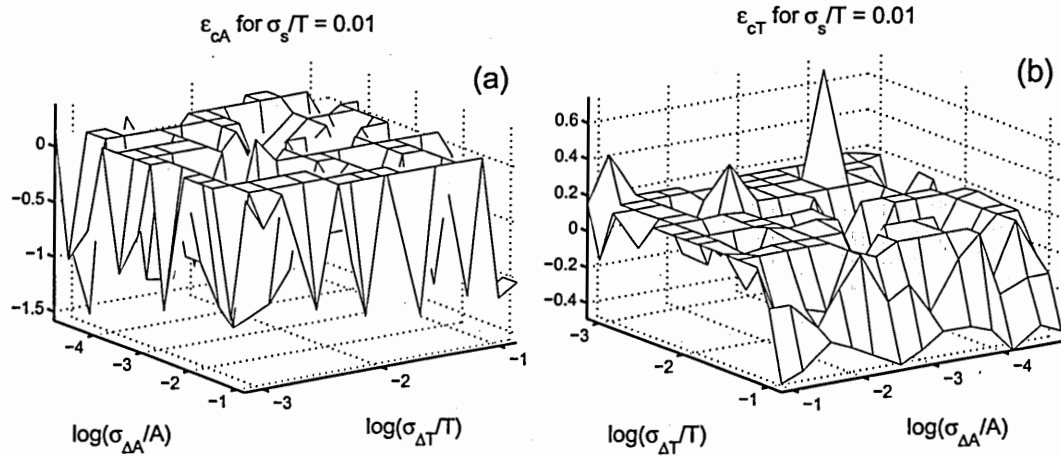


Figure 5.22: Extraction errors for the correlation times of the (a) correlated amplitude jitter, $\epsilon_{\Delta A_e}$ and (b) timing jitter, $\epsilon_{\Delta T_e}$, obtained with the uncompensated direct method. σ_A/A —normalized total amplitude jitter. σ_T/T —normalized total timing jitter. σ_s/T —normalized root-mean-squared pulse width.

5.4.3 Error Compensation

Examining Figs. 5.18 through 5.21 (as well as the corresponding plots in Section B.1), we see that the errors are *systematic* for all values except the correlation times. This pattern suggests that it should be possible to compensate, at least partially, for the errors. To this end, we have implemented a compensation routine in MATLAB. The routine takes, as its arguments, the extracted jitter values and the pulse width.

5.4.3.1 General Compensation Algorithm

We begin the compensation by normalizing both the newly extracted values (those to be compensated) and the simulated-then-extracted values to the corresponding periods. In other words, we convert σ_s to $\hat{\sigma}_s$, $\sigma_{\Delta J}$ to $\hat{\sigma}_{\Delta J}$, and so on. This normalization allows us to compare the two data sets. We then choose simulated-then-extracted pulse width closest to that of the pulse train under investigation, and examine the corresponding extracted-jitter-versus-simulated-jitter surfaces. (Note that the program chooses the nearest pulse width; it does not interpolate between pulse widths. The pulse-width dependence of the errors is quite weak, so interpolation is unnecessary. Further, three-dimensional interpolation is more time-consuming than two- or one-dimensional interpolation, and avoiding it speeds up the routine.)

For each extracted jitter parameter, the domain of timing-jitter/amplitude-jitter combinations can be divided into three regions. The first domain is combinations that have been simulated and for which the uncompensated routine errs less than a specified threshold value. (We have set this threshold error at 0.005). In this region, no compensation is required; we do nothing. This do-nothing case is employed *only in the timing-jitter case* to eliminate unnecessary compensation, since there is such a large region of low error in the timing extraction; in the amplitude-jitter case, we always attempt compensation. The second domain is simulated combinations for which the error is greater than this threshold. Here, we treat the extracted

value as the independent variable while treating the true, simulated value as the dependent variable. We then interpolate to estimate the true value. The third domain of jitter combinations is those that have not been simulated. Since the simulated-then-extracted jitters extend all the way to zero, any combinations that fall outside the simulated domain must be greater than the simulated values. In this case, we extrapolate and then proceed as in the second region.

5.4.3.2 Amplitude Jitter

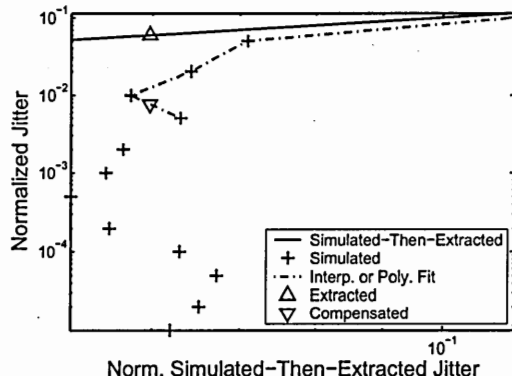


Figure 5.23: Compensation of the uncorrelated-amplitude-jitter extraction.

Compensating the amplitude-jitter errors is simplified by compensating the timing-jitter¹⁰ first, and using the compensated timing jitter values. (For reasons of consistency, we describe the amplitude-noise compensation first in this document) This approach reduces the dimensionality of the interpolation from two to one. Unfortunately, as noted before, the parabolic dependence of the timing-noise power and the constant nature of the amplitude-noise power mean that, when $\hat{\sigma}_{\Delta T} > \hat{\sigma}_{\Delta A}$ the power due to timing jitter dominates the amplitude-jitter power and the characterization routine overestimates the amplitude jitter. This pattern makes compensating for the amplitude error quite challenging. This difficulty is illustrated by the nearly

¹⁰ See Subsubsection 5.4.3.3.

horizontal portion of the simulated-then-extracted trace of Fig. 5.23. Because of this difficulty, we introduce an additional step in the compensation of the amplitude jitter; as a final check, since the amplitude noise is only *overestimated*, we take the minimum of the uncompensated and compensated values.

It should be made explicit that the compensated value for each of the three amplitude-noise parameters is computed independently from the uncompensated value. This approach is different from that employed in the timing-jitter case¹¹.

The compensated amplitude-extraction-error surface and contours for an RMS pulse width of 1 % are shown in Figs. 5.24 and 5.25). See Section C.1 for all amplitude-error plots.

The surface plots each have the same general shape as the uncompensated plot, but the maximum extraction error is reduced (most clearly visible in the surface plots), and the domain of error below 30 % is considerably enlarged, (most evident in the enhanced triangular regions in lower right of the contour plots). As before, the correlated-jitter extraction is the least accurate, but, for all pulse widths and all amplitude-jitter contributions, the error remains below 0.30 so long as

$$\hat{\sigma}_{\Delta A}^{0.60} \gtrsim 1.5\hat{\sigma}_T . \quad (5.77)$$

This region of low error is larger than that observed for the uncompensated case, but it can still be loosely approximated by

$$\hat{\sigma}_{\Delta A} \gtrsim \hat{\sigma}_T . \quad (5.78)$$

¹¹ See 5.4.3.3.

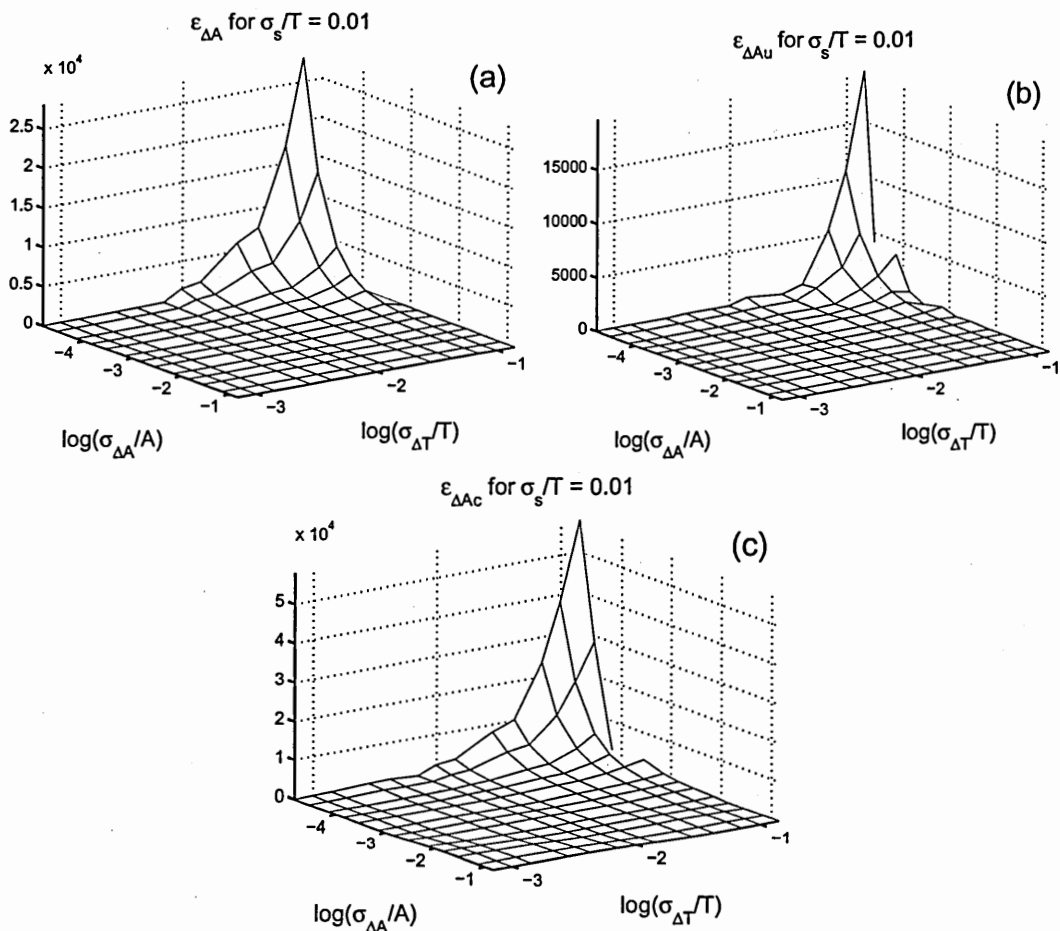


Figure 5.24: Extraction errors for (a) total amplitude jitter, $\epsilon_{\Delta A}$, (b) uncorrelated amplitude jitter, $\epsilon_{\Delta Au}$, and (c) correlated amplitude jitter, $\epsilon_{\Delta Ac}$, obtained with the compensated direct method. σ_A/A —normalized total amplitude jitter. σ_T/T —normalized total timing jitter. σ_s/T —normalized root-mean-squared pulse width.

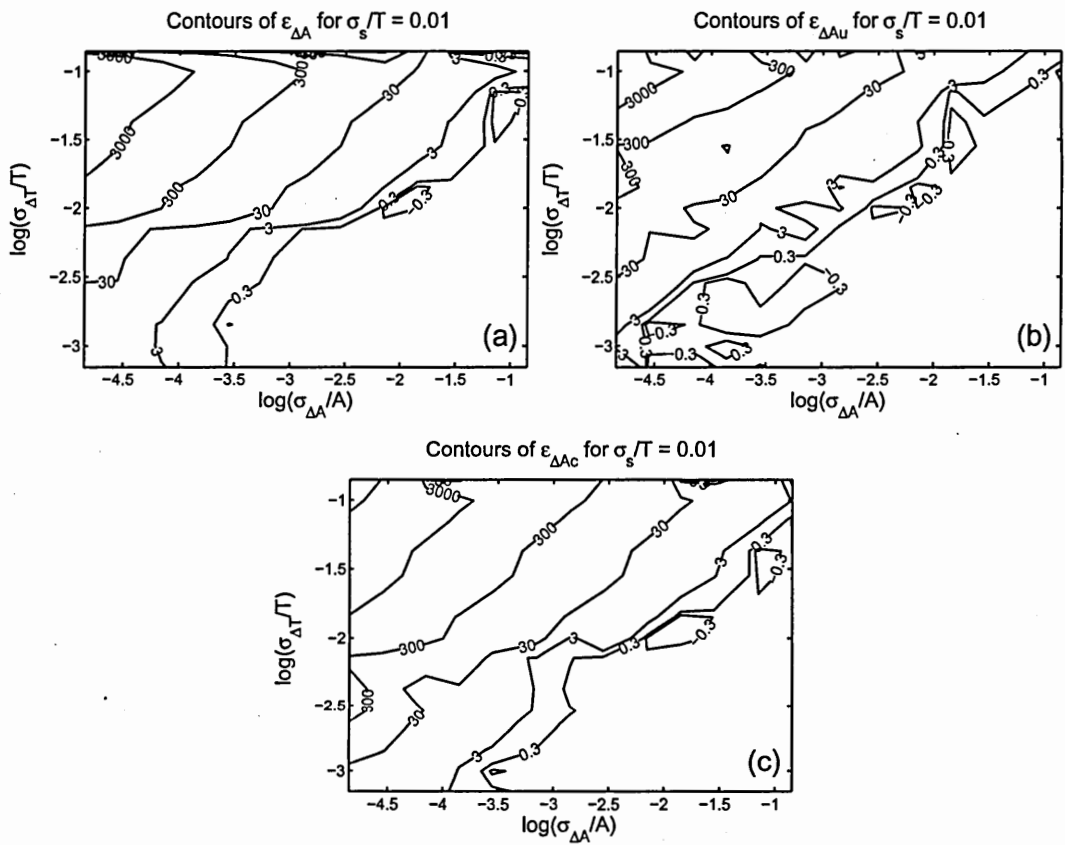


Figure 5.25: The contours of the plots shown in 5.24

5.4.3.3 Timing Jitter

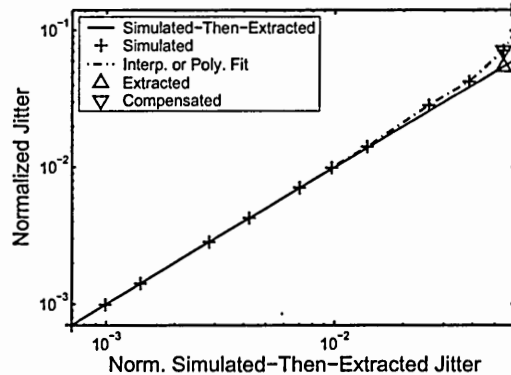


Figure 5.26: Compensation of the total-timing-jitter extraction.

Compensating the timing-jitter errors is simplified by the timing-jitter error's independence from the amplitude jitter; the two-dimensional interpolation is reduced to a one-dimensional interpolation, illustrated in Fig. 5.26. The compensated timing-error surfaces obtained for $\hat{\sigma}_s = 0.01$ are presented in Fig. 5.27. (As these plots are now quite flat, the contour plots are no longer helpful and have been left out.) See Section C.2 for the plots associated with all simulated temporal widths.

It should be pointed out that only the compensated values of the total and uncorrelated timing jitter are computed from the uncompensated values. The compensated correlated timing jitter is computed by applying taking the RMS difference between the compensated total and uncorrelated jitter (exactly the way the uncompensated correlated timing noise is computed from the uncompensated total and uncorrelated noise). This approach is different from that employed in the amplitude-jitter case¹².

Importantly, though not surprisingly, the errors are still independent of the amplitude jitter. Further, in all cases, the plots are clearly more planer, and the

¹² See Subsubsection 5.4.3.2.

region over which $|\varepsilon| < 30\%$ is extended to

$$\hat{\sigma}_T \lesssim 0.071 . \quad (5.79)$$

This is an improvement of more than a factor of two. Beyond this limit, the program can over- or underestimate. With compensation, the timing-jitter error surfaces are flat enough that contour plots are not helpful, so we do not present them here.

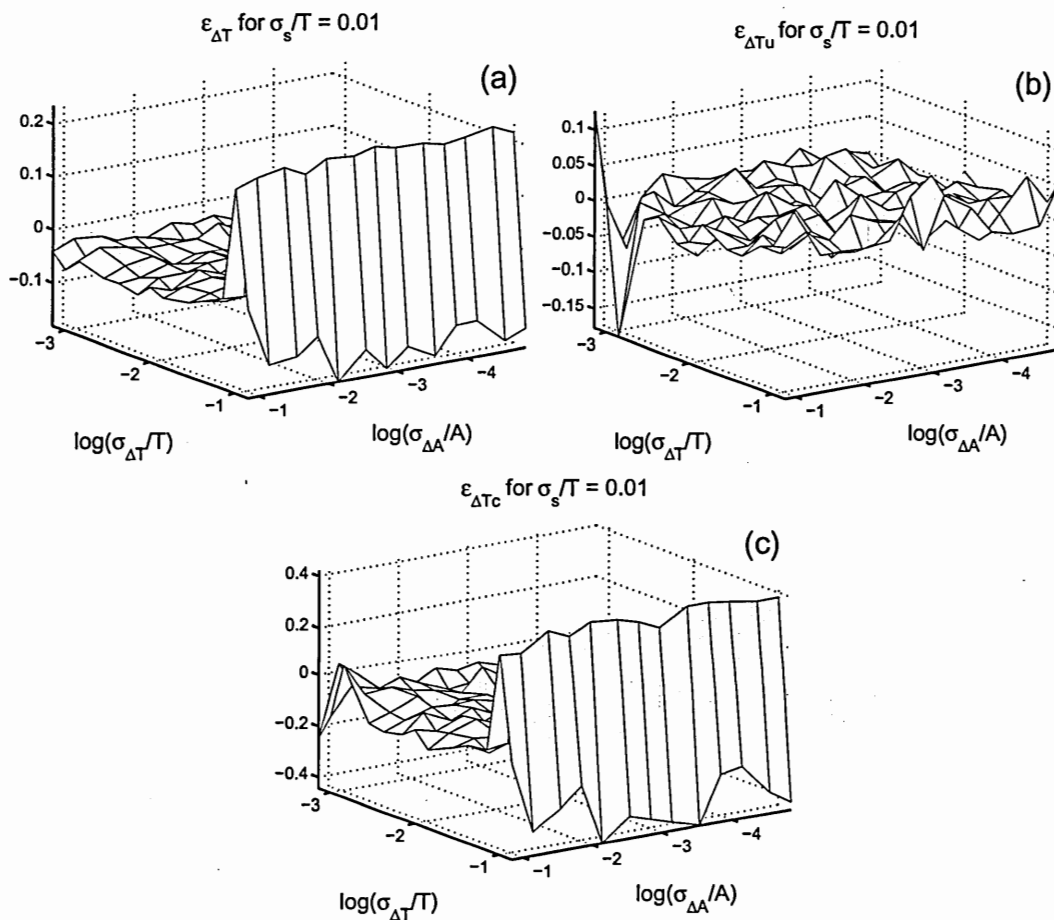


Figure 5.27: Extraction errors for (a) total timing jitter, $\varepsilon_{\Delta T}$, (b) uncorrelated timing jitter, $\varepsilon_{\Delta T_u}$, and (c) correlated timing jitter, $\varepsilon_{\Delta T_c}$, obtained with the compensated direct method. σ_A/A —normalized total amplitude jitter. σ_T/T —normalized total timing jitter. σ_s/T —normalized root-mean-squared pulse width.

5.4.3.4 Correlation Times

The correlation-time error surfaces do not show a deterministic trend, so there is no way to compensate for their errors. Thus, for the correlation-times, the compensation routine simply returns the input values, and the with-compensation error surfaces are identical to the without-compensation surfaces. We will, therefore, omit these plots from this document.

5.4.4 Experiment

To validate the performance of the direct jitter-characterization scheme, we compare the results obtained when it and the oscilloscope technique¹³ are applied to two very different pulsed lasers. Before examining the results of these experiments, we will discuss the experimental setup, the data-acquisition routine, and the lasers under investigation.

5.4.4.1 Experimental Details

5.4.4.1.1 Experimental Setup The experimental setup employed in the oscilloscope measurement consists of a digital sampling oscilloscope (Tektronix model 11801B), a sampling head (Textronix model SD-30) with a specified bandwidth of 40 GHz, and a photoreceiver (Newport model D-15ir) with a specified impulse response of 15 ps. We measured the trigger jitter of the oscilloscope/sampling head combination to be 1.7 ps.

In the direct spectral measurement, the setup consisted of an Agilent 8564EC radio-frequency spectrum analyzer and the same D-15ir photoreceiver. The RFSA records spectra of exactly 6001 points, has an operational band specified as 9 kHz to 40 GHz, and a dynamic range of 100 dB when operating with a logarithmic vertical

¹³ See Subsubsection 5.3.1.1.

scale and with a level scale of 10 dB/division. The noise floor of the RFSA varies with frequency, trending upward. The largest value is -114 dBm/Hz, measured at 27.0 GHz.

Early versions of this setup incorporated an electronic variable attenuator (Hewlett-Packard model 8156A), the optical output of which could be remotely disabled. The attenuator was employed to automatically measure the noise floor of the experiment. This arrangement had two problems. First, the insertion loss of the attenuator was 4.3 dB, reducing the dynamic range between the power of the detected pulse train and the noise floor of the oscilloscope. The second problem was that the attenuator, even with its output disabled, was leaky, resulting in small, but measurable signal power being recorded during the noise-floor measurement. The attenuator has therefore been eliminated from the setup. The noise floor is measured separately, immediately after each all the signal measurement.

5.4.4.1.2 Resolution The Agilent 8564EC RFSA employed for our spectral measurements (like every Hewlett-Packard/Agilent 856X-series RFSA) has four logarithmic level scales: 1, 2, 5, and 10 dB/division. Since the number of divisions is fixed at 10, the dynamic range is simply 10 times the level scale. In Table 5.1, we summarize the marker resolutions and the measurement resolutions that correspond to each level-scale setting. Note that, as we suggested, the multiplicative resolution of the correlated-jitter measurement is approximately 4.8 dB. All of the experiments described in this document were performed with the 10-dB/division scale, so the bottom row of the table applies.

5.4.4.1.3 Minimum Measurable Jitter The noise floor of the RFSA is low enough, with respect to the power in the harmonic peaks in our experiments, that the dynamic range of the instrument determines the minimum measurable jitter¹⁴.

¹⁴ See Subsubsection 5.4.1.4.

Table 5.1: Jitter-measurement resolutions when using an Agilent 856X.

Level Scale (dB/division)	∂P (dB)	$\partial\sigma_{\Delta J}$ (dB)	$\partial\sigma_{\Delta J_u}$ (dB)	$\partial\sigma_{\Delta J_c}$ (dB)
1	1/60	0.017	0.017	4.7
2	1/30	0.033	0.033	4.7
5	1/12	0.082	0.082	4.7
10	1/6	0.17	0.17	4.7

∂P —marker resolution. $\partial\sigma_{\Delta J}$ —resolution of total amplitude or timing jitter. $\partial\sigma_{\Delta J_u}$ —resolution of uncorrelated amplitude or timing jitter. $\partial\sigma_{\Delta J_c}$ —resolution of correlated amplitude or timing jitter.

The 856X-series RFSAs record spectra with only a fixed number of data points: 601. Consequently, for each jitter parameter that is to be measured, there is only one choice of minimum measurable value. The minimum measurable jitters for each measurement, assuming $h_{\max} = 7$, are summarized in Table 5.2. Again, the experiments described in this document were performed with the 10-dB/division scale, so the bottom row applies.

5.4.4.1.4 Hybrid Spectrum and Averaging Given the Agilent RFSA's fixed (and small) number of data points, it is difficult to recorded multiple harmonics with the fine resolution required. The span of the recorded spectrum must be *at least* $2f_{\text{rep}}$ and preferably several times the repetition frequency. For high-rate sources ($f_{\text{rep}} > 1$ GHz), this span works out to be at least 2 GHz, and can easily be as high as 50 GHz. Another problem associated with wide-span spectra is that the harmonic peaks cannot be resolved from the correlated-noise band. Simply splicing together a number of narrow spectra to create one wide-span spectrum will not solve the problem. We have found that doing so takes so very long that experimental drift occurs during the measurement, making the recorded spectrum useless.

Table 5.2: Minimum measurable jitters when using an Agilent 856X.

Level Scale (dB/division)	\hat{P}_{DR} (dB)	$\hat{\sigma}_{A,\min}$	$\hat{\sigma}_{T,\min}$	$\hat{\sigma}_{A_u,\min}$	$\hat{\sigma}_{T_u,\min}$	$\hat{\sigma}_{J_c,\min}$
1	10	7.7	0.18	7.7	0.18	0.0
2	20	2.4	0.056	2.4	0.056	0.0
5	50	0.077	$1.8 \cdot 10^{-3}$	0.077	$1.8 \cdot 10^{-3}$	0.0
10	100	$2.4 \cdot 10^{-4}$	$5.6 \cdot 10^{-6}$	$2.4 \cdot 10^{-4}$	$5.6 \cdot 10^{-6}$	0.0

The table assumes $N_{pt} = 601$ and $h_{\max} = 7$. \hat{P}_{DR} —dynamic range. $\hat{\sigma}_{A,\min}$ —minimum measurable normalized total amplitude jitter. $\hat{\sigma}_{T,\min}$ —minimum measurable normalized total timing jitter. $\hat{\sigma}_{A_u,\min}$ —minimum measurable normalized uncorrelated amplitude jitter. $\hat{\sigma}_{T_u,\min}$ —minimum measurable normalized uncorrelated timing jitter. $\hat{\sigma}_{J_c,\min}$ —minimum measurable normalized correlated amplitude or timing jitter. N_{pt} —number of points. h_{\max} —maximum harmonic.

Our solution to these problems is a “hybrid” spectrum. The hybrid spectrum is assembled in three steps:

- A single spectrum, spanning the entire frequency region of interest, is recorded. The result is called the “coast-to-coast” spectrum.
- For each harmonic, a spectrum consisting of the harmonic peak and its immediate surroundings is recorded. This result is called the “zoomed” spectrum.
- Each of the harmonic peaks of the coast-to-coast spectrum (and a few surrounding points) is replaced by the corresponding zoomed spectrum.

The result of these manipulations is a spectrum consisting of approximately $601(H+1)$ points, where H is the number of harmonics. (Note that, if the minimum harmonic is 1, $H = h_{\max}$.) This data set has fine spectral resolution where the pulse train’s spectrum is most “interesting” and coarse resolution where the spectrum is nearly flat.

Lastly, it should be pointed out that temporal averaging (multiple traces averaged together) is employed to ensure a smooth signal. The coast-to-coast and zoomed spectra are averaged to the same degree.

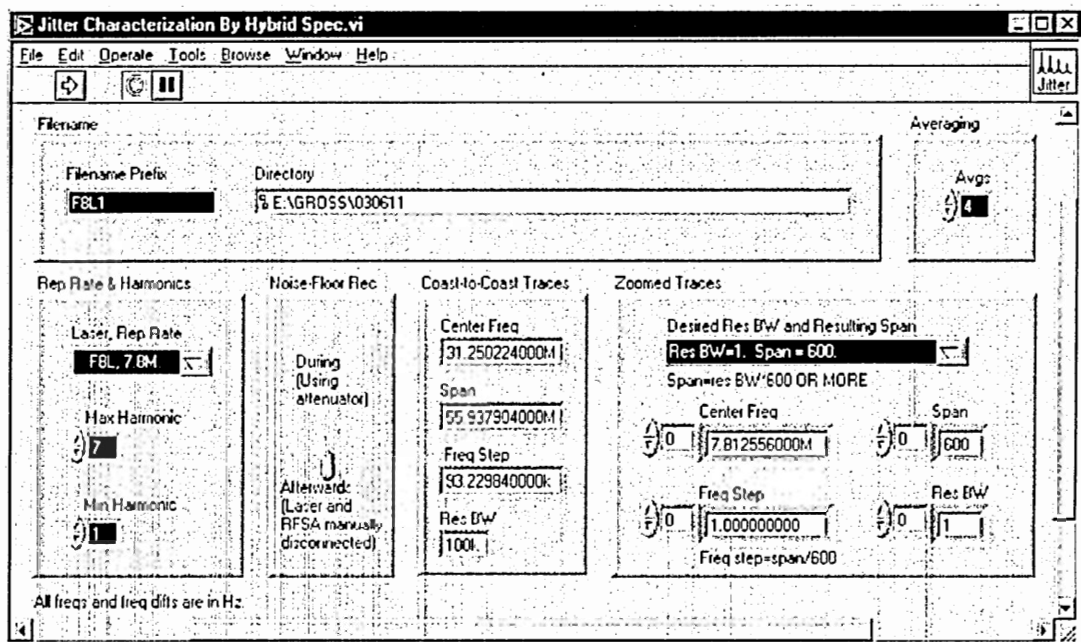


Figure 5.28: The front panel of the LabVIEW data-acquisition routine. White-on-black boxes are controls (inputs); black-on-white boxes are indicators (outputs). The spectra are displayed by a subroutine (not shown) as they are measured and then recorded.

5.4.4.1.5 Data-Acquisition Routine We have written a LabVIEW program to control the RFSA and record the components of the hybrid spectrum. (Note that the hybrid spectrum is actually assembled later, by the MATLAB characterization routine.) The LabVIEW program takes as its inputs the directory and filename prefix using which all the spectra should be saved, the number of averages to employ, the repetition rate, the minimum and maximum harmonics to be recorded, and the desired span and resolution bandwidth of the zoomed-in traces. The “front panel” of the program is displayed in Fig. 5.28.

5.4.4.1.6 Gain-Switched Laser Diode Our first experiment involves a gain-switched laser diode¹⁵. As a directly-modulated laser, we expect noise to be dominated by the uncorrelated contribution¹⁶.

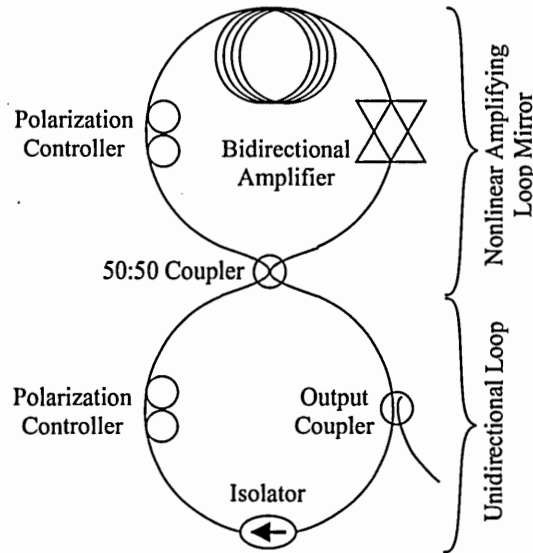


Figure 5.29: The figure-eight laser.

5.4.4.1.7 Figure-Eight Laser The second laser examined is a passively mode-locked fiber laser, specifically a figure-eight laser (F8L, Fig. 5.29) [80], [81], the noise of which we expect to be dominated by its correlated component¹⁷. Further, we expect that the correlation time of the F8L's correlated jitter will be on the order of its cavity round-trip time, τ_{RT} , (128 ns) or its photon lifetime τ_{γ} , (~ 140 ns).

The F8L presents an experimental difficulty not encountered in the measurement of the gain-switched laser. Because the F8L is *passively* mode-locked, it is not tied to any external clock signal; there is no retiming of the pulses on each circuit of the cavity, as would be the case in an actively mode-locked laser. (For this reason,

¹⁵ Specifically, this laser is the first stage of the Picosecond-Pulse Source, which is described in Subsection 2.4.1.

¹⁶ See Subsection 1.5.3.

¹⁷ See Subsection 1.5.3.

the jitter of a PML laser is often described in terms of pulse-to-pulse jitter [23], [64].) The repetition rate of the laser can therefore drift with time, and the harmonic peaks, especially the higher ones, can shift during a measurement. If averaging is used, this shift will result in broadened, shortened harmonic peaks. Consequently, when measuring the jitter of the figure-eight laser, it is important to minimize the number of averages.

5.4.4.2 Results

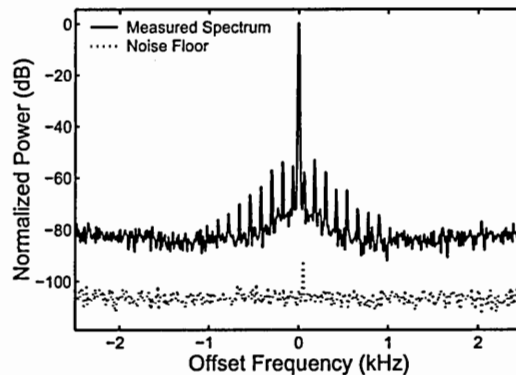


Figure 5.30: The seventh harmonic of the gain-switched laser diode's power spectrum. This spectrum was recorded with a 10-Hz step size and 10-Hz resolution bandwidth.

5.4.4.2.1 Gain-Switched Laser Diode The seventh harmonic of the gain-switched laser diode's spectrum is displayed in Fig. 5.30. It is important to note two features of this spectrum. First, the noiseband of the laser is always well above the noise floor of the measurement, indicating that (a) the results should be sound and (b) significant uncorrelated jitter will be measured. Second, there are prominent noise spurs at multiples of 120 Hz. Given the 120-Hz spacing, and the absence of these lines from the F8L spectrum described below, we believe these spurs may result from leakage of the 60-Hz laboratory power grid into the system.

The jitter parameters measured for the GS LD with the oscilloscope technique and those measured with the direct spectral technique are summarized in Tables 5.3 and 5.4, respectively. The total timing jitter reported by the direct technique (4.9 ps) closely agrees with that reported by the oscilloscope (5.1 ps). The total amplitude jitter, meanwhile, agrees only approximately. The amplitude jitters reported by the direct spectral technique are probably overestimates, since the magnitude of the timing jitter is so large¹⁸. Thus, the total amplitude jitter reported by the oscilloscope method (0.19) is probably the more accurate value. As expected, the uncorrelated timing and amplitude jitter represents the vast majority of total, while the correlated contributions are very much smaller. The reported correlation times are essentially meaningless, since there is virtually no correlated noise.

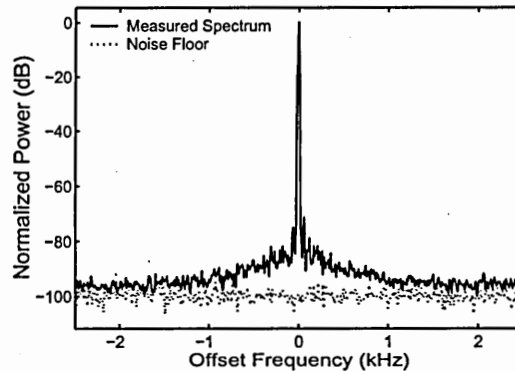


Figure 5.31: The seventh harmonic of the figure-eight laser's power spectrum. This spectrum was recorded with a 10-Hz step size and 10-Hz resolution bandwidth.

5.4.4.2.2 Figure-Eight Laser The jitter parameters measured for the F8L with the two techniques are also summarized in Tables 5.3 and 5.4. In this case, the timing jitter of the laser is less than the trigger jitter of the oscilloscope, so all we can say from the oscilloscope method is that the total jitter is less than 1.7 ps. The jitter reported by the spectral technique (200 fs) is somewhat less than the minimum jitter found in Table 5.2 (710 fs, computed using $h_{\max} = 7$ and $T = 128$ ns). However, this situation

¹⁸ See Subsubsection 5.4.2.1.

is not too worrisome; the computation of the minimum jitter¹⁹ was approximate and only intended to provide an order-of-magnitude estimate. Returning to the results, we see that, as expected, the correlated contribution dominates, and there is very little uncorrelated jitter. The correlation times are of *approximately* the same magnitude, differing by a factor of about 2.6. Further, the correlation times are approximately $7\tau_\gamma$ to $13\tau_\gamma$. These results are in rough agreement with our predictions.

Table 5.3: Jitter measured with the oscilloscope method.

Laser	$\sigma_{\Delta T}$ (ps)	$\sigma_{\Delta A}$
LD	5.1	0.19
F8L	< 1.7*	0.015

*Measurement limited by 1.7-ps trigger jitter of oscilloscope. LD—laser diode. F8L—figure-eight laser. $\sigma_{\Delta T}$ —RMS total timing jitter. $\sigma_{\Delta A}$ —RMS total amplitude jitter. RMS—root-mean-square.

Table 5.4: Jitter measured with the direct spectral method.

Laser	$\sigma_{\Delta T}$ (ps)	$\sigma_{\Delta T_u}$ (ps)	$\sigma_{\Delta T_c}$ (ps)	$\sigma_{\Delta A}$	$\sigma_{\Delta A_u}$	$\sigma_{\Delta A_c}$	σ_{c_T} (μ s)	σ_{c_A} (μ s)
LD	4.9	5.0	0.0	0.68	0.62	0.29	7800	710
F8L	0.19	0.0	0.19	$1.4 \cdot 10^{-4}$	$4.5 \cdot 10^{-6}$	$1.3 \cdot 10^{-4}$	0.68	1.8

LD—laser diode. F8L—figure-eight laser. $\sigma_{\Delta T}$ —RMS total timing jitter. $\sigma_{\Delta T_u}$ —RMS uncorrelated timing jitter. $\sigma_{\Delta T_c}$ —RMS correlated timing jitter. $\sigma_{\Delta A}$ —RMS total amplitude jitter. $\sigma_{\Delta A_u}$ —RMS uncorrelated amplitude jitter. $\sigma_{\Delta A_c}$ —RMS correlated amplitude jitter. σ_{c_T} —RMS correlation timing of correlated timing jitter. σ_{c_A} —RMS correlation amplitude of correlated timing jitter. RMS—root-mean-square.

¹⁹ See Subsubsection 5.4.1.4.

5.5 Commentary

5.5.1 Uncorrelated and Correlated Jitter

We have derived a method of extracting all eight jitter parameters of a pulse train directly from an RF spectrum containing ≥ 2 harmonics. This method relies, in part, on a non-integrating, pointwise measurement of uncorrelated jitter. We have shown, through simulation, that this technique exhibits systematic errors that can be compensated. According to additional simulations, with compensation, the scheme can extract total, uncorrelated, and correlated amplitude jitter with error less than 30 % as long as the normalized RMS amplitude jitter is approximately less than the normalized RMS timing jitter. These same simulations indicate that the routine can extract the the total, uncorrelated, and correlated timing jitters with error less than 30 % as long as the the RMS total timing jitter is less than approximately 7.1 % of the bit period. We have also shown, using experiments performed with a gain-switched laser diode and a figure-eight laser, that the method's results (a) are plausible and (b) agree with total-jitter measurements made using an oscilloscope.

5.5.2 Super-Mode Jitter

The jitter-characterization scheme described in this chapter does not explicitly extract the super-mode jitter of a pulse train from its RF spectrum. In addition, the simulation described in Subsection 5.4.2 does not incorporate this kind of noise. The direct spectral jitter-characterization routine would integrate the super-mode noise when computing the total jitter and, *so long as the probe point is chosen far from any super-mode spur*, would exclude it from the uncorrelated-jitter computation. Thus, the method would count the super-mode jitter as correlated jitter.

5.5.3 Resolution and Minimum Measurable Jitter

We have derived analytical methods of estimating the resolution and minimum measurable jitter of the direct spectral jitter-characterization method. When a Hewlett-Packard/Agilent 8456X-series RF spectrum analyzer is used, the total and uncorrelated jitter can be extracted with a multiplicative resolution between 0.017 and 0.16 dB, and the correlated jitter can be extracted with a resolution of 4.7 dB. With the same RFSA, the minimum measurable normalized total amplitude jitter and normalized uncorrelated amplitude jitter lie between 7.7 and $2.4 \cdot 10^{-4}$. The minimum normalized total timing jitter and normalized uncorrelated timing jitter that can be measured are lower by a factor of $2\pi h_{\max}$. The minimum measurable correlated amplitude or correlated timing jitter is 0. It is important to note that there is a trade-off between fine resolution and small measurable jitter.

5.5.4 Application to Data Streams

If the pulse train were modulated to become a data stream, the modulation, since it is not periodic, would appear in the spectrum as amplitude noise. Indeed, since half of the pulses would be multiplied by one (equivalent to no jitter), and half would be multiplied by zero (-100 % jitter) the modulation would be equivalent to RMS amplitude jitter of $1/\sqrt{2} = 0.707$. This very large amplitude “noise” would fill in the spaces between the harmonics in the spectrum, making extraction of the amplitude or timing jitter impossible. Further, because these “noise” corresponding to the modulation invalidates our assumption of small jitter, the analysis presented in this chapter would not apply. Thus, the jitter-characterization routine presented here is not applicable to data streams, only to pulse trains.

CHAPTER 6

Mixing-Based Jitter-Characterization Method

6.1 Roadmap

In Chapter 6, we present a spectral jitter-measurement technique based on mixing the detected pulse train with sinusoids that are in phase and in quadrature phase. This method extracts the total, uncorrelated, and correlated timing and amplitude jitter. Section 6.2 summarizes the problem the method is designed to address. Section 6.3 reviews previous work in the field. Section 6.4 is the heart of this chapter; in this section, we derive the spectra of the in-phase and quadrature-phase mixing products, describe a means of extracting all the jitter parameters, and assess the performance of the jitter-characterization technique with simulations. Section 6.5 is a commentary.

6.2 The Problem

The mixing-based spectral method of jitter measurement is a very popular technique. This method was developed to measure residual jitter¹, and has two additional advantages over the direct spectral technique: a lower minimum RFSA bandwidth and

¹ See Subsection 1.5.2.

physical separation of the timing from the amplitude jitter. As discussed previously², it is useful (in a diagnostic sense) to extract the uncorrelated and correlated contributions of the jitter. The mixing scheme, as it has been employed, does not extract these components. The purpose of this chapter is extend this method to distinguish between the uncorrelated and correlated contributions.

6.3 Previous Work

6.3.1 Experimental Setup

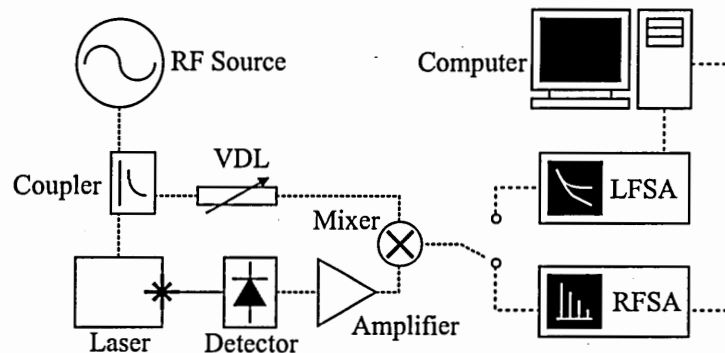


Figure 6.1: The experimental setup of the mixing-based jitter-characterization method. RF—radio-frequency. RFSA—radio-frequency spectrum analyzer. LFSA—low-frequency RFSA. VDL—variable delay line.

In the mixing technique (Fig. 6.1) [58], [60], [61], [63], [91], [113], [168], [169], [177]–[182], two experiments are required in order to determine the total timing and amplitude jitter. In the first experiment the detected pulse train is electronically mixed with (multiplied by) a local-oscillator (LO) signal that is in phase with the train. In the second, the train is mixed with a signal that is in phase quadrature. The mixing process (a) moves the spectrum to a new center frequency and (b) separates

² See Subsection 1.5.3.

the timing jitter from the amplitude jitter³. In general, the LO's repetition frequency can be any harmonic, h_{LO} , of the repetition frequency of the laser. In this document, we will assume the repetition rates of the LO and the laser are equal; $h_{LO} = 1$. In this case, the spectrum will be centered at DC.

6.3.2 Residual Jitter

The mixing-based spectral technique for jitter measurement was originally developed [58] to allow measurement of residual total timing jitter [58]–[61]. To measure residual jitter, the delays of the LO and drive signals are chosen so that *each pulse is mixed with the RF peak that produced it* (or one produced at the same time, in the case of two synchronized sources). If we assume the noises of the RF source and laser are additive, any timing noise present in the RF source's output will cancel, and the residual *timing* noise will be measured. Interestingly, any *amplitude* variations in the RF sinusoid should result in similarly signed variations in the corresponding pulses. Thus, if we assume additive noise, the amplitude jitter measured by this technique will be neither residual nor absolute, but rather some product of the noise of the source and the residual noise. We feel it must be pointed out that a laser is a highly nonlinear device, so the noises of the laser and RF synthesizer are not additive.

6.3.3 The Ideal Case: Square and Sawtooth Waves

In the ideal case, the signal mixed in phase with the detected pulse train would be square wave (Fig. 6.2a), while the signal mixed in quadrature would be a sawtooth wave (Fig. 6.2a). The mixing product (Fig. 6.2b) resulting from the in-phase mixing will be a near duplicate of the pulse train (as long as the pulse is narrow compared to the width of the positive fraction of the square wave). In the quadrature-phase case,

³ See Subsubsection 6.4.1.1.

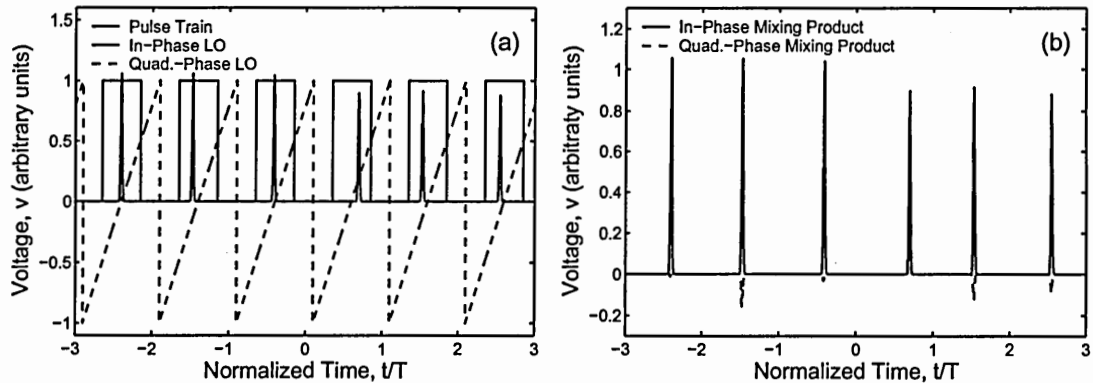


Figure 6.2: (a) A noisy pulse train with the ideal in-phase and quadrature-phase local-oscillator signals: square and sawtooth waves, respectively. (b) The resulting mixing products. LO—local oscillator. t —time. T —period.

the product signal (Fig. 6.2b) is a series of pulses whose amplitudes are proportional to the mistiming (timing jitter) of the detected train. Thus, the quadrature-phase mixing serves as a *phase detector*, while the in-phase mixing produces a signal duplicating the jitter of the laser output. Hence, if we are only concerned with the *timing* jitter, we need only record one spectrum, the quadrature-phase spectrum. We still must perform the in-phase experiment, but we need only record the mean voltage of the in-phase mixing product, which is employed as a reference by which to calibrate the mixer⁴ [183].

6.3.4 The Real Case: Sine Waves

In practice, the local-oscillator signal is usually a fraction the drive signal, in which case the LO signal is a sinusoid. Even when the LO signal is generated by a different source which is synchronized with the drive signal, it is difficult to generate square and sawtooth waves of sufficient quality at multi-GHz repetition rates required. In either case, the in-phase and quadrature-phase signals have identical shapes, with one merely being a time-shifted version of the other (Fig. 6.3a).

⁴ See Paragraph 6.4.1.2.1.

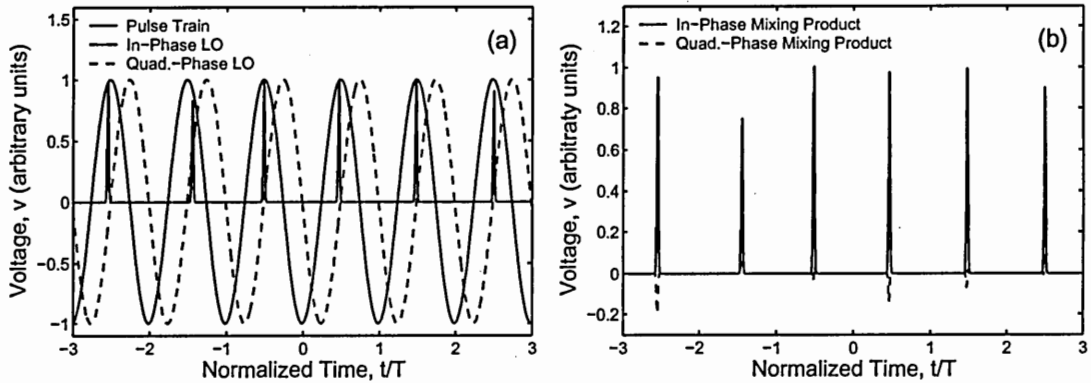


Figure 6.3: (a) A noisy pulse train with the in-phase and quadrature-phase sine waves used as local-oscillator signals in real-world experiments. (b) The resulting mixing products. LO—local oscillator. t —time. T —period.

As long as both the pulse width and timing jitter are much smaller than the repetition period, the in-phase sinusoid approximates an in-phase square pulse, and the quadrature-phase sinusoid approximates a quadrature-phase sawtooth wave. Thus, the mixing products (Fig. 6.3b) are approximations of those obtained in the ideal square-and-sawtooth case.

6.3.5 Remarks

6.3.5.1 Residual Jitter

The above analysis assumes that the noises of the RF source and laser are additive. Unfortunately, lasers are highly nonlinear devices. It is, therefore, difficult to say what, exactly this technique measures, but it certainly *does not* measure the residual timing jitter. However, this method is very commonly used to measure timing jitter [58], [60], [61], [63], [91], [113], [168], [169], [177]–[182], so it bears close investigation.

6.3.5.2 Uncorrelated and Correlated Jitter

Before the author's work, no researcher has shown how the mixing technique can be employed to extract the uncorrelated and correlated components of the jitter.

6.4 Present Contribution

6.4.1 Theory

6.4.1.1 Spectra of the Mixing Products

The goal of this subsection is the derivation of analytical expressions for the spectra of the in-phase and quadrature-phase mixing products. Before beginning the analysis, it may be helpful to provide a short preview of our approach.

In our derivation, we will proceed as follows:

- Express the mixing-product spectra in terms of the Fourier transforms of the mixing sinusoids and the noisy train.
- Argue that we can approximate the Fourier transform of the noisy train with the square root of the PSD.
- Convolve the square root of the PSD with each of the transforms of the sinusoids.
- Evaluate the squared magnitude to arrive at the spectra of the mixing products.

One final note before beginning: as in the previous chapter, we will use T as a shorthand for the repetition period of the laser, which is equal to the bit period of each OTDM channel, T_{sys} .

As a first step, let us reproduce Eq. 5.5, the equation for the voltage of the detected noisy pulse train:

$$\begin{aligned}
v_{\text{NT}}(t) &= \sum_j \{ A + \underbrace{\Delta A[j]}_{\text{amp. jitter}} \} s(t - jT - \underbrace{\Delta T[j]}_{\text{timing jitter}}); \\
\Delta J &= \underbrace{\Delta J_u}_{\text{uncorr.}} + \underbrace{\Delta J_c}_{\text{corr.}}.
\end{aligned} \tag{6.1}$$

We assume that the first harmonic is to be mixed down to baseband. In this case, the local-oscillator voltage, v_{LO} is a sinusoid with frequency ω_{rep} . In particular, the in-phase and quadrature-phase local oscillators, $v_{\text{LO,in}}$ and $v_{\text{LO,quad}}$, are given by

$$\begin{aligned}
v_{\text{LO,in}}(t) &= \cos(\omega_{\text{rep}}t); \\
v_{\text{LO,quad}}(t) &= \sin(\omega_{\text{rep}}t).
\end{aligned} \tag{6.2}$$

The voltage resulting from mixing v_{NT} with v_{LO} will be

$$v_{\text{mix}}(t) = k_{\text{mix}} v_{\text{LO}}(t) v_{\text{NT}}(t), \tag{6.3}$$

where k_{mix} is a constant scaler corresponding to the efficiency of the mixer. Further, v_{LO} represents $v_{\text{mix,in}}$ or $v_{\text{mix,quad}}$, the mixing product in the in-phase or the quadrature-phase case, respectively.

Recall that the PSD of any random process x , is Φ_x , given by [163]

$$\begin{aligned}
\Phi_x(\omega) &\equiv \mathcal{F}(\mathcal{E}(\phi_x(t, t + \tau))) \\
&= \mathcal{E}(|X(\omega)|^2).
\end{aligned} \tag{6.4}$$

Here, ϕ_x , Φ_x , and X are the autocorrelation, PSD, and Fourier transform of x , respectively. The \mathcal{F} and \mathcal{E} operators denote Fourier transformation and expectation, respectively. We want to compute the PSD of the mixing products:

$$\begin{aligned}
\Phi_{v_{\text{mix}}}(\omega) &\equiv \mathcal{F}(\mathcal{E}(\phi_{v_{\text{mix}}}(t, t + \tau))) \\
&= \mathcal{E}(|V_{\text{mix}}(\omega)|^2).
\end{aligned} \tag{6.5}$$

Here again, the capitalization of v_{mix} indicates its Fourier transform. Perhaps the most obvious approach to calculating each of the mixing products' spectra is by evaluating the transform of the autocorrelation of that product. Unfortunately, v_{mix} is difficult to calculate, so the first line of Eq. 6.5 is not appealing. The second line, however, shows promise, because it contains

$$V_{\text{mix}}(\omega) = V_{\text{LO}}(\omega) \otimes V_{\text{NT}}(\omega) , \quad (6.6)$$

and because V_{NT} is similar to $\Phi_{v_{\text{NT}}}$, the spectrum of the noisy pulse train, which we have already computed.

Thus, we would like to make the following approximation:

$$|V_{\text{LO}}(\omega) \otimes V_{\text{NT}}(\omega)|^2 \simeq \left| V_{\text{LO}}(\omega) \otimes \sqrt{\Phi_{v_{\text{NT}}}(\omega)} \right|^2 . \quad (6.7)$$

Because the noise terms are independent, when we compute $\Phi_{v_{\text{NT}}}$ from V_{NT} , (according to the second line of Eq. 6.4) all the cross terms vanish. The terms of V_{NT} can therefore be assigned, one-to-one, to the terms of $\Phi_{v_{\text{NT}}}$. The validity of Eq. 6.7 then boils down to whether the phase of V_{NT} is even. Close examination reveals that $\angle(V_{\text{NT}})$ has approximately even symmetry so long as V_{PT} , the Fourier transformation of the noise-free pulse train, dominates V_{NT} . In other words, so long as the noise is small (which we already assumed to derive the spectrum of the noisy train), Eq. 6.7 is a valid approximation.

We can now calculate the spectra of the mixing products by using Eq. 6.7. We assume the pulse is narrow with respect to the bit slot, which means that the spectral envelope due to the pulse shape is wide with respect to the repetition frequency. We also note that the comb and uncorrelated-noise spectrum are periodic with period ω_{rep} . Lastly, we simplify the result by noting that we are only interested in frequencies on the interval $[0, \omega_{\text{rep}}/2]$. Finally,

$$\begin{aligned} \Phi_{v_{\text{mix},\text{in}}}(\omega) &\simeq k_{\text{mix}} \{2\pi\}^2 \Phi_{v_{\text{NT}}}(\omega + \omega_{\text{rep}}) ; \\ \Phi_{v_{\text{mix},\text{quad}}}(\omega) &\simeq \{A\omega_{\text{rep}}\}^2 k_{\text{mix}} \frac{\{2\pi\}^2}{T} \underbrace{|S(\omega + \omega_{\text{rep}})|^2}_{\text{pulse shape}} \underbrace{\Phi_{\Delta T}(\omega + \omega_{\text{rep}})}_{\text{timing jitter}} . \end{aligned} \quad (6.8)$$

For convenience, we reproduce (and combine) Eqs 5.25 and 5.26 here:

$$\begin{aligned}
\Phi_{\text{NT}}(\omega) &\simeq \frac{1}{T} \underbrace{|S(\omega)|^2}_{\text{pulse shape}} \left\{ \underbrace{A^2 \text{III}(\omega/\omega_{\text{rep}})}_{\text{freq. comb}} + \underbrace{\Phi_{\Delta A}(\omega)}_{\text{amp. jitter}} + \underbrace{A^2 \omega^2 \Phi_{\Delta T}(\omega)}_{\text{timing jitter}} \right\}; \\
\Phi_{\Delta J}(\omega) &\equiv \underbrace{\sigma_{\Delta J_u}^2}_{\text{uncorr. jitter}} + \underbrace{\frac{1}{T} \sum_k \check{\Phi}_{\Delta J_c}(\omega - k\omega_{\text{rep}})}_{\text{corr. jitter}}; \\
\text{III}(\omega/\omega_{\text{rep}}) &\equiv \omega_{\text{rep}} \sum_k \delta(\omega - k\omega_{\text{rep}}). \tag{6.9}
\end{aligned}$$

It is important to note four important features of Eq. 6.8:

- The normalized in-phase spectrum differs only by a constant from the spectrum of the noisy train itself. This result is not surprising, given that the in-phase LO signal is nearly constant over the duration of each (narrow) pulse.
- The quadrature-phase spectrum contains only timing noise and a pulse-shape envelope; extraction of the timing jitter should be simple and accurate.
- The timing noise in the quadrature-phase spectrum is *not* scaled by a quadratic-in-frequency factor as it is in the direct method.
- The difference between the spectra of the uncorrelated and correlated contributions is unchanged from the direct case; our technique for discriminating between the two still applies.

The manner in which the various pulse-train parameters manifest in the spectrum, are illustrated by the example spectra plotted in Figs 6.4 through 6.10. Note that the first two figures (Figs. 6.4 and 6.5) appear identical, because of the lack of noise and the narrow span of the spectra.

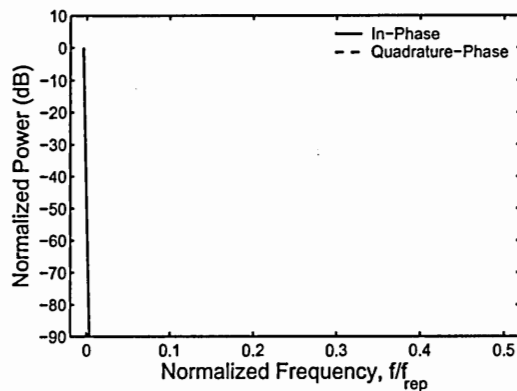


Figure 6.4: The mixing-product spectra of a train of *impulses* (infinitely narrow pulses) with *no* jitter. Only the spike of the in-phase spectrum is visible.

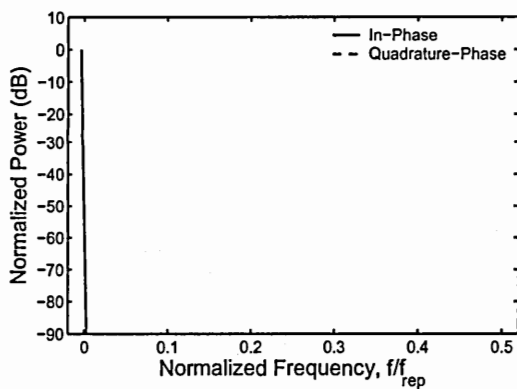


Figure 6.5: The mixing-product spectra of a train of finite-width *pulses* with no jitter. The root-mean-squared duration of the pulse is 5 % of the period. These spectra appear identical to those in the previous figure.

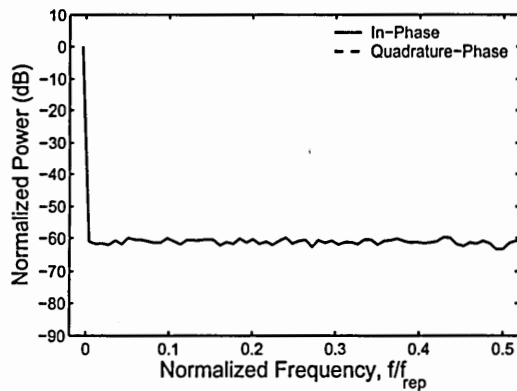


Figure 6.6: The mixing-product spectra of an impulse pulse train with only *uncorrelated amplitude* jitter equal to 1 % of the mean amplitude. The quadrature-phase spectrum is not apparent.

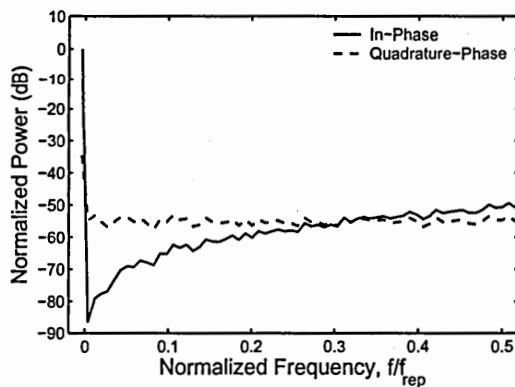


Figure 6.7: The mixing-product spectra of an impulse pulse train with only *uncorrelated timing* jitter equal to 1 % of the mean period.

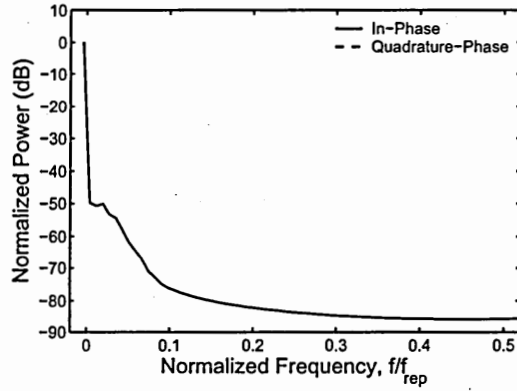


Figure 6.8: The mixing-product spectra of an impulse train with only *correlated amplitude* jitter equal to 1 % of the mean amplitude. The quadrature-phase spectrum is not apparent.

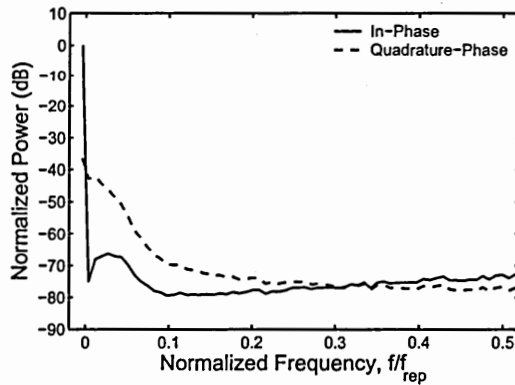


Figure 6.9: The mixing-product spectra of an impulse train with only *correlated timing* jitter equal to 1 % of the mean amplitude.

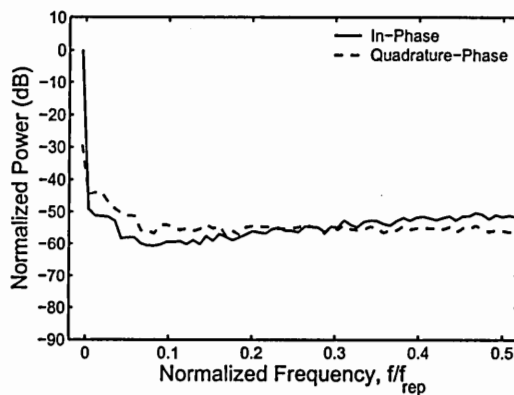


Figure 6.10: The mixing-product spectra of a *pulse* train with all four jitter contributions. Each contribution is equal to 1 % of the mean amplitude or period.

6.4.1.2 Measurement Procedure

Now that we have the expressions for the spectra of the mixing products, we follow a procedure very much like that employed in the direct case⁵ to extract all the jitter components.

6.4.1.2.1 Normalization The recorded spectra are only $f_{\text{rep}}/2$ wide, so (a) we do not have multiple harmonic peaks with which to normalize the spectrum to its envelope, but (b) this is not a problem, because the spectrum is likely narrow compared to the envelope. Consequently, for this analysis, we assume the envelope is nearly flat in the region of interest ($S(\omega) \simeq S(0)$). We do, however, need to normalize both spectra to the *power* in the 0-frequency peak of the in-phase spectrum.

If we are not interested in the amplitude noise, we can perform the normalization without recording the in-phase spectrum. We must still perform the in-phase experiment, but we need only measure the mean of $v_{\text{mix,in}}$. Recall that the mean of any function, f is equal to the DC value of the Fourier transform, F :

$$F(0) = \langle f(t) \rangle , \quad (6.10)$$

where the angle brackets denote the ensemble average. From Eq. 6.4, we know there is a magnitude-squared relationship between the the spectrum and the transform:

$$\Phi_f(\omega) = \mathcal{E} (|F(\omega)|^2) . \quad (6.11)$$

So, for any function, the power spectral density at DC is related to the mean of the function by

$$\Phi_f(0) = \mathcal{E} (|\langle f(t) \rangle|^2) . \quad (6.12)$$

In our case, $f = v_{\text{min,in}}$, and the mean will be due to the deterministic part of the signal (the noise-free pulse train), so the expectation operation may be dropped. The *power*

⁵ See Subsubsection 5.4.1.2.

in the DC peak, $P_{pk}[0]$ will be given by the product of the PSD and the resolution bandwidth, Δf_{res} , used to record the quadrature-phase spectrum:

$$P_{pk}[0] = \Delta f_{res} |\langle v_{mix,in}(t) \rangle|^2, \quad (6.13)$$

and we can normalize the quadrature-phase spectrum without recording the in-phase spectrum.

Performing either type of normalization eliminates the mixer's conversion efficiency and any other losses [183]. The normalized spectra (Fig. 6.11) are denoted with a hat and are given by

$$\begin{aligned} \hat{\Phi}_{v_{mix,in}}(\omega) &\simeq \hat{\Phi}_{v_{NT}}(\omega + \omega_{rep}); \\ \hat{\Phi}_{v_{mix,quad}}(\omega) &\simeq \omega_{rep} \Phi_{\Delta T}(\omega). \end{aligned} \quad (6.14)$$

Recall, for comparison, Eq. 5.27 for the normalized spectrum in the direct case:

$$\hat{\Phi}_{NT}(\omega) \simeq \frac{1}{\omega_{rep} A^2} \left\{ A^2 \text{III}(\omega/\omega_{rep}) + \Phi_{\Delta A}(\omega) + A^2 \omega^2 \Phi_{\Delta T}(\omega) \right\}. \quad (6.15)$$

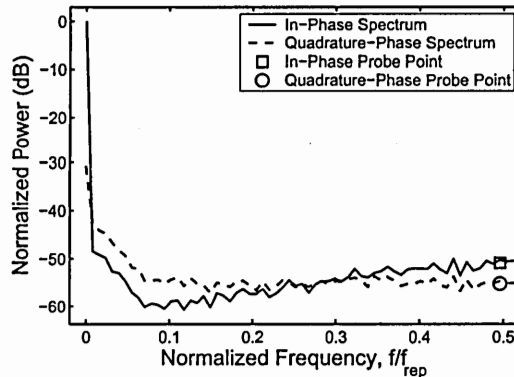


Figure 6.11: Illustration of the measurement procedure. Both spectra are normalized to the peak of the in-phase spectrum. The noisebands are integrated to compute the total jitter, and the probe points are used to extract the uncorrelated jitter.

6.4.1.2.2 Total Jitter The total timing jitter is obtained from the integrated noise-band power of the normalized quadrature-phase spectrum, $P_{mix,quad}$. Once we

know $\sigma_{\Delta T}$, we extract $\sigma_{\Delta A}$ from the normalized noise power of the in-phase spectrum, $\Phi_{\text{mix,in}}$. Approximating ω^2 as its mean on the $(0, \omega_{\text{rep}}/2]$ interval, $\omega_{\text{rep}}^2/12$, yields

$$\begin{aligned}\hat{\sigma}_{\Delta T} &= \frac{1}{2\pi} \sqrt{\hat{P}_{\text{mix,quad}}} ; \\ \hat{\sigma}_{\Delta A} &= \sqrt{\hat{P}_{\text{mix,in}} - \frac{(\omega_{\text{rep}}\sigma_{\Delta T})^2}{12}} .\end{aligned}\quad (6.16)$$

6.4.1.2.3 Uncorrelated Jitter Similarly, the uncorrelated timing-noise contribution is extracted by measuring the PSD of the quadrature-phase mixing product at probe frequency ω_p , far from DC (Fig. 6.11). The uncorrelated amplitude noise can then be determined from the in-phase spectrum.

$$\begin{aligned}\hat{\sigma}_{\Delta T_u} &= \sqrt{\frac{\hat{\Phi}_{v_{\text{mix,quad}}}(\omega_p)}{2\pi T}} ; \\ \hat{\sigma}_{\Delta A_u} &= \sqrt{\omega_{\text{rep}} \hat{\Phi}_{v_{\text{mix,in}}}(\omega_p) - \omega_p^2 \sigma_{\Delta T_u}^2} .\end{aligned}\quad (6.17)$$

6.4.1.2.4 Correlated Jitter We compute the correlated contribution as in the direct case, from

$$\sigma_{\Delta J_c} = \sqrt{\sigma_{\Delta J}^2 + \sigma_{\Delta J_u}^2} .\quad (6.18)$$

6.4.1.2.5 Correlation Time The correlation times are computed much as in the direct case. Let ϖ_{in} and ϖ_{quad} be the RMS spectral widths of the in-phase and quadrature-phase spectra, respectively. Since the quadrature-phase spectrum contains only timing jitter, it is easy to compute the correlation bandwidth of the correlated timing noise from the RMS width of the quadrature-phase spectrum, ϖ_{quad} :

$$\varpi_T \simeq \varpi_{\text{quad}} .\quad (6.19)$$

To compute the amplitude-jitter correlation bandwidth, we substitute the ϖ_T that we just computed as well as $h = 1$ and $\varpi[h] = \varpi_{\text{in}}$ into Eq. 5.36. The result is

$$\varpi_A \simeq \omega_{\text{rep}}^2 \{ \varpi_{\text{in}} - \varpi_T \} .\quad (6.20)$$

Lastly, we use Eq. 5.37 to compute both correlation times:

$$\sigma_{c_j} = \frac{1}{\varpi_J} . \quad (6.21)$$

6.4.1.2.6 Measurement Routine We have implemented a routine, in MATLAB, to carry out all these manipulations on a (simulated or experimental) spectrum. Our measurement routine, which represents a significant fraction of the work described in this chapter, is validated in Subsection 6.4.2.

6.4.1.3 Resolution

We can estimate the resolution of the mixing method by the same process we employed for the direct method⁶. Given the similarity between the equations for extraction of the jitter parameters in the direct and mixing cases⁷, it is to be expected that the mixing-method resolutions will be of the same order as those of the direct-method case. We will therefore not bore the reader with the derivations, but only present the results.

6.4.1.3.1 Total Jitter The resolutions of the normalized total timing and amplitude jitter are equal to each other and to those obtained in the direct case:

$$\partial\sigma_J \sim 1 + \partial P' - \frac{1}{\partial P'} . \quad (6.22)$$

6.4.1.3.2 Uncorrelated Jitter Likewise, the resolutions of the normalized uncorrelated timing and amplitude jitter equal each other and those found in the direct case:

$$\partial\sigma_{J_u} \sim 1 + \partial P' - \frac{1}{\partial P'} . \quad (6.23)$$

⁶ See Subsubsection 5.4.1.3

⁷ See Subsections 5.4.1.2 and 6.4.1.2, respectively.

6.4.1.3.3 Correlated Jitter The resolutions of the normalized correlated timing and amplitude jitter are also unchanged in the mixing case:

$$\partial\sigma_{\Delta J_e} \sim 1 + \partial\sigma'_{\Delta J} - \frac{1}{\partial\sigma'_{\Delta J}}. \quad (6.24)$$

6.4.1.4 Minimum Measurable Jitter

The minimum jitter measurable with the mixing method can be estimated the same way the minimum jitter measurable with the direct method was⁸. Consequently, we will present only the results of our analysis, not the analysis itself.

6.4.1.4.1 Total Jitter The minimum measurable normalized total amplitude jitter is given by

$$\hat{\sigma}_{\Delta A, \min} \sim \sqrt{\frac{N_{\text{pt}} - 1}{\Delta \overline{P}_{\text{DR}}}}. \quad (6.25)$$

Meanwhile, the minimum measurable normalized total timing jitter is

$$\hat{\sigma}_{\Delta T, \min} \sim \frac{1}{2\pi} \sqrt{\frac{N_{\text{pt}} - 1}{\Delta \overline{P}_{\text{DR}}}}. \quad (6.26)$$

6.4.1.4.2 Uncorrelated Jitter The minimum uncorrelated amplitude jitter is

$$\hat{\sigma}_{\Delta A_u, \min} \sim \sqrt{2\pi} \sqrt{\frac{N_{\text{pt}} - 1}{\Delta \overline{P}_{\text{DR}}}}. \quad (6.27)$$

Similarly, the minimum measurable normalized uncorrelated jitter is given by

$$\hat{\sigma}_{\Delta T_u, \min} \sim \frac{1}{\sqrt{2\pi}} \sqrt{\frac{N_{\text{pt}} - 1}{\Delta \overline{P}_{\text{DR}}}}. \quad (6.28)$$

6.4.1.4.3 Correlated Jitter Just as in the direct spectral measurement, the correlated contribution is computed from the RMS difference between the total and uncorrelated noise. Thus, the minimum measurable normalized amplitude and timing jitter are both 0.

⁸ See Subsubsection 5.4.1.4.

6.4.2 Simulation

We have written a MATLAB routine to (a) simulate the mixing of a noisy pulse train with in-phase and quadrature-phase sinusoids and (b) compute the spectra of the mixing products. This routine comprises a large portion of the work described in this chapter. As the noisy train is generated by the same routine described for the direct-spectral case, the program offers independent control of all the same parameters. In these simulations, the total jitter and the pulse width vary as follows:

- $\hat{\sigma}_T$ from 0 to 0.1 in 14 steps (as in the direct case).
- $\hat{\sigma}_A$ from 0 to 0.1 in 14 steps (as in the direct case)..
- $\hat{\sigma}_s$ from 0 to 0.1 in 5 steps (two fewer than the direct case)..

Consequently, 980 amplitude-jitter/timing-jitter/pulse-width combinations are represented.

In these simulations, the mixing-product spectra are computed by averaging the spectra of 32 mixing-product signals. Each mixing product is the result of multiplying a noisy train consisting of 128 pulses by a sinusoid (in-phase or quadrature-phase) containing 128 periods. As in the direct case, each mixing-product spectrum is computed by evaluating the squared magnitude of the Fourier transform of the signal. The probe-frequency offset is chosen to be $f_{\text{rep}}/2$, and, once again, nine spectral values are used to smooth the probe points.

6.4.2.1 Amplitude Jitter

Given the similarity of the in-phase spectrum to the direct spectrum⁹ and given the similarity of the measurement procedures for the mixing method to that of the direct method¹⁰, we might expect the mixing technique to exhibit amplitude-jitter-

⁹ See the first line of Eq. 6.8 and Eq. 5.25, respectively.

¹⁰ See Subsubsections 6.4.1.2 and 6.4.1.2, respectively.

extraction errors similar to those observed in the direct case. We would not be disappointed. Indeed, the error-surface plots (and the corresponding contour plots) obtained with the mixing technique for total, uncorrelated, and correlated amplitude jitter for each of the five simulated pulse widths bear a very strong resemblance to the corresponding plots obtained with the direct method. The error surfaces and contour plots corresponding to an RMS temporal width of 0.05 are shown in Figs. 6.12 and 6.13, while those for all values of $\hat{\sigma}_s$ are included in Section D.1.

Because of the similarity, the positive aspects of the direct amplitude-jitter extraction are maintained here. Still, even in the worst case, the magnitude of the error is less than 30 % as long as

$$\hat{\sigma}_A \gtrsim 1.5\hat{\sigma}_T . \quad (6.29)$$

In other words, very roughly speaking, the error is low so long as

$$\hat{\sigma}_A \gtrsim \hat{\sigma}_T , \quad (6.30)$$

just as in the direct case. This fact is most evident in the contour plots. Once again, the correlated-jitter extraction, because of the indirect method of computation, is the least accurate of the three amplitude-jitter extractions. Unfortunately, the negative aspects of the direct method are present as well: for combinations where the normalized timing jitter is much larger than the normalized amplitude jitter, the routine reports an amplitude jitter that depends more on the timing noise than on the amplitude noise. Consequently, extreme overestimation occurs when $\sigma_A/A \ll \sigma_T/T$ (the far corner of the surface plots).

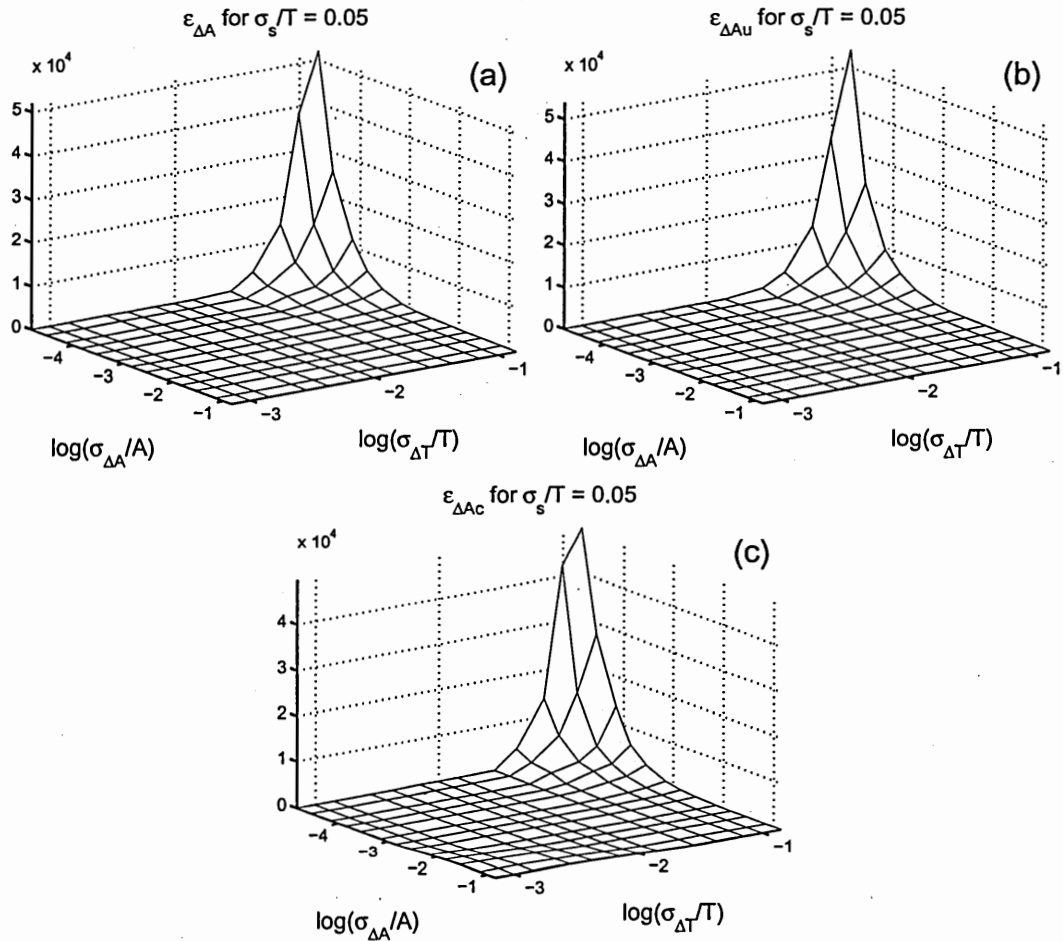


Figure 6.12: Extraction errors for (a) total amplitude jitter, $\epsilon_{\Delta A}$, (b) uncorrelated amplitude jitter, $\epsilon_{\Delta Au}$, and (c) correlated amplitude jitter, $\epsilon_{\Delta Ac}$, obtained with the uncompensated mixing method. σ_A/A —normalized total amplitude jitter. σ_T/T —normalized total timing jitter. σ_s/T —normalized root-mean-squared pulse width.

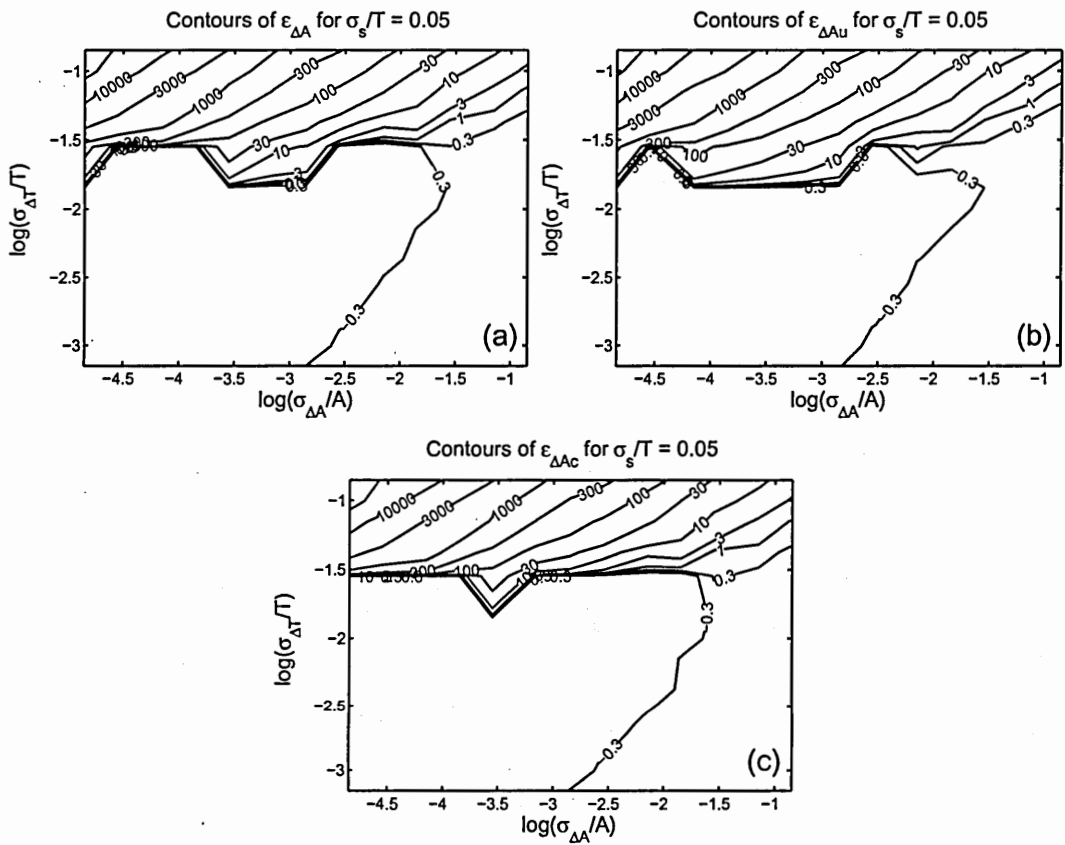


Figure 6.13: The contours of the plots shown in 6.12

6.4.2.2 Timing Jitter

Given that the quadrature-phase spectrum contains only timing noise, we expect that the mixing method will extract the timing jitter with greater accuracy than the direct technique. The timing-extraction-error surface plots obtained for an RMS temporal width of 5 % of the period are shown in 6.14, and those obtained for all widths are presented in Section D.2. (We do not show the contour plots as they are not very illustrative.) Note that the orientation of the axes is different not only from that of the amplitude-error surface plots, but also from that of the timing-error surface plots presented in the direct-measurement chapter; the axes have been arranged to best present the dependence of the error on the true amplitude and timing noise. The plotted surfaces validate our expectations.

The surface plots are somewhat rough, with departures from the local mean of up to about 15 %. Fortunately, as in the direct method, the local mean is approximately independent of the amplitude jitter. However, for most of the 15 surfaces, $|\epsilon| < 0.3$ for the entire simulated domain. For $\hat{\sigma}_s$ of 0.05 and 0.10, on the other hand, there is underestimation of the total and uncorrelated timing jitter for combinations of large amplitude jitter and small timing jitter (the right corners of the surface plots). These dips come about because the quadrature-phase mixing does not completely isolate the timing noise, as our analysis suggests. Some amount of amplitude noise “leaks” into the quadrature-phase trace, leading to overestimation in the extraction of the total and uncorrelated timing jitter. This process is negligible in the narrow-pulse cases, but when the normalized RMS pulse width is larger than about 5 %, overestimation occurs. Because the overestimation of the uncorrelated jitter is greater than the overestimation of the total jitter, *underestimation* of the correlated timing jitter results. Ignoring this corner of the surfaces obtained with normalized RMS pulse widths of 5 % and 10 %, all three timing jitters are extracted with error less than 30 % for all pulse widths and for all simulated jitter combinations.

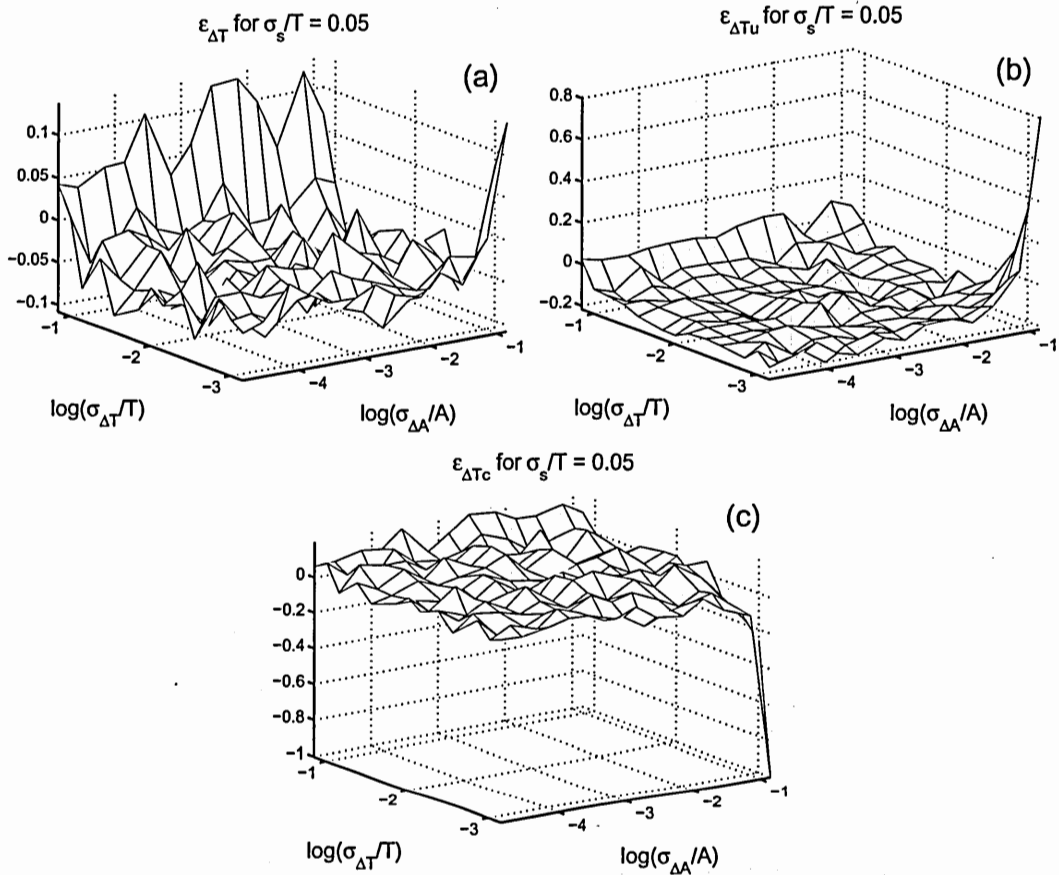


Figure 6.14: Extraction errors for (a) total timing jitter, $\epsilon_{\Delta T}$, (b) uncorrelated timing jitter, $\epsilon_{\Delta T_u}$, and (c) correlated timing jitter, $\epsilon_{\Delta T_c}$, obtained with the uncompensated mixing method. σ_A/A —normalized total amplitude jitter. σ_T/T —normalized total timing jitter. σ_s/T —normalized root-mean-squared pulse width.

6.4.2.3 Correlation Time

The correlation-time-extraction surface plots corresponding to $\hat{\sigma}_s = 0.05$ are shown in Fig. 6.15; the remainder are presented in Section D.3. The correlation-time error surfaces the correlated timing jitter are very flat. For the correlated amplitude jitter, however, the correlation-time error surfaces are far from smooth. Once again, we should point out that the correlation time was fixed at $5T$ during these simulations, so the correlation-time extraction was not fully tested.

As we proposed in the direct case, the problem with the correlation-time extraction may be due to insufficient spectral resolution in the measurement.

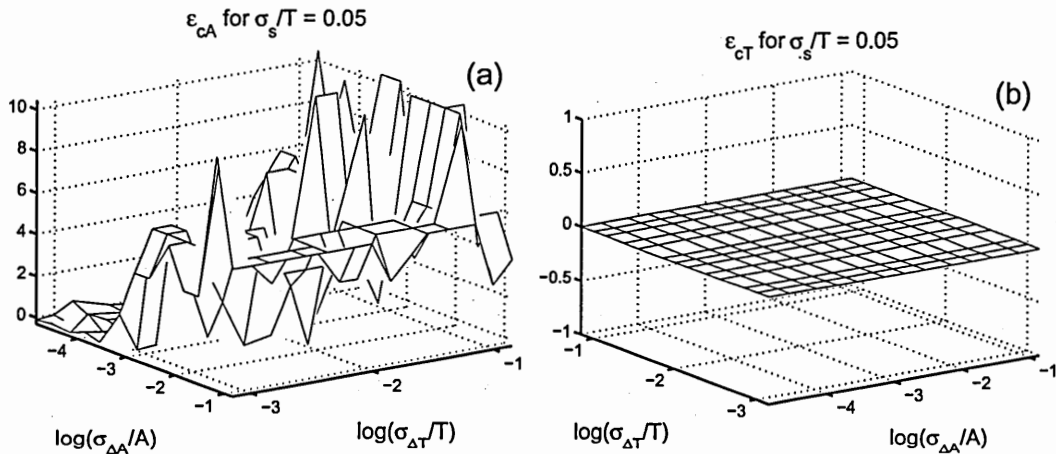


Figure 6.15: Extraction errors for the correlation times of the (a) correlated amplitude jitter, $\epsilon_{\Delta A_c}$ and (b) timing jitter, $\epsilon_{\Delta T_c}$, obtained with the uncompensated mixing method. σ_A/A —normalized total amplitude jitter. σ_T/T —normalized total timing jitter. σ_s/T —normalized root-mean-squared pulse width.

6.4.3 Error Compensation

The simulations presented above reveal that the mixing method exhibits *systematic* errors, as the direct case. We can therefore employ the same error-compensation routine applied in the direct case¹¹. Note that the difference in shape between the uncompensated timing-jitter-error surfaces obtained with the direct technique and those obtained with the mixing-based method does not affect the compensation routine.

6.4.3.1 Amplitude Jitter

Because of the similarity between the in-phase and direct spectra (Eq. 5.25 and the first line of Eq. 6.8), and between the amplitude-jitter-error plots of the uncompensated mixing and direct methods, we expect the amplitude-jitter-error surfaces and their contours obtained with the compensated mixing method to be similar to those obtained with the compensated direct method. The surface and contour plots associated with an RMS width of 0.05 are shown in Figs. 5.24 to 5.25, while those associated with all widths are shown in an appendix (Section C.1). As these plots indicate, the expected similarity is indeed observed. Just as in the direct case, the compensated amplitude-jitter-error plots have the same general shape as the uncompensated plots. However, for each pulse width, the compensated method has a lower maximum error (most apparent in the surface plots), and a larger region of error less than 30 % (most evident in contour plots). The enlarged domain of low error is described by the following inequality.

$$\hat{\sigma}_A^{1.3} \gtrsim 1.5\hat{\sigma}_T . \quad (6.31)$$

As before, the correlated-amplitude-jitter extraction is the least accurate.

¹¹ See Subsection 5.4.3.

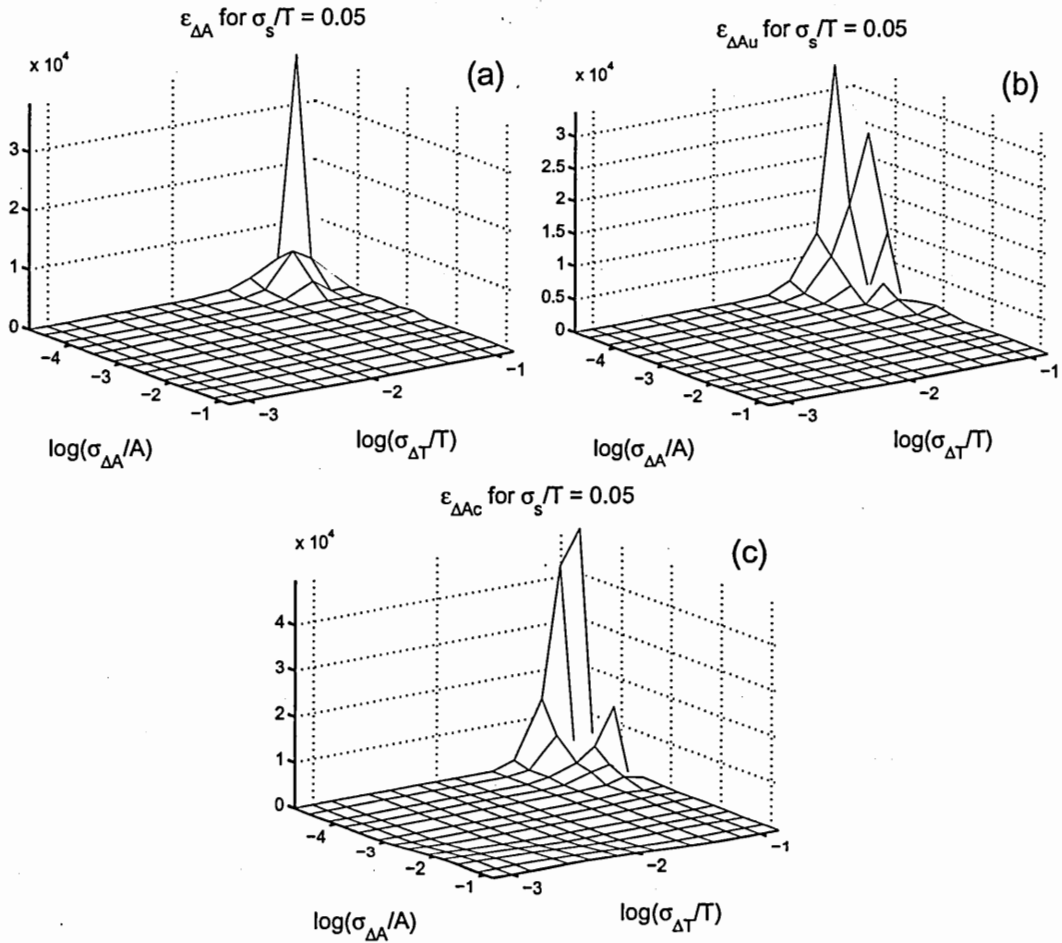


Figure 6.16: Extraction errors for (a) total amplitude jitter, $\epsilon_{\Delta A}$, (b) uncorrelated amplitude jitter, $\epsilon_{\Delta Au}$, and (c) correlated amplitude jitter, $\epsilon_{\Delta Ac}$, obtained with the compensated mixing method. σ_A/A —normalized total amplitude jitter. σ_T/T —normalized total timing jitter. σ_s/T —normalized root-mean-squared pulse width.

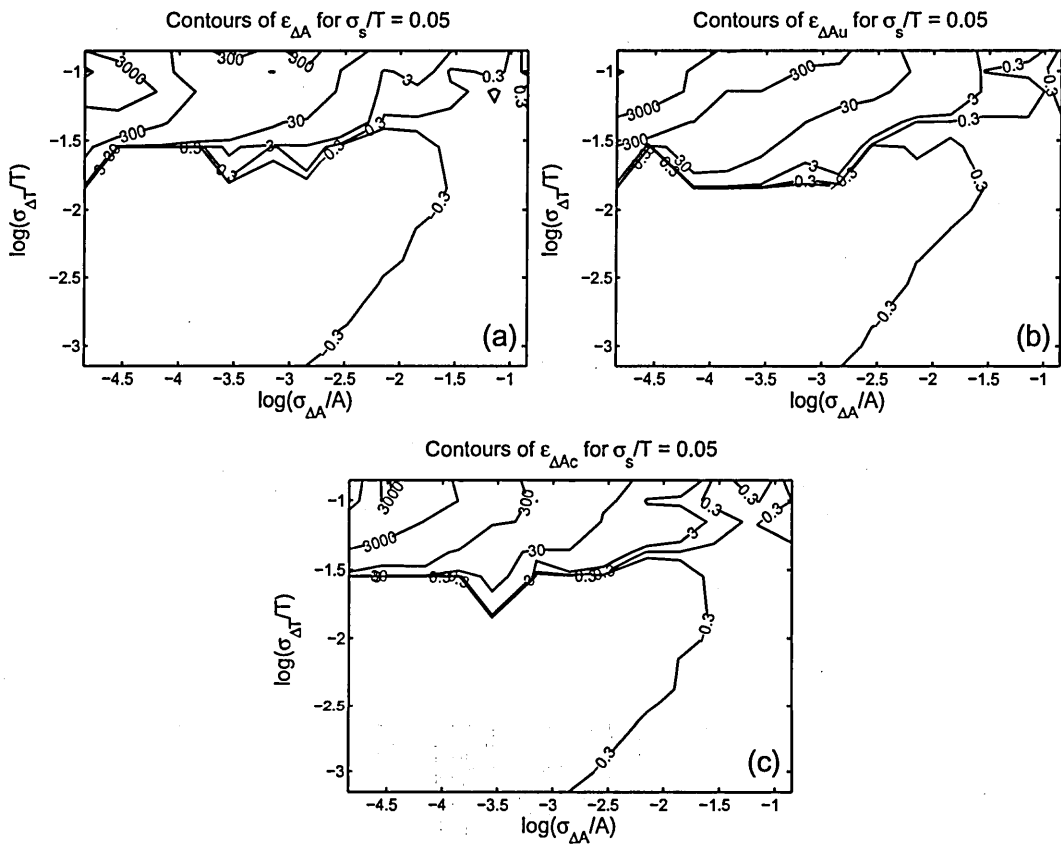


Figure 6.17: The contours of the plots shown in 6.16

6.4.3.2 Timing Jitter

The timing-jitter-error surfaces obtained, with compensation, for the case of $\hat{\sigma}_s = 0.05$ are shown in Fig. 6.18. Those obtained for all simulated pulse widths are relegated, for compactness, to an appendix (Section E.2).

Since the timing-jitter errors associated with the compensated mixing method are so small, the compensation has little effect on the timing-jitter-error surfaces; it merely flattens them somewhat. However, since the magnitude of the error was less than 0.30 for nearly all jitter combinations for each pulse width *before compensation*, it is no surprise that the error is still below our threshold *after* compensation. The exceptional points correspond to combinations of high amplitude jitter, low timing noise, and RMS pulse widths of 5 % and 10 %, as we described before.

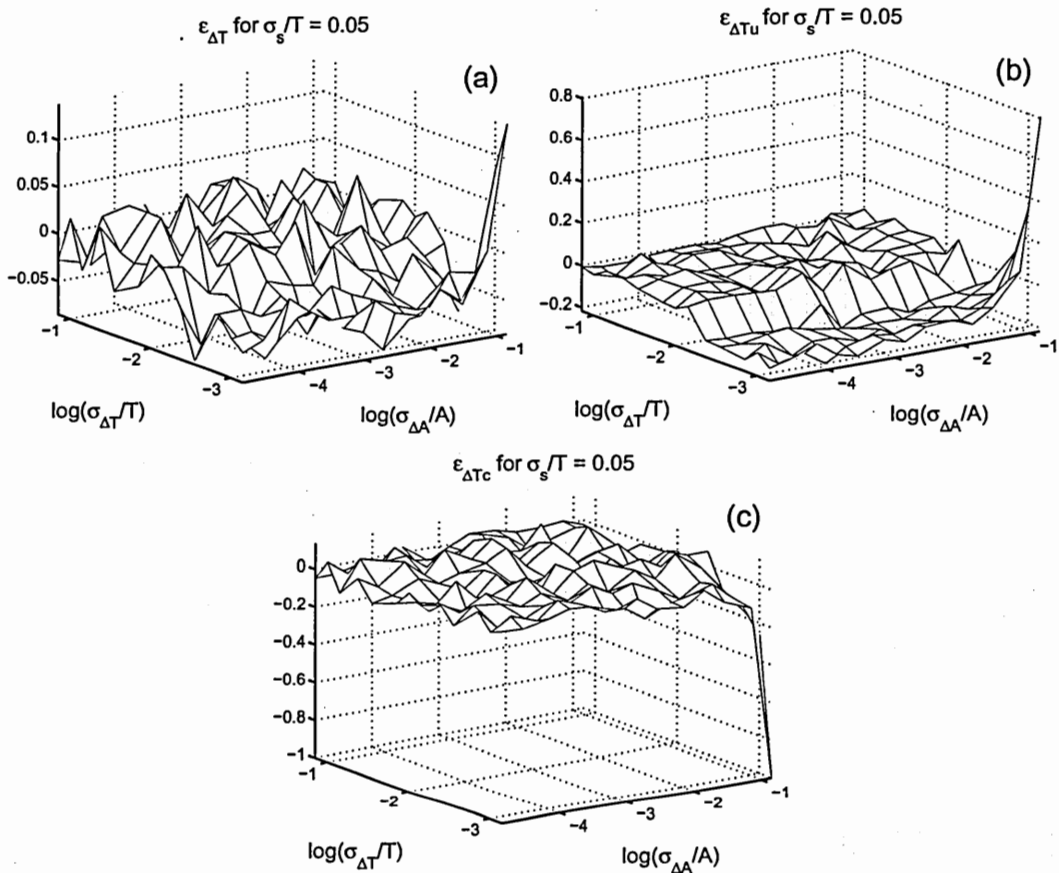


Figure 6.18: Extraction errors for (a) total timing jitter, $\epsilon_{\Delta T}$, (b) uncorrelated timing jitter, $\epsilon_{\Delta T_u}$, and (c) correlated timing jitter, $\epsilon_{\Delta T_c}$, obtained with the compensated mixing method. σ_A/A —normalized total amplitude jitter. σ_T/T —normalized total timing jitter. σ_s/T —normalized root-mean-squared pulse width.

6.4.3.3 Correlation Time

Because the error in the extraction of the uncompensated correlation is so small, we make no attempt to compensate for these errors. Thus, the compensated extraction-error surfaces are identical to the uncompensated case and are omitted from this document.

6.4.3.4 Experiment

Although we have performed no experiments with the mixing-based technique, a few comments concerning experimental are warranted. First, as in the direct case, the noise floor of the measurement must be carefully considered, especially if the jitter of a very low-noise laser is the characterized. Second, the resolution and minimum-measurable jitter of this technique are more difficult to determine. In the mixing technique, the spectrum of the pulse train under scrutiny is downshifted to baseband. A typical RF spectrum analyzer have finite low-frequency cut-off. Consequently, a special, low-frequency spectrum analyzer (LFSA) must be employed to record the lowest-frequency portions of each spectrum. The high-frequency cut-off of the LFSA will be lower than $f_{\text{rep}}/2$. So, both instruments must be employed and the resulting spectra must be spliced together. (Note that great care must be taken, during the experiments, to ensure that the LFSA and RFSA spectra line up at the overlap [183].)

6.5 Commentary

6.5.1 Absolute and Residual Jitter

The mixing-based total-jitter measurement was introduced to enable the measurement of total residual timing jitter. (This method does not claim to measure the residual

amplitude jitter.) Unfortunately, since lasers are inherently nonlinear, the method does not, in fact, extract the residual timing jitter. However, this method is commonly used and is therefore of considerable interest.

6.5.2 Advantages of the Mixing Technique

It should be pointed out that the mixing scheme has two advantages and (unrelated to residual jitter) over the direct method.

6.5.2.1 Just One Harmonic

The phase-detection behavior of the mixing method (the physical separation of the timing noise into the quadrature-phase mixing product) means that only one harmonic need be recorded. Indeed, if only the timing jitter is of interest, we need only record the quadrature-phase spectrum (and the mean voltage of the in-phase product). Thus, timing-jitter measurements are considerably simplified.

6.5.2.2 Lower-Bandwidth Spectrum Analyzer

Because only one spectrum need be recorded, and because the mixing technique downshifts the center frequency of the pulse train's spectrum, it allows us to measure the jitter of a high-rate pulse-source without resorting to an extremely broadband (and expensive) RF spectrum analyzer. The direct technique requires the RFSA to have a bandwidth of *at least* $2f_{\text{rep}}$. For modern, multi-GHz lasers, this requirement is quite stringent. The mixing method, by contrast, requires an RFSA bandwidth of just $0.5f_{\text{rep}}$. This requirement is four times easier to meet.

6.5.3 Disadvantages of the Mixing Technique

The disadvantages of the of the mixing technique are directly related to the advantages, and are, therefore, also twofold.

6.5.3.1 Exactly One Harmonic

In the direct spectral technique, *multiple* harmonics can be employed to increase the accuracy of the measurement¹². In the mixing-based spectral technique, one, and only one, harmonic is employed, so this means of accuracy enhancement is unavailable.

6.5.3.2 Additional, Low-Frequency Spectrum Analyzer

In the mixing method, as mentioned in Subsubsection 6.4.3.4, a special low-frequency spectrum analyzer (LFSA) must be employed to record the lower-frequency portion of the mixing-product spectra while an RFSA must be employed to record the higher-frequency portion. This additional complexity and expense is a significant drawback of the mixing-based method.

6.5.4 Uncorrelated and Correlated Jitter

We have derived a method of extracting all six jitter parameters of a pulse train RF spectrum of the in-phase and quadrature-phase mixing products. Simulations indicate that this technique exhibits systematic errors, similar to those observed in the direct version, and that these errors can be compensated. With this compensation, the scheme can extract timing jitters with error less than 30 % for almost all simulated combinations of pulse duration, amplitude noise, and timing noise. Similarly, the measurement routine can extract amplitude jitters with error less than 30 % as long

¹² See Subsubsection 5.4.1.2.

as the normalized RMS timing jitter is approximately less than the normalized RMS amplitude jitter.

6.5.5 Super-Mode Jitter

The remarks concerning the extraction of super-mode jitter by the direct spectral method¹³ apply to the mixing-based technique. The mixing technique would count any super-mode noise as correlated noise.

6.5.6 Resolution and Minimum Measurable Jitter

The resolution and minimum measurable jitter of the mixing-base method are on par with those of the direct method.

6.5.7 Application to Data Streams

The argument we made concerning the the direct spectral jitter characterization¹⁴ applies equally to the mixing method. The mixing-based jitter characterization can only be applied to pulse trains, not to data streams.

¹³ See Subsection 5.5.2.

¹⁴ See Subsection 5.5.4.

CHAPTER 7

Conclusions

In Chapter 7, we *briefly* summarize and comment of the work we have presented.

7.1 Introduction

7.1.1 Motivation

Sources of high-quality optical-pulse trains are needed for a number of applications, optical communications in particular.

7.1.2 Optical Communications

Optical time-division multiplexing offers greater spectral efficiency as well as simpler construction and operation, when compared with wavelength-division multiplexing. An OTDM pulse source must meet several strict performance criteria; in particular the source must have very low timing and amplitude jitter and very low pedestals.

7.1.3 Jitter Tutorial

Timing and amplitude jitter can each be divided into determinist and random (stochastic) types. Each of these types, in turn, can be divided into one of two orthogonal

sets: (a) absolute and residual or (b) uncorrelated (memoryless or white), correlated (drift or red) and super-mode. The uncorrelated, correlated and super-mode contributions originate from distinct mechanisms in the components of the laser source and in any fiber downstream. It is important to discriminate between all these noise components, when measuring jitter, in order to reduce them.

7.2 Picosecond-Pulse Source

We have demonstrated that a gain-switched distributed-feedback laser diode, when cascaded with pulse-compression and pedestal-suppression stages, can meet most of the performance requirements placed on an OTDM pulse source. Unfortunately, the pulse width and especially the noise of the GS DFB LD create problems which cannot be easily corrected.

7.3 Pulse-Train Gain-Switching

We have shown that gain-switching by an electrical pulse train can reduce the pulse width as well as the timing jitter and amplitude jitter of the resultant optical pulse train, compared to gain-switching by an equal-power sine wave. However, when the sine wave has power equal to that used to drive the electronic pulse generator employed in the pulse-drive case, the advantages vanish.

7.4 Temporal-Multiplexing Amplitude Jitter

Temporal multiplexing converts any finite pedestal of the pulse train (which often remains after pulse compression) into slow, correlated amplitude jitter, as quantified by our analysis. This phenomenon is responsible for the strict requirement placed on

the pedestal level of an OTDM source. Fortunately, we have demonstrated that even a substantial pedestal can be reduced to an almost arbitrarily low level by employing a nonlinear amplifying loop mirror as an intensity filter.

7.5 Direct Jitter Characterization

The direct spectral technique of jitter measurement measures the absolute timing and amplitude jitter of the pulse train under examination from two or more harmonics of the train's RF spectrum. (We have shown that employing more than two harmonics increases the accuracy of the measurement.) We have extended this method to extract the the uncorrelated and correlated contributions of the absolute timing and amplitude noise.

Our simulations indicate that the extended technique exhibits systematic errors, which can be substantially compensated. The compensated method can extract the timing-noise components with high accuracy for nearly all simulated combinations of timing and amplitude jitter. (Only combinations with total timing jitter greater than a few percent of the period yield small error.) The amplitude-noise contributions can be extracted over a smaller, but still significant domain. Our experiments, performed with gain-switched and mode-locked lasers, verify that this technique agrees not only with the oscilloscope method, but also with our expectations.

7.6 Mixing-Based Jitter Characterization

The mixing-based spectral technique was developed as a means of measuring the residual timing jitter of laser driven by an RF signal by mixing the detected train with sinusoids that are in phase and in quadrature phase with respect to the pulse train. Unfortunately, lasers are highly nonlinear devices, so this method does not, in

fact, measure residual jitter. As in the direct case, we have extended this scheme to extract the uncorrelated and correlated contributions of the noise. Our simulations indicate that this jitter-characterization scheme exhibits systematic errors very much like those of the direct method, and these errors can also be compensated. The timing-jitter accuracy of the compensated is slightly greater than the direct method's, while the amplitude-noise accuracy is nearly the same. Depending on one's application (the pulse train being under investigation) and on one's equipment (a LFSA or a high-bandwidth RFSA), either the direct or mixing-based method may be the more applicable.

7.7 Commentary

Much work remains, and will always remain, in the understanding, control, and measurement of jitter in telecommunications. Lasers with extremely low noise have been constructed, but, as data rates climb ever higher, ever quieter lasers are required. We can characterize very small jitters with very fine resolution, but, as laser noise slips ever lower, ever more precise jitter-characterization techniques are needed. Like Alice and the Red Queen in *Through the Looking-Glass*, who must constantly run to stay in one place; like predator and prey, who must constantly evolve keener senses, greater speed, or sharper minds to keep pace with each other [184]; optical engineers must constantly improve their designs to remain competitive not only with each other, but also with themselves.

APPENDIX A

Root-Mean-Squared and Peak-to-Peak Jitter

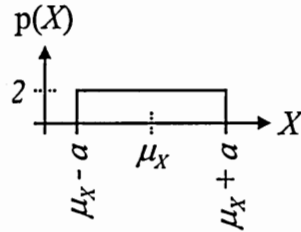


Figure A.1: A random variable, X , with a uniform probability distribution function, p_X . μ_X —the mean of X . a —a constant.

Consider a random variable, X , with a probability density function, p_X , that is uniform from $\mu_X - a$ to $\mu_X + a$, where μ_X is the mean of X [163], [164]. From Fig. A.1, it is clear that the peak-to-peak deviation of X , ΔX_{PP} , is $2a$. The variance, σ_X^2 is given by the expected value of the square of the deviation:

$$\begin{aligned}\sigma_X^2 &\equiv \mathcal{E} \{ (X - \mu_X)^2 \} \\ &\equiv \int_{-\infty}^{\infty} (X - \mu_X)^2 dX \\ &= \frac{a^2}{3}.\end{aligned}\tag{A.1}$$

The standard deviation is the square root of the variance. Thus, the ratio of the standard deviation to the peak-to-peak deviation is the reciprocal of the square root of 12:

$$\frac{\sigma_X}{\Delta X_{pp}} = \frac{1}{2\sqrt{3}}.\tag{A.2}$$

APPENDIX B

Simulation Results: Uncompensated Direct Method

B.1 Amplitude Jitter

On the next few pages, the extraction-error surfaces, obtained with the uncompensated direct method, for total, uncorrelated, and correlated amplitude jitter are plotted against the normalized total amplitude jitter and the normalized total timing jitter, for each of seven normalized RMS pulse widths. The contours of these surfaces are also included.

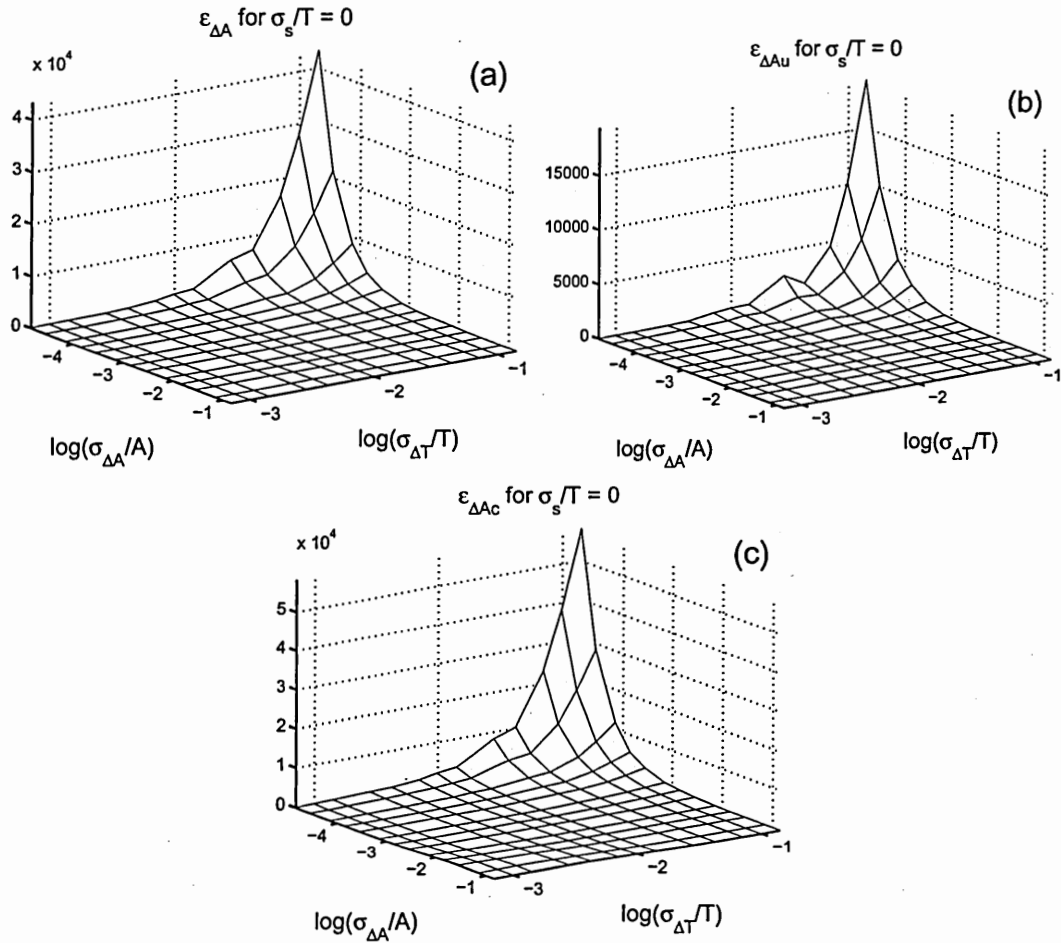


Figure B.1: Extraction errors for (a) total amplitude jitter, $\epsilon_{\Delta A}$, (b) uncorrelated amplitude jitter, $\epsilon_{\Delta A_u}$, and (c) correlated amplitude jitter, $\epsilon_{\Delta A_c}$, obtained with the uncompensated direct method. σ_A/A —normalized total amplitude jitter. σ_T/T —normalized total timing jitter. σ_s/T —normalized root-mean-squared pulse width.

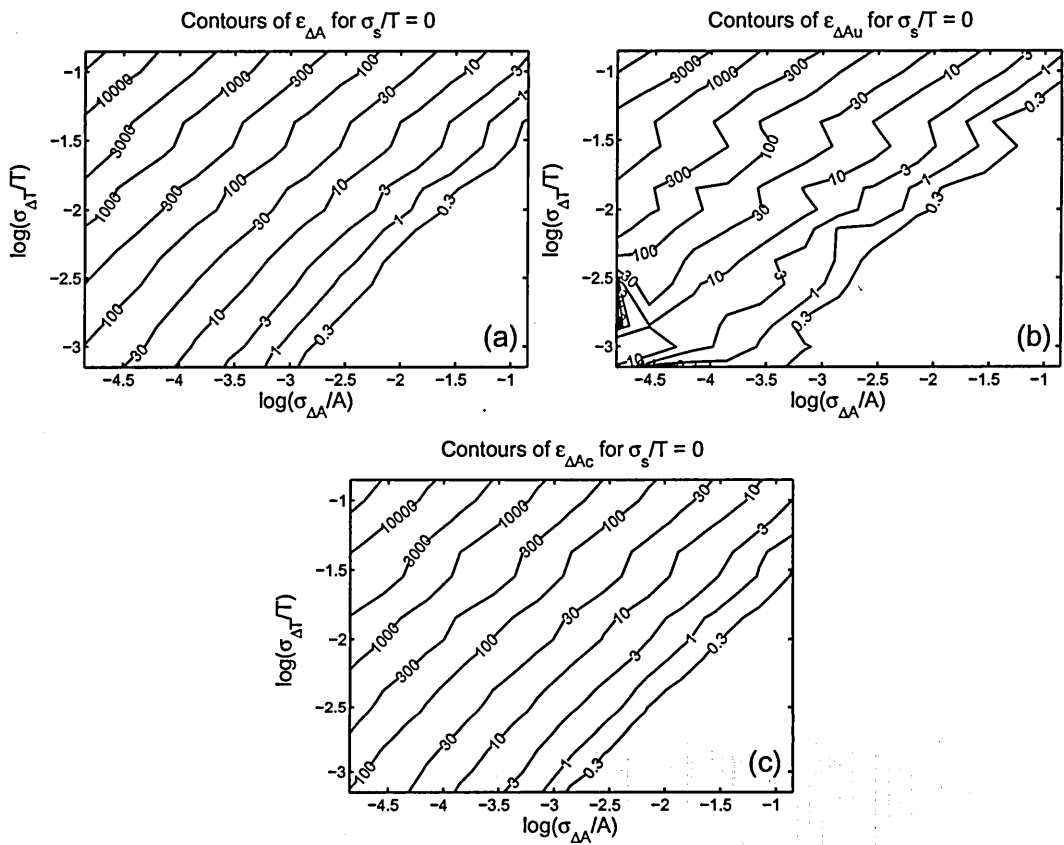


Figure B.2: The contours of the plots shown in B.1

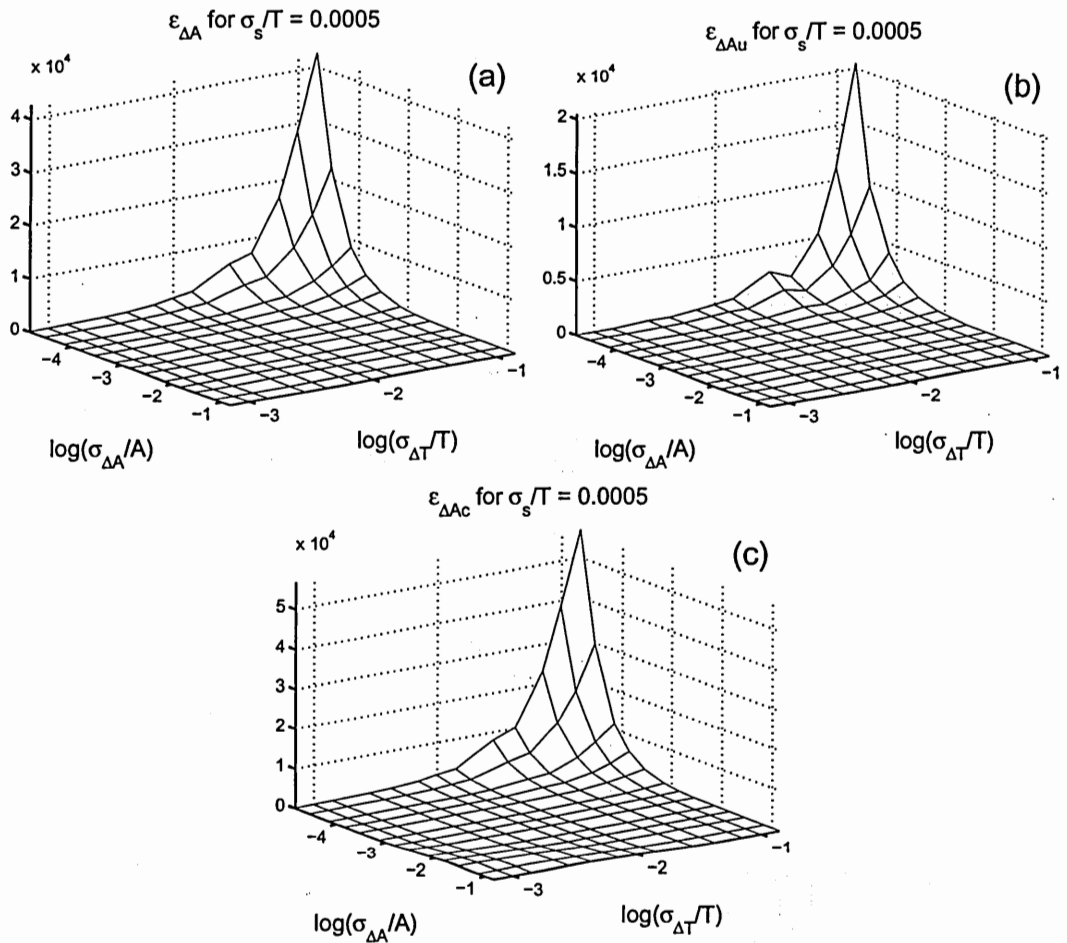


Figure B.3: Extraction errors for (a) total amplitude jitter, $\epsilon_{\Delta A}$, (b) uncorrelated amplitude jitter, $\epsilon_{\Delta A_u}$, and (c) correlated amplitude jitter, $\epsilon_{\Delta A_c}$, obtained with the uncompensated direct method. σ_A/A —normalized total amplitude jitter. σ_T/T —normalized total timing jitter. σ_s/T —normalized root-mean-squared pulse width.

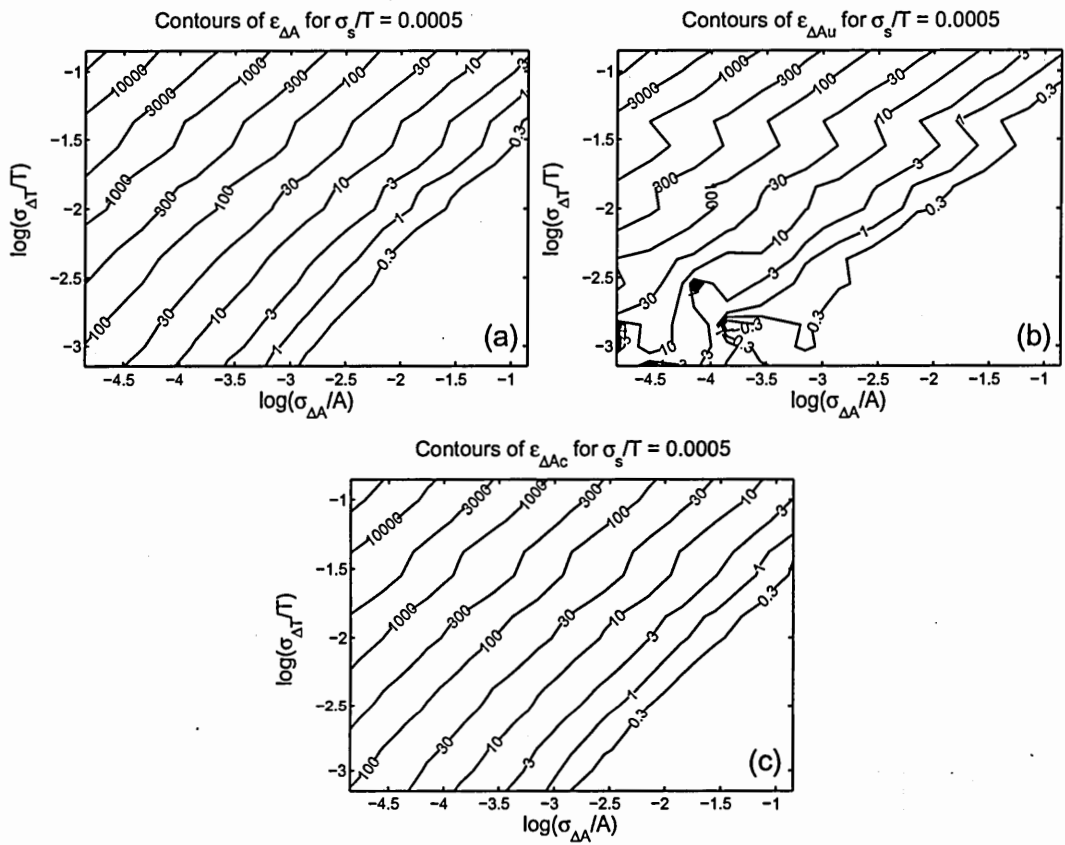


Figure B.4: The contours of the plots shown in B.3

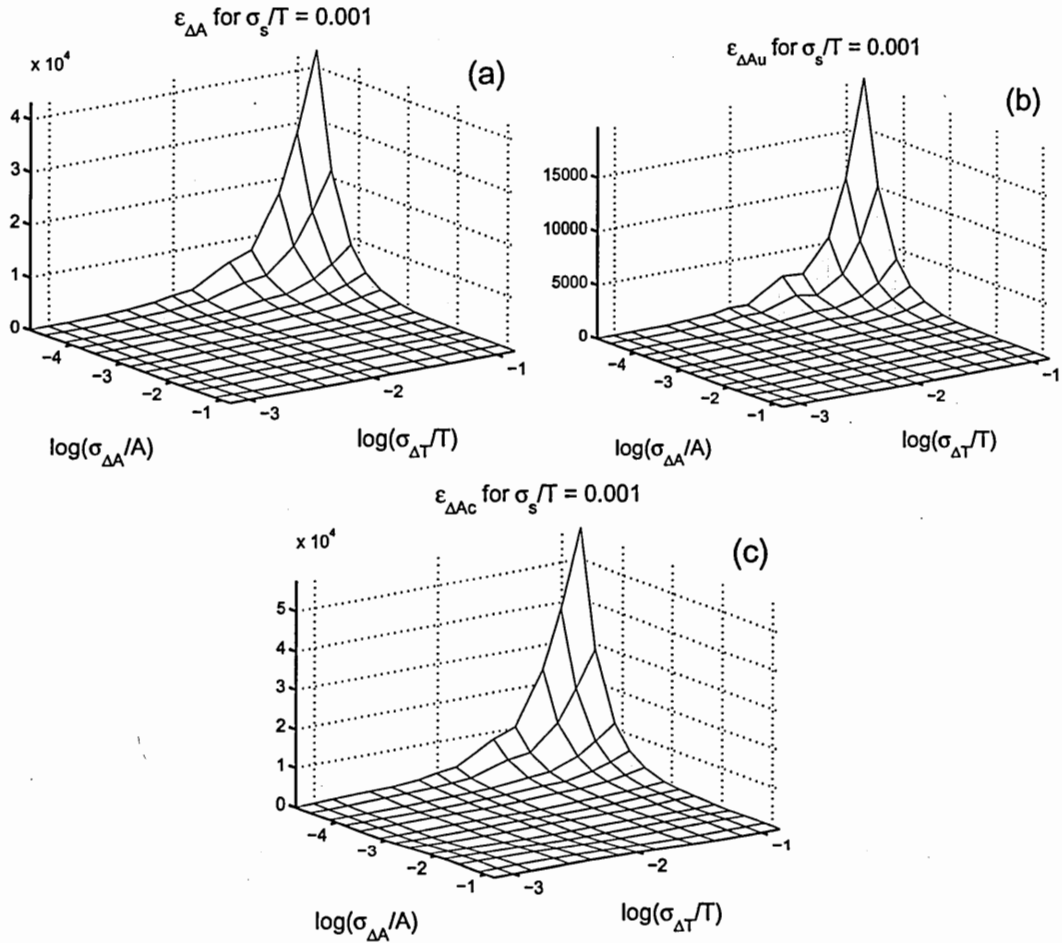


Figure B.5: Extraction errors for (a) total amplitude jitter, $\epsilon_{\Delta A}$, (b) uncorrelated amplitude jitter, $\epsilon_{\Delta A_u}$, and (c) correlated amplitude jitter, $\epsilon_{\Delta A_c}$, obtained with the uncompensated direct method. σ_A/A —normalized total amplitude jitter. σ_T/T —normalized total timing jitter. σ_s/T —normalized root-mean-squared pulse width.

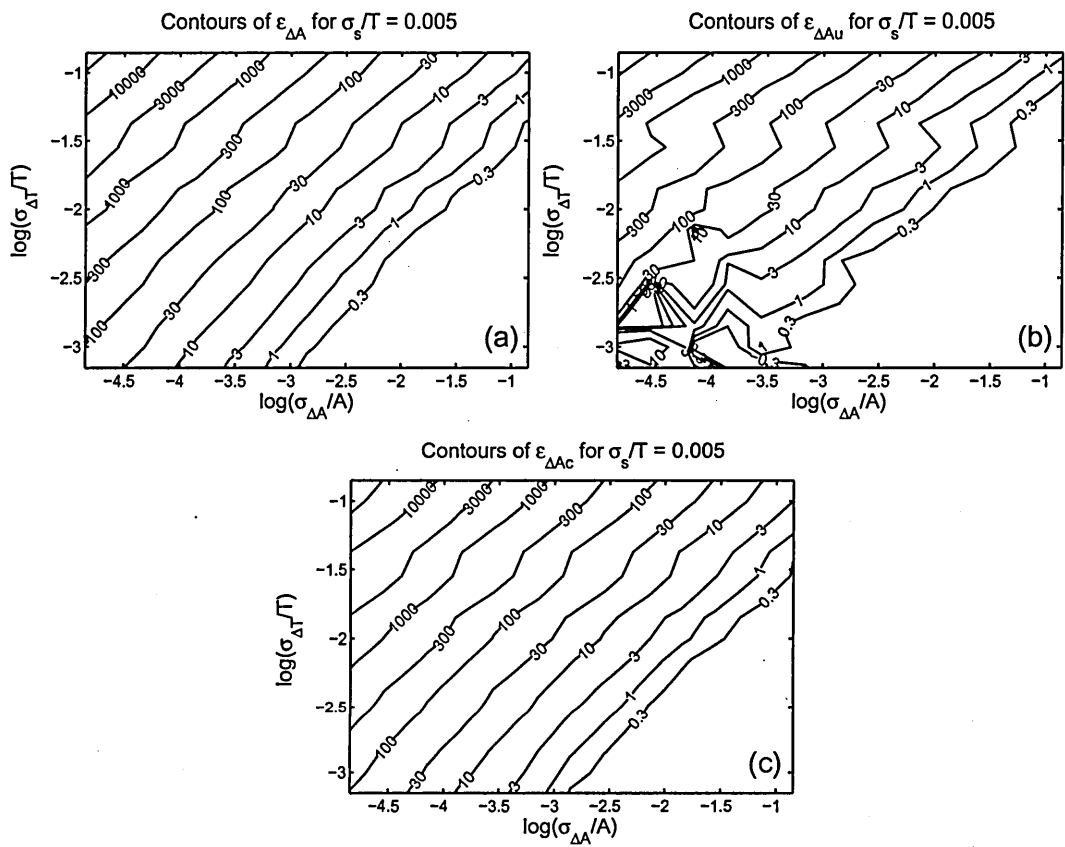


Figure B.6: The contours of the plots shown in B.5

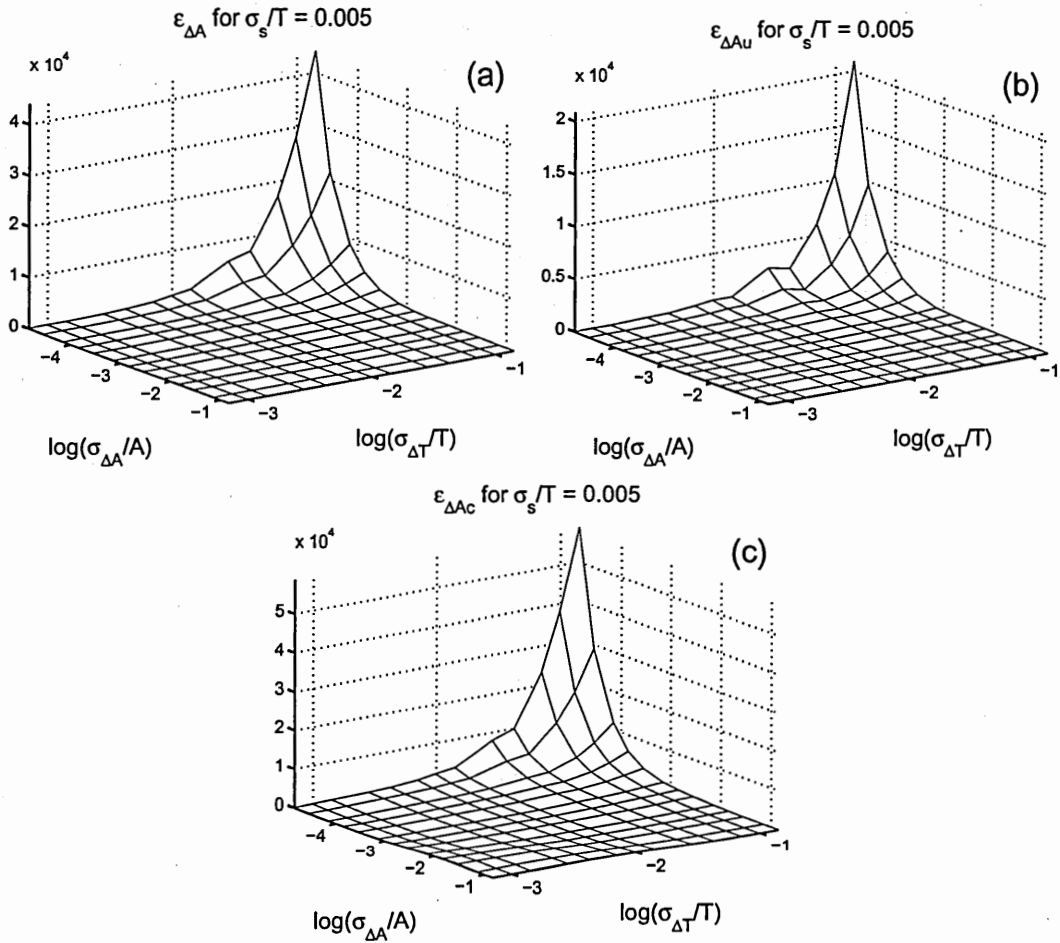


Figure B.7: Extraction errors for (a) total amplitude jitter, $\epsilon_{\Delta A}$, (b) uncorrelated amplitude jitter, $\epsilon_{\Delta Au}$, and (c) correlated amplitude jitter, $\epsilon_{\Delta Ac}$, obtained with the uncompensated direct method. σ_A/A —normalized total amplitude jitter. σ_T/T —normalized total timing jitter. σ_s/T —normalized root-mean-squared pulse width.

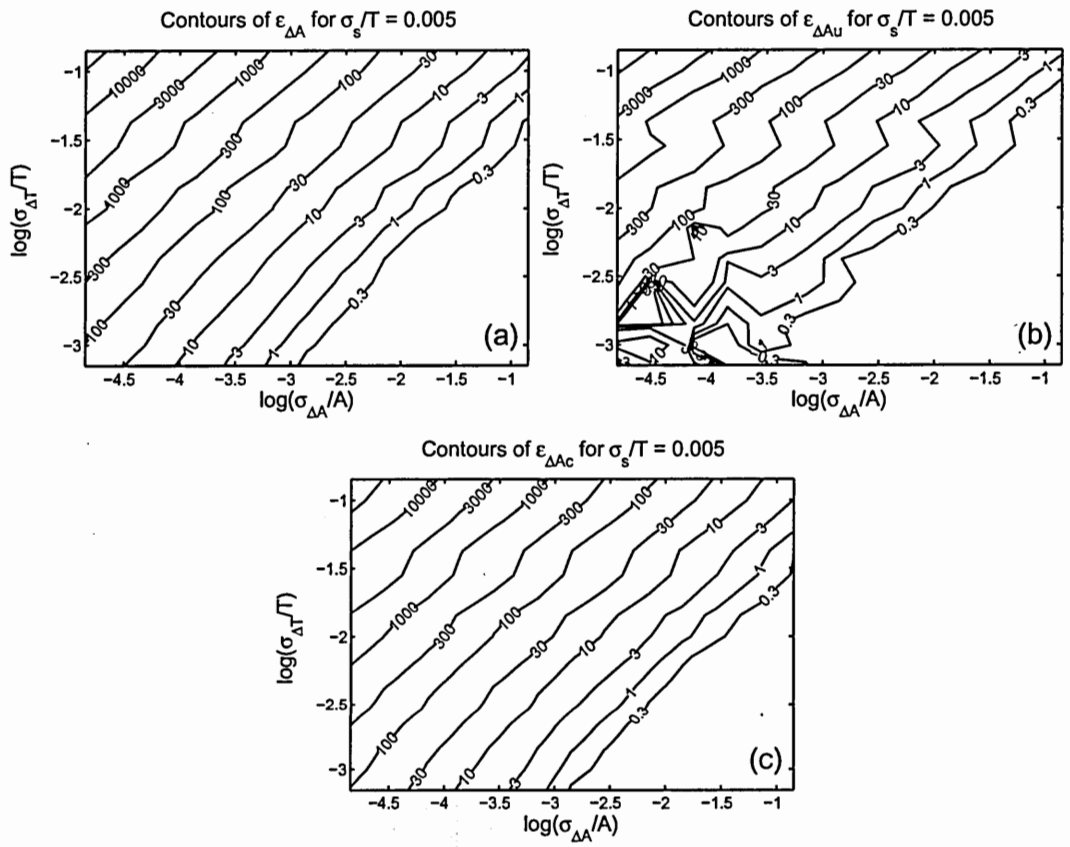


Figure B.8: The contours of the plots shown in B.7

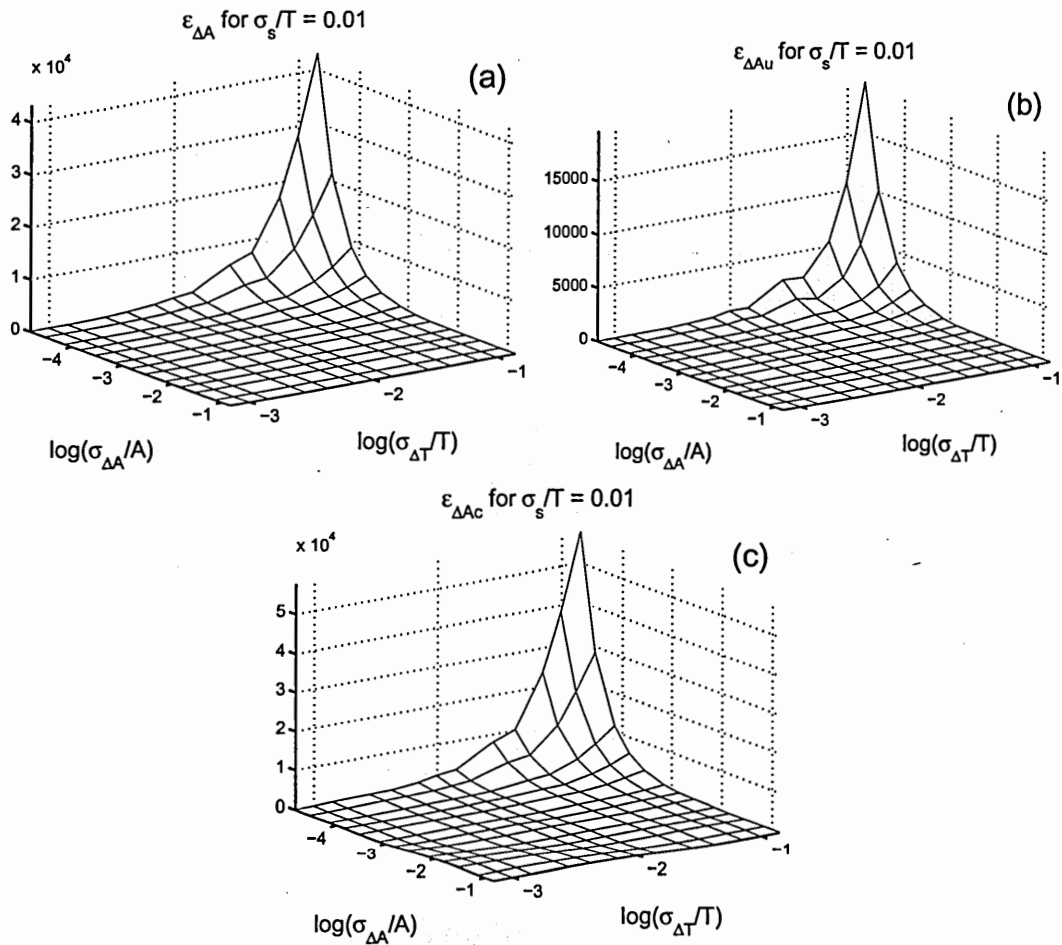


Figure B.9: Extraction errors for (a) total amplitude jitter, $\epsilon_{\Delta A}$, (b) uncorrelated amplitude jitter, $\epsilon_{\Delta A_u}$, and (c) correlated amplitude jitter, $\epsilon_{\Delta A_c}$, obtained with the uncompensated direct method. σ_A/A —normalized total amplitude jitter. σ_T/T —normalized total timing jitter. σ_s/T —normalized root-mean-squared pulse width.

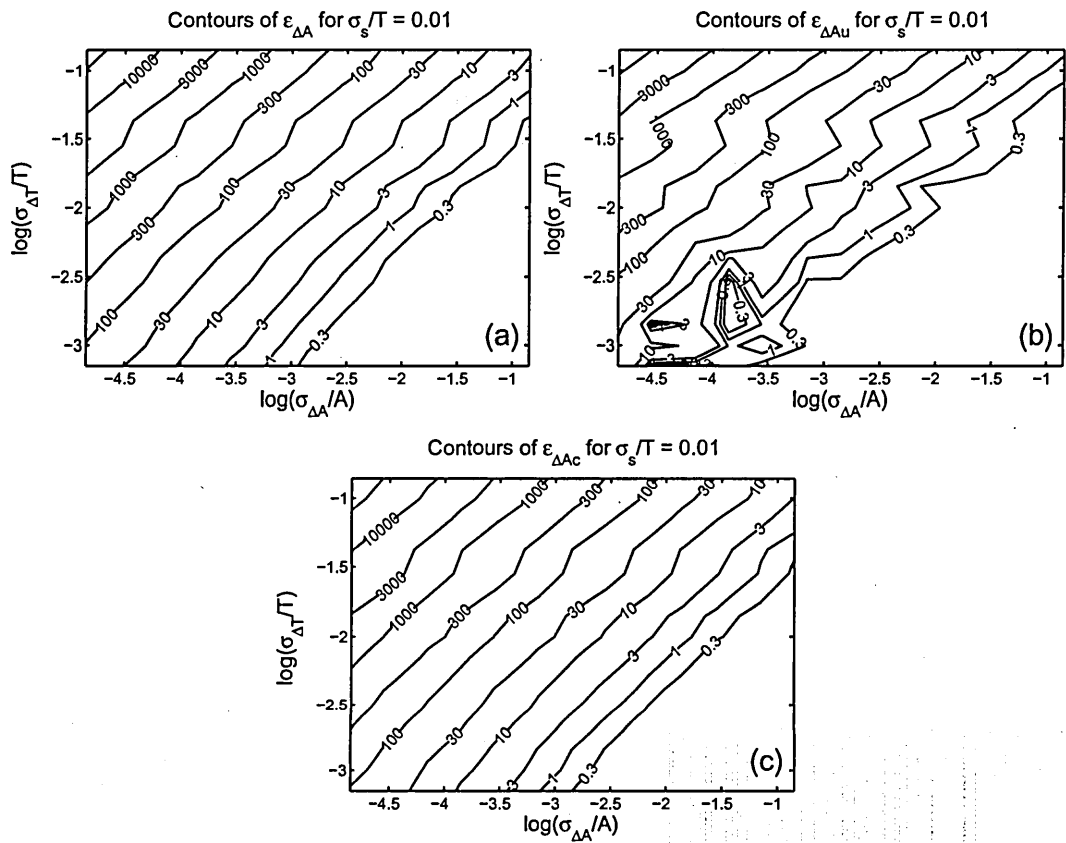


Figure B.10: The contours of the plots shown in B.9

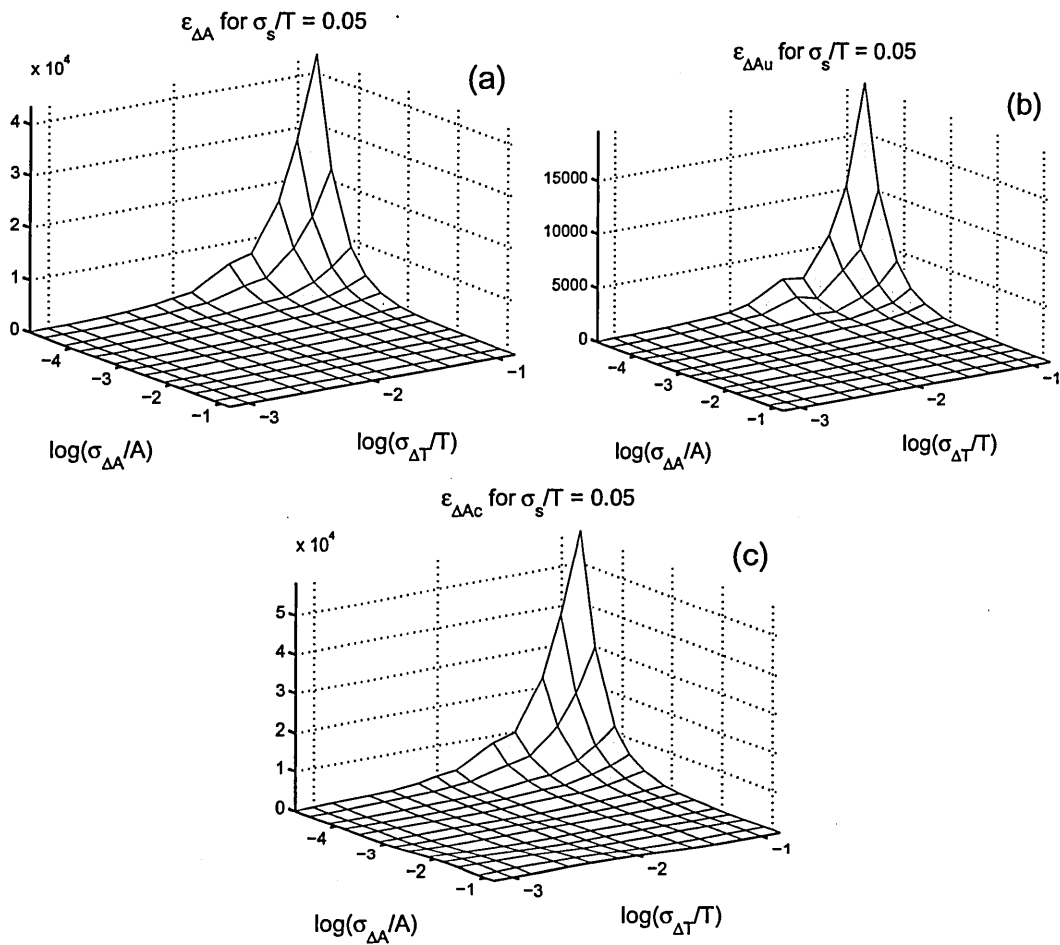


Figure B.11: Extraction errors for (a) total amplitude jitter, $\epsilon_{\Delta A}$, (b) uncorrelated amplitude jitter, $\epsilon_{\Delta A_u}$, and (c) correlated amplitude jitter, $\epsilon_{\Delta A_c}$, obtained with the uncompensated direct method. σ_A/A —normalized total amplitude jitter. σ_T/T —normalized total timing jitter. σ_s/T —normalized root-mean-squared pulse width.

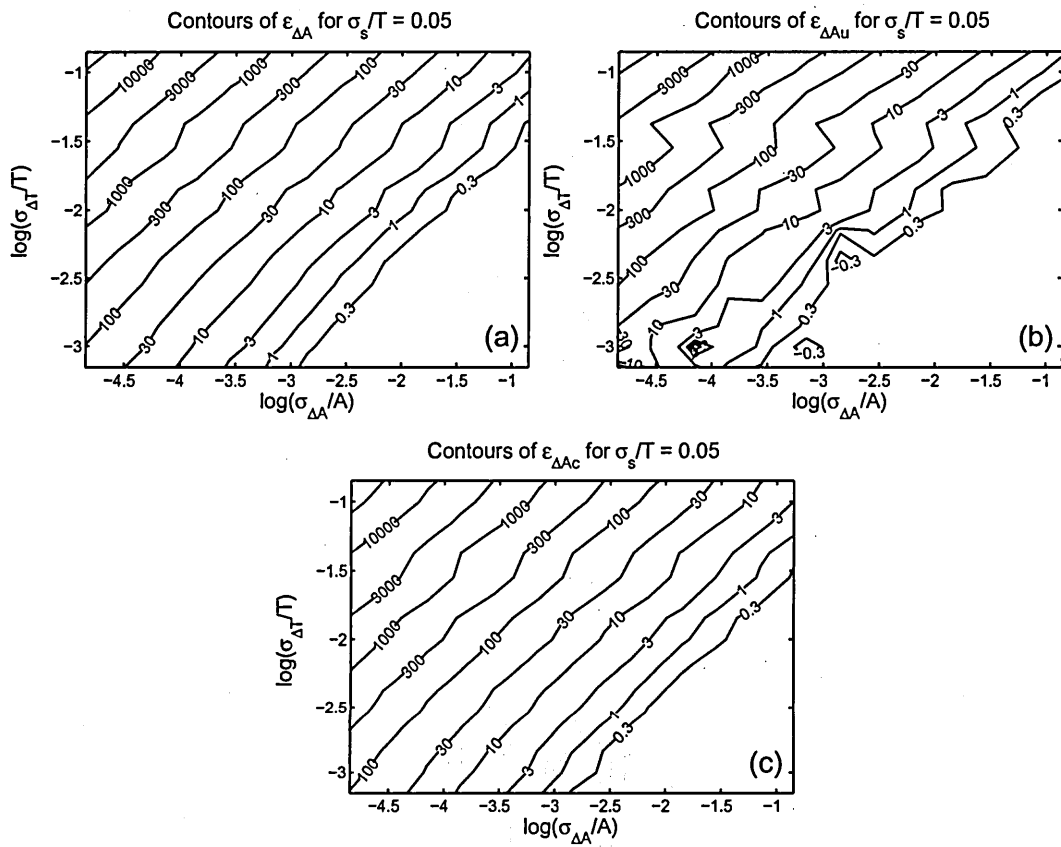


Figure B.12: The contours of the plots shown in B.11

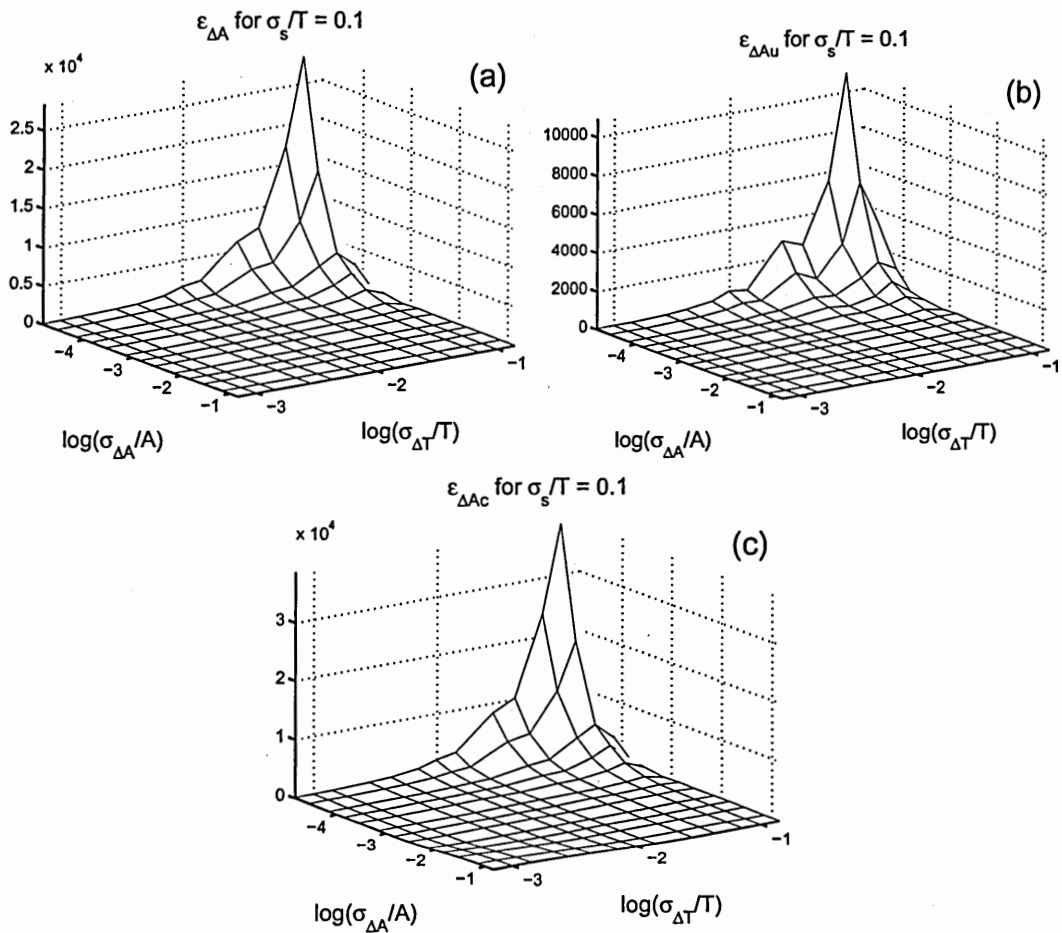


Figure B.13: Extraction errors for (a) total amplitude jitter, $\epsilon_{\Delta A}$, (b) uncorrelated amplitude jitter, $\epsilon_{\Delta Au}$, and (c) correlated amplitude jitter, $\epsilon_{\Delta Ac}$, obtained with the uncompensated direct method. σ_A/A —normalized total amplitude jitter. σ_T/T —normalized total timing jitter. σ_s/T —normalized root-mean-squared pulse width.

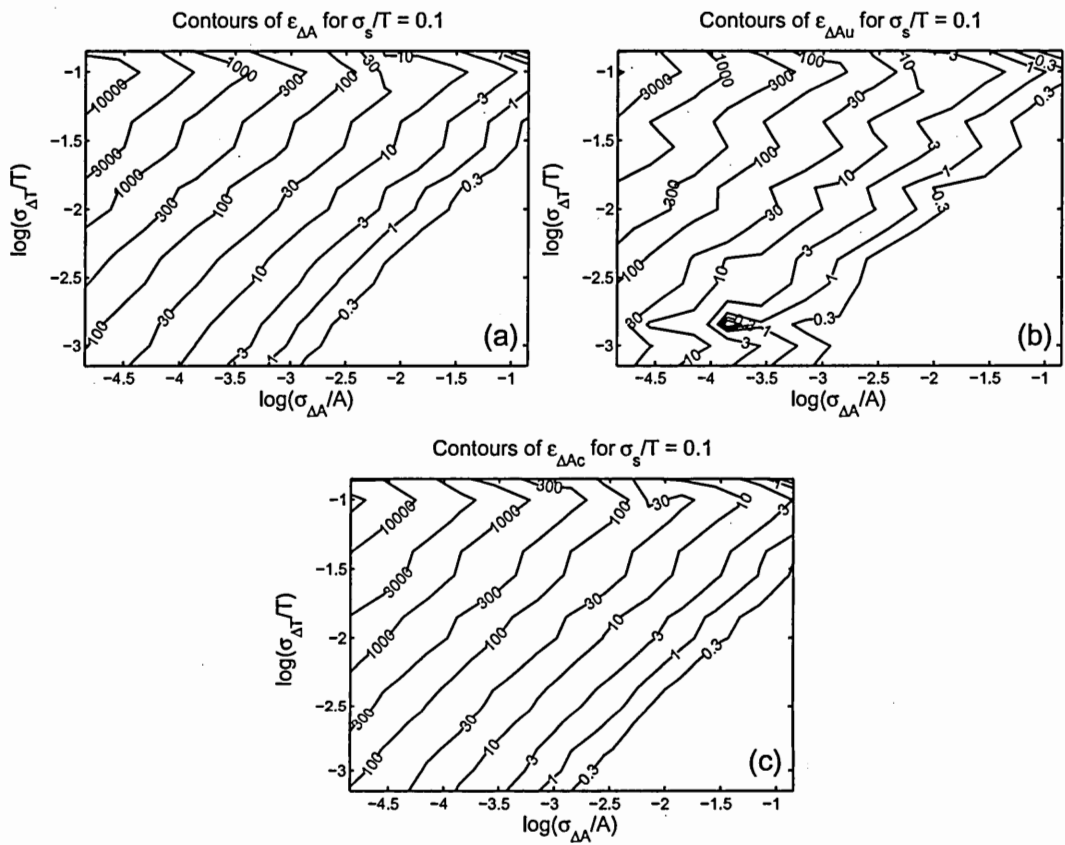


Figure B.14: The contours of the plots shown in B.13

B.2 Timing Jitter

On the next few pages, the extraction-error surfaces, obtained with the uncompensated direct method, for total, uncorrelated, and correlated timing jitter are plotted against the normalized total amplitude jitter and the normalized total timing jitter, for each of seven normalized RMS pulse widths. The contours of these surfaces are also included.

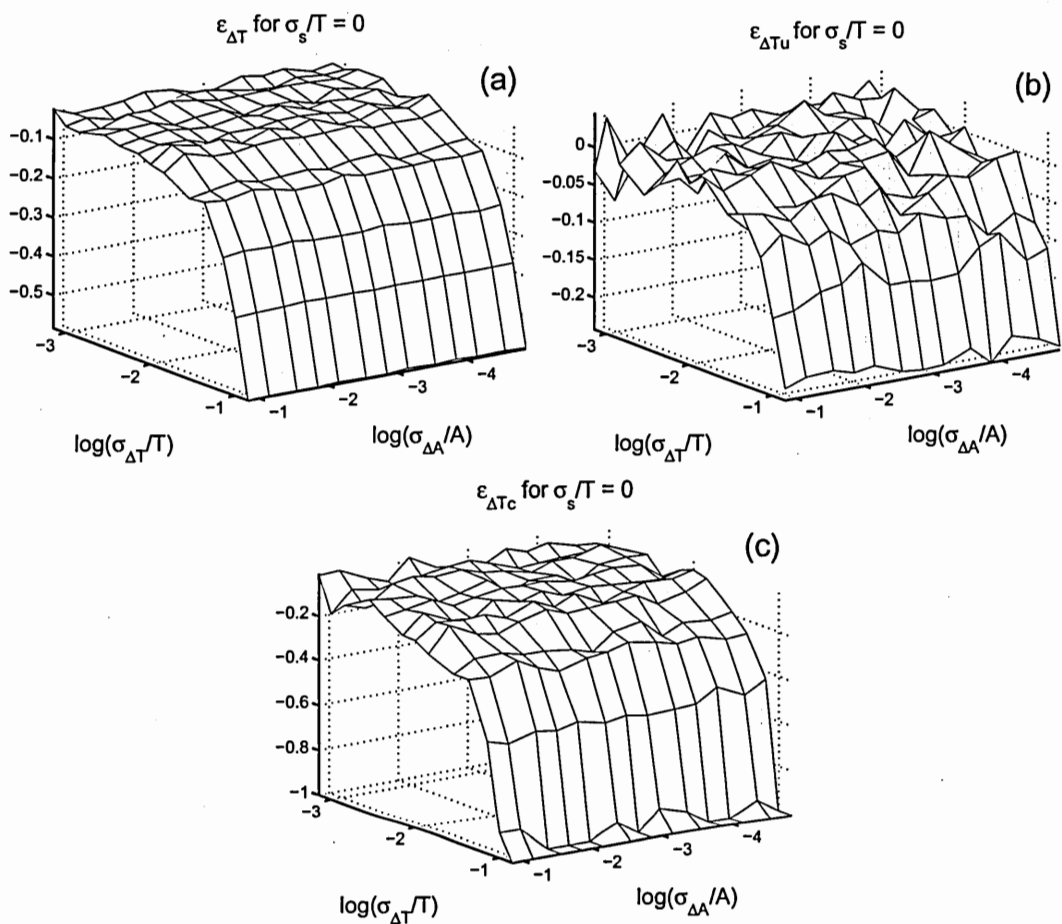


Figure B.15: Extraction errors for (a) total timing jitter, $\epsilon_{\Delta T}$, (b) uncorrelated timing jitter, $\epsilon_{\Delta T_u}$, and (c) correlated timing jitter, $\epsilon_{\Delta T_c}$, obtained with the uncompensated direct method. σ_A/A —normalized total amplitude jitter. σ_T/T —normalized total timing jitter. σ_s/T —normalized root-mean-squared pulse width.

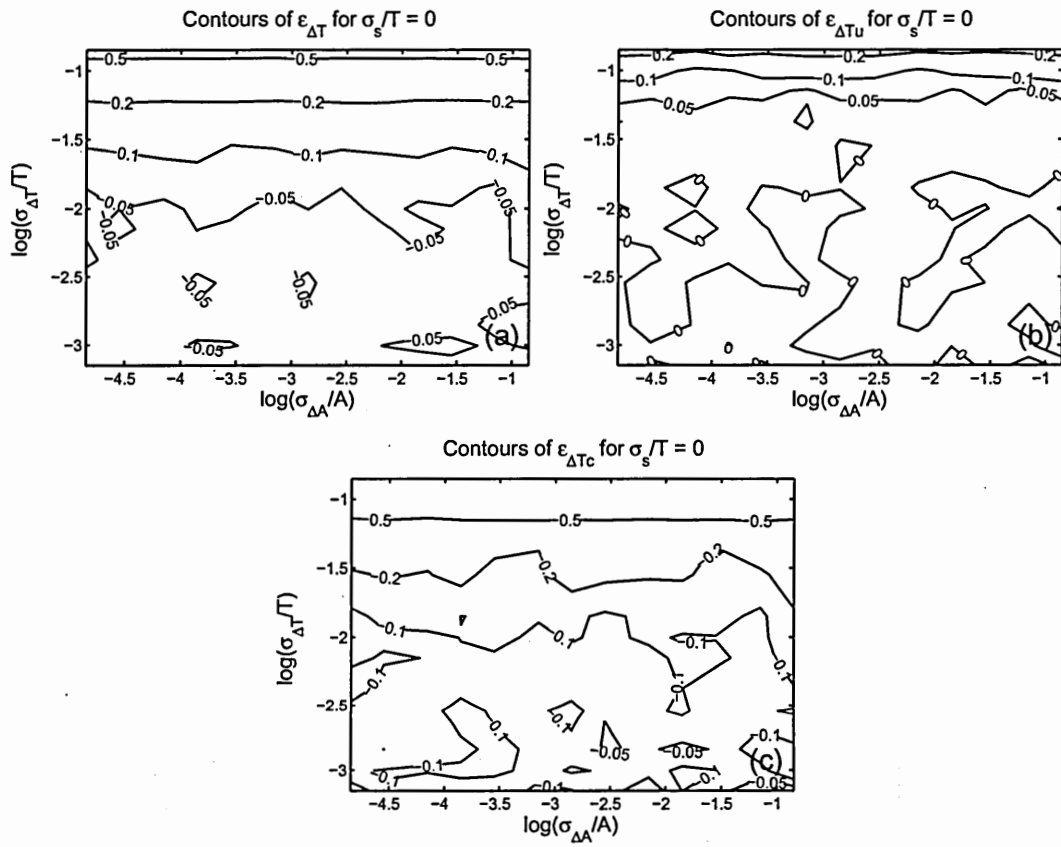


Figure B.16: The contours of the plots shown in B.15

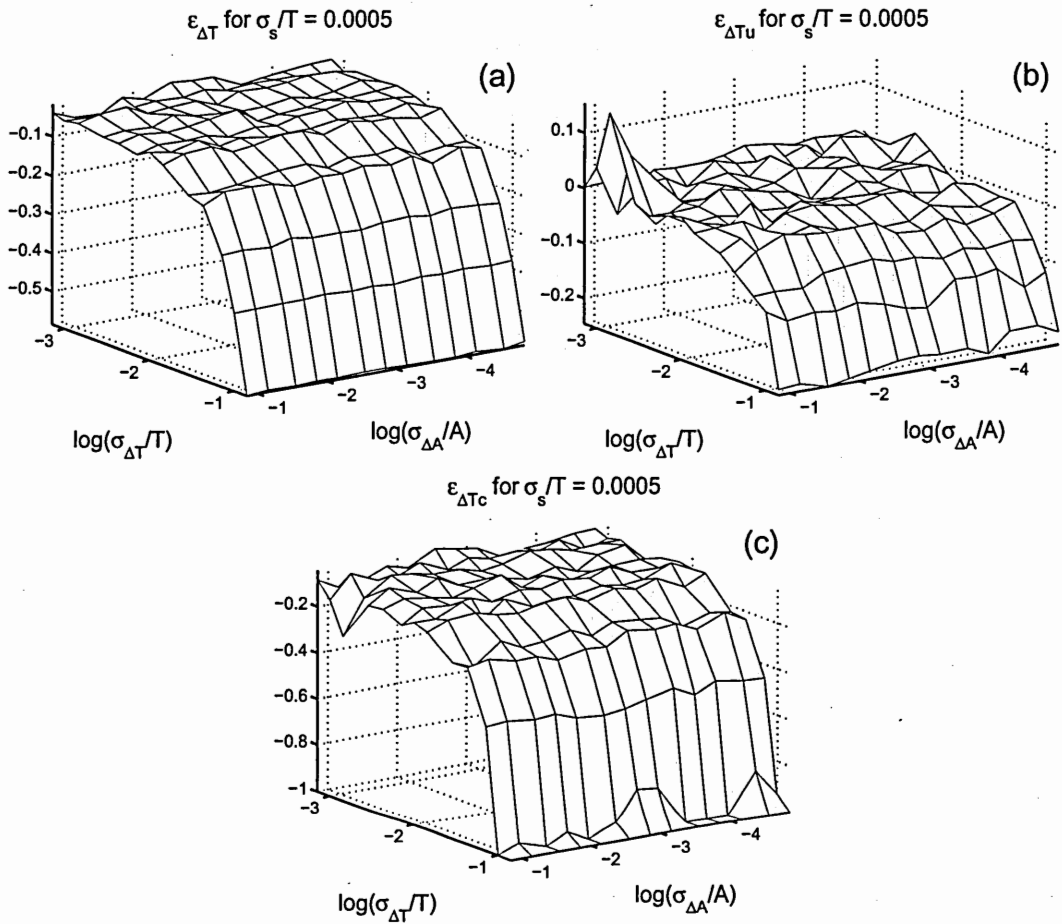


Figure B.17: Extraction errors for (a) total timing jitter, $\epsilon_{\Delta T}$, (b) uncorrelated timing jitter, $\epsilon_{\Delta Tu}$, and (c) correlated timing jitter, $\epsilon_{\Delta Tc}$, obtained with the uncompensated direct method. σ_A/A —normalized total amplitude jitter. σ_T/T —normalized total timing jitter. σ_s/T —normalized root-mean-squared pulse width.

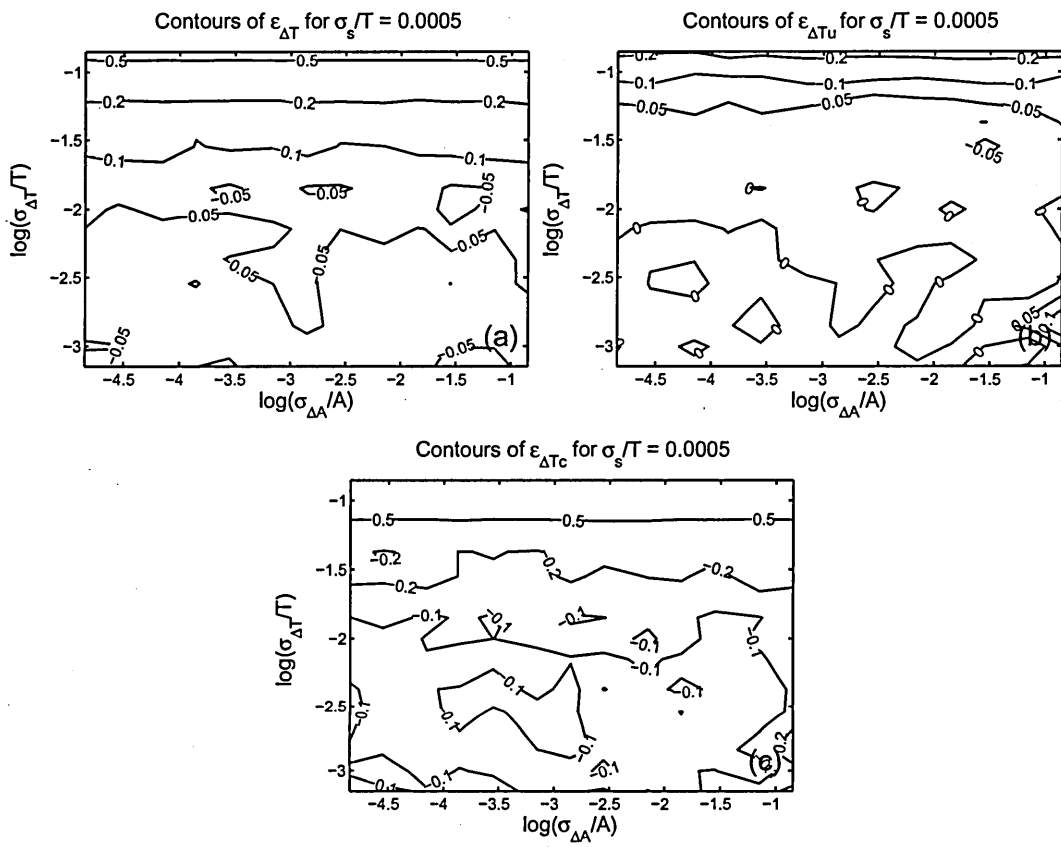


Figure B.18: The contours of the plots shown in B.17

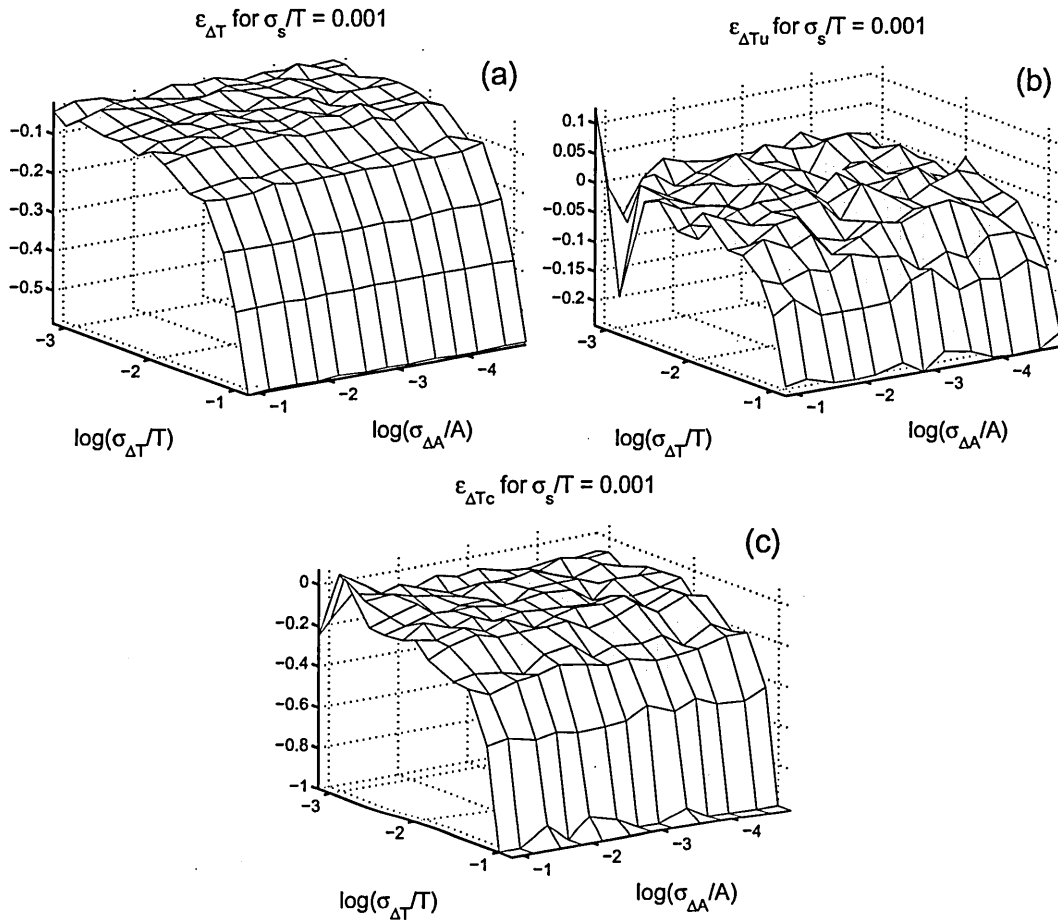


Figure B.19: Extraction errors for (a) total timing jitter, $\epsilon_{\Delta T}$, (b) uncorrelated timing jitter, $\epsilon_{\Delta T_u}$, and (c) correlated timing jitter, $\epsilon_{\Delta T_c}$, obtained with the uncompensated direct method. σ_A/A —normalized total amplitude jitter. σ_T/T —normalized total timing jitter. σ_s/T —normalized root-mean-squared pulse width.

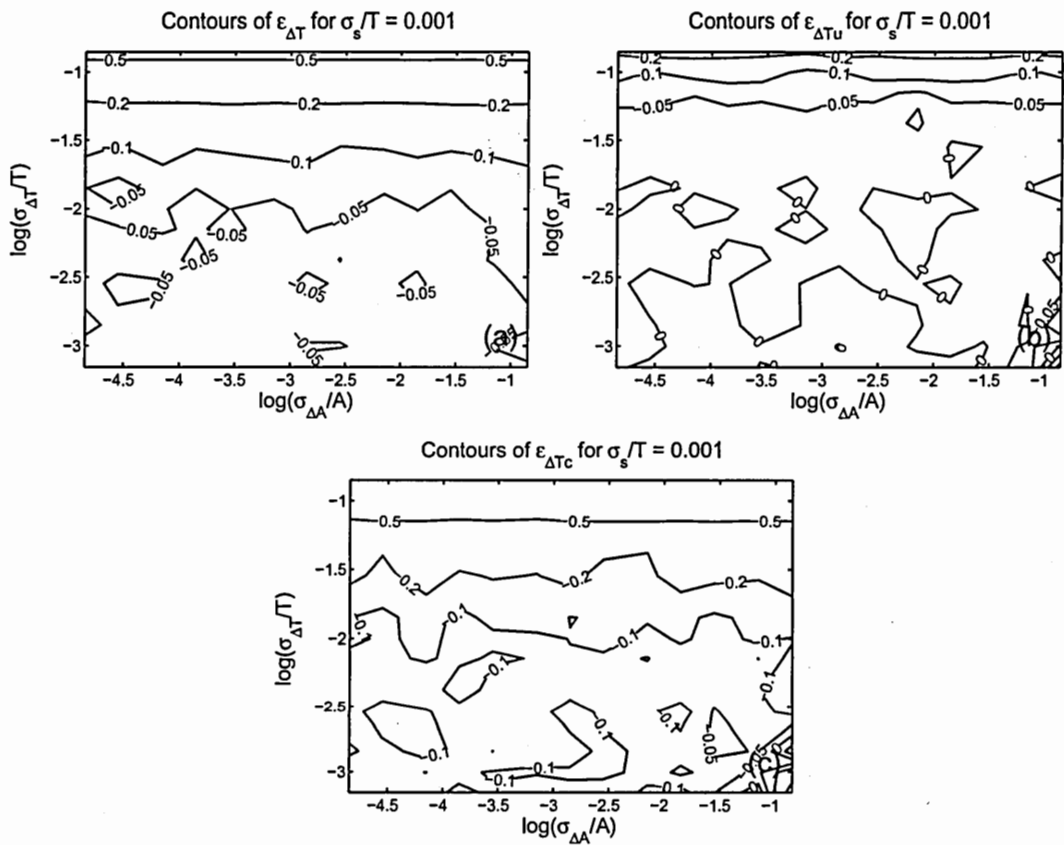


Figure B.20: The contours of the plots shown in B.19

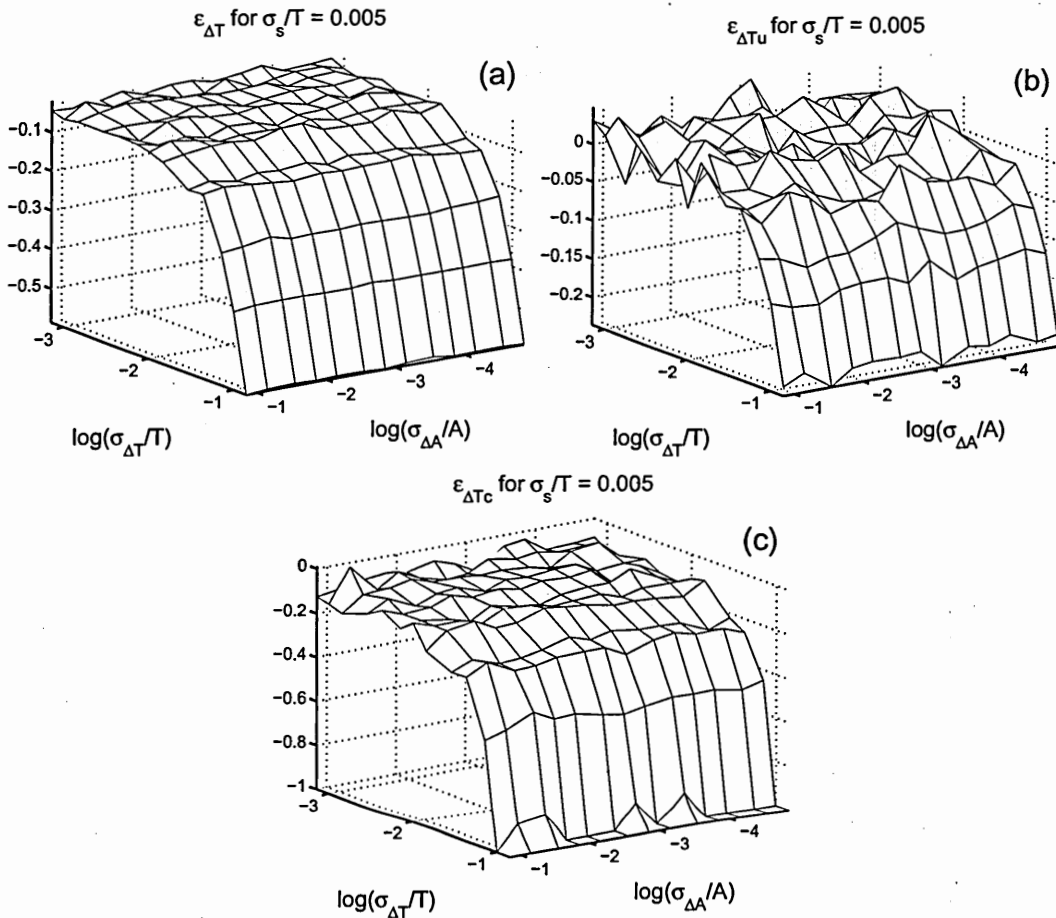


Figure B.21: Extraction errors for (a) total timing jitter, $\epsilon_{\Delta T}$, (b) uncorrelated timing jitter, $\epsilon_{\Delta T_u}$, and (c) correlated timing jitter, $\epsilon_{\Delta T_c}$, obtained with the uncompensated direct method. σ_A/A —normalized total amplitude jitter. σ_T/T —normalized total timing jitter. σ_s/T —normalized root-mean-squared pulse width.

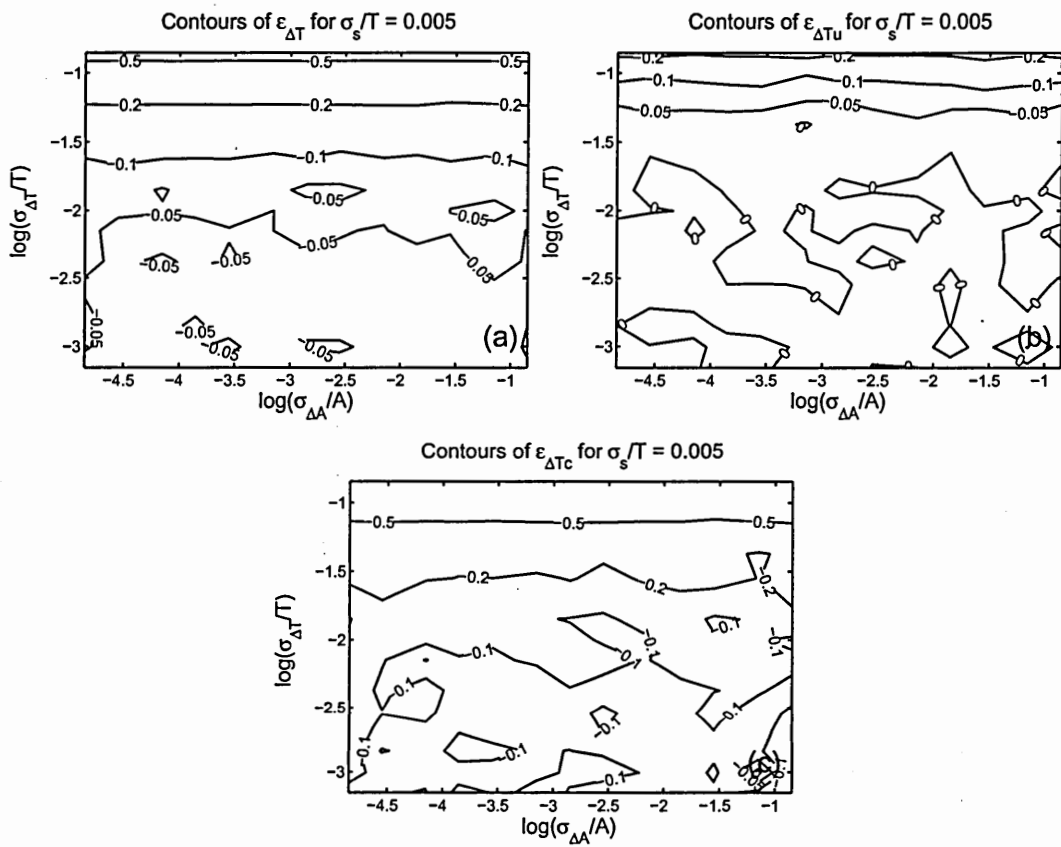


Figure B.22: The contours of the plots shown in B.21

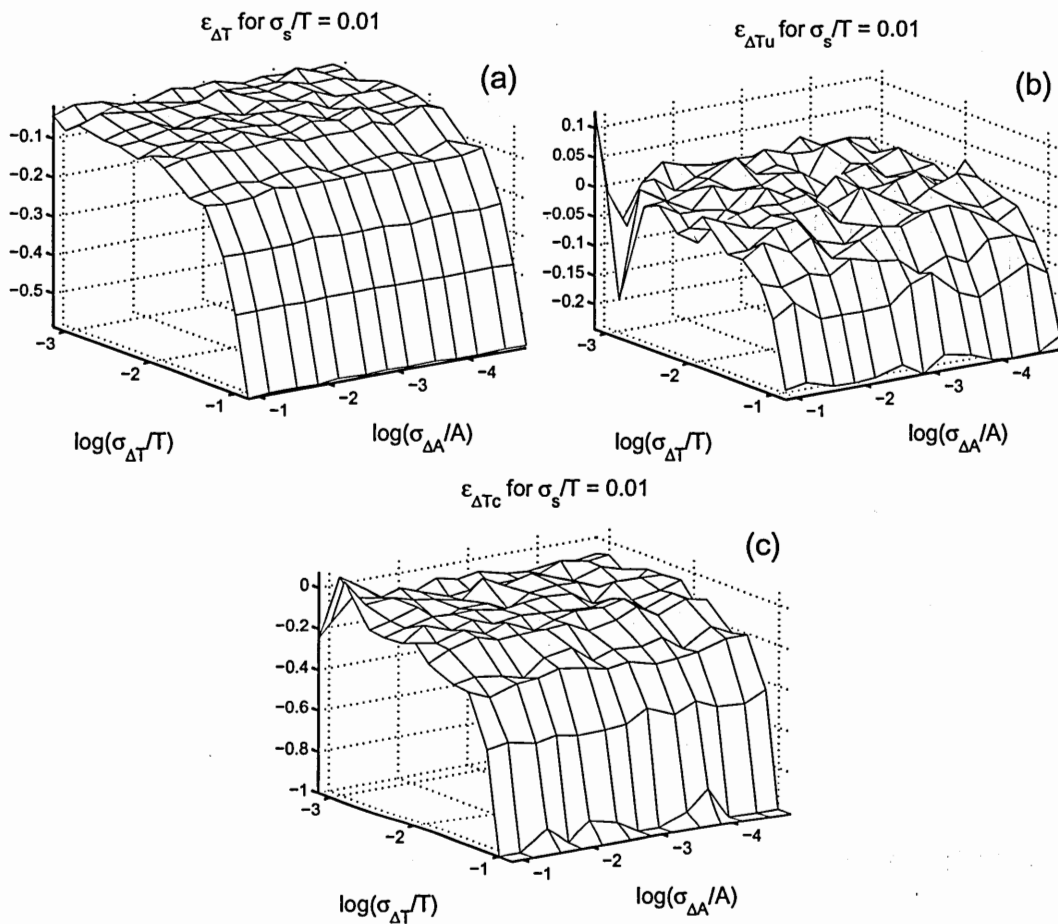


Figure B.23: Extraction errors for (a) total timing jitter, $\epsilon_{\Delta T}$, (b) uncorrelated timing jitter, $\epsilon_{\Delta T_u}$, and (c) correlated timing jitter, $\epsilon_{\Delta T_c}$, obtained with the uncompensated direct method. σ_A/A —normalized total amplitude jitter. σ_T/T —normalized total timing jitter. σ_s/T —normalized root-mean-squared pulse width.

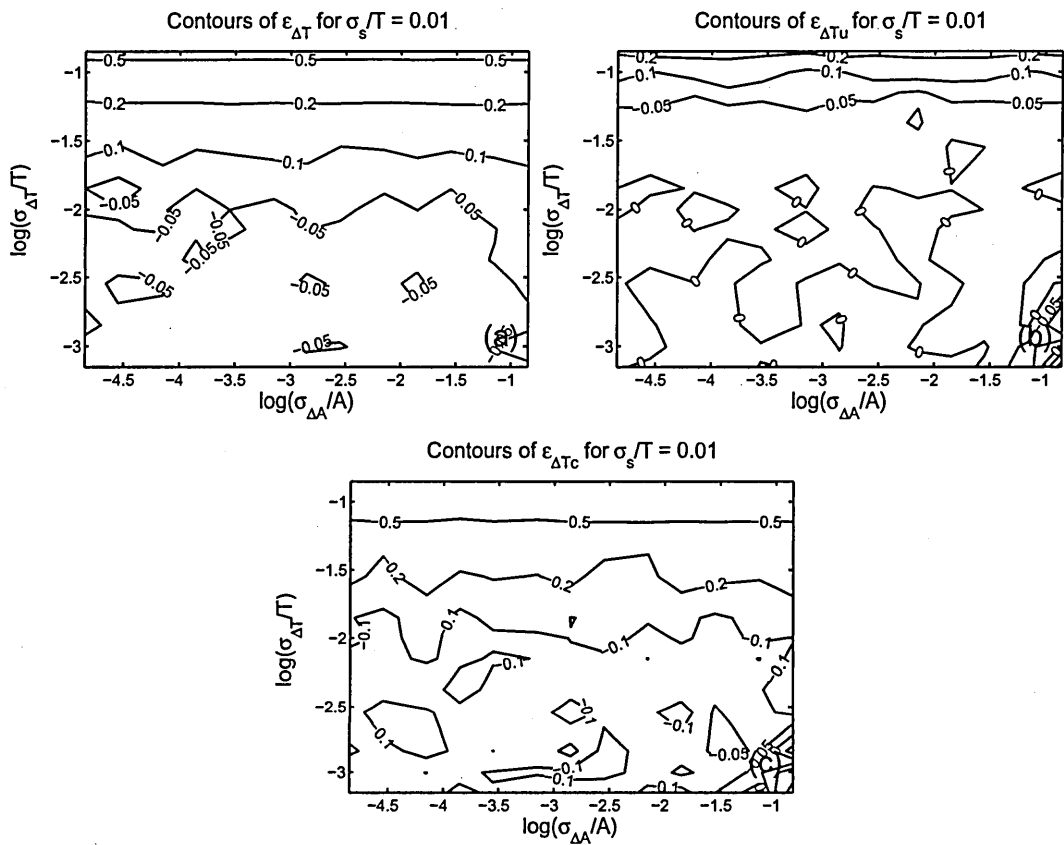


Figure B.24: The contours of the plots shown in B.23

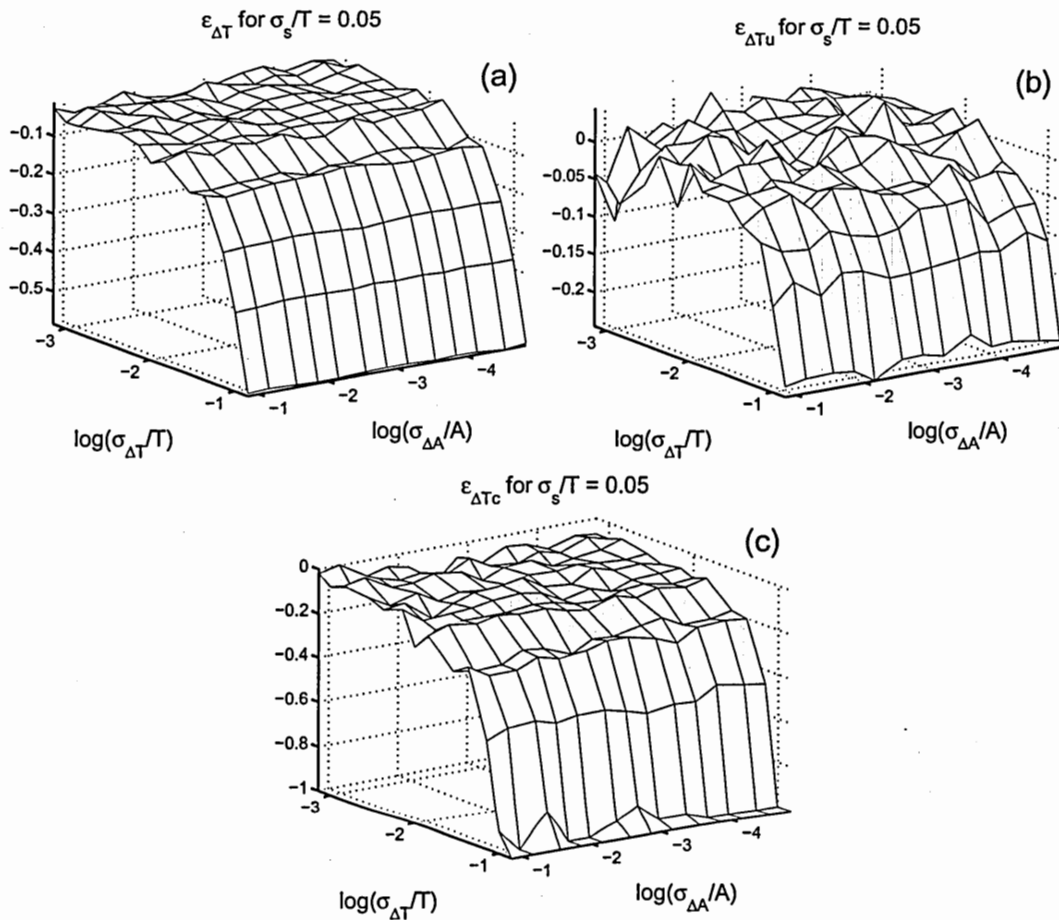


Figure B.25: Extraction errors for (a) total timing jitter, $\epsilon_{\Delta T}$, (b) uncorrelated timing jitter, $\epsilon_{\Delta T_u}$, and (c) correlated timing jitter, $\epsilon_{\Delta T_c}$, obtained with the uncompensated direct method. σ_A/A —normalized total amplitude jitter. σ_T/T —normalized total timing jitter. σ_s/T —normalized root-mean-squared pulse width.

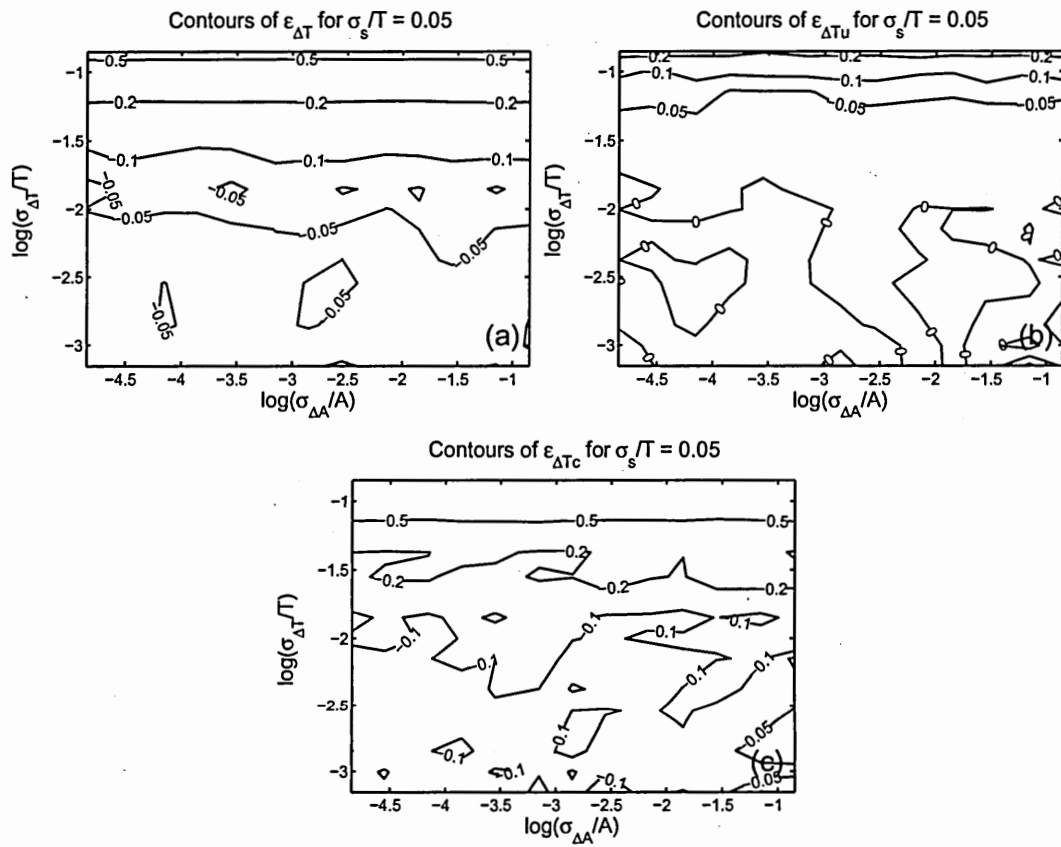


Figure B.26: The contours of the plots shown in B.25

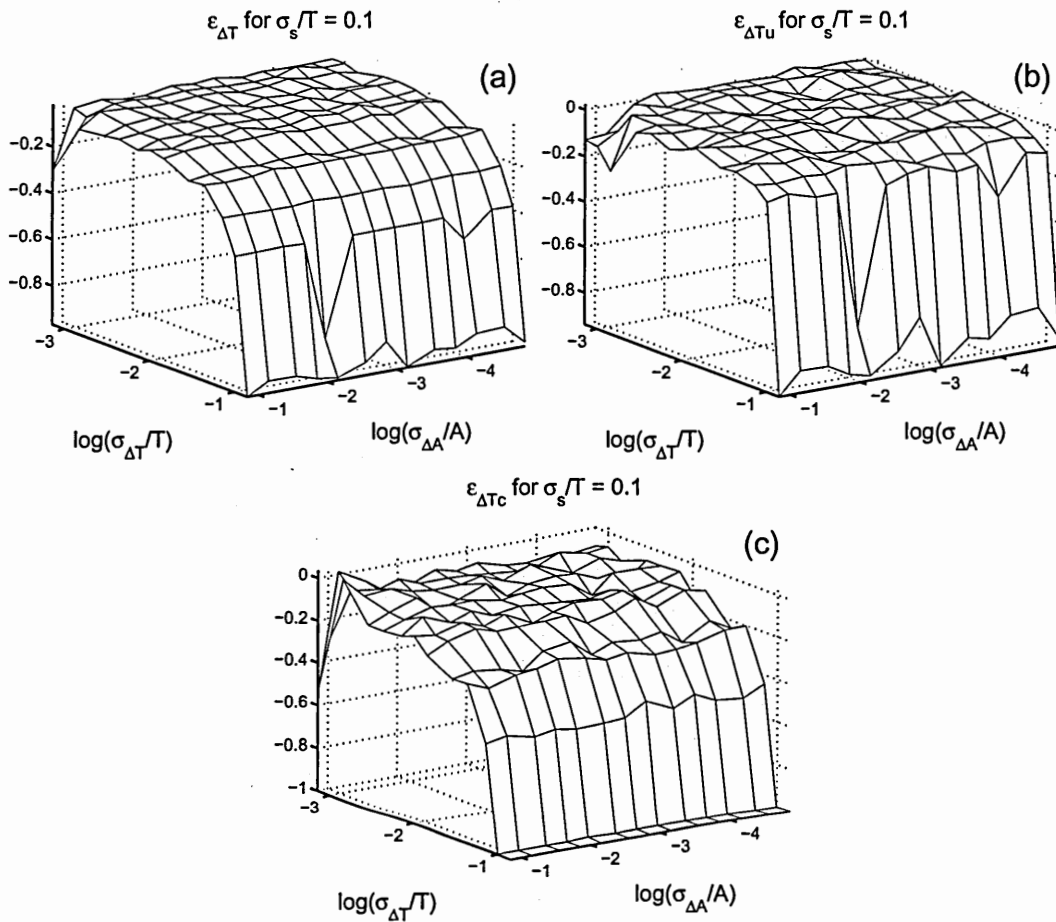


Figure B.27: Extraction errors for (a) total timing jitter, $\epsilon_{\Delta T}$, (b) uncorrelated timing jitter, $\epsilon_{\Delta T_u}$, and (c) correlated timing jitter, $\epsilon_{\Delta T_c}$, obtained with the uncompensated direct method. σ_A/A —normalized total amplitude jitter. σ_T/T —normalized total timing jitter. σ_s/T —normalized root-mean-squared pulse width.

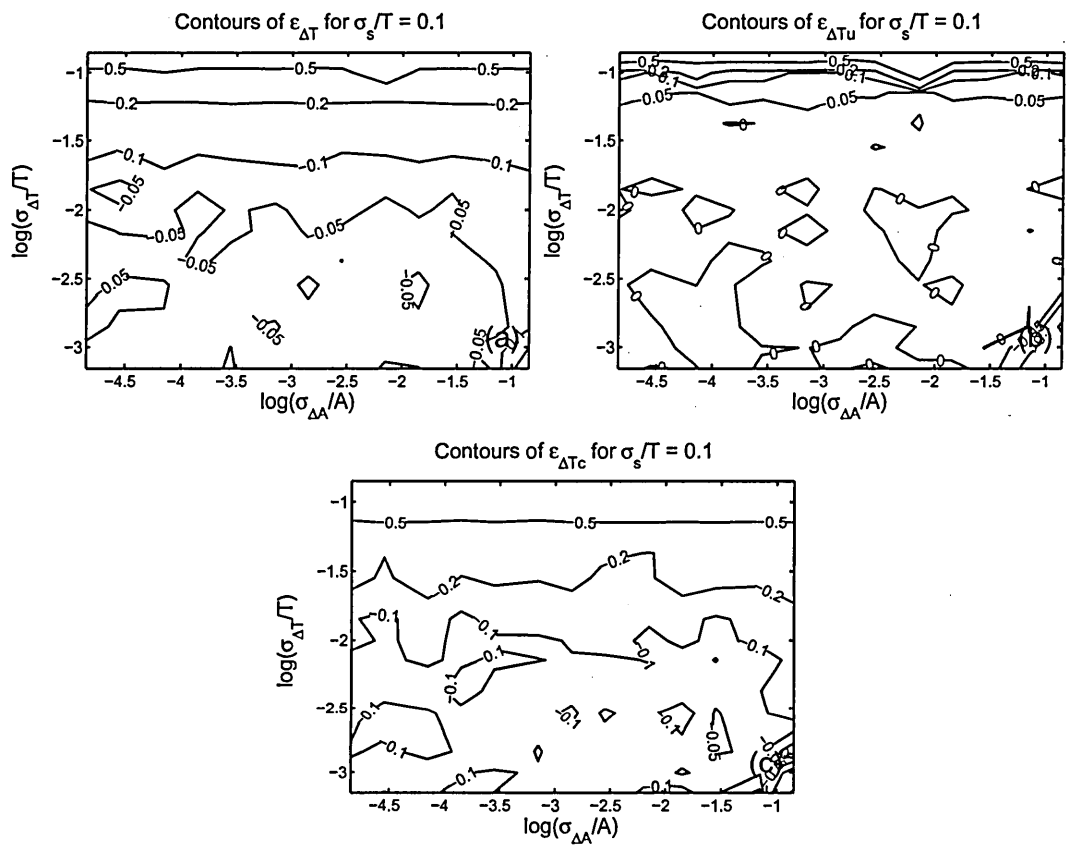


Figure B.28: The contours of the plots shown in B.27

B.3 Correlation Time

On the next few pages, the extraction-error surfaces, obtained with the uncompensated direct method, for the correlation times of the correlated amplitude and timing jitter are plotted against the normalized total amplitude jitter and the normalized total timing jitter, for each of seven normalized RMS pulse widths.

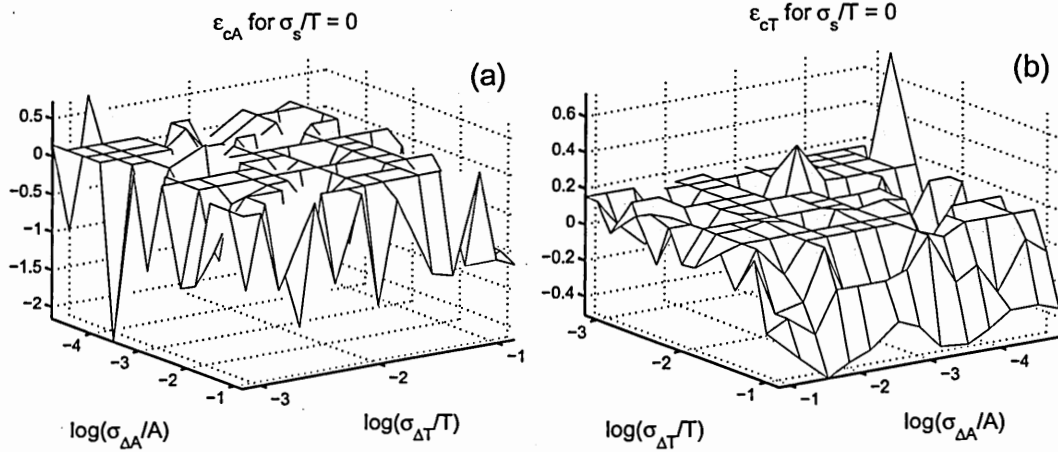


Figure B.29: Extraction errors for the correlation times of the (a) correlated amplitude jitter, $\epsilon_{\Delta A_c}$ and (b) timing jitter, $\epsilon_{\Delta T_c}$, obtained with the uncompensated direct method. σ_A/A —normalized total amplitude jitter. σ_T/T —normalized total timing jitter. σ_s/T —normalized root-mean-squared pulse width.

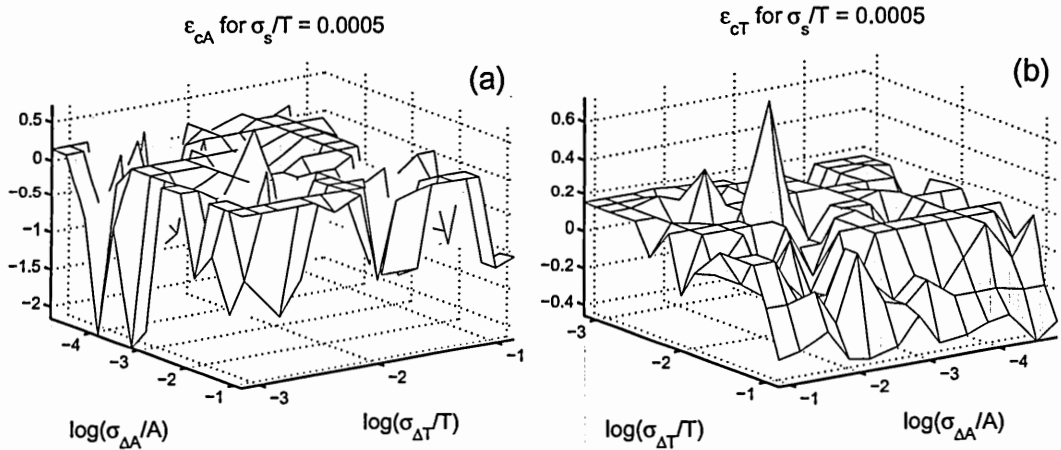


Figure B.30: Extraction errors for the correlation times of the (a) correlated amplitude jitter, $\epsilon_{\Delta A_c}$ and (b) timing jitter, $\epsilon_{\Delta T_c}$, obtained with the uncompensated direct method. σ_A/A —normalized total amplitude jitter. σ_T/T —normalized total timing jitter. σ_s/T —normalized root-mean-squared pulse width.

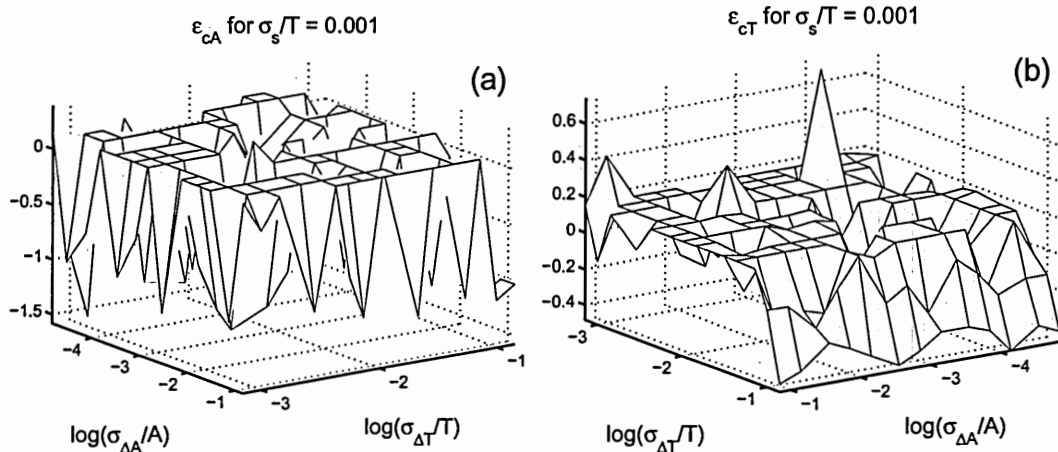


Figure B.31: Extraction errors for the correlation times of the (a) correlated amplitude jitter, $\epsilon_{\Delta A_c}$ and (b) timing jitter, $\epsilon_{\Delta T_c}$, obtained with the uncompensated direct method. σ_A/A —normalized total amplitude jitter. σ_T/T —normalized total timing jitter. σ_s/T —normalized root-mean-squared pulse width.

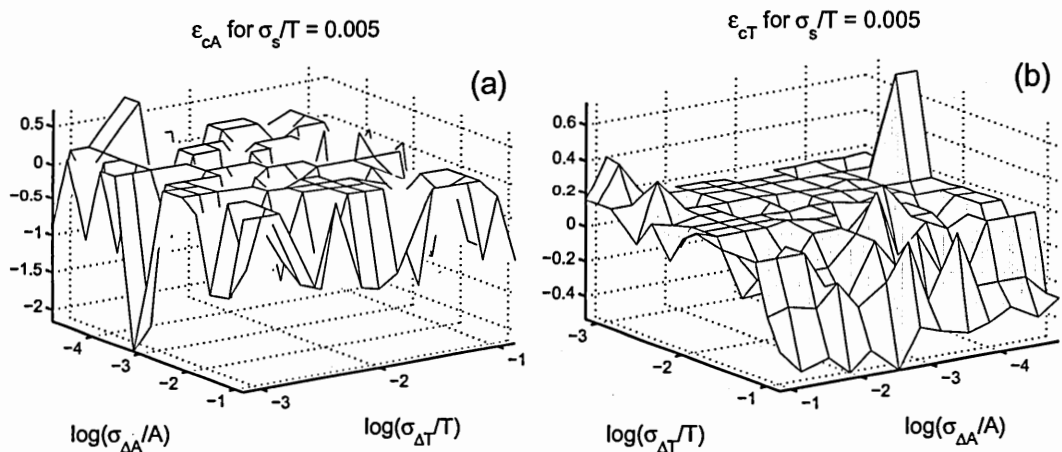


Figure B.32: Extraction errors for the correlation times of the (a) correlated amplitude jitter, $\epsilon_{\Delta A_c}$ and (b) timing jitter, $\epsilon_{\Delta T_c}$, obtained with the uncompensated direct method. σ_A/A —normalized total amplitude jitter. σ_T/T —normalized total timing jitter. σ_s/T —normalized root-mean-squared pulse width.

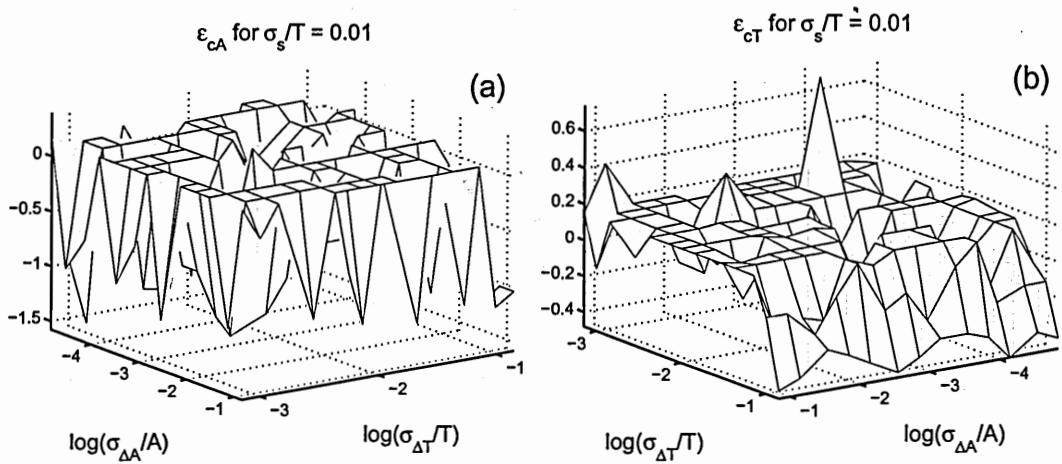


Figure B.33: Extraction errors for the correlation times of the (a) correlated amplitude jitter, $\epsilon_{\Delta A_c}$ and (b) timing jitter, $\epsilon_{\Delta T_c}$, obtained with the uncompensated direct method. σ_A/A —normalized total amplitude jitter. σ_T/T —normalized total timing jitter. σ_s/T —normalized root-mean-squared pulse width.

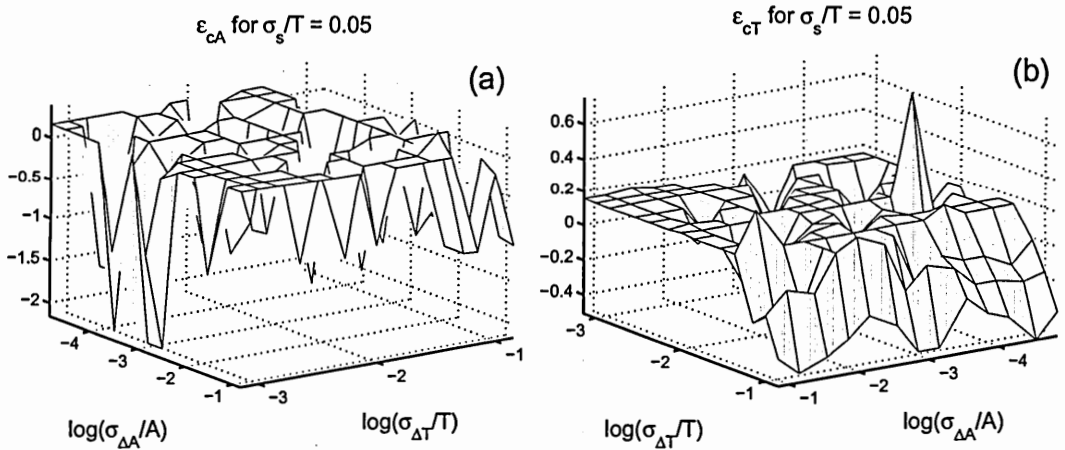


Figure B.34: Extraction errors for the correlation times of the (a) correlated amplitude jitter, $\epsilon_{\Delta A_c}$ and (b) timing jitter, $\epsilon_{\Delta T_c}$, obtained with the uncompensated direct method. σ_A/A —normalized total amplitude jitter. σ_T/T —normalized total timing jitter. σ_s/T —normalized root-mean-squared pulse width.

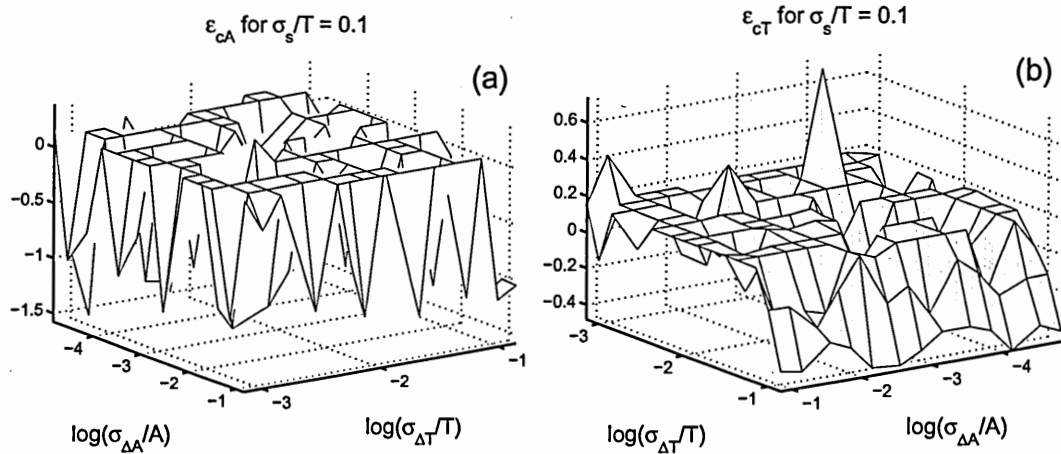


Figure B.35: Extraction errors for the correlation times of the (a) correlated amplitude jitter, $\epsilon_{\Delta A_e}$ and (b) timing jitter, $\epsilon_{\Delta T_e}$, obtained with the uncompensated direct method. σ_A/A —normalized total amplitude jitter. σ_T/T —normalized total timing jitter. σ_s/T —normalized root-mean-squared pulse width.

APPENDIX C

Simulation Results: Compensated Direct Method

C.1 Amplitude Jitter

On the next few pages, the extraction-error surfaces, obtained with the compensated direct method, for total, uncorrelated, and correlated amplitude jitter are plotted against the normalized total amplitude jitter and the normalized total timing jitter, for each of seven normalized RMS pulse widths. The contours of these surfaces are also included.

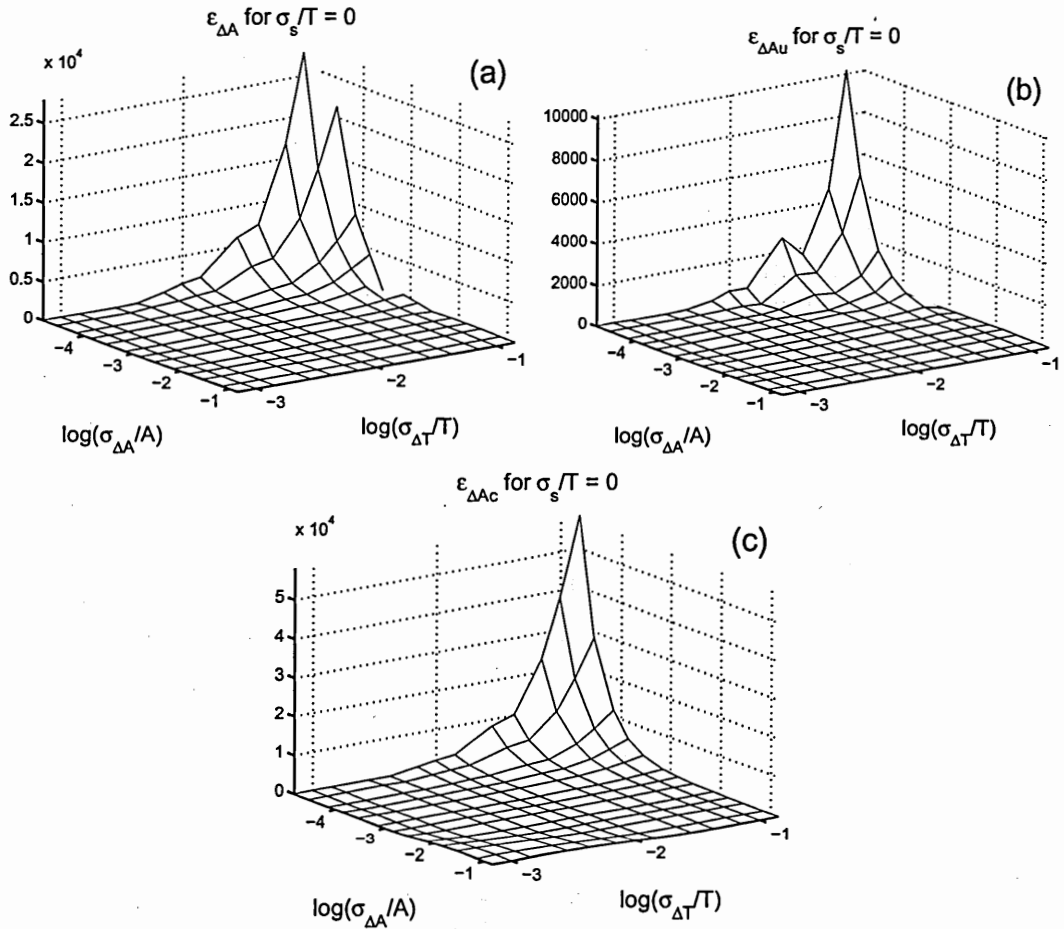


Figure C.1: Extraction errors for (a) total amplitude jitter, $\epsilon_{\Delta A}$, (b) uncorrelated amplitude jitter, $\epsilon_{\Delta A_u}$, and (c) correlated amplitude jitter, $\epsilon_{\Delta A_c}$, obtained with the compensated direct method. σ_A/A —normalized total amplitude jitter. σ_T/T —normalized total timing jitter. σ_s/T —normalized root-mean-squared pulse width.

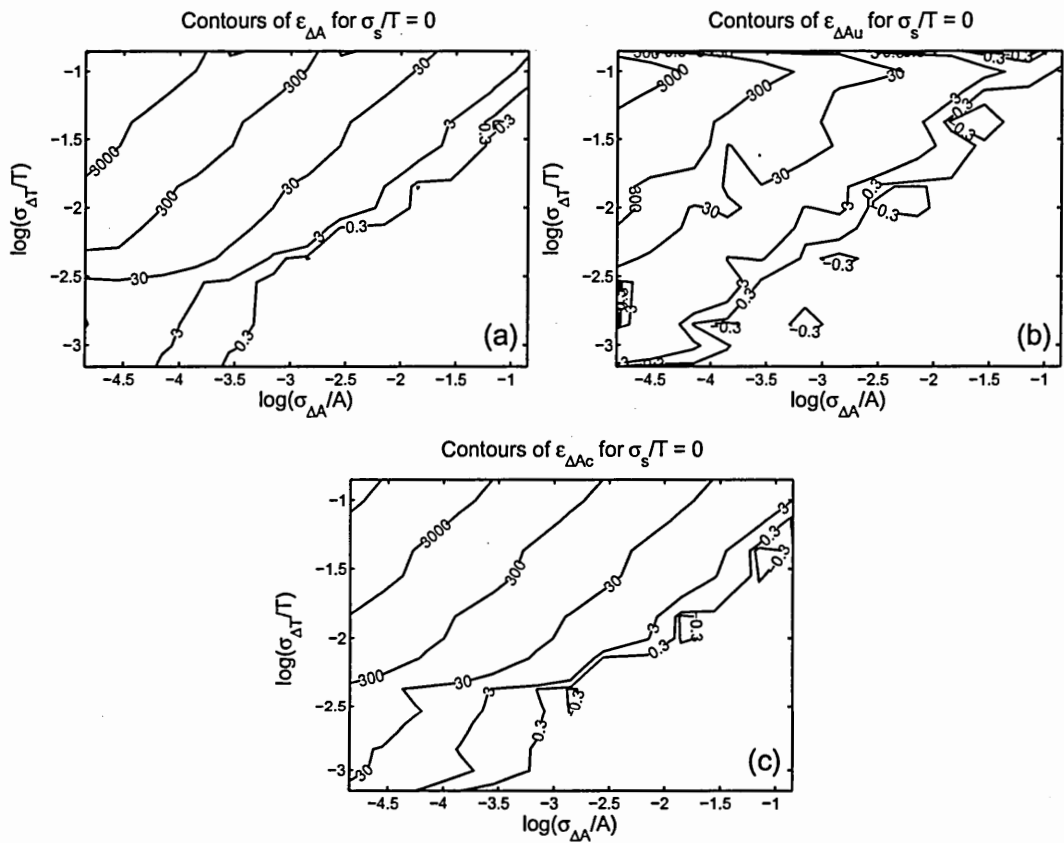


Figure C.2: The contours of the plots shown in C.1

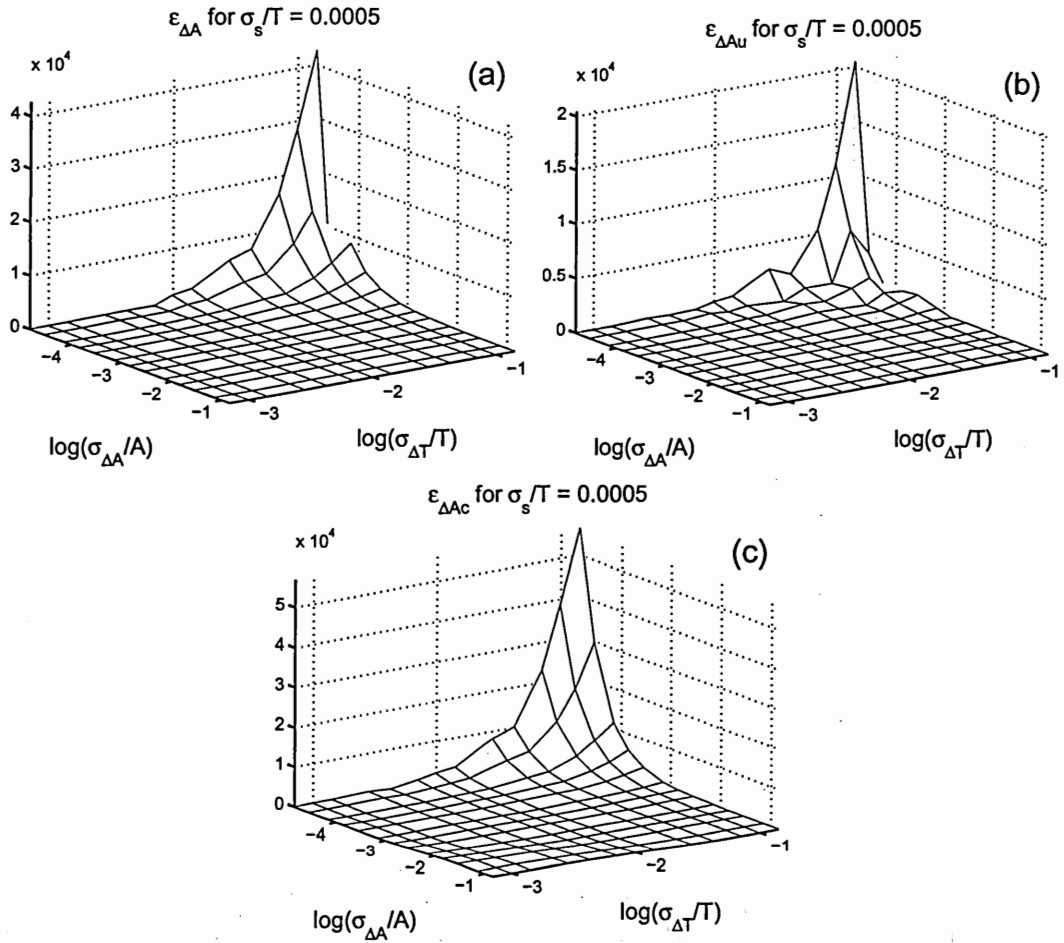


Figure C.3: Extraction errors for (a) total amplitude jitter, $\epsilon_{\Delta A}$, (b) uncorrelated amplitude jitter, $\epsilon_{\Delta A_u}$, and (c) correlated amplitude jitter, $\epsilon_{\Delta A_c}$, obtained with the compensated direct method. σ_A/A —normalized total amplitude jitter. σ_T/T —normalized total timing jitter. σ_s/T —normalized root-mean-squared pulse width.

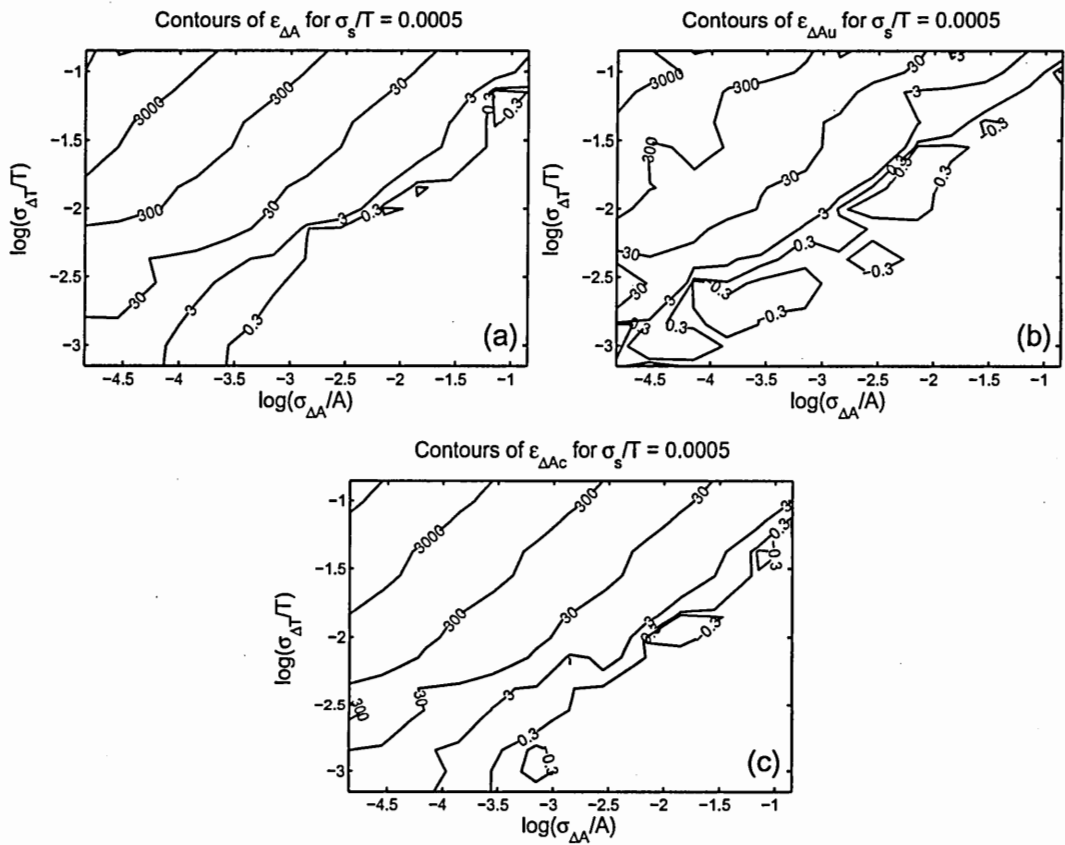


Figure C.4: The contours of the plots shown in C.3

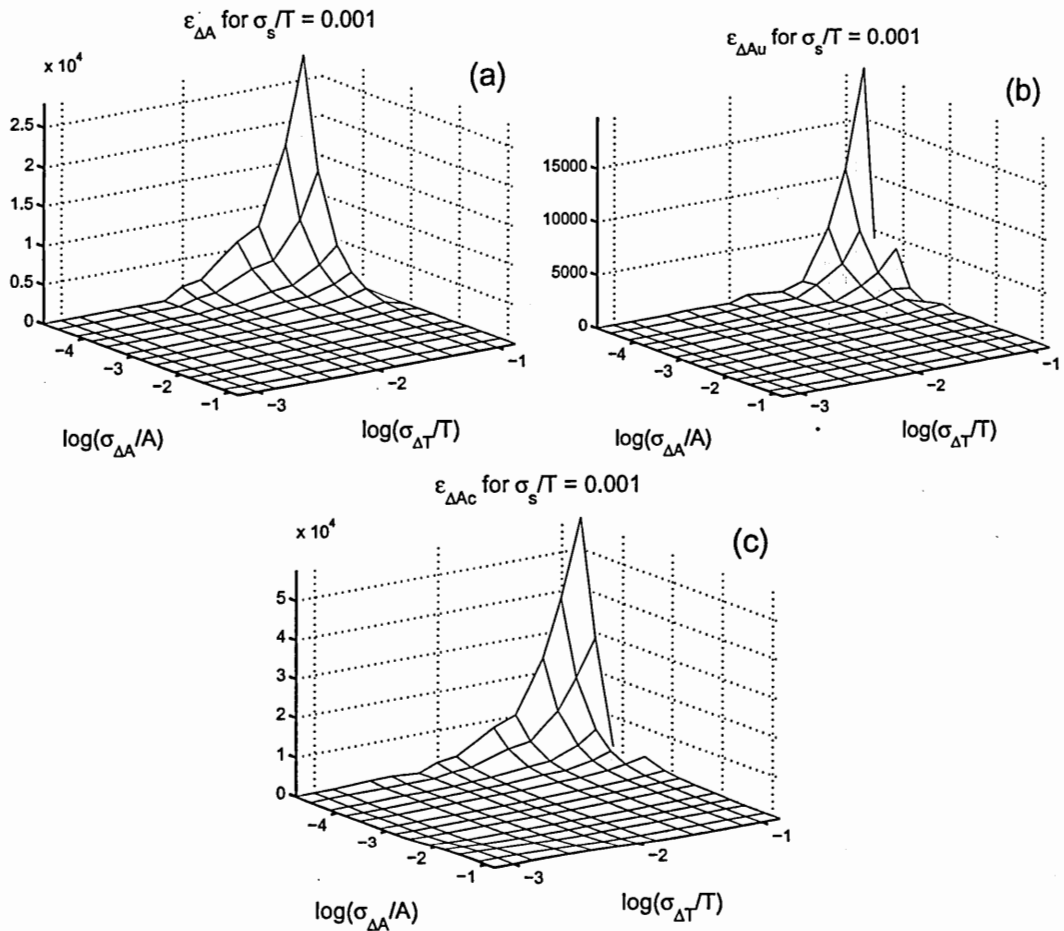


Figure C.5: Extraction errors for (a) total amplitude jitter, $\epsilon_{\Delta A}$, (b) uncorrelated amplitude jitter, $\epsilon_{\Delta A_u}$, and (c) correlated amplitude jitter, $\epsilon_{\Delta A_c}$, obtained with the compensated direct method. σ_A/A —normalized total amplitude jitter. σ_T/T —normalized total timing jitter. σ_s/T —normalized root-mean-squared pulse width.

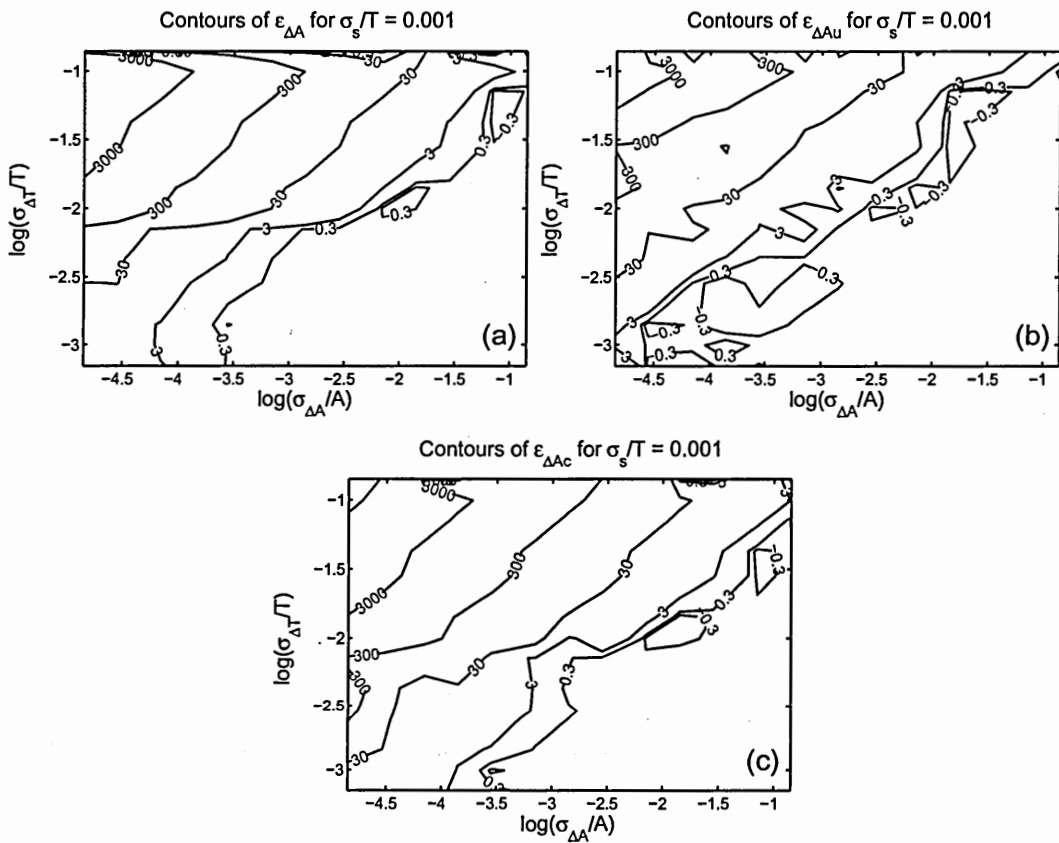


Figure C.6: The contours of the plots shown in C.5

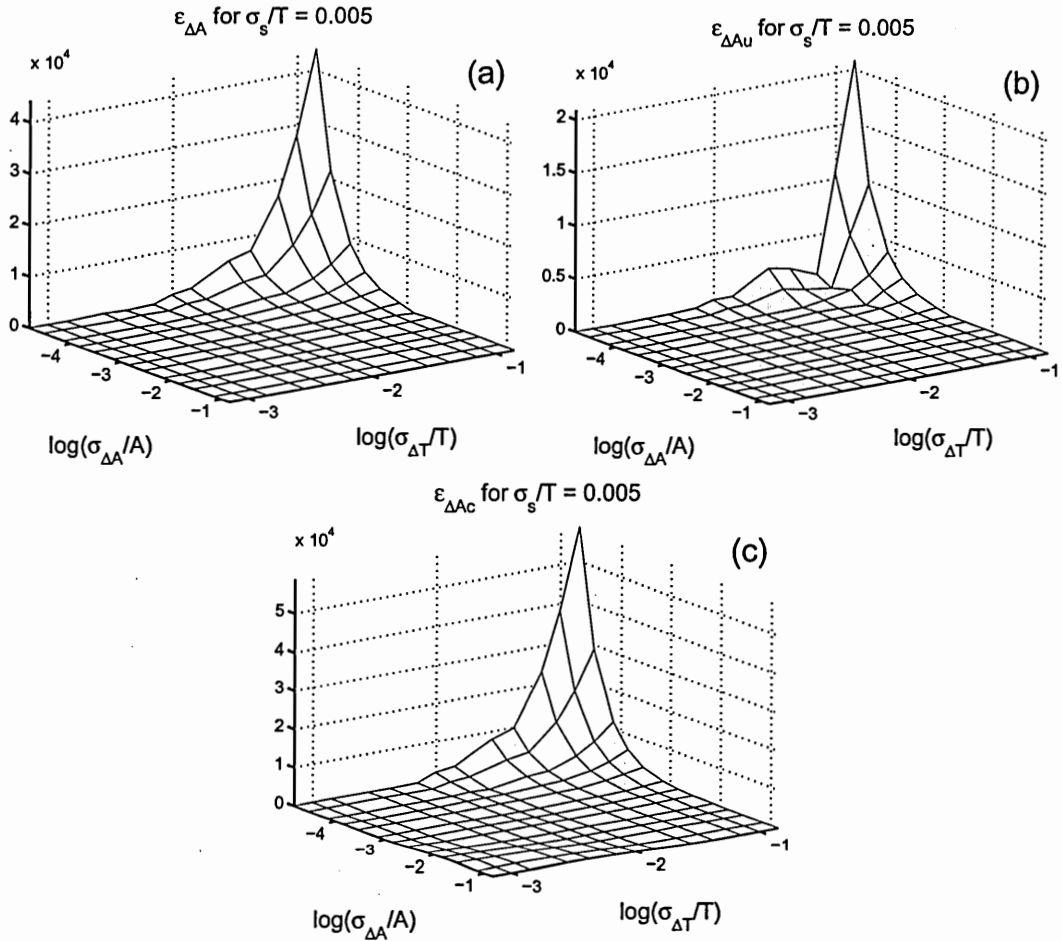


Figure C.7: Extraction errors for (a) total amplitude jitter, $\epsilon_{\Delta A}$, (b) uncorrelated amplitude jitter, $\epsilon_{\Delta Au}$, and (c) correlated amplitude jitter, $\epsilon_{\Delta Ac}$, obtained with the compensated direct method. σ_A/A —normalized total amplitude jitter. σ_T/T —normalized total timing jitter. σ_s/T —normalized root-mean-squared pulse width.

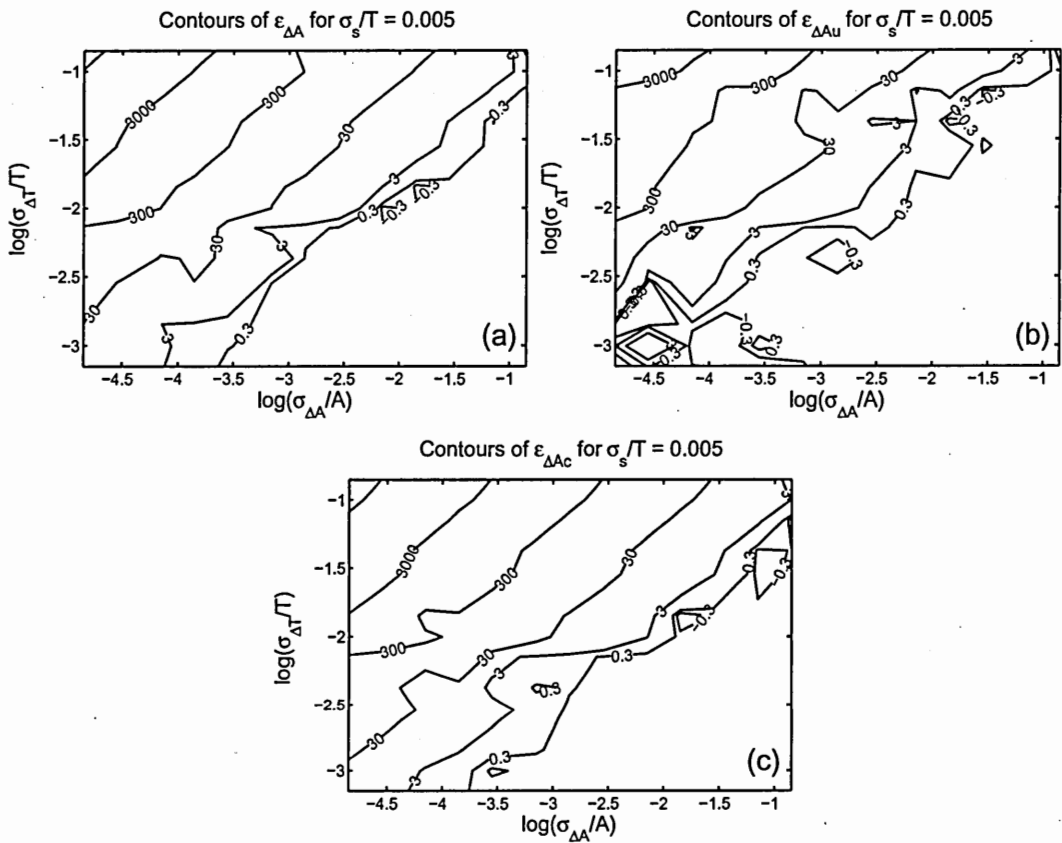


Figure C.8: The contours of the plots shown in C.7

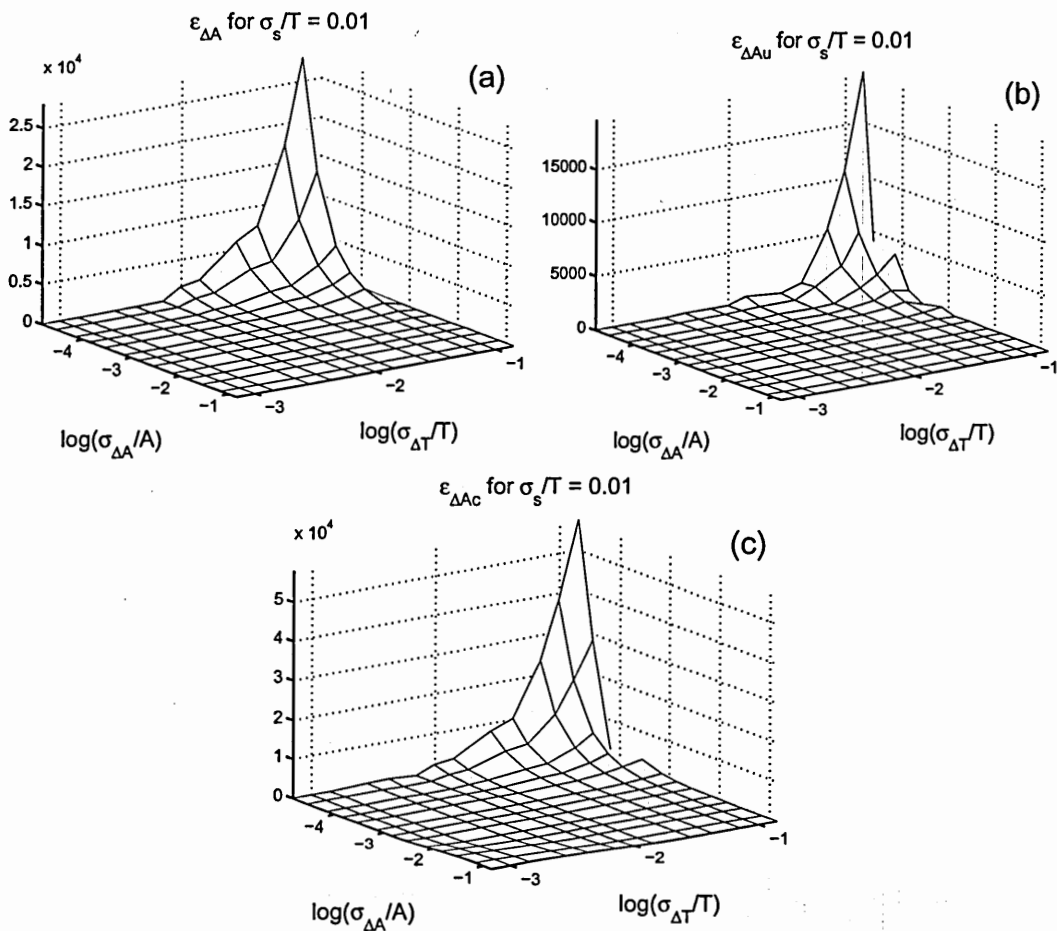


Figure C.9: Extraction errors for (a) total amplitude jitter, $\epsilon_{\Delta A}$, (b) uncorrelated amplitude jitter, $\epsilon_{\Delta A_u}$, and (c) correlated amplitude jitter, $\epsilon_{\Delta A_c}$, obtained with the compensated direct method. σ_A/A —normalized total amplitude jitter. σ_T/T —normalized total timing jitter. σ_s/T —normalized root-mean-squared pulse width.

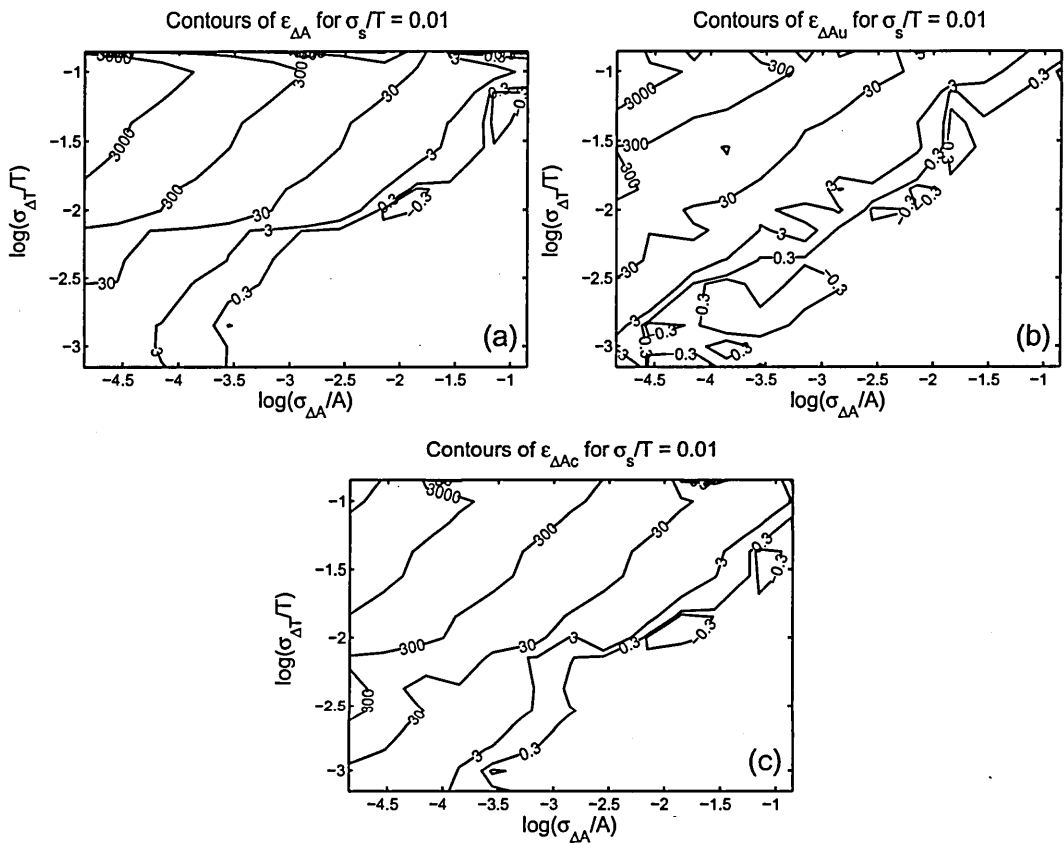


Figure C.10: The contours of the plots shown in C.9

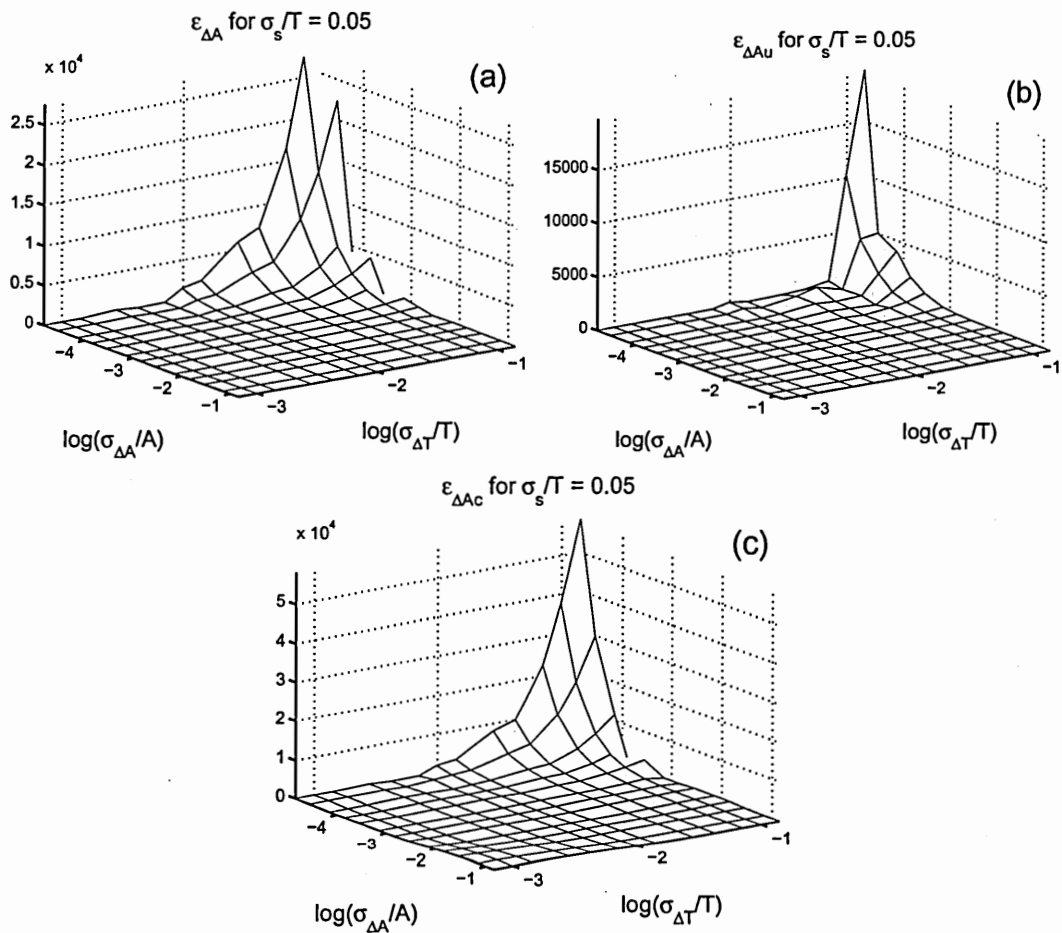


Figure C.11: Extraction errors for (a) total amplitude jitter, $\epsilon_{\Delta A}$, (b) uncorrelated amplitude jitter, $\epsilon_{\Delta A_u}$, and (c) correlated amplitude jitter, $\epsilon_{\Delta A_c}$, obtained with the compensated direct method. σ_A/A —normalized total amplitude jitter. σ_T/T —normalized total timing jitter. σ_s/T —normalized root-mean-squared pulse width.

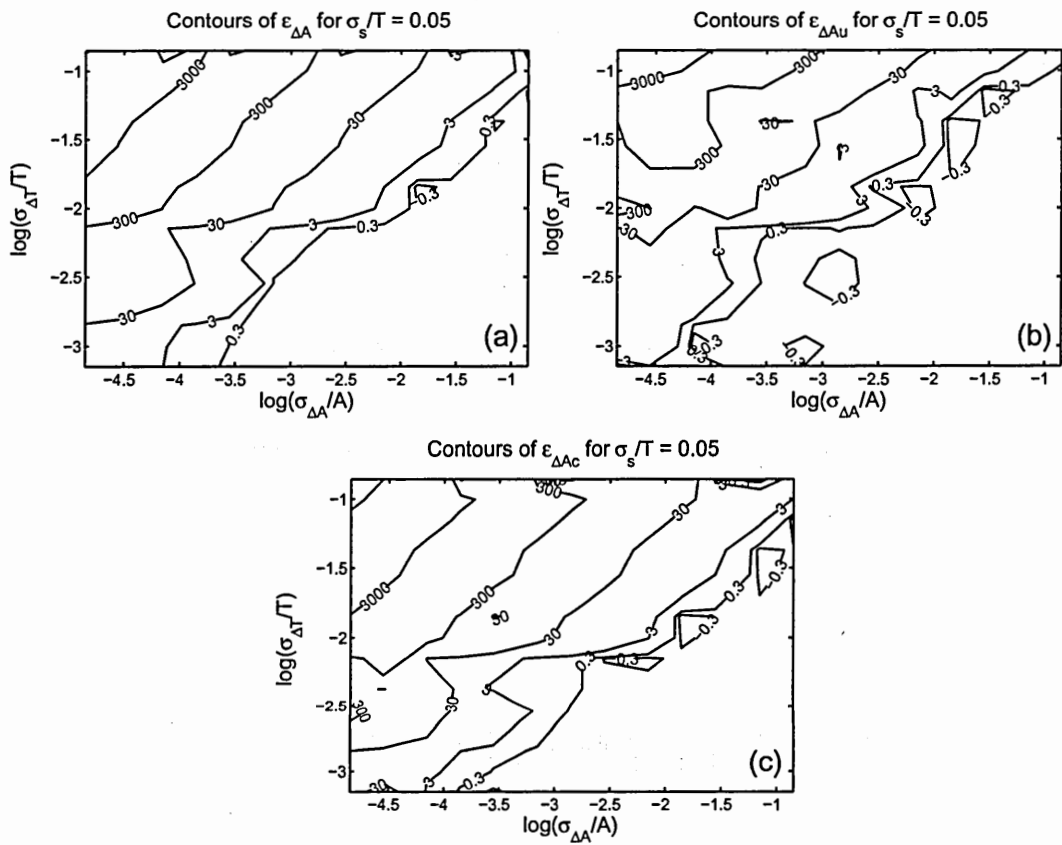


Figure C.12: The contours of the plots shown in C.11

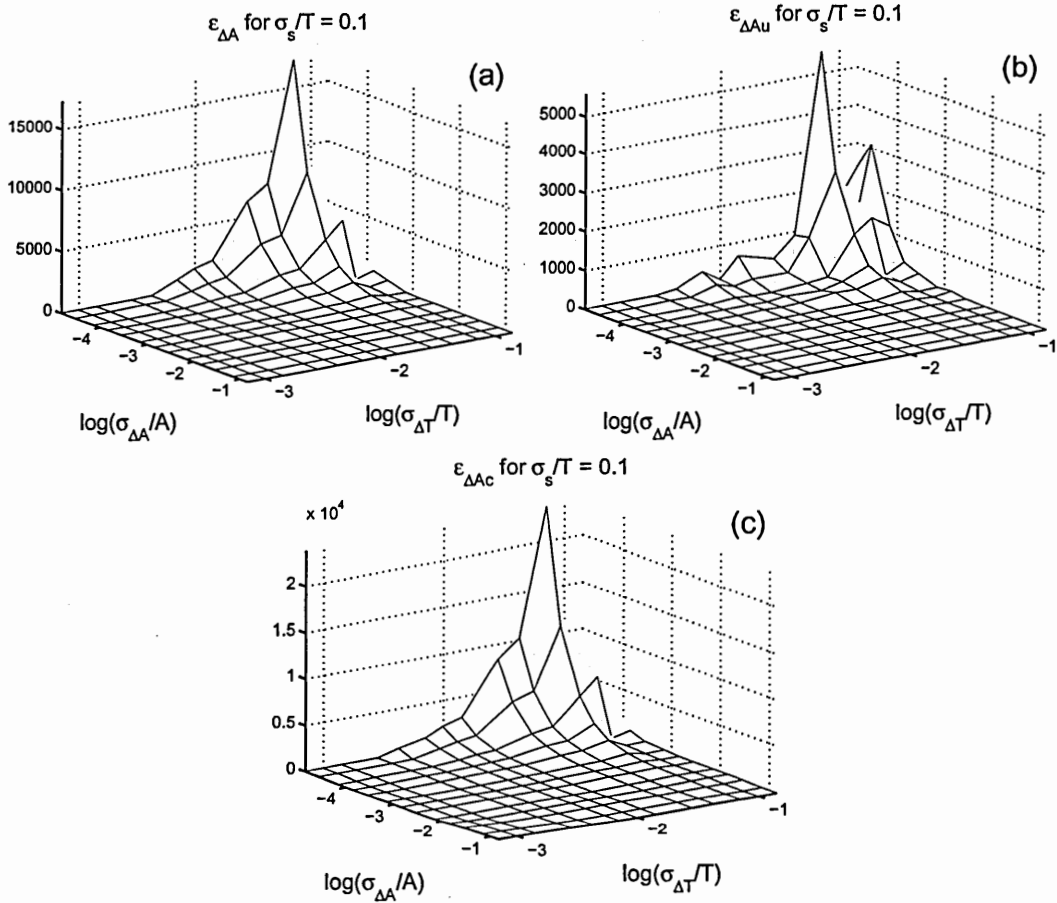


Figure C.13: Extraction errors for (a) total amplitude jitter, $\epsilon_{\Delta A}$, (b) uncorrelated amplitude jitter, $\epsilon_{\Delta A_u}$, and (c) correlated amplitude jitter, $\epsilon_{\Delta A_c}$, obtained with the compensated direct method. σ_A/A —normalized total amplitude jitter. σ_T/T —normalized total timing jitter. σ_s/T —normalized root-mean-squared pulse width.

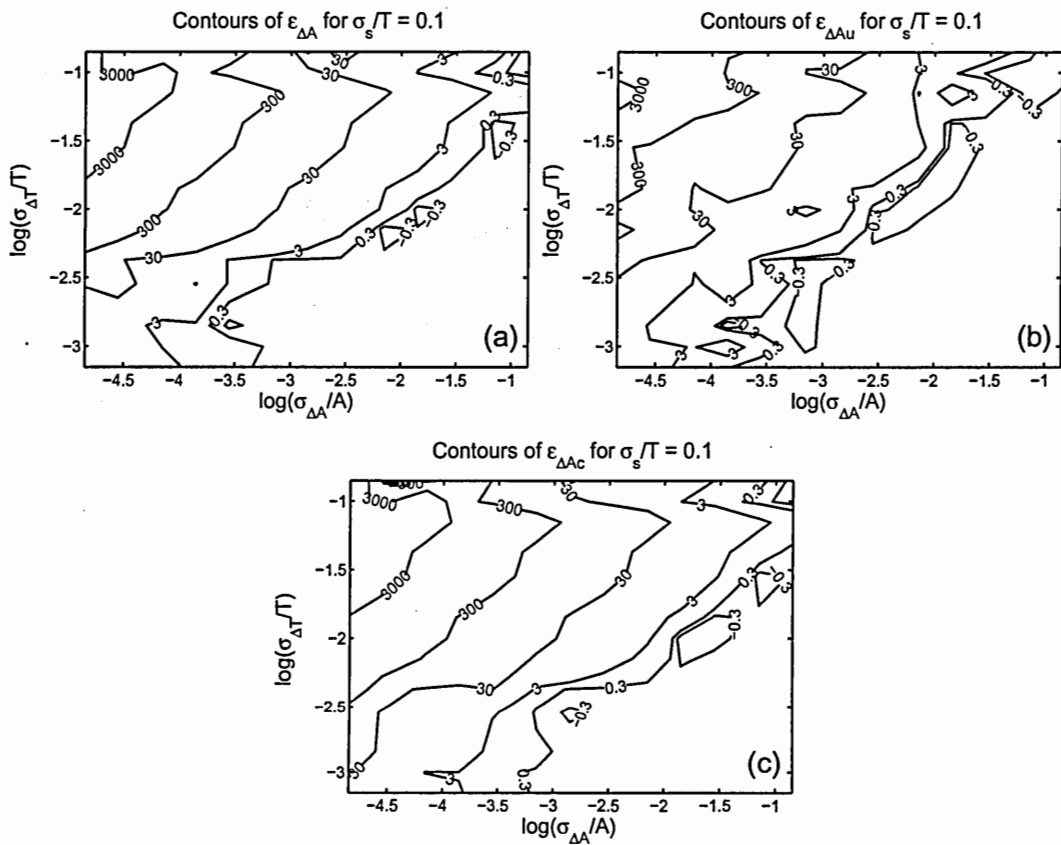


Figure C.14: The contours of the plots shown in C.13

C.2 Timing Jitter

On the next few pages, the extraction-error surfaces, obtained with the compensated direct method, for total, uncorrelated, and correlated timing jitter are plotted against the normalized total amplitude jitter and the normalized total timing jitter, for each of seven normalized RMS pulse widths.

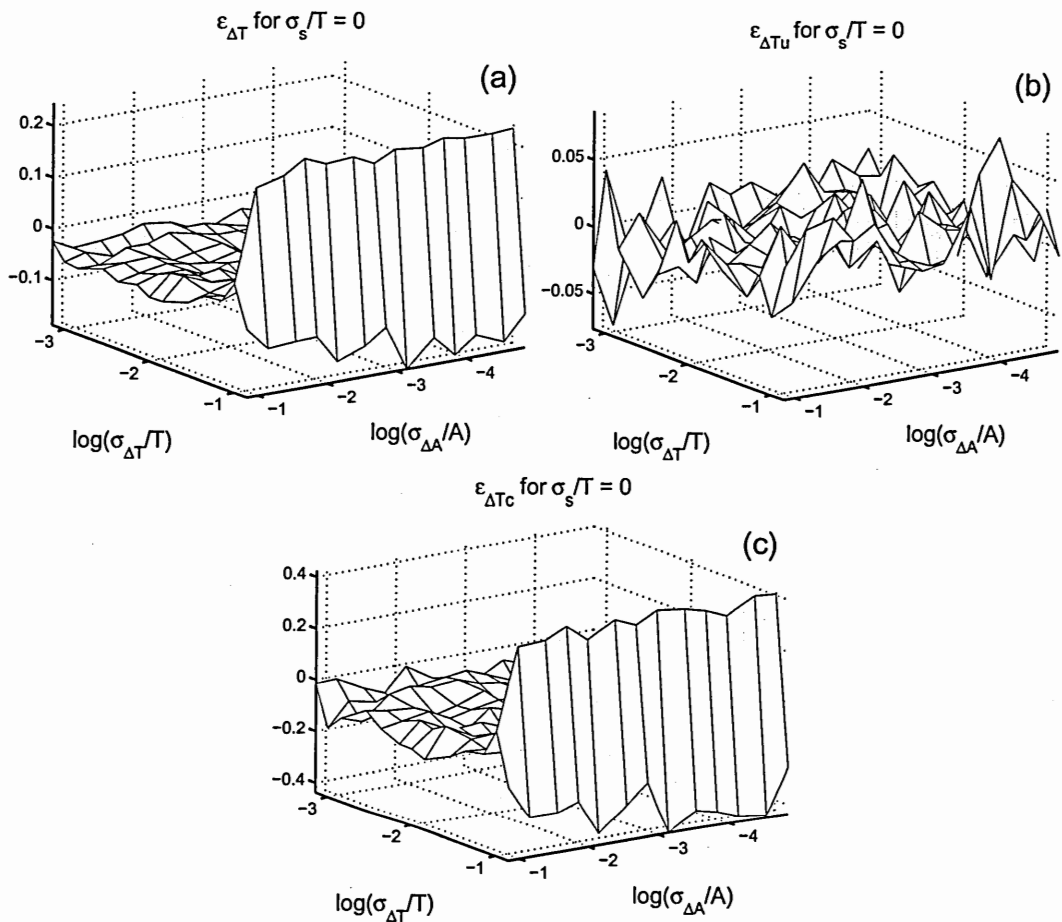


Figure C.15: Extraction errors for (a) total timing jitter, $\epsilon_{\Delta T}$, (b) uncorrelated timing jitter, $\epsilon_{\Delta T_u}$, and (c) correlated timing jitter, $\epsilon_{\Delta T_c}$, obtained with the compensated direct method. σ_A/A —normalized total amplitude jitter. σ_T/T —normalized total timing jitter. σ_s/T —normalized root-mean-squared pulse width.

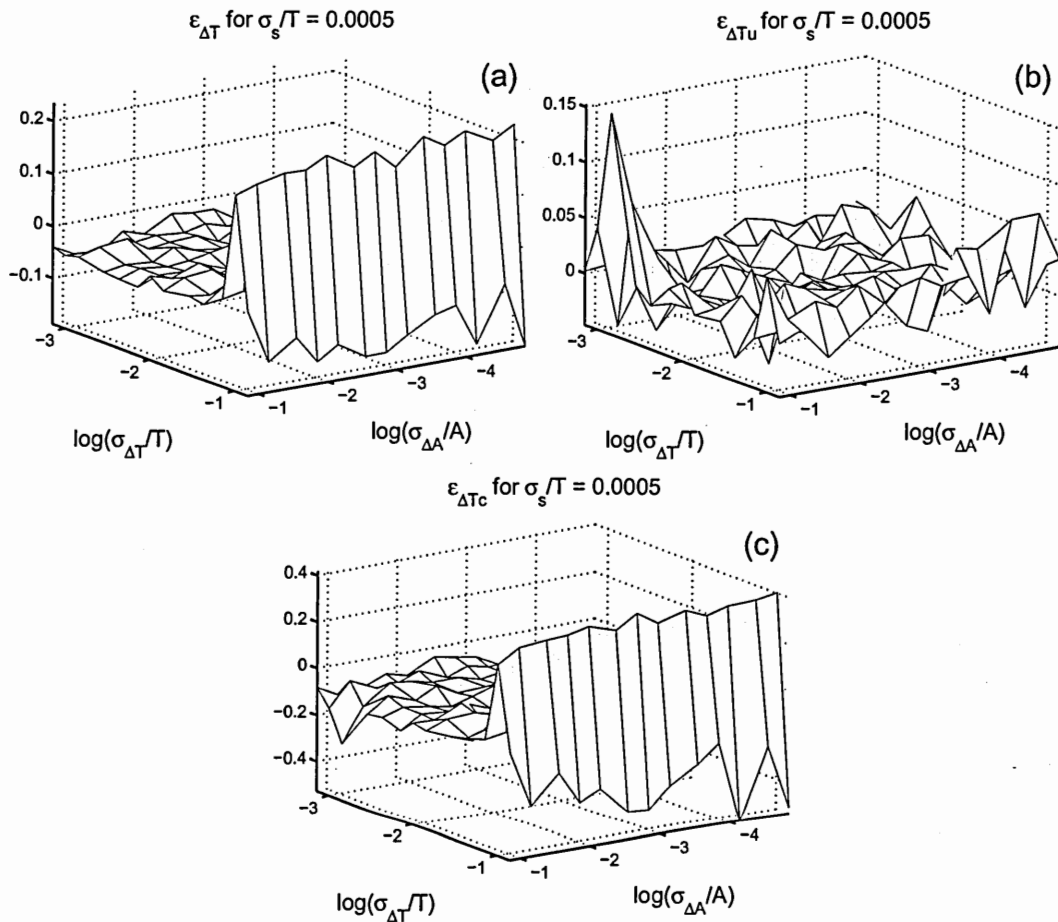


Figure C.16: Extraction errors for (a) total timing jitter, $\epsilon_{\Delta T}$, (b) uncorrelated timing jitter, $\epsilon_{\Delta T_u}$, and (c) correlated timing jitter, $\epsilon_{\Delta T_c}$, obtained with the compensated direct method. σ_A/A —normalized total amplitude jitter. σ_T/T —normalized total timing jitter. σ_s/T —normalized root-mean-squared pulse width.

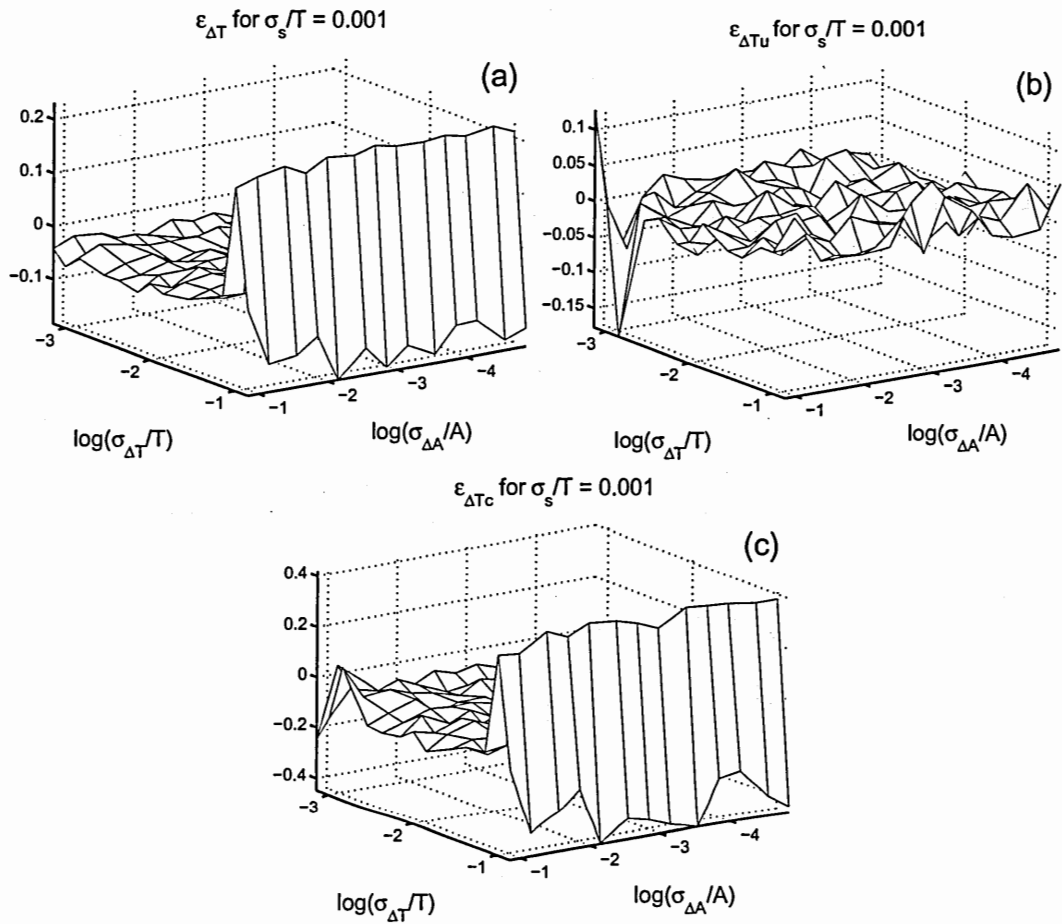


Figure C.17: Extraction errors for (a) total timing jitter, $\epsilon_{\Delta T}$, (b) uncorrelated timing jitter, $\epsilon_{\Delta T_u}$, and (c) correlated timing jitter, $\epsilon_{\Delta T_c}$, obtained with the compensated direct method. σ_A/A —normalized total amplitude jitter. σ_T/T —normalized total timing jitter. σ_s/T —normalized root-mean-squared pulse width.

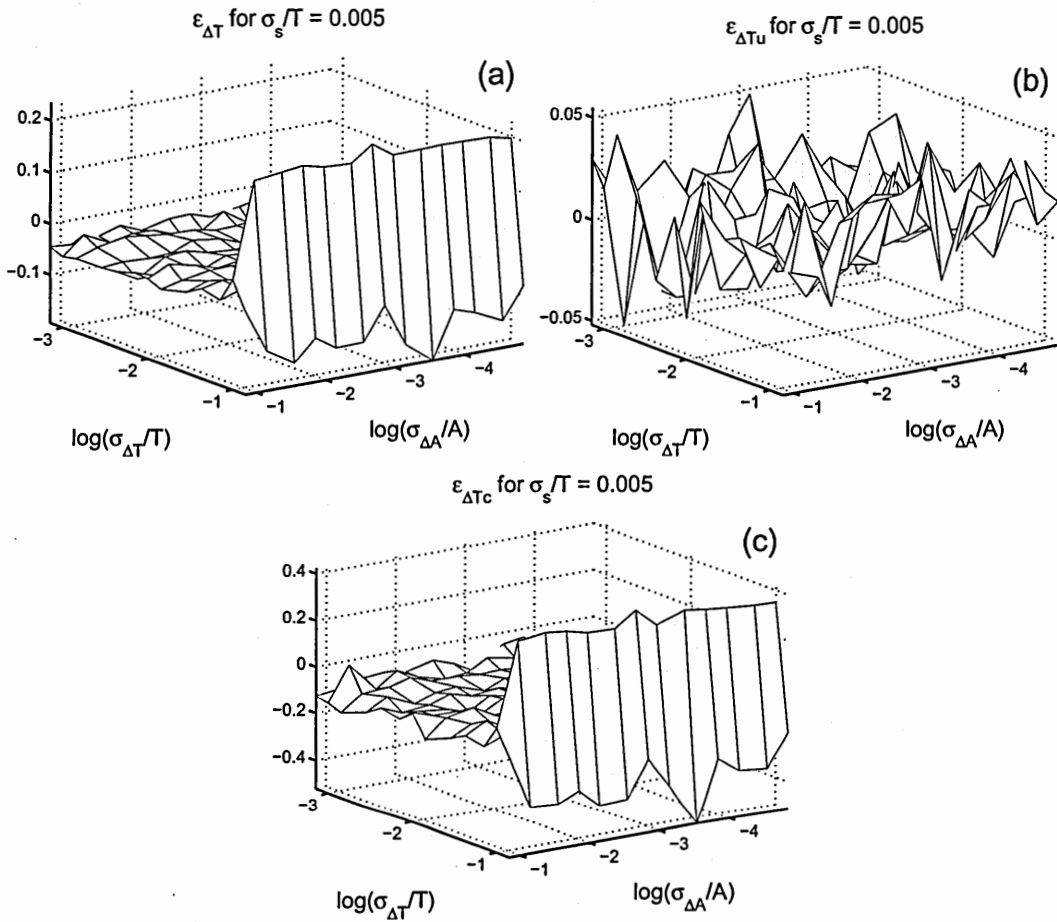


Figure C.18: Extraction errors for (a) total timing jitter, $\epsilon_{\Delta T}$, (b) uncorrelated timing jitter, $\epsilon_{\Delta T_u}$, and (c) correlated timing jitter, $\epsilon_{\Delta T_c}$, obtained with the compensated direct method. σ_A/A —normalized total amplitude jitter. σ_T/T —normalized total timing jitter. σ_s/T —normalized root-mean-squared pulse width.

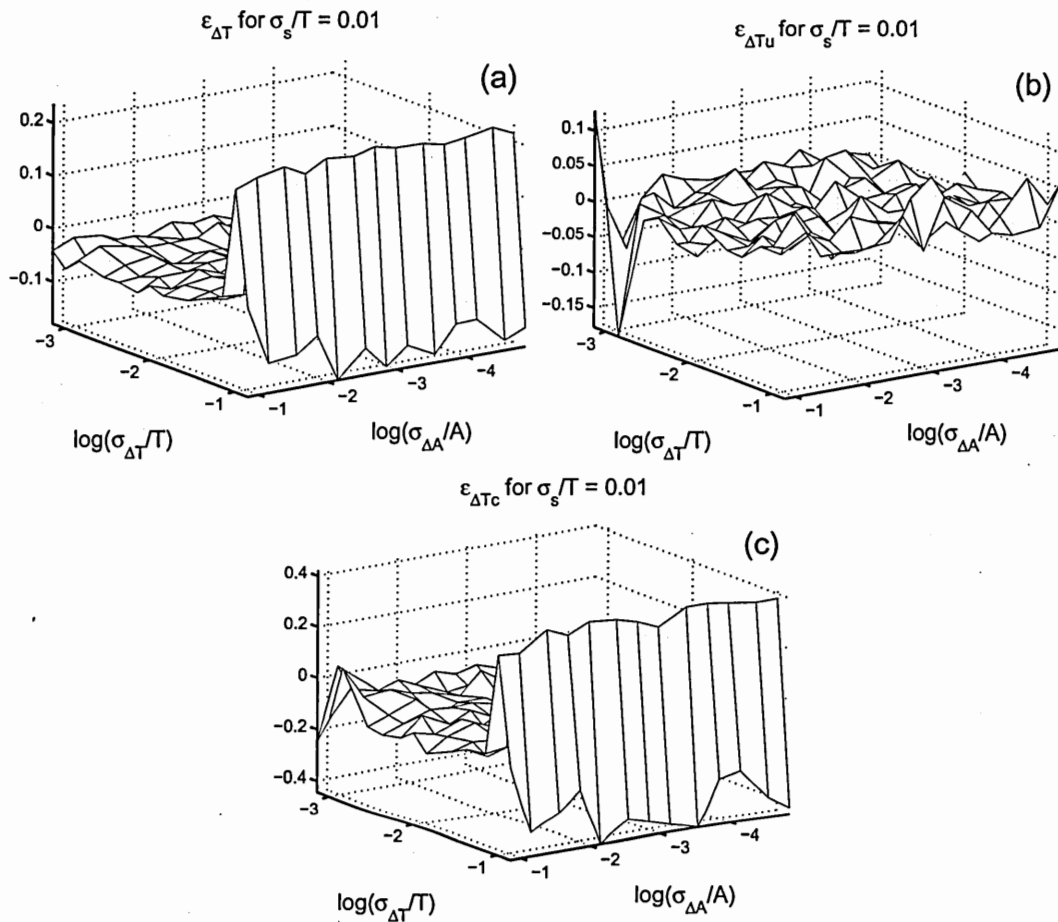


Figure C.19: Extraction errors for (a) total timing jitter, $\epsilon_{\Delta T}$, (b) uncorrelated timing jitter, $\epsilon_{\Delta T_u}$, and (c) correlated timing jitter, $\epsilon_{\Delta T_c}$, obtained with the compensated direct method. σ_A/A —normalized total amplitude jitter. σ_T/T —normalized total timing jitter. σ_s/T —normalized root-mean-squared pulse width.

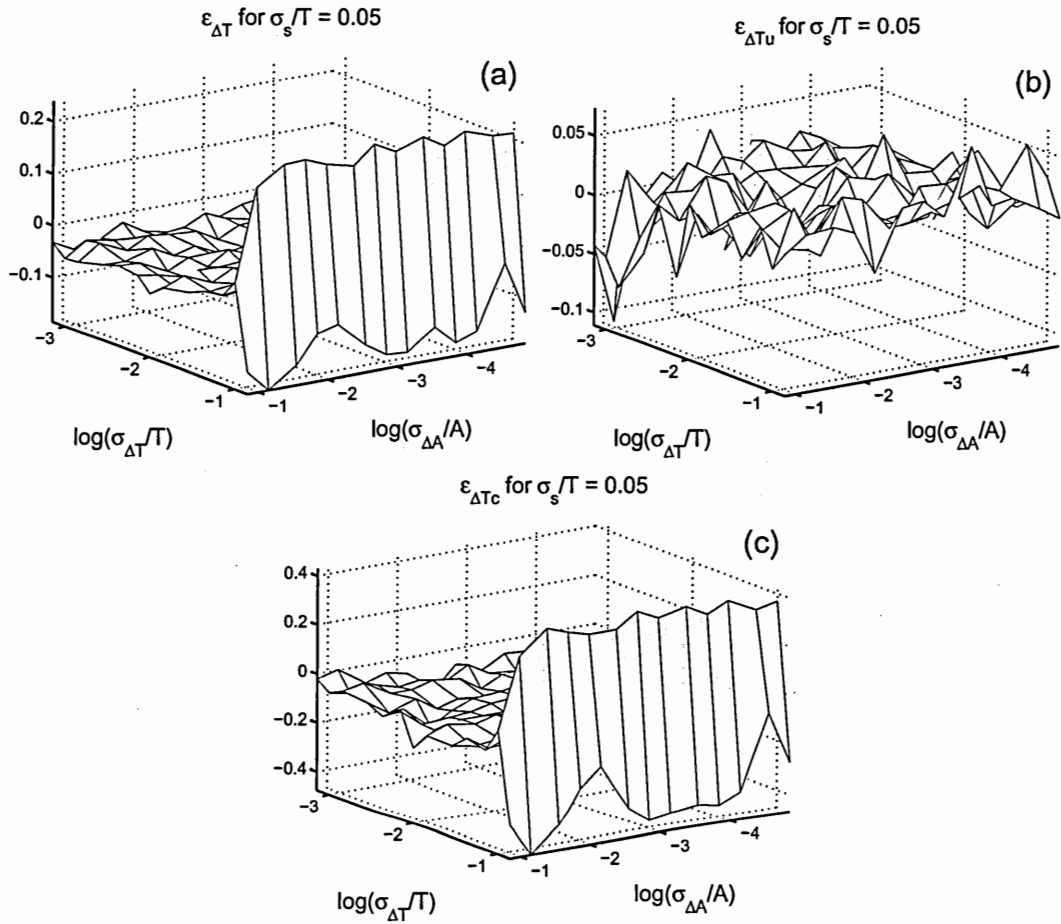


Figure C.20: Extraction errors for (a) total timing jitter, $\epsilon_{\Delta T}$, (b) uncorrelated timing jitter, $\epsilon_{\Delta T_u}$, and (c) correlated timing jitter, $\epsilon_{\Delta T_c}$, obtained with the compensated direct method. σ_A/A —normalized total amplitude jitter. σ_T/T —normalized total timing jitter. σ_s/T —normalized root-mean-squared pulse width.

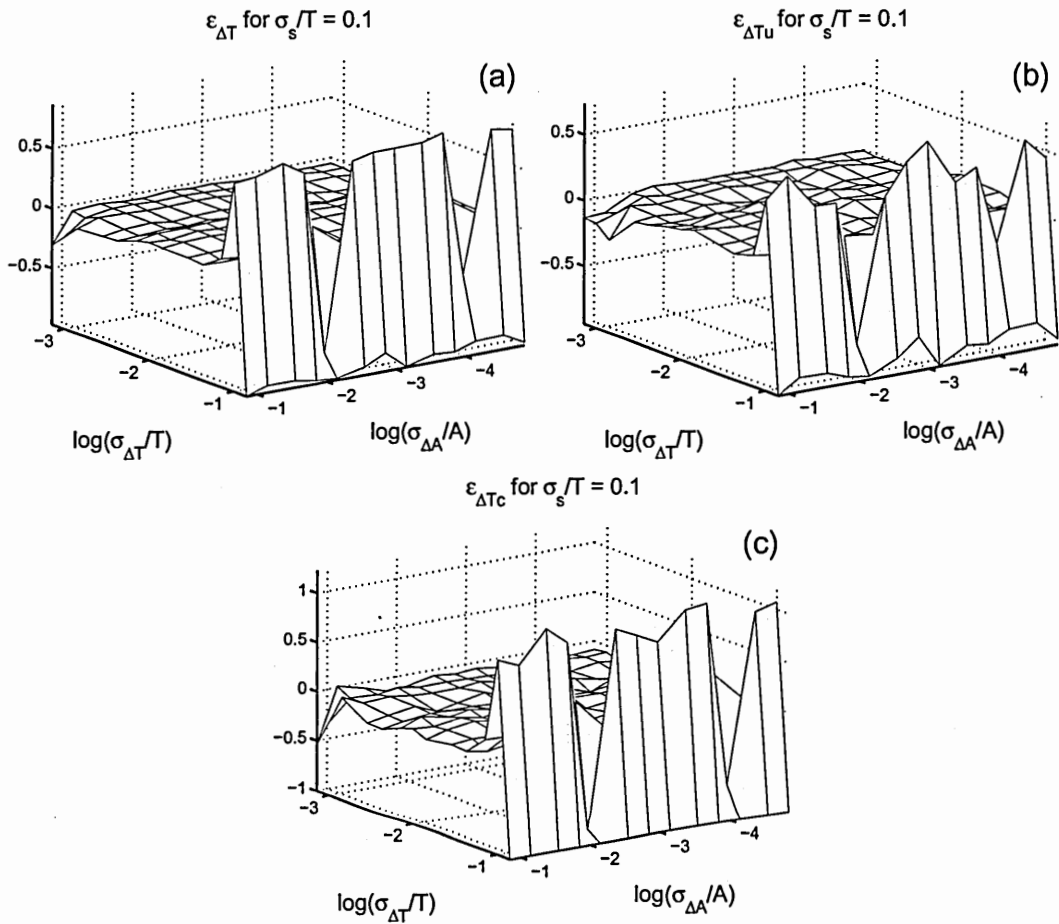


Figure C.21: Extraction errors for (a) total timing jitter, $\epsilon_{\Delta T}$, (b) uncorrelated timing jitter, $\epsilon_{\Delta T_u}$, and (c) correlated timing jitter, $\epsilon_{\Delta T_c}$, obtained with the compensated direct method. σ_A/A —normalized total amplitude jitter. σ_T/T —normalized total timing jitter. σ_s/T —normalized root-mean-squared pulse width.

C.3 Correlation Time

The compensation routine does nothing to the correlation times. Therefore, the correlation-time-error plots of the compensated direct technique are identical to those of the uncompensated direct method¹ and are omitted.

¹ See Section B.3.

APPENDIX D

Simulation Results: Uncompensated Mixing Method

D.1 Amplitude Jitter

On the next few pages, the extraction-error surfaces, obtained with the uncompensated mixing method, for total, uncorrelated, and correlated amplitude jitter are plotted against the normalized total amplitude jitter and the normalized total timing jitter, for each of seven normalized RMS pulse widths. The contours of these surfaces are also included.

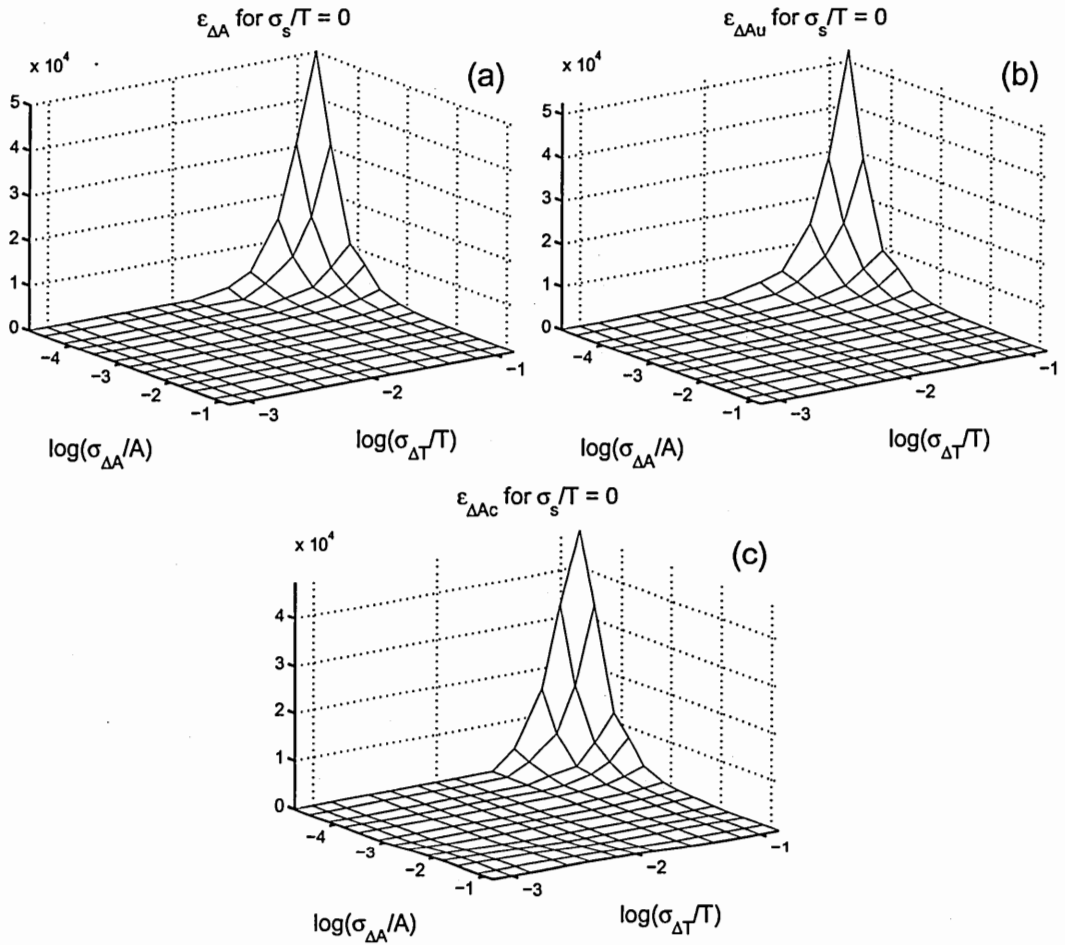


Figure D.1: Extraction errors for (a) total amplitude jitter, $\epsilon_{\Delta A}$, (b) uncorrelated amplitude jitter, $\epsilon_{\Delta A_u}$, and (c) correlated amplitude jitter, $\epsilon_{\Delta A_c}$, obtained with the uncompensated mixing method. σ_A/A —normalized total amplitude jitter. σ_T/T —normalized total timing jitter. σ_s/T —normalized root-mean-squared pulse width.

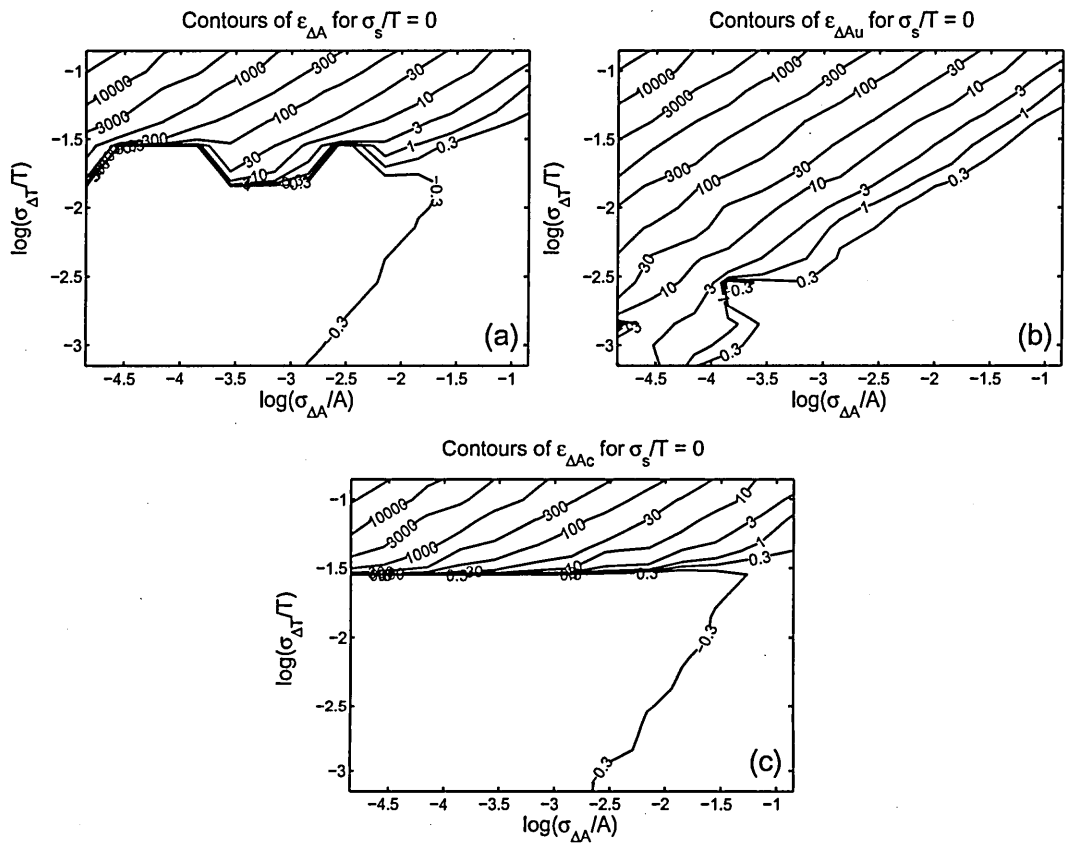


Figure D.2: The contours of the plots shown in D.1

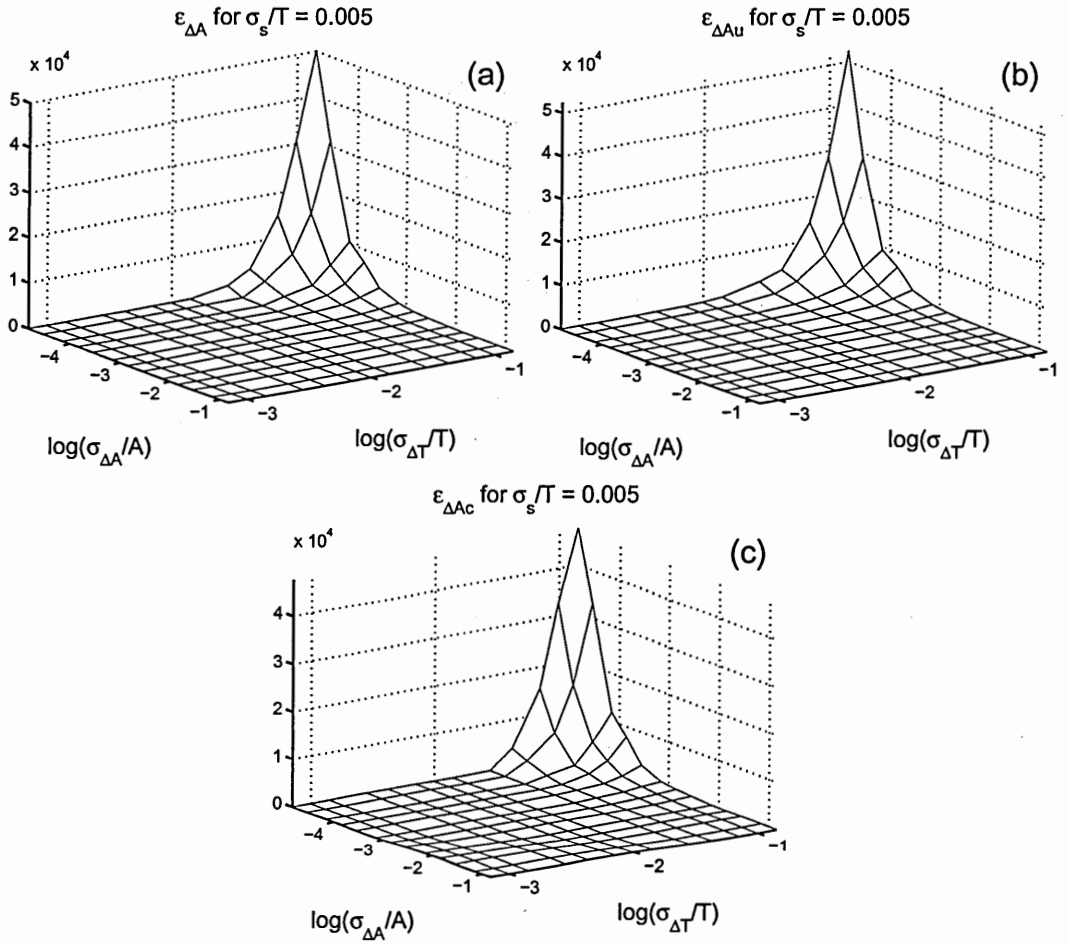


Figure D.3: Extraction errors for (a) total amplitude jitter, $\epsilon_{\Delta A}$, (b) uncorrelated amplitude jitter, $\epsilon_{\Delta Au}$, and (c) correlated amplitude jitter, $\epsilon_{\Delta Ac}$, obtained with the uncompensated mixing method. σ_A/A —normalized total amplitude jitter. σ_T/T —normalized total timing jitter. σ_s/T —normalized root-mean-squared pulse width.

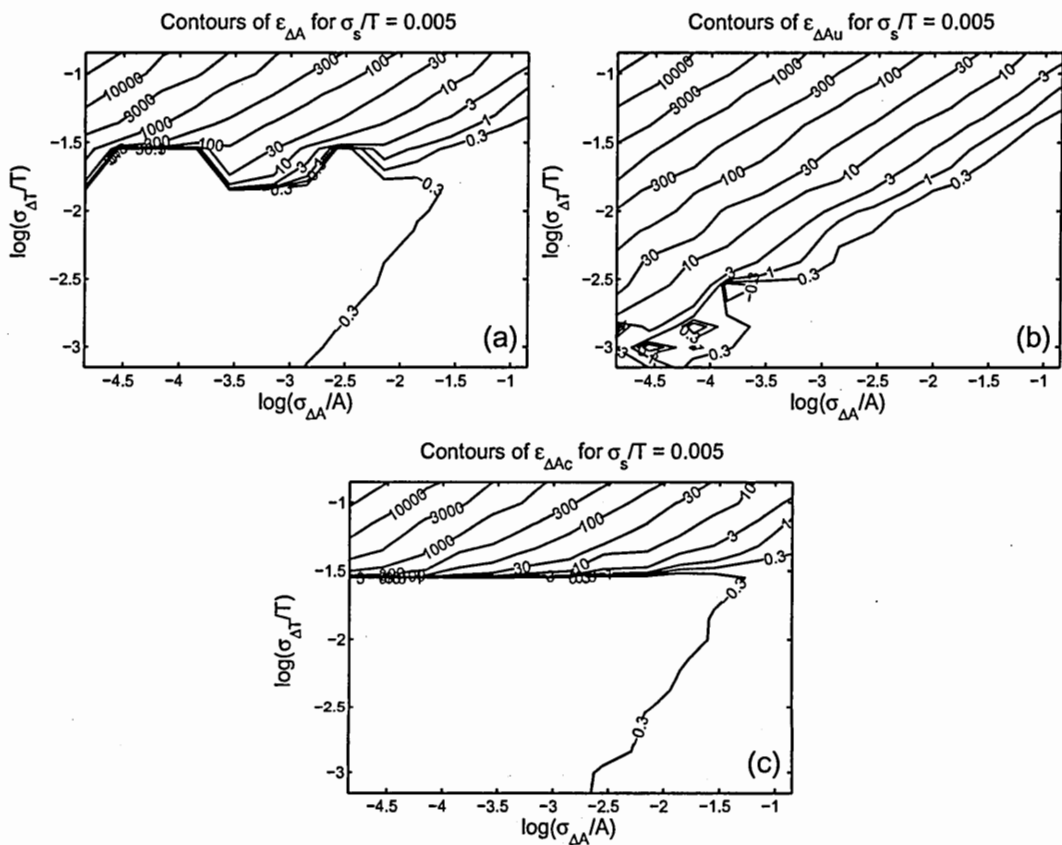


Figure D.4: The contours of the plots shown in D.3

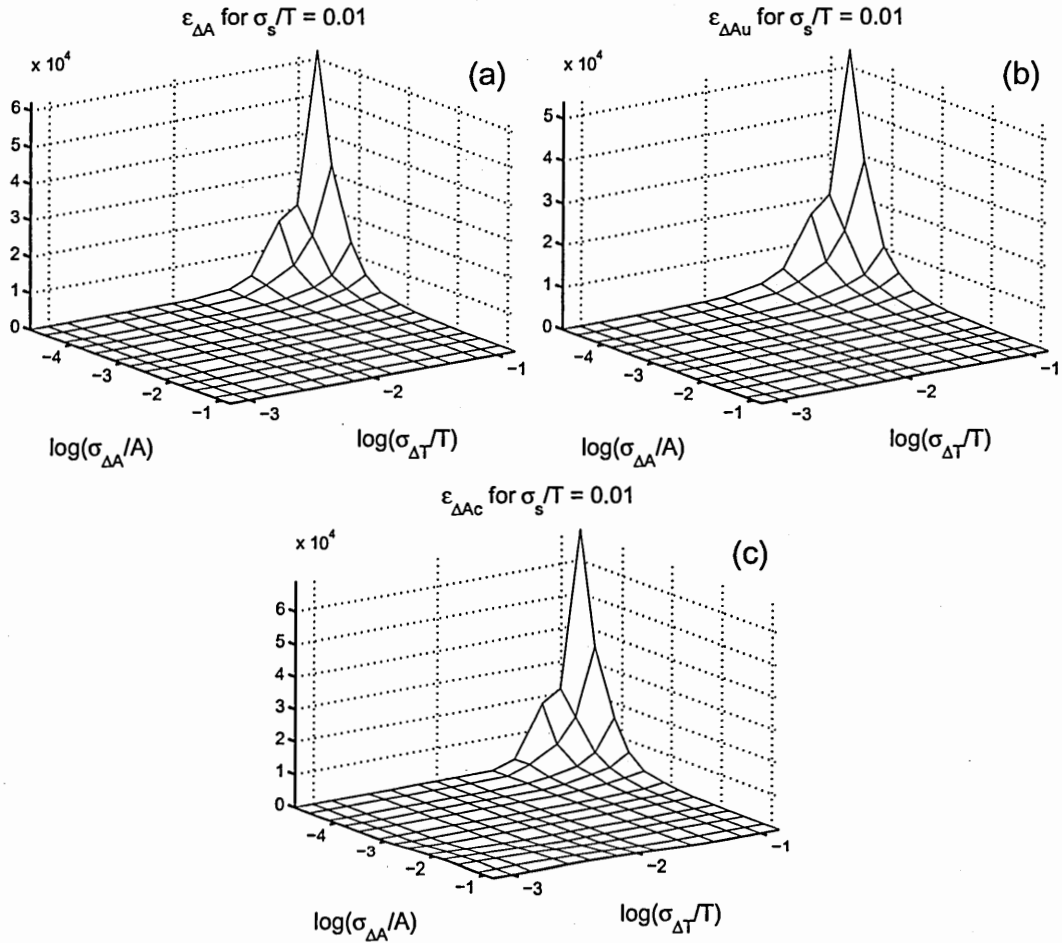


Figure D.5: Extraction errors for (a) total amplitude jitter, $\epsilon_{\Delta A}$, (b) uncorrelated amplitude jitter, $\epsilon_{\Delta Au}$, and (c) correlated amplitude jitter, $\epsilon_{\Delta Ac}$, obtained with the uncompensated mixing method. σ_A/A —normalized total amplitude jitter. σ_T/T —normalized total timing jitter. σ_s/T —normalized root-mean-squared pulse width.

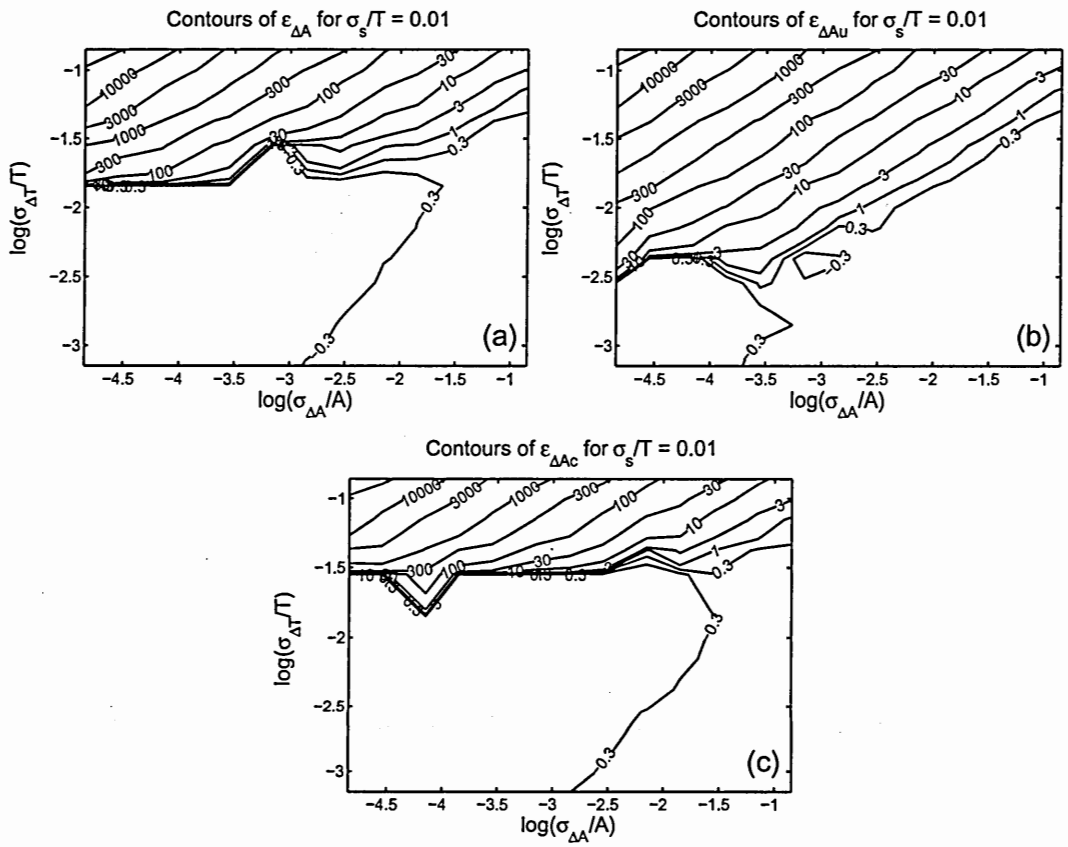


Figure D.6: The contours of the plots shown in D.5

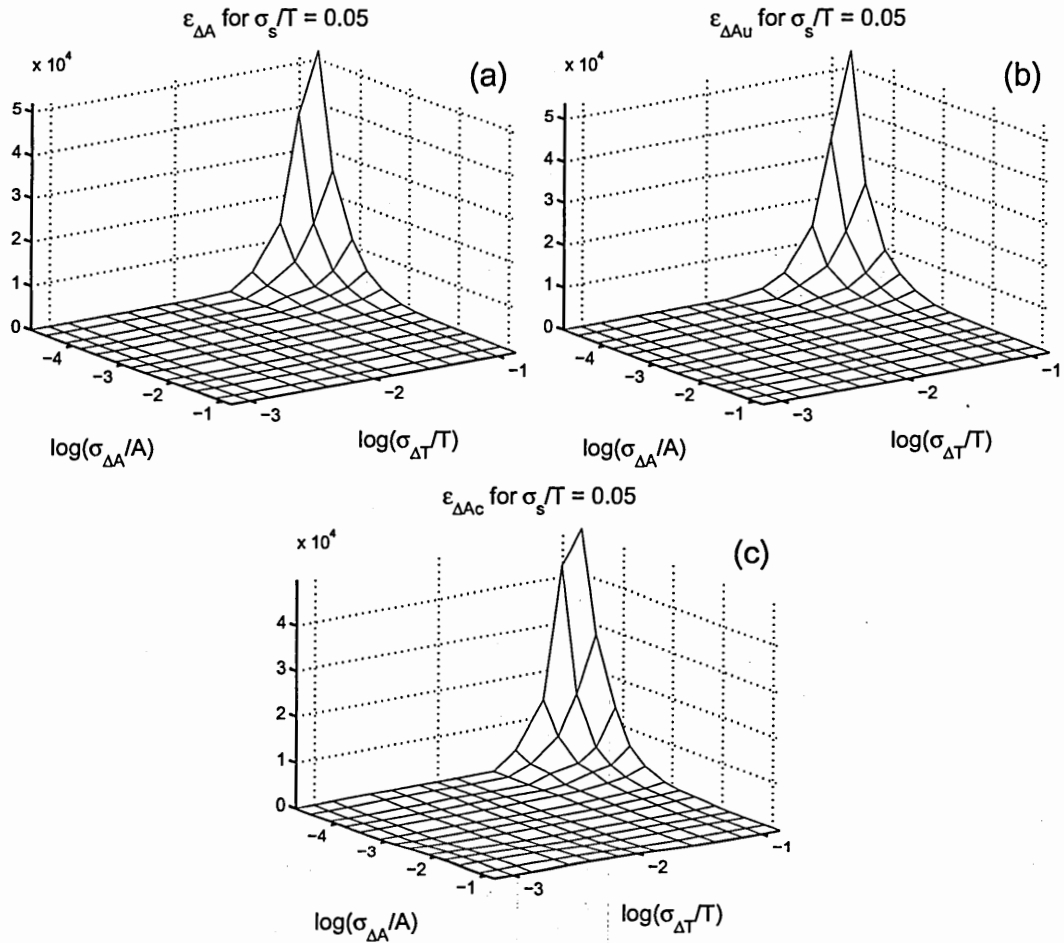


Figure D.7: Extraction errors for (a) total amplitude jitter, $\epsilon_{\Delta A}$, (b) uncorrelated amplitude jitter, $\epsilon_{\Delta Au}$, and (c) correlated amplitude jitter, $\epsilon_{\Delta Ac}$, obtained with the uncompensated mixing method. σ_A/A —normalized total amplitude jitter. σ_T/T —normalized total timing jitter. σ_s/T —normalized root-mean-squared pulse width.

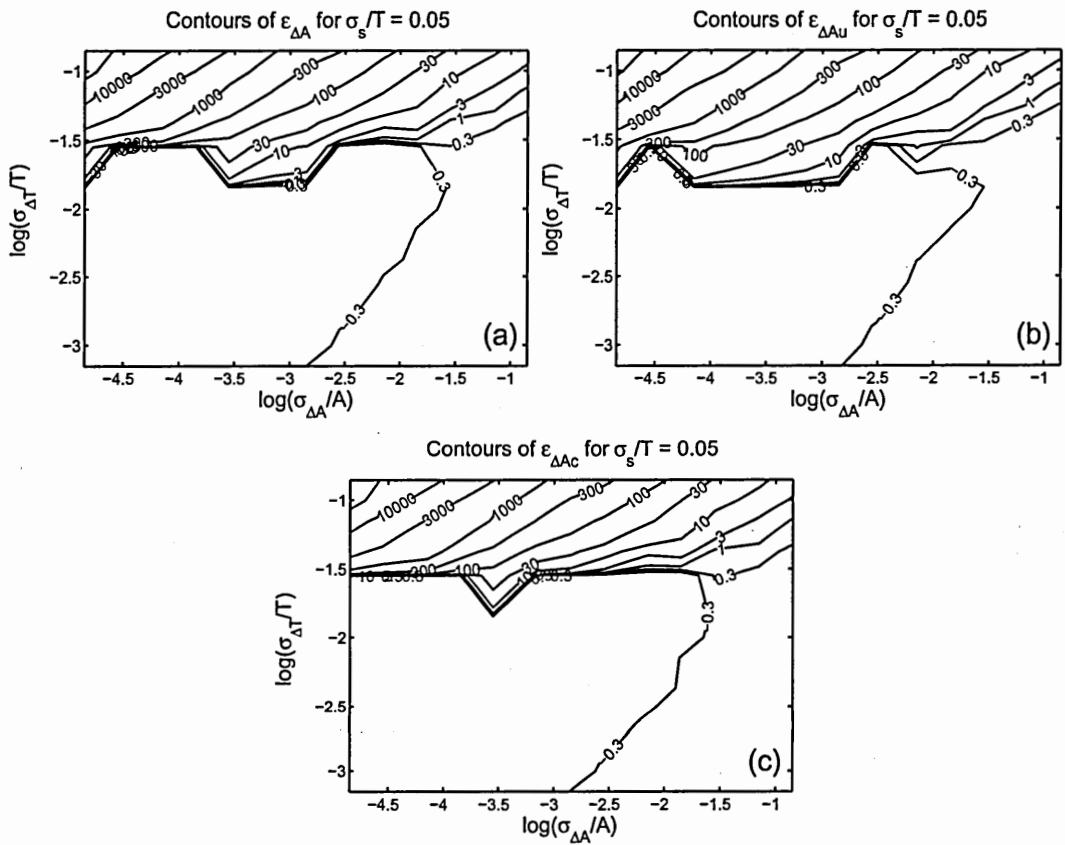


Figure D.8: The contours of the plots shown in D.7

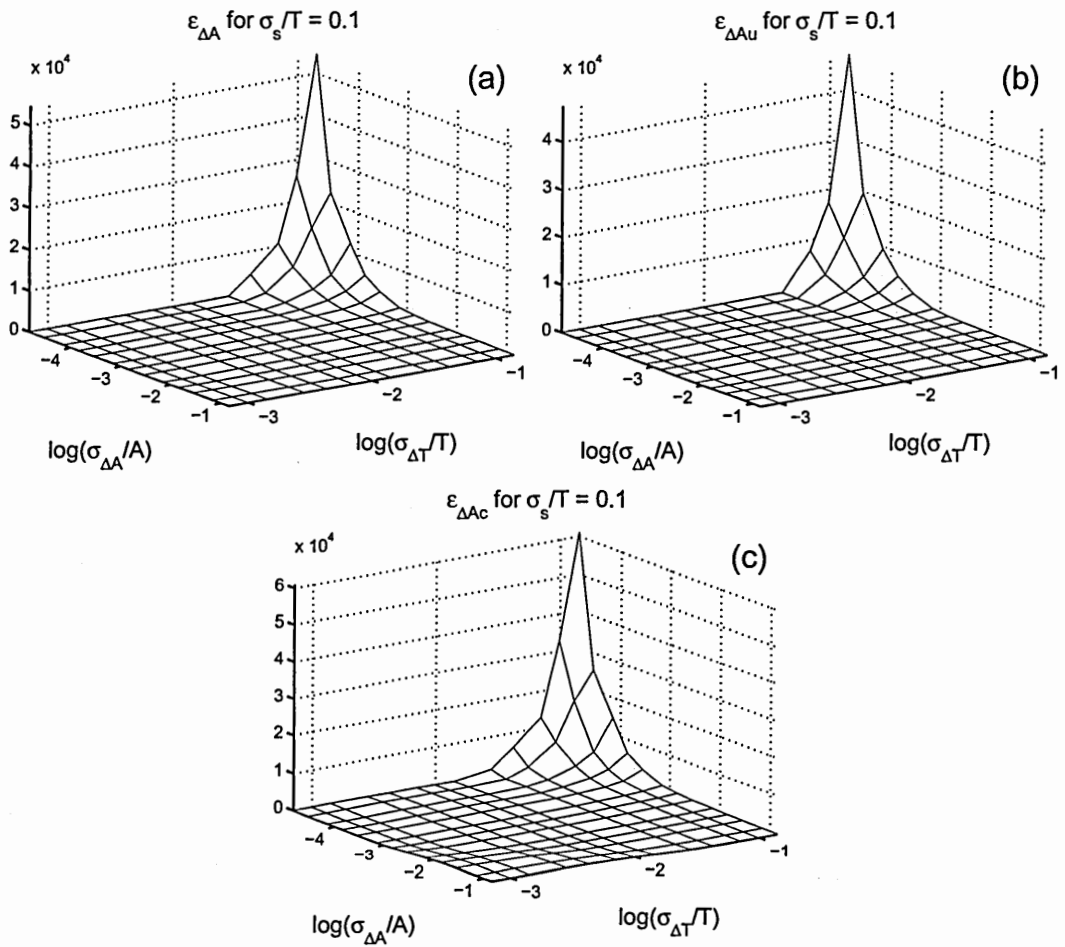


Figure D.9: Extraction errors for (a) total amplitude jitter, $\epsilon_{\Delta A}$, (b) uncorrelated amplitude jitter, $\epsilon_{\Delta Au}$, and (c) correlated amplitude jitter, $\epsilon_{\Delta Ac}$, obtained with the uncompensated mixing method. σ_A/A —normalized total amplitude jitter. σ_T/T —normalized total timing jitter. σ_s/T —normalized root-mean-squared pulse width.

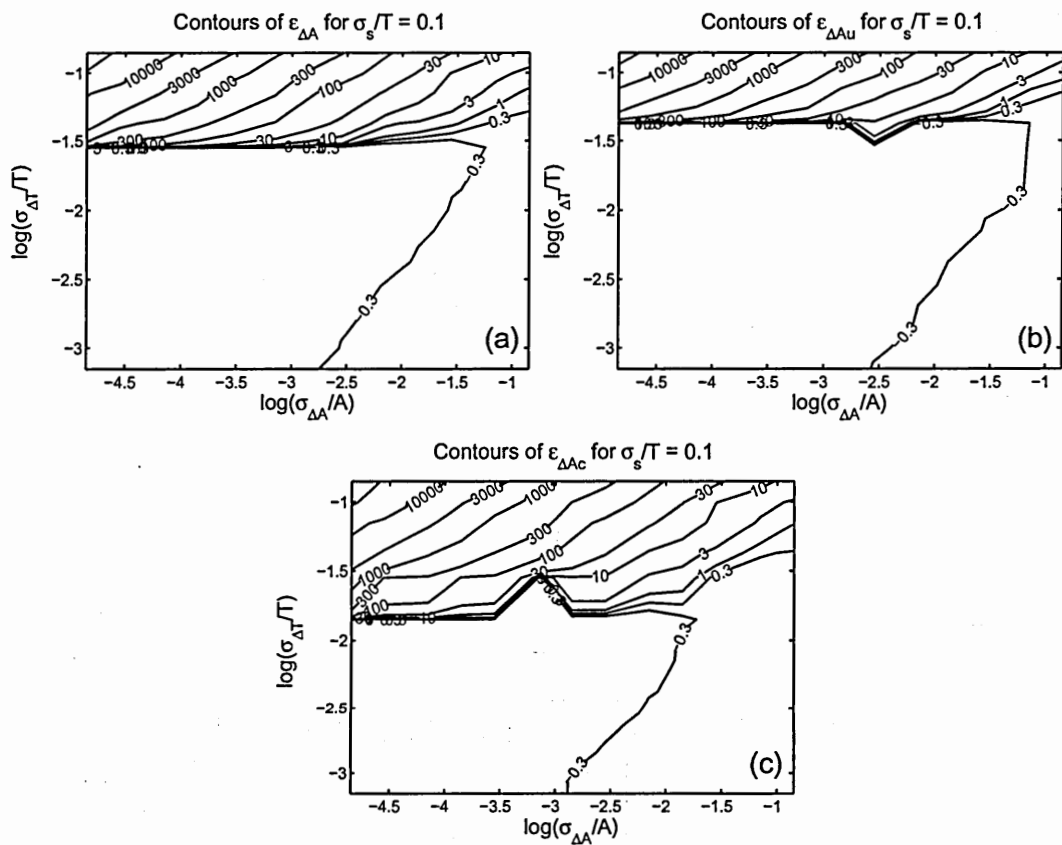


Figure D.10: The contours of the plots shown in D.9

D.2 Timing Jitter

On the next few pages, the extraction-error surfaces, obtained with the uncompensated mixing method, for total, uncorrelated, and correlated timing jitter are plotted against the normalized total amplitude jitter and the normalized total timing jitter, for each of seven normalized RMS pulse widths.

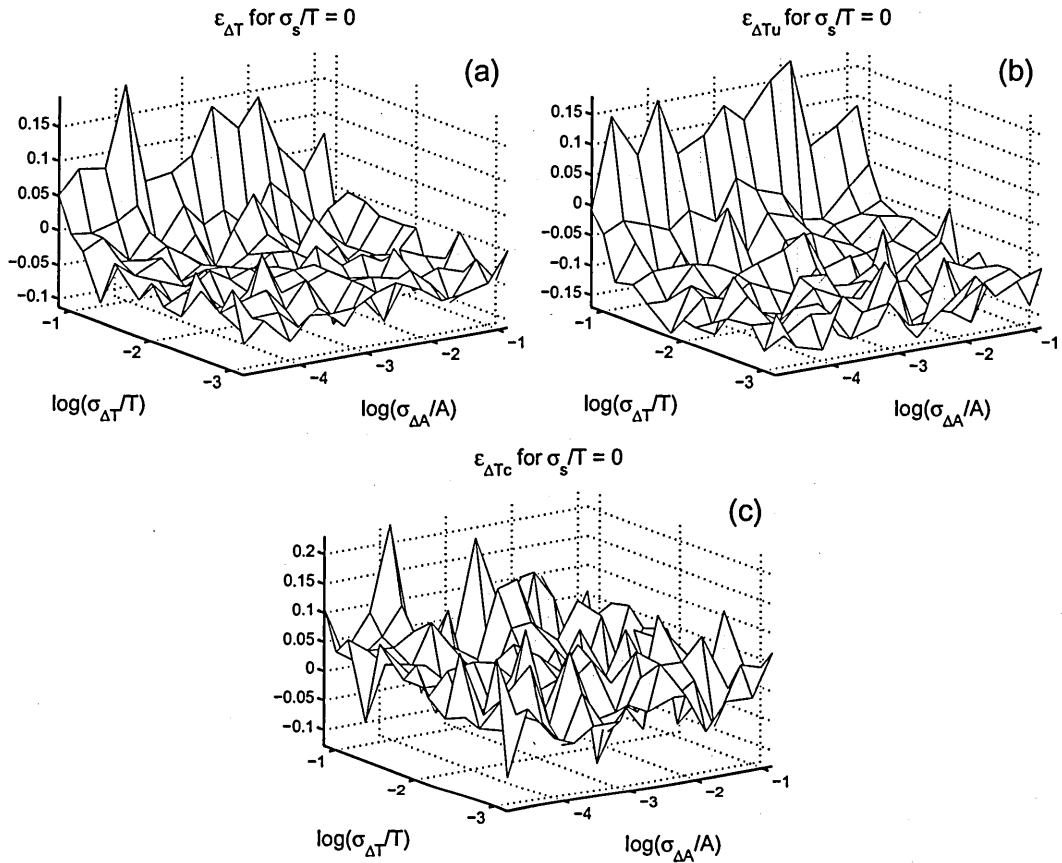


Figure D.11: Extraction errors for (a) total timing jitter, $\epsilon_{\Delta T}$, (b) uncorrelated timing jitter, $\epsilon_{\Delta T_u}$, and (c) correlated timing jitter, $\epsilon_{\Delta T_c}$, obtained with the uncompensated mixing method. σ_A/A —normalized total amplitude jitter. σ_T/T —normalized total timing jitter. σ_s/T —normalized root-mean-squared pulse width.

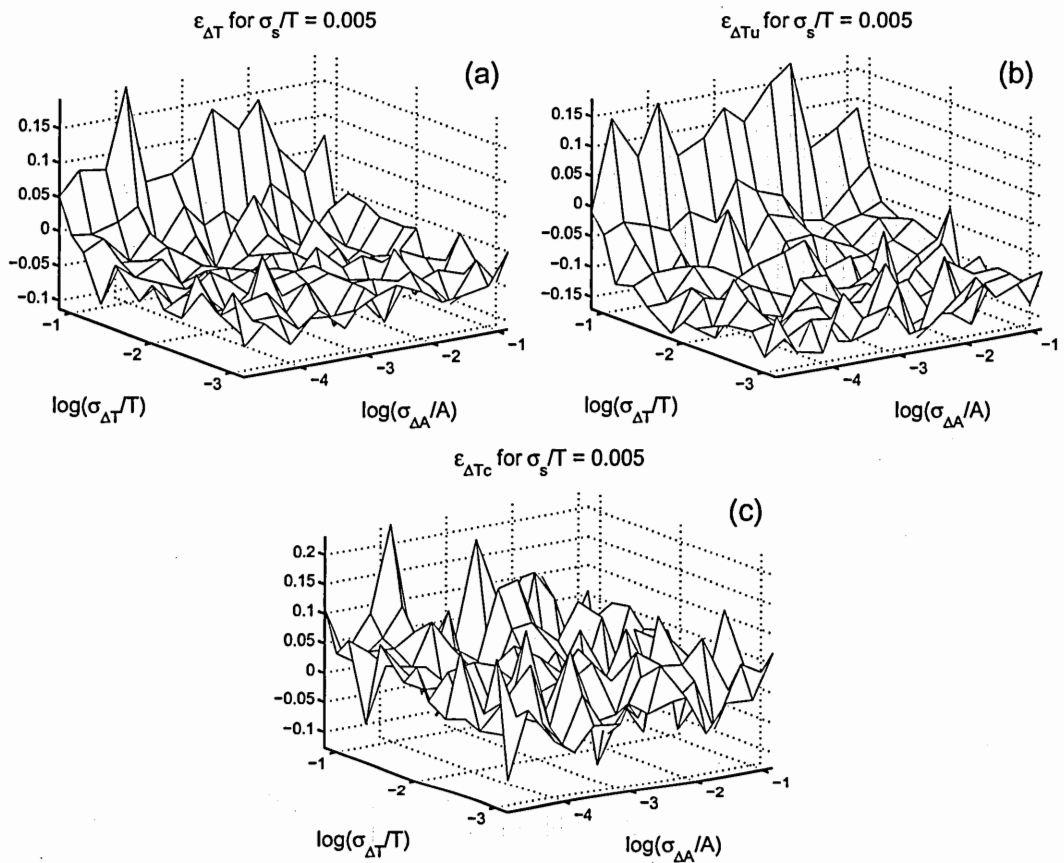


Figure D.12: Extraction errors for (a) total timing jitter, $\epsilon_{\Delta T}$, (b) uncorrelated timing jitter, $\epsilon_{\Delta T_u}$, and (c) correlated timing jitter, $\epsilon_{\Delta T_c}$, obtained with the uncompensated mixing method. σ_A/A —normalized total amplitude jitter. σ_T/T —normalized total timing jitter. σ_s/T —normalized root-mean-squared pulse width.

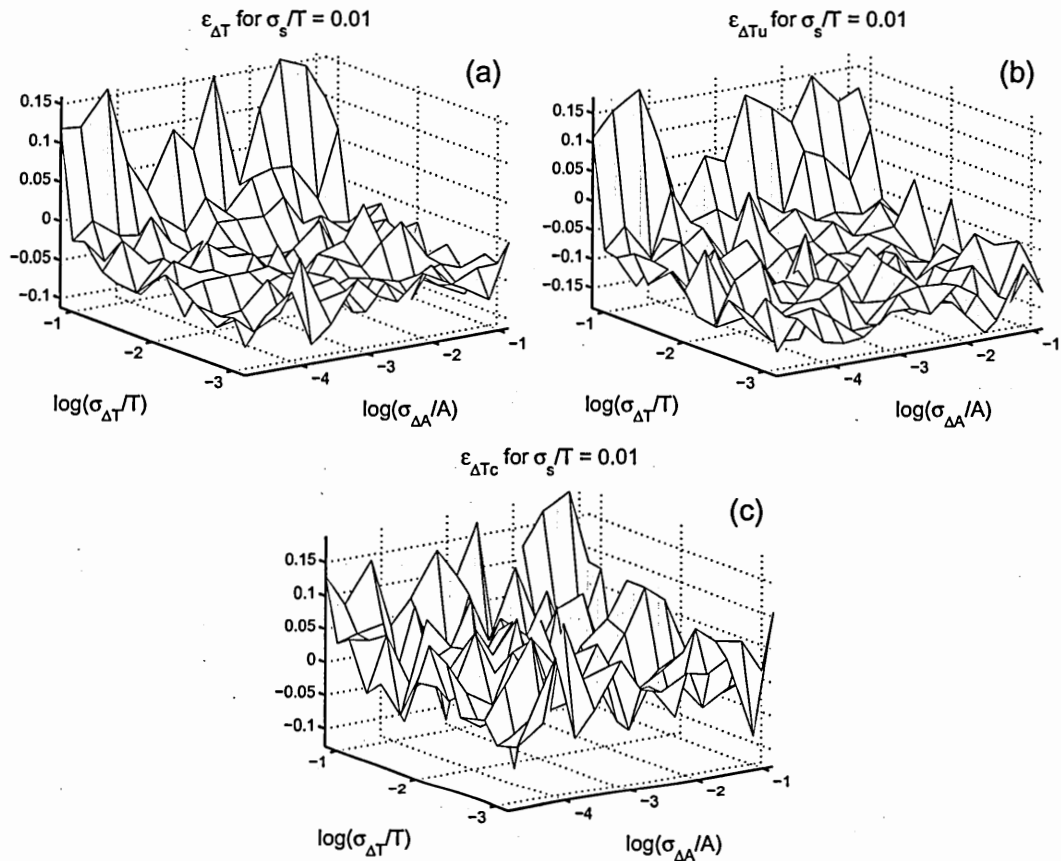


Figure D.13: Extraction errors for (a) total timing jitter, $\epsilon_{\Delta T}$, (b) uncorrelated timing jitter, $\epsilon_{\Delta T_u}$, and (c) correlated timing jitter, $\epsilon_{\Delta T_c}$, obtained with the uncompensated mixing method. σ_A/A —normalized total amplitude jitter. σ_T/T —normalized total timing jitter. σ_s/T —normalized root-mean-squared pulse width.

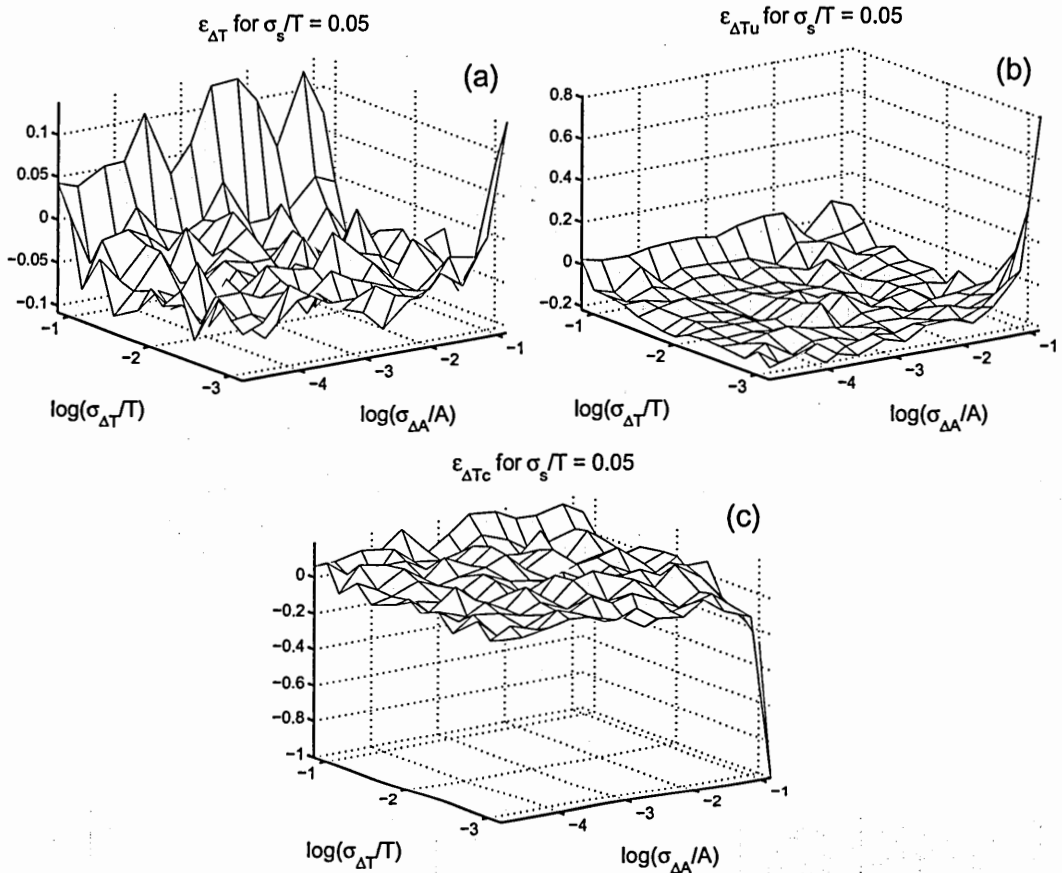


Figure D.14: Extraction errors for (a) total timing jitter, $\epsilon_{\Delta T}$, (b) uncorrelated timing jitter, $\epsilon_{\Delta T_u}$, and (c) correlated timing jitter, $\epsilon_{\Delta T_c}$, obtained with the uncompensated mixing method. σ_A/A —normalized total amplitude jitter. σ_T/T —normalized total timing jitter. σ_s/T —normalized root-mean-squared pulse width.

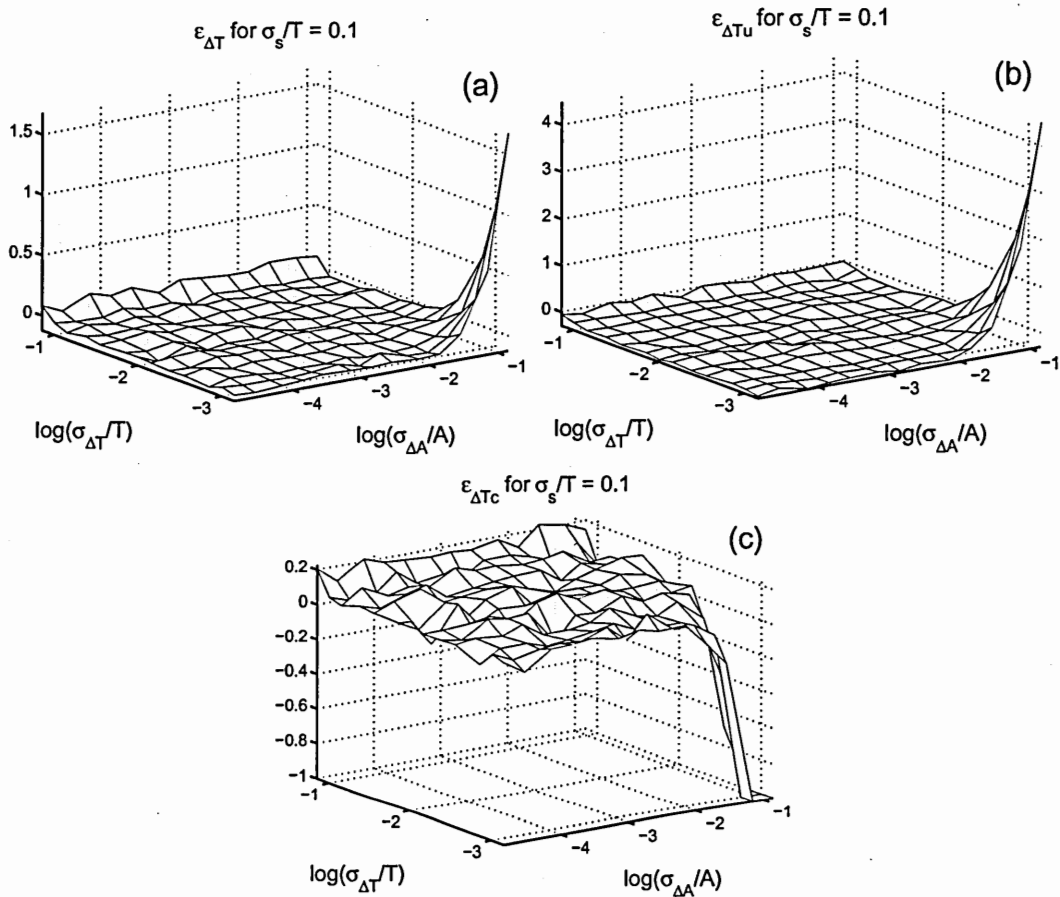


Figure D.15: Extraction errors for (a) total timing jitter, $\epsilon_{\Delta T}$, (b) uncorrelated timing jitter, $\epsilon_{\Delta T_u}$, and (c) correlated timing jitter, $\epsilon_{\Delta T_c}$, obtained with the uncompensated mixing method. σ_A/A —normalized total amplitude jitter. σ_T/T —normalized total timing jitter. σ_s/T —normalized root-mean-squared pulse width.

D.3 Correlation Time

On the next few pages, the extraction-error surfaces, obtained with the uncompensated mixing method, for the correlation times of the correlated amplitude and timing jitter are plotted against the normalized total amplitude jitter and the normalized total timing jitter, for each of seven normalized RMS pulse widths.

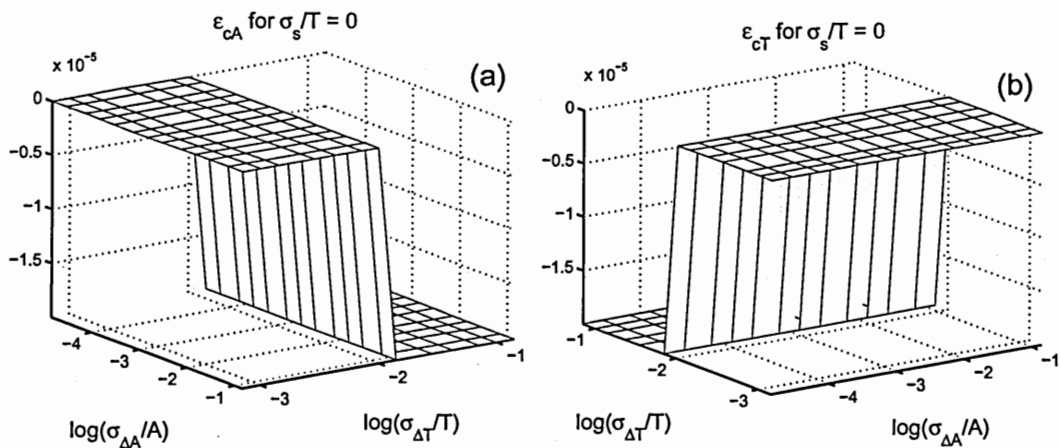


Figure D.16: Extraction errors for the correlation times of the (a) correlated amplitude jitter, $\epsilon_{\Delta A_c}$ and (b) timing jitter, $\epsilon_{\Delta T_c}$, obtained with the uncompensated mixing method. σ_A/A —normalized total amplitude jitter. σ_T/T —normalized total timing jitter. σ_s/T —normalized root-mean-squared pulse width.

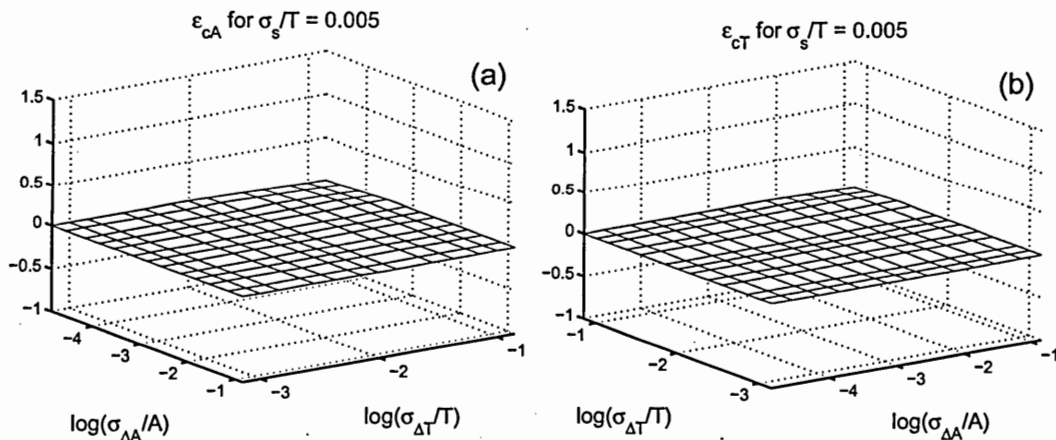


Figure D.17: Extraction errors for the correlation times of the (a) correlated amplitude jitter, $\epsilon_{\Delta A_c}$ and (b) timing jitter, $\epsilon_{\Delta T_c}$, obtained with the uncompensated mixing method. σ_A/A —normalized total amplitude jitter. σ_T/T —normalized total timing jitter. σ_s/T —normalized root-mean-squared pulse width.

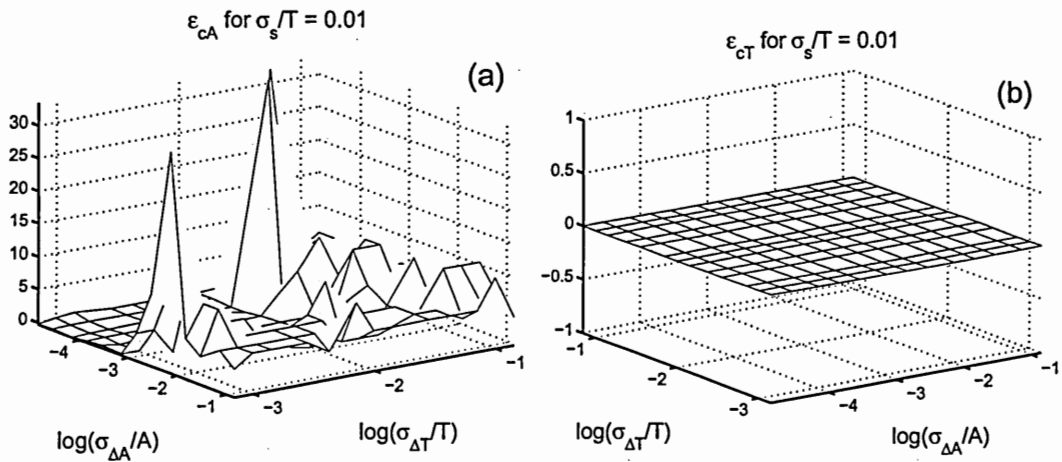


Figure D.18: Extraction errors for the correlation times of the (a) correlated amplitude jitter, $\epsilon_{\Delta A_c}$ and (b) timing jitter, $\epsilon_{\Delta T_c}$, obtained with the uncompensated mixing method. σ_A/A —normalized total amplitude jitter. σ_T/T —normalized total timing jitter. σ_s/T —normalized root-mean-squared pulse width.

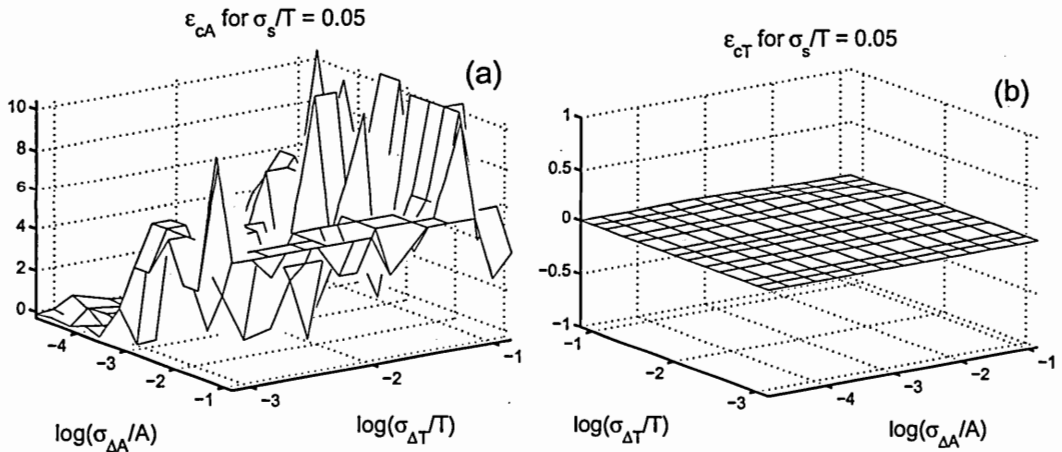


Figure D.19: Extraction errors for the correlation times of the (a) correlated amplitude jitter, $\epsilon_{\Delta A_c}$ and (b) timing jitter, $\epsilon_{\Delta T_c}$, obtained with the uncompensated mixing method. σ_A/A —normalized total amplitude jitter. σ_T/T —normalized total timing jitter. σ_s/T —normalized root-mean-squared pulse width.

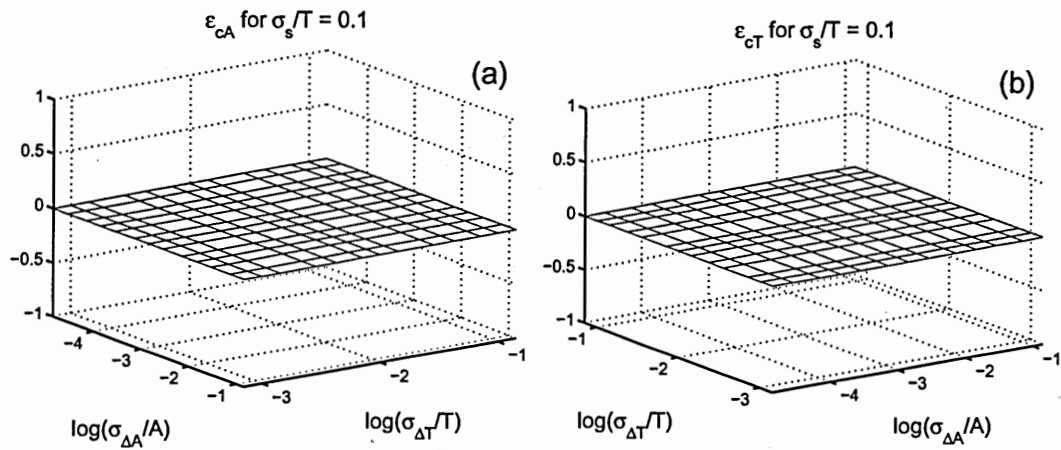


Figure D.20: Extraction errors for the correlation times of the (a) correlated amplitude jitter, $\epsilon_{\Delta A_c}$ and (b) timing jitter, $\epsilon_{\Delta T_c}$, obtained with the uncompensated mixing method. σ_A/A —normalized total amplitude jitter. σ_T/T —normalized total timing jitter. σ_s/T —normalized root-mean-squared pulse width.

APPENDIX E

Simulation Results: Compensated Mixing Method

E.1 Amplitude Jitter

On the next few pages, the extraction-error surfaces, obtained with the compensated mixing method, for total, uncorrelated, and correlated amplitude jitter are plotted against the normalized total amplitude jitter and the normalized total timing jitter, for each of seven normalized RMS pulse widths. The contours of these surfaces are also included.

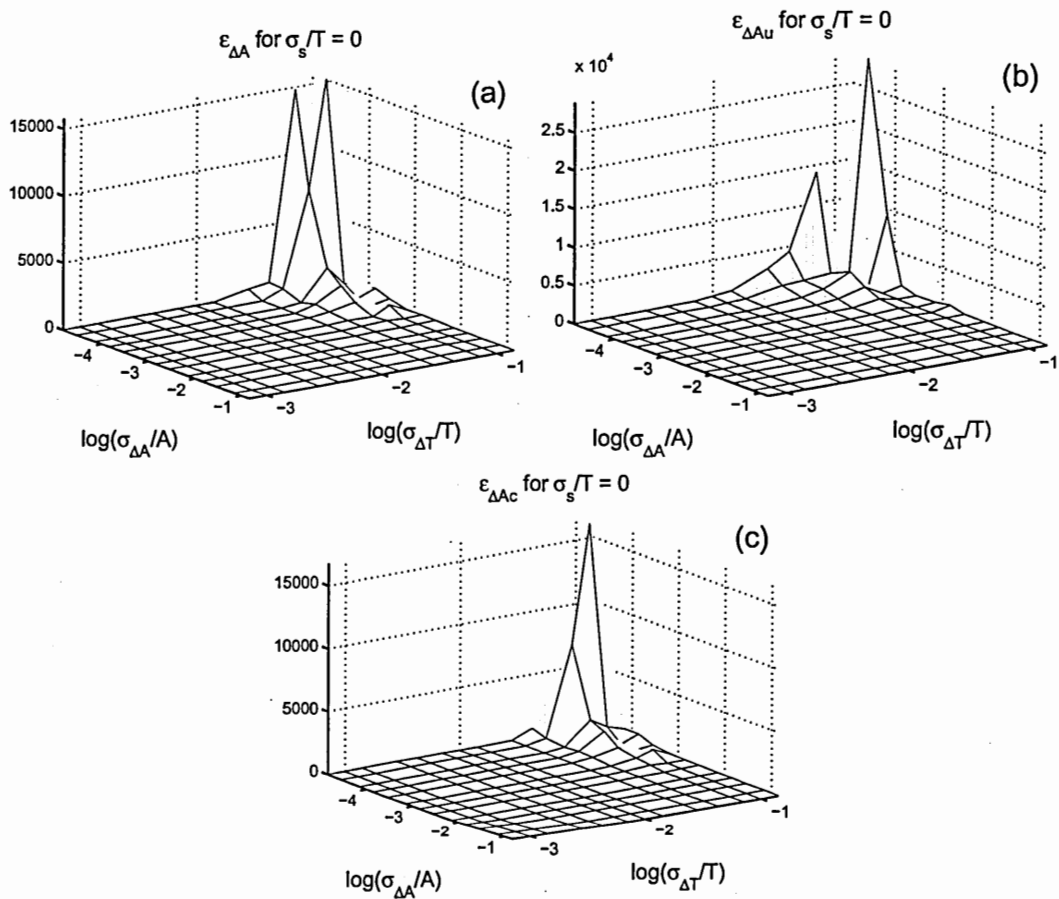


Figure E.1: Extraction errors for (a) total amplitude jitter, $\epsilon_{\Delta A}$, (b) uncorrelated amplitude jitter, $\epsilon_{\Delta Au}$, and (c) correlated amplitude jitter, $\epsilon_{\Delta Ac}$, obtained with the compensated mixing method. σ_A/A —normalized total amplitude jitter. σ_T/T —normalized total timing jitter. σ_s/T —normalized root-mean-squared pulse width.

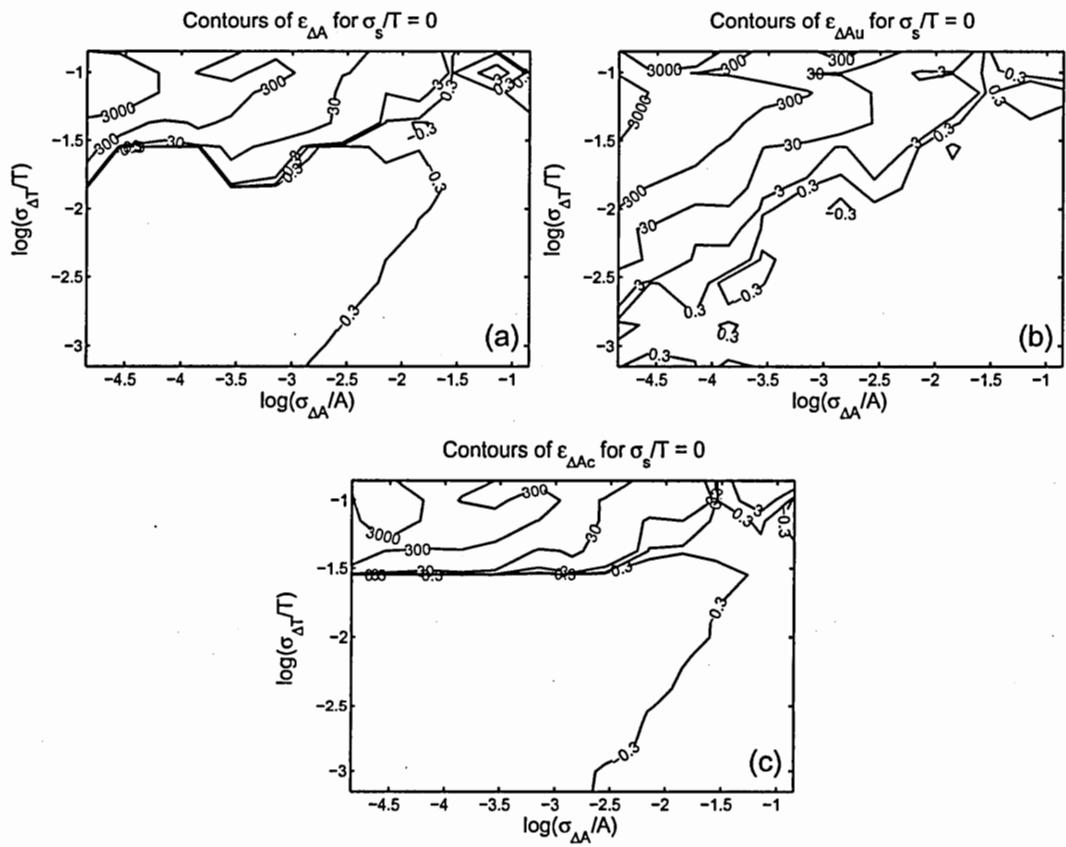


Figure E.2: The contours of the plots shown in E.1

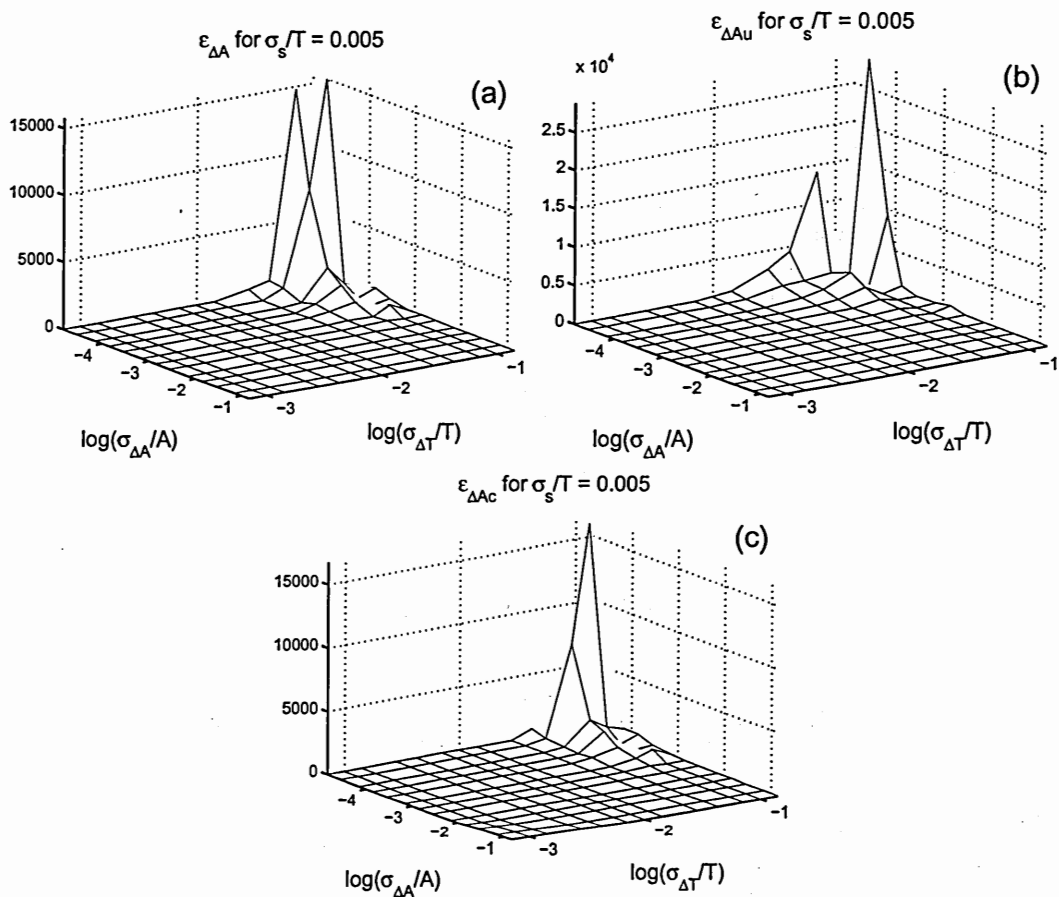


Figure E.3: Extraction errors for (a) total amplitude jitter, $\epsilon_{\Delta A}$, (b) uncorrelated amplitude jitter, $\epsilon_{\Delta Au}$, and (c) correlated amplitude jitter, $\epsilon_{\Delta Ac}$, obtained with the compensated mixing method. σ_A/A —normalized total amplitude jitter. σ_T/T —normalized total timing jitter. σ_s/T —normalized root-mean-squared pulse width.

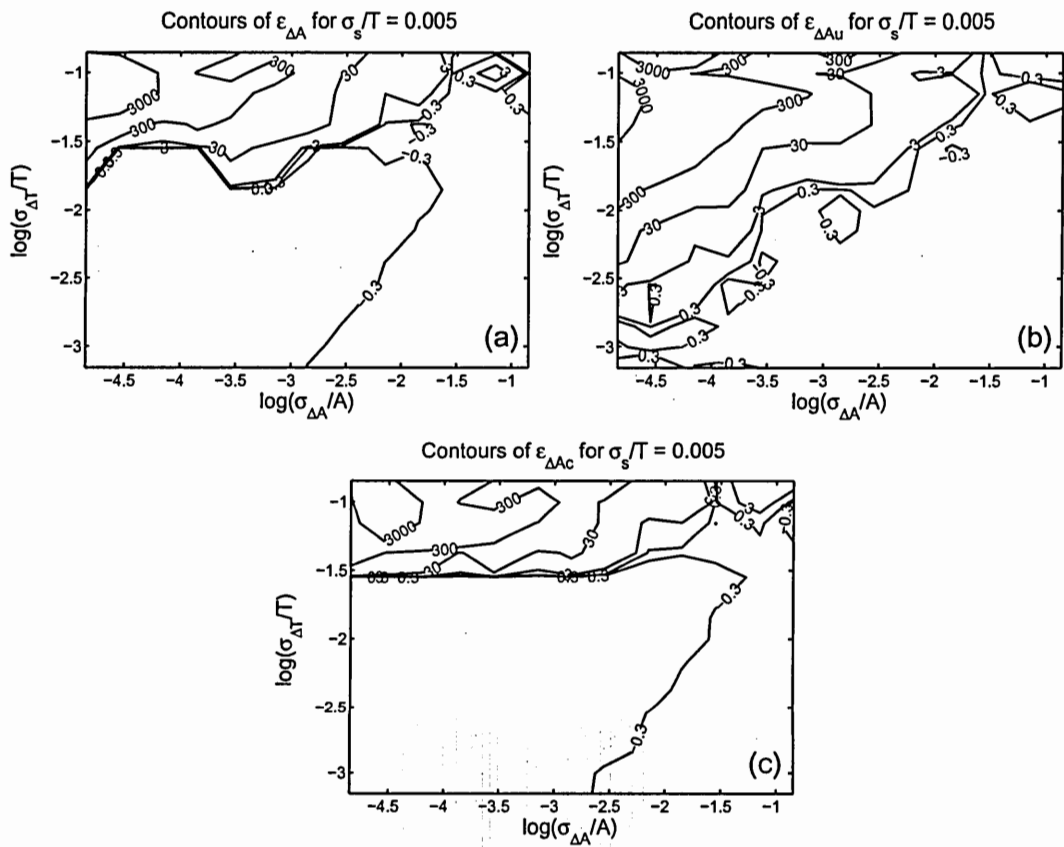


Figure E.4: The contours of the plots shown in E.3

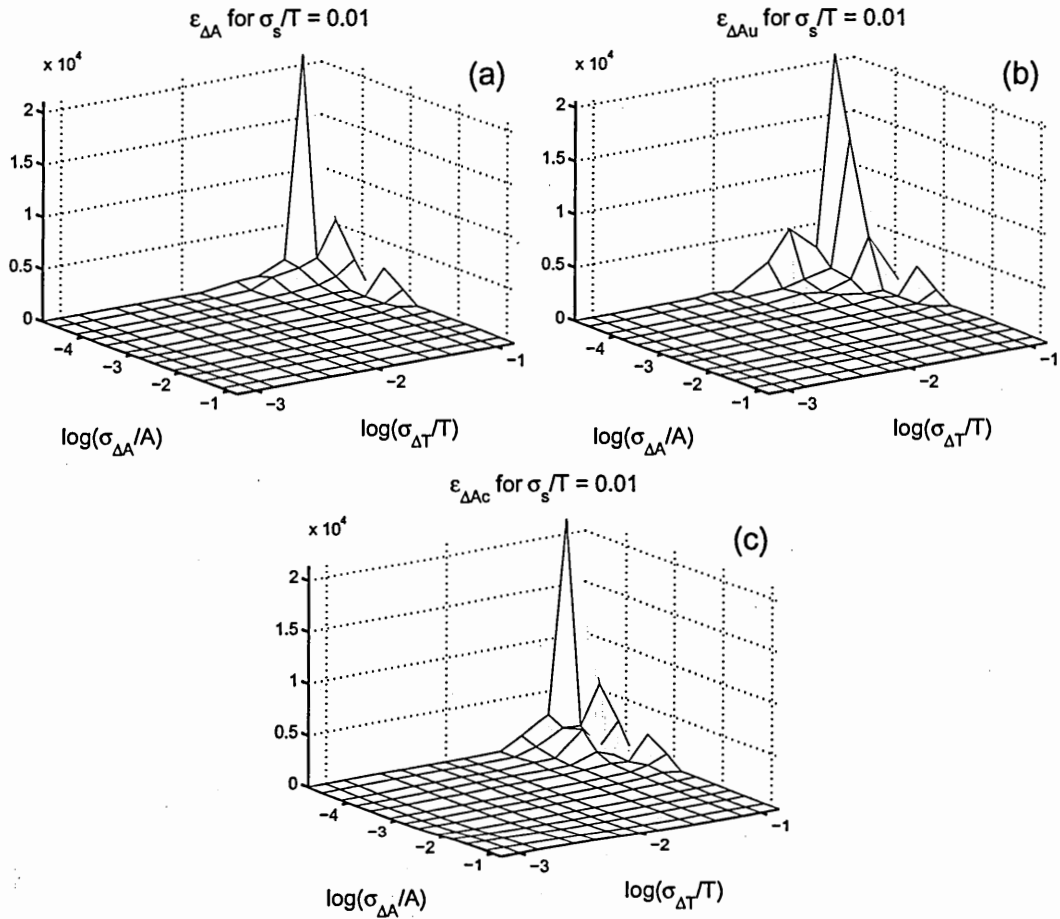


Figure E.5: Extraction errors for (a) total amplitude jitter, $\epsilon_{\Delta A}$, (b) uncorrelated amplitude jitter, $\epsilon_{\Delta Au}$, and (c) correlated amplitude jitter, $\epsilon_{\Delta Ac}$, obtained with the compensated mixing method. σ_A/A —normalized total amplitude jitter. σ_T/T —normalized total timing jitter. σ_s/T —normalized root-mean-squared pulse width.

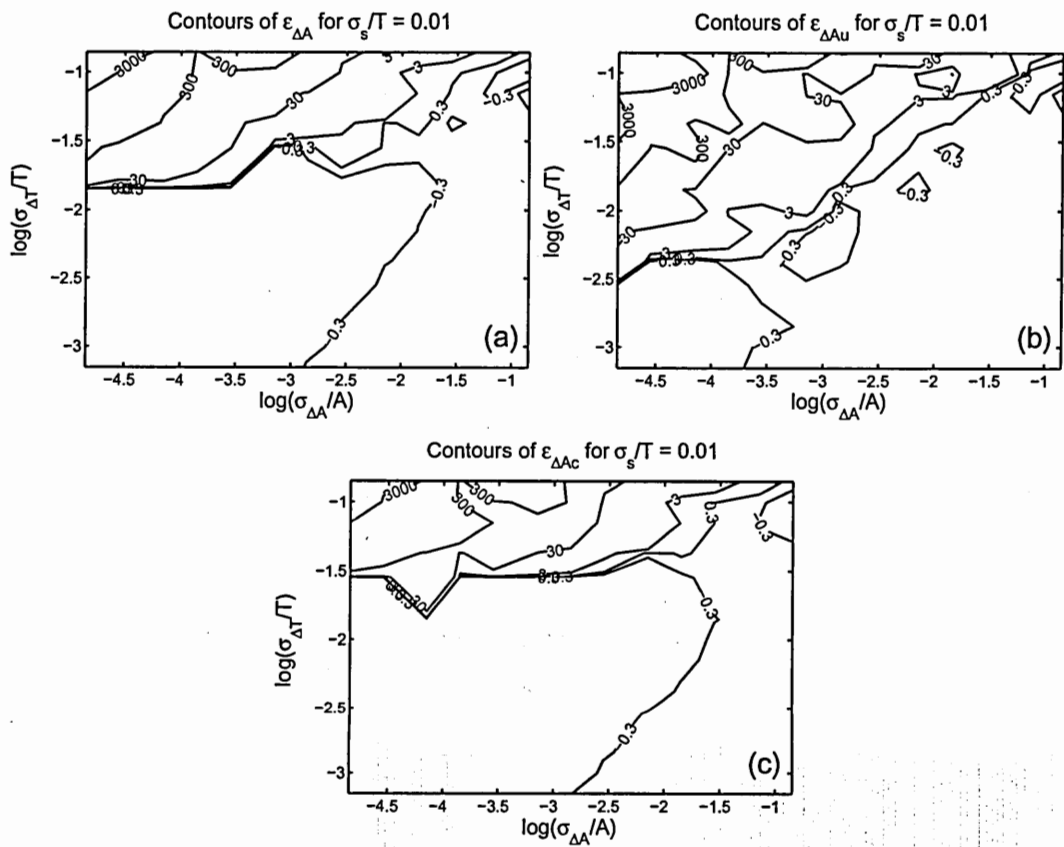


Figure E.6: The contours of the plots shown in E.5

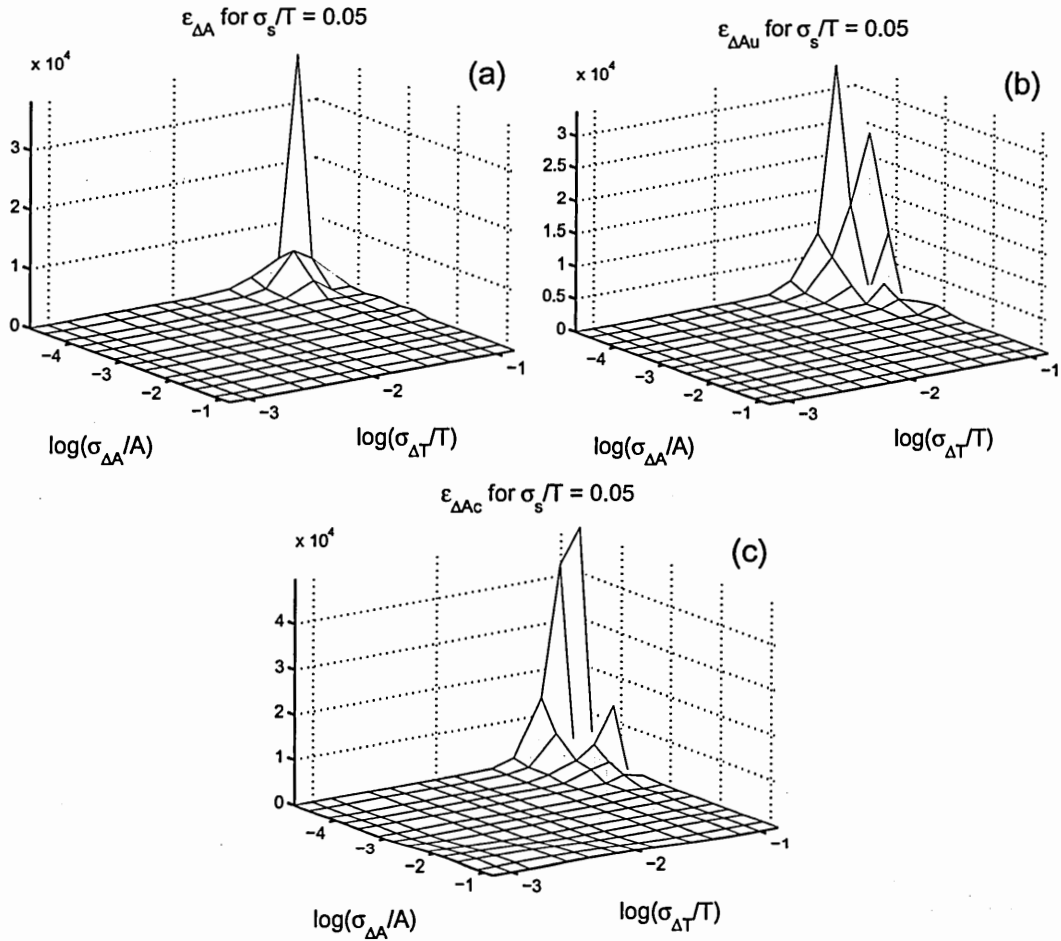


Figure E.7: Extraction errors for (a) total amplitude jitter, $\epsilon_{\Delta A}$, (b) uncorrelated amplitude jitter, $\epsilon_{\Delta A_u}$, and (c) correlated amplitude jitter, $\epsilon_{\Delta A_c}$, obtained with the compensated mixing method. σ_A/A —normalized total amplitude jitter. σ_T/T —normalized total timing jitter. σ_s/T —normalized root-mean-squared pulse width.

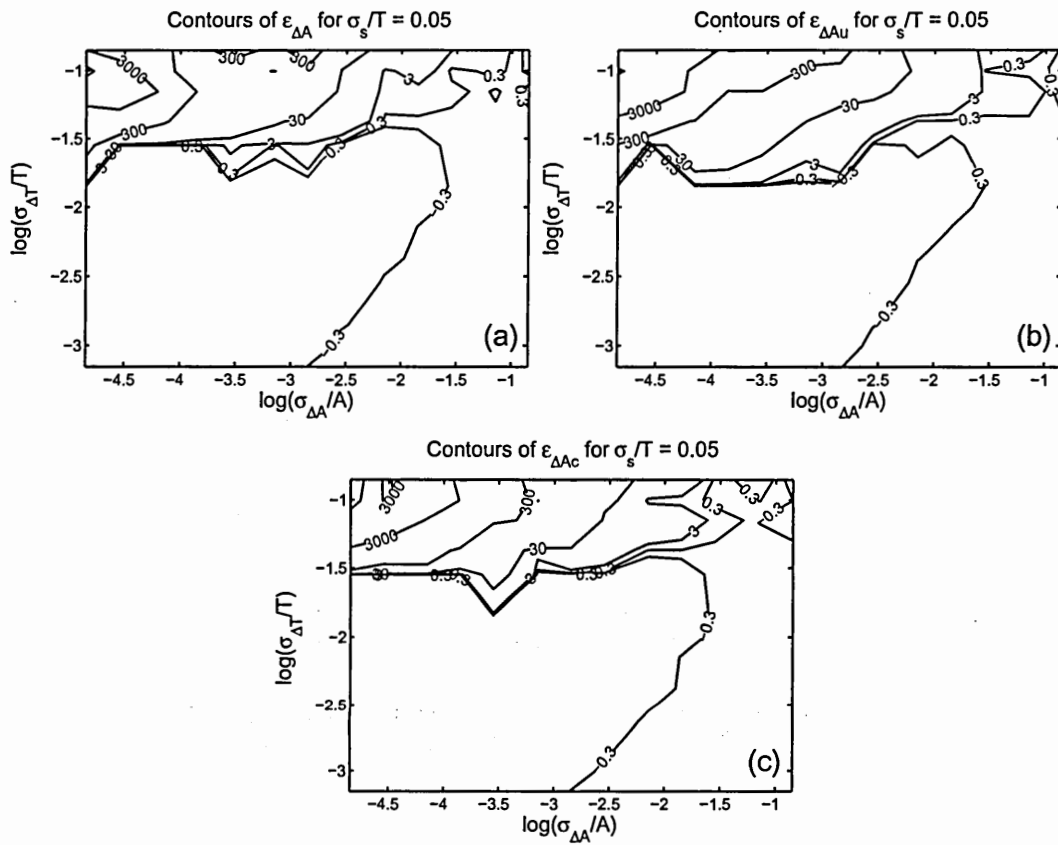


Figure E.8: The contours of the plots shown in E.7

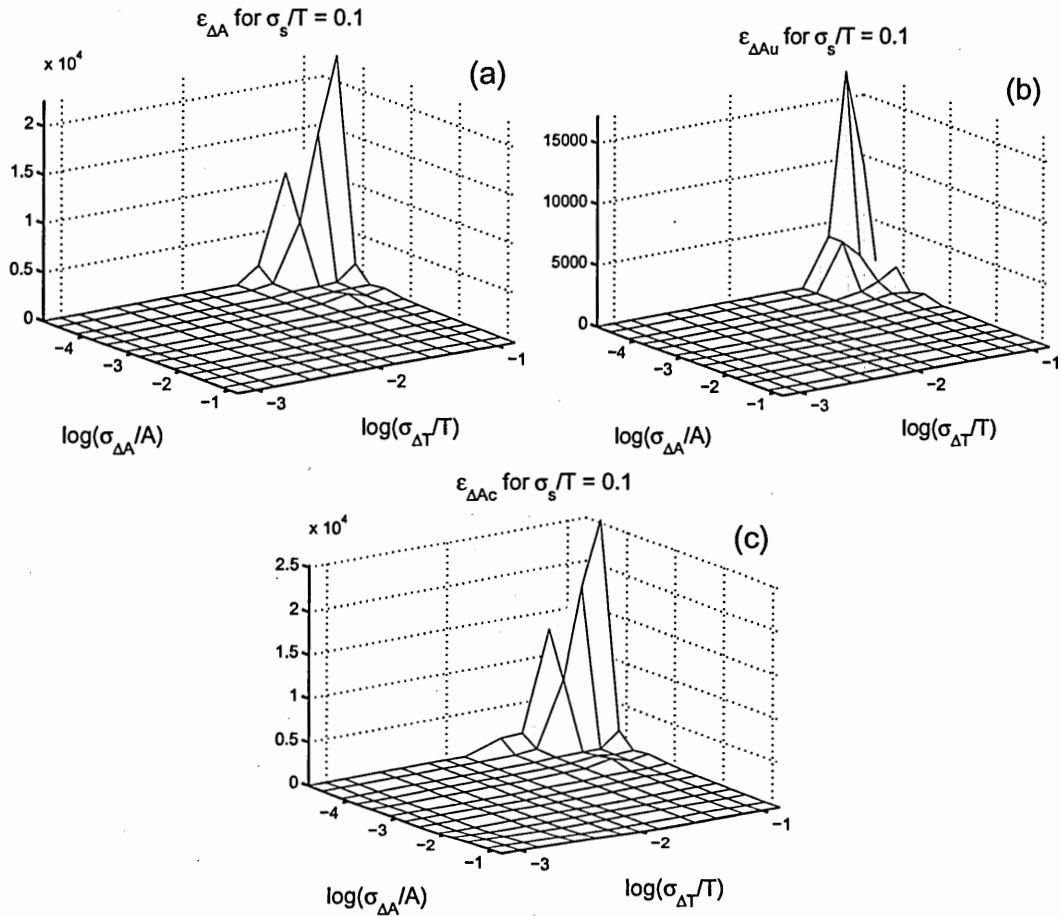


Figure E.9: Extraction errors for (a) total amplitude jitter, $\epsilon_{\Delta A}$, (b) uncorrelated amplitude jitter, $\epsilon_{\Delta A_u}$, and (c) correlated amplitude jitter, $\epsilon_{\Delta A_c}$, obtained with the compensated mixing method. σ_A/A —normalized total amplitude jitter. σ_T/T —normalized total timing jitter. σ_s/T —normalized root-mean-squared pulse width.

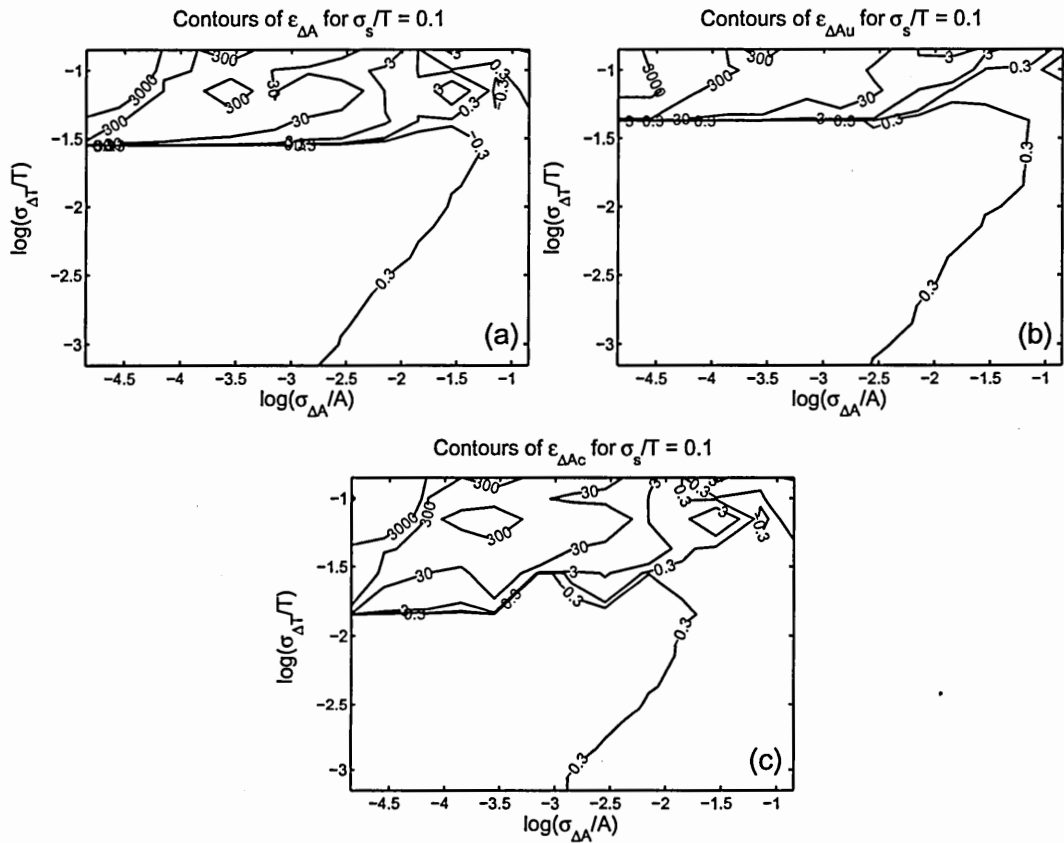


Figure E.10: The contours of the plots shown in E.9

E.2 Timing Jitter

On the next few pages, the extraction-error surfaces, obtained with the compensated mixing method, for total, uncorrelated, and correlated timing jitter are plotted against the normalized total amplitude jitter and the normalized total timing jitter, for each of seven normalized RMS pulse widths.

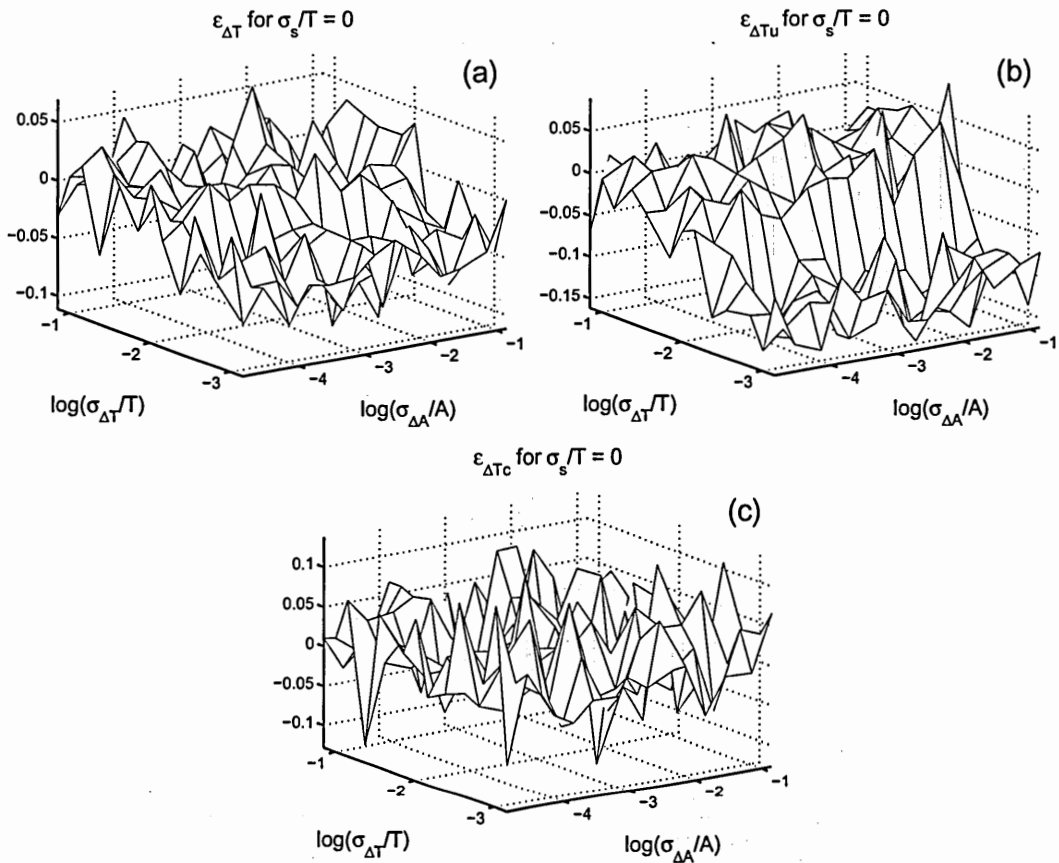


Figure E.11: Extraction errors for (a) total timing jitter, $\epsilon_{\Delta T}$, (b) uncorrelated timing jitter, $\epsilon_{\Delta T_u}$, and (c) correlated timing jitter, $\epsilon_{\Delta T_c}$, obtained with the compensated mixing method. σ_A/A —normalized total amplitude jitter. σ_T/T —normalized total timing jitter. σ_s/T —normalized root-mean-squared pulse width.

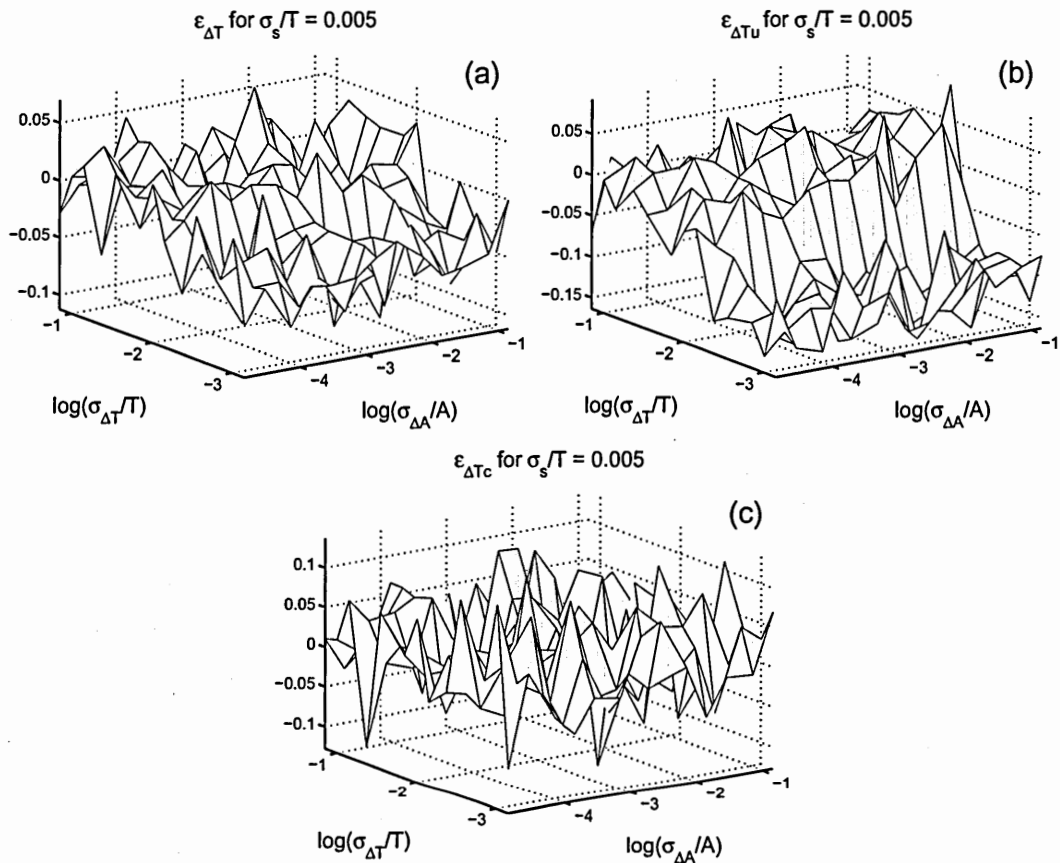


Figure E.12: Extraction errors for (a) total timing jitter, $\epsilon_{\Delta T}$, (b) uncorrelated timing jitter, $\epsilon_{\Delta T_u}$, and (c) correlated timing jitter, $\epsilon_{\Delta T_c}$, obtained with the compensated mixing method. σ_A/A —normalized total amplitude jitter. σ_T/T —normalized total timing jitter. σ_s/T —normalized root-mean-squared pulse width.

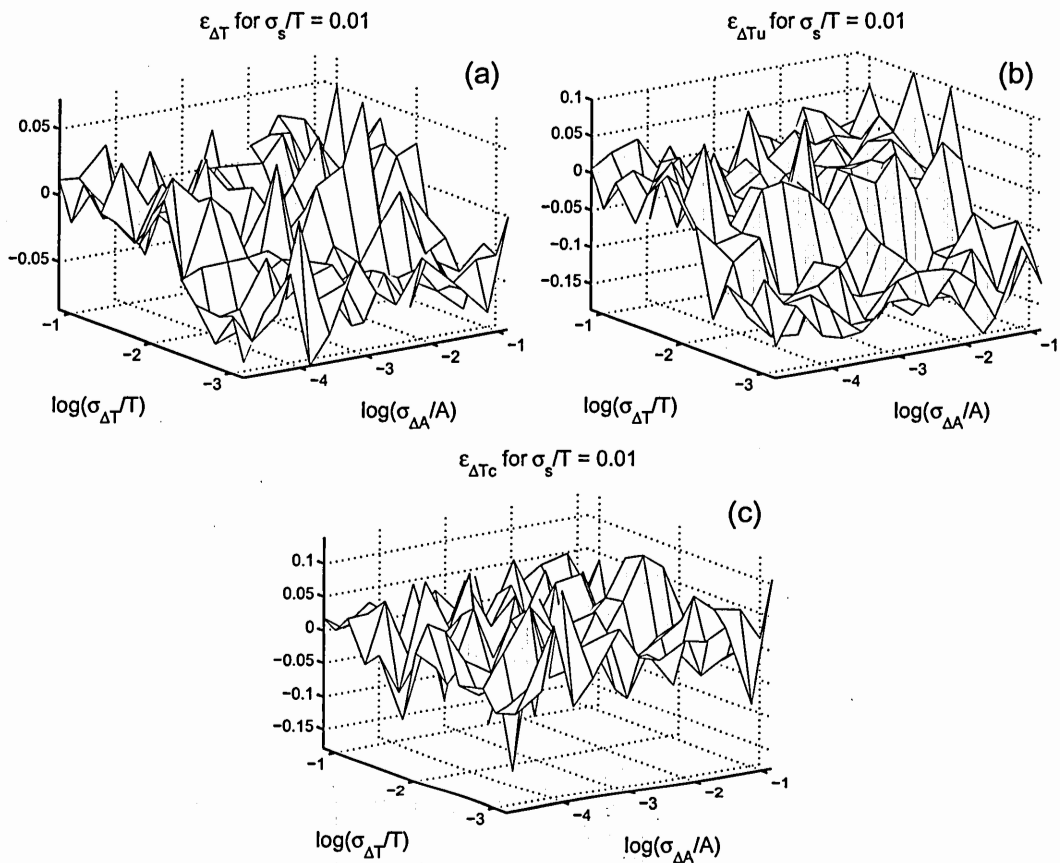


Figure E.13: Extraction errors for (a) total timing jitter, $\epsilon_{\Delta T}$, (b) uncorrelated timing jitter, $\epsilon_{\Delta T_u}$, and (c) correlated timing jitter, $\epsilon_{\Delta T_c}$, obtained with the compensated mixing method. σ_A/A —normalized total amplitude jitter. σ_T/T —normalized total timing jitter. σ_s/T —normalized root-mean-squared pulse width.

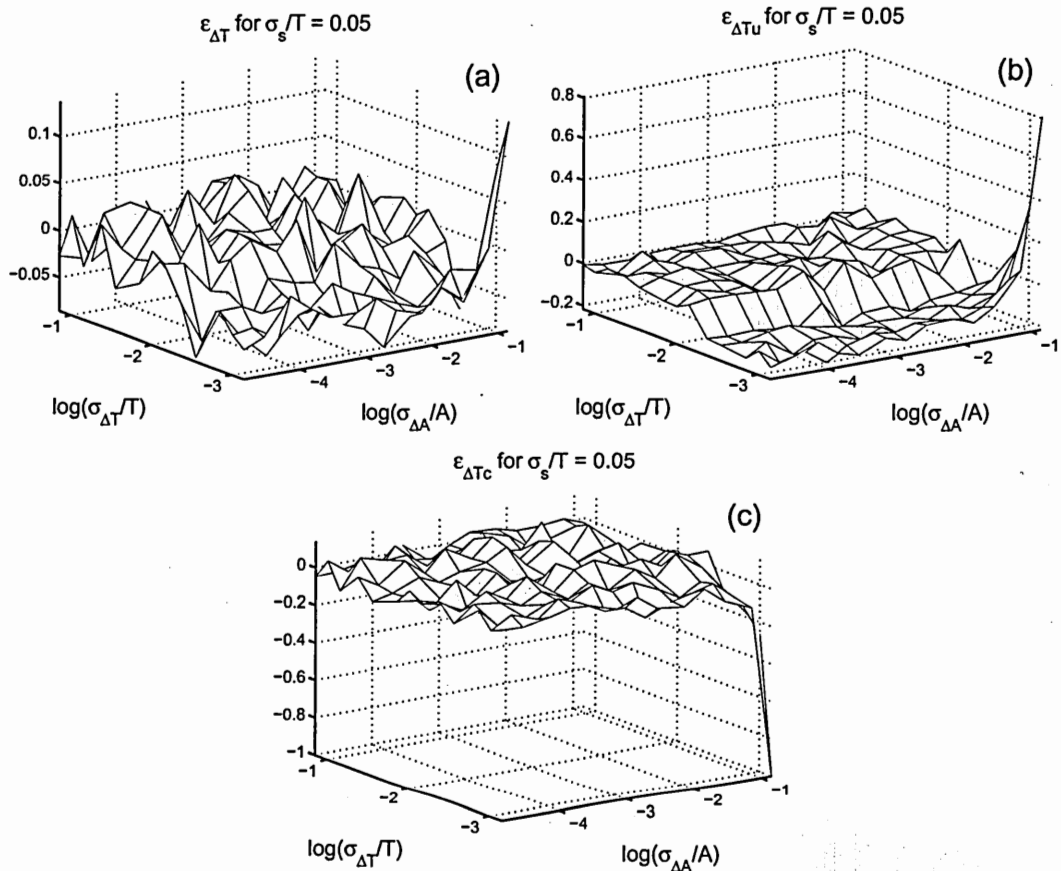


Figure E.14: Extraction errors for (a) total timing jitter, $\epsilon_{\Delta T}$, (b) uncorrelated timing jitter, $\epsilon_{\Delta T_u}$, and (c) correlated timing jitter, $\epsilon_{\Delta T_c}$, obtained with the compensated mixing method. σ_A/A —normalized total amplitude jitter. σ_T/T —normalized total timing jitter. σ_s/T —normalized root-mean-squared pulse width.

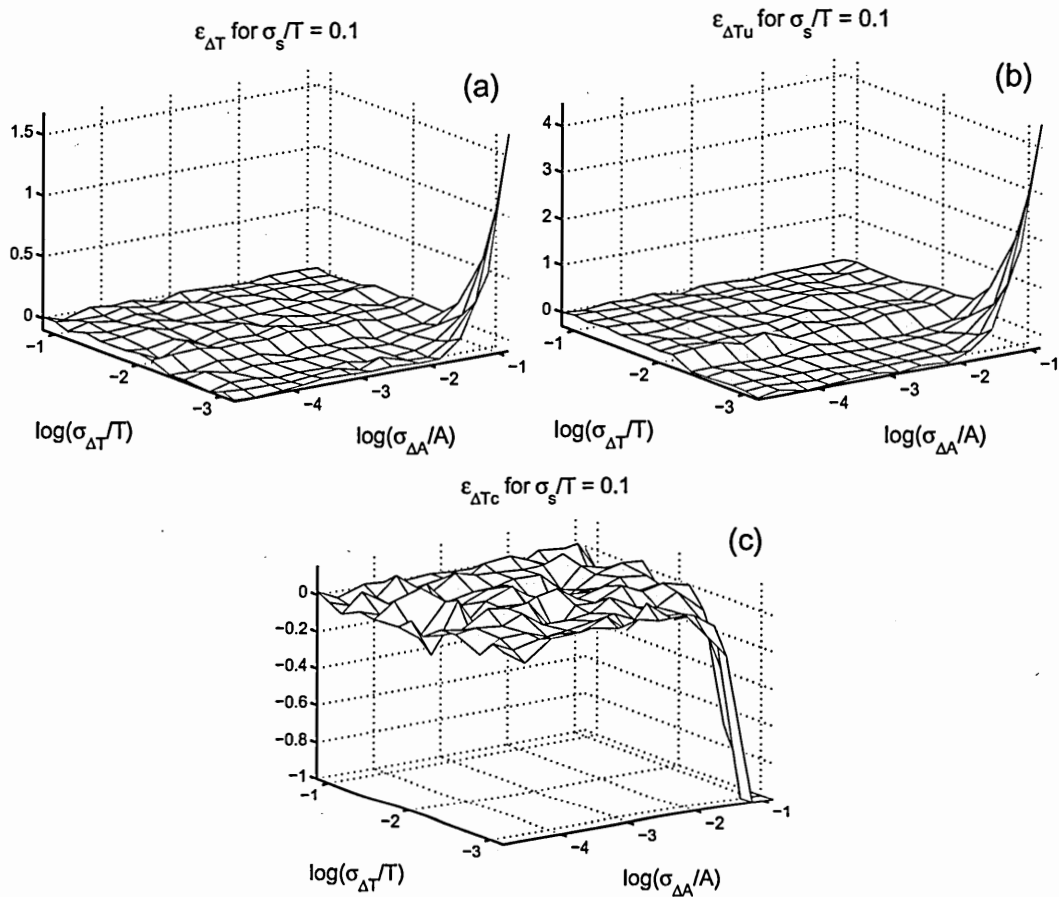


Figure E.15: Extraction errors for (a) total timing jitter, $\epsilon_{\Delta T}$, (b) uncorrelated timing jitter, $\epsilon_{\Delta T_u}$, and (c) correlated timing jitter, $\epsilon_{\Delta T_c}$, obtained with the compensated mixing method. σ_A/A —normalized total amplitude jitter. σ_T/T —normalized total timing jitter. σ_s/T —normalized root-mean-squared pulse width.

E.3 Correlation Time

The compensation routine does nothing to the correlation times. Therefore, the correlation-time-error plots of the compensated mixing technique are identical to those of the uncompensated mixing method¹ and are omitted.

¹ See Section D.3

Bibliography

- [1] J. C. Twichell and R. Helkey, "Phase-encoded optical sampling for analog-to-digital converters," *IEEE Photon. Technol. Lett.*, vol. 12, pp. 1237–1239, Sept. 2000.
- [2] P. W. Juodawlkis, J. C. Twichell, J. L. Wasserman, and R. C. Williamson, "Measurement of mode-locked laser timing jitter using phase-encoded optical sampling," in *Proc. CLEO 2000*, 2000, pp. 78–79.
- [3] M. Currie, T. R. Clark, and P. J. Matthews, "Photonic analog-to-digital conversion by distributed phase modulation," *IEEE Photon. Technol. Lett.*, vol. 12, pp. 1689–1691, Dec. 2000.
- [4] W. Ng, R. Stephens, D. Persechini, and K. V. Reddy, "Ultra-low jitter mode-locking of Er-fibre laser at 10GHz and its application in photonic sampling for analogue-to-digital conversion," *Electron. Lett.*, vol. 37, pp. 113–115, Nov. 2001.
- [5] C. M. DePriest, P. J. Delfyett, J. H. Abeles, and A. Braun, "Ultrahigh-stability photonic sampling streams from an actively-modelocked semiconductor diode ring laser," in *Proc. CLEO 2001*, 2001, pp. 89–90.
- [6] P. W. Juodawlkis, J. C. Twichell, J. L. Wasserman, G. E. Betts, and R. C. Williamson, "Measurement of mode-locked laser timing jitter by use of phase-encoded optical sampling," *Opt. Lett.*, pp. 289–291, Mar. 2001.
- [7] M. Currie, "High-speed, photonic analog-to-digital conversion using phase modulation," in *Proc. CLEO 2001*, 2001, pp. 68–69.
- [8] R. L. Fork, C. V. Shank, R. Yen, and W. J. Tomlinson, "Femtosecond white-light continuum pulses," *Opt. Lett.*, vol. 8, pp. 1–3, Jan. 1983.
- [9] T. Udem, J. Reichert, R. Holzwarth, , and T. W. Hansch, "Absolute optical frequency measurement of the cesium D1 line with a mode-locked laser," *Phys. Rev. Lett.*, vol. 82, pp. 3568–3571, May 1999.
- [10] S. A. Diddams, D. J. Jones, J. Ye, S. T. Cundiff, J. L. Hall, J. K. Ranka, R. Windeler, R. Holzwarth, T. Udem, and T. W. Hansch, "Direct link between microwave and optical frequencies with a 300 THz femtosecond laser comb," *Phys. Rev. Lett.*, vol. 84, pp. 5102–5105, May 2000.

- [11] R. Holzwarth, T. Udem, T. W. Hansch, J. C. Knight, W. C. Knight, and P. S. J. Russell, "Optical frequency synthesizer for precision spectroscopy," *Phys. Rev. Lett.*, vol. 85, pp. 2264–2267, Sept. 2000.
- [12] D. J. Jones, S. A. Diddams, J. K. Ranka, A. Stentz, R. S. Winderler, J. L. Hall, , and S. T. Cundiff, "Carrier-envelope phase control of femtosecond mode-locked lasers and direct optical frequency synthesis," *Science*, vol. 288, pp. 635–639, Aug. 2000.
- [13] J. Ye, J. L. Hall, and S. A. Diddams, "Precision phase control of an ultrawide-bandwidth femtosecond laser: A network of ultrastable frequency marks across the visible spectrum," *Opt. Lett.*, vol. 25, pp. 1675–1677, Nov. 2000.
- [14] S. A. Diddams, T. Udem, J. C. Bergquist, E. A. Curtis, R. E. Drullinger, L. Hollberg, W. M. Itano, W. D. Lee, C. W. Oates, K. Vogel, and D. J. Wineland, "An optical clock based on a single trapped $^{199}\text{Hg}^+$ atom," *Science*, vol. 293, pp. 825–828, Aug. 2001.
- [15] R. J. Jones and J.-C. Diels, "Stabilization of femtosecond lasers for optical frequency metrology and direct optical to radio frequency synthesis," *Phys. Rev. Lett.*, vol. 86, pp. 3288–3291, Apr. 2001.
- [16] T. M. Fortiera, D. J. Jones, S. A. Diddams, J. L. Hall, J. Ye, S. T. Cundiff, and R. S. Windeler, "Carrier-envelope phase stabilization of modelocked lasers," in *Proc. SPIE*, vol. 4271, 2001, pp. 183–192.
- [17] L. Hollberg, S. A. Diddams, E. A. Curtis, C. W. Oates, and R. W. Fox, "Optical frequency standards and measurements," *IEEE J. Quantum Electron.*, vol. 37, pp. 1502–1513, Dec. 2001.
- [18] R. Holzwarth, M. Zimmermann, T. Udem, and T. W. Hansch, "Optical clockworks and the measurement of laser frequencies with a mode-locked frequency comb," *IEEE J. Quantum Electron.*, vol. 37, pp. 1493–1501, Dec. 2001.
- [19] T. Udem, R. Holzwarth, and T. W. Hansch, "Optical frequency metrology," *Nature*, vol. 415, pp. 233–236, Mar. 2002.
- [20] K. L. Corwin, N. R. Newbury, J. M. Dudley, S. Coen, S. A. Diddams, K. Weber, and R. S. Windler, "Fundamental noise limitations to supercontinuum generation in microstructure fiber," *Phys. Rev. Lett.*, vol. 90, Mar. 2003, 113904.
- [21] K. L. Corwin, N. R. Newbury, J. M. Dudley, S. Coen, S. A. Diddams, B. R. Washburn, K. Weber, and R. S. Windler, "Fundamental amplitude noise limitations to supercontinuum spectra generated in microstructure fiber," *Appl. Phys. B*, 2003, to be published.

- [22] N. R. Newbury, B. R. Washburn, K. L. Corwin, and R. S. Windler, "Noise amplification during supercontinuum generation in microstructure fiber," *Opt. Lett.*, 2003, to be published.
- [23] L. A. Jiang, S. T. Wong, M. E. Grein, E. P. Ippen, and H. A. Haus, "Measuring timing jitter with optical cross correlations," *IEEE J. Quantum Electron.*, vol. 38, pp. 1047–11 052, Aug. 2002.
- [24] T. F. Carruthers, Naval Research Laboratory, Washington, DC (personal communication), 2002.
- [25] H. N. Ereifej, R. Holzlohner, G. M. Carter, and C. R. Menyuk, "Intersymbol interference and timing jitter measurements in a 40-Gb/s long-haul dispersion-managed soliton system," *IEEE Photon. Technol. Lett.*, vol. 14, pp. 343–345, Mar. 2002.
- [26] D. A. Leep and D. A. Holm, "Spectral measurement of timing jitter in gain-switched semiconductor lasers," *Appl. Phys. Lett.*, vol. 60, pp. 2451–2453, May 1992.
- [27] M. C. Gross, M. Hanna, K. M. Patel, and S. E. Ralph, "Reduction of power fluctuations in ultrafast optically time-division-multiplexed pulse trains by use of a nonlinear amplifying loop mirror," *IEEE Photon. Technol. Lett.*, vol. 14, pp. 690–692, May 2002.
- [28] ———, "Use of nonlinear amplifying loop mirror to reduce power fluctuations in ultrafast optically time-division-multiplexed pulse trains," in *Proc. CLEO 2002*, 2002, pp. 460–461.
- [29] A. Papoulis, *The Fourier Integral and Its Applications*. New York: McGraw-Hill, 1962.
- [30] L. M. *et al.*, "The emerging digital economy," U.S. Dept. Commerce, Tech. Rep., 1998.
- [31] J. A. Buck, *Fundamentals of Optical Fibers*. New York: John Wiley & Sons, 1995.
- [32] G. P. Agrawal, *Nonlinear Fiber Optics*, 2nd ed. New York: John Wiley & Sons, 1997.
- [33] J. C. Palais, *Fiber Optical Communications*, 4th ed. New York: Prentice-Hall, 1998.
- [34] A. Borella, G. Cancellieri, and F. Chiaraluce, *Wavelength Division Multiple Access Optical Networks*. Norwood, MA: Artech House, 1998.

- [35] T. G. Ulmer, M. C. Gross, K. M. Patel, J. T. Simmons, P. W. Juodawlkis, B. R. Washburn, W. S. Astar, A. J. SpringThorpe, R. P. Kenan, C. M. Verber, and S. E. Ralph, "160-Gb/s optically time-division multiplexed link with all-optical demultiplexing," *J. Lightwave Technol.*, vol. 18, pp. 1964–1977, Dec. 2000.
- [36] S. A. Hamilton, B. S. Robinson, T. E. Murphy, S. J. Savage, and E. P. Ippen, "100 gb/s optical time-division multiplexed networks," *J. Lightwave Technol.*, vol. 20, pp. 2086–2100, Dec. 2002.
- [37] T. G. Ulmer, M. C. Gross, K. M. Patel, R. P. Kenan, S. E. Ralph, C. M. Verber, and A. J. SpringThorpe, "Optical time-division demultiplexing with resonant-cavity-enhanced surface-emitted second-harmonic generation," in *Proc. CLEO 2000*, 2000, pp. 195–196.
- [38] T. G. Ulmer, "Resonant-cavity-enhanced surface-emitted second-harmonic generation for optical time-division demultiplexing," Ph.D. dissertation, Georgia Inst. of Tech., 2000.
- [39] K. L. Hall and B. S. Robinson, "Bit error rate characterization of 100 Gb/s all-optical demultiplexers," in *Proc. CLEO '99*, 1999, pp. 214–215.
- [40] N. S. Patel, K. A. Rauschenbach, and K. L. Hall, "40 Gb/s demultiplexing using an ultrafast nonlinear interferometer (UNI)," *IEEE Photon. Technol. Lett.*, vol. 8, pp. 1695–1697, Dec. 1994.
- [41] V. W. S. Chan, K. L. Hall, E. Modiano, and K. A. Rauschenbach, "Architectures and technologies for high-speed optical data networks," *J. Lightwave Technol.*, vol. 16, pp. 2146–2168, Dec. 1998.
- [42] J. P. Sokoloff, B. P. McGinnis, S. G. Lee, and H. Sasabe, "Efficiently packaged ultrafast demultiplexers for high bandwidth optical TDN systems," *Electron. Lett.*, vol. 33, pp. 1648–1650, Sept. 1997.
- [43] G. R. Williams, M. Vaziri, K. H. Ahn, B. C. Barnett, and M. N. Islam, "Soliton logic gate using low-birefringence fiber in a nonlinear loop mirror," *Opt. Lett.*, vol. 20, pp. 1671–1673, Aug. 1995.
- [44] K. H. Ahn, X. D. Cao, Y. Liang, B. C. Barnett, S. Chaikammerd, and M. N. Islam, "Cascadability and functionality of all-optical low-birefringent nonlinear optical loop mirror: Experimental demonstration," *J. Opt. Soc. Am. B*, vol. 14, pp. 1228–1236, May 1997.
- [45] T. J. Xia, Y. Liang, K. H. Ahn, J. W. Lou, O. Boyraz, Y.-H. Kao, X. D. Kao, X. D. Cao, S. Chaikammerd, J. K. Andersen, and M. N. Islam, "All-optical packet-drop demonstration using 100-Gb/s words by integrating fiber-based components," *IEEE Photon. Technol. Lett.*, vol. 10, pp. 153–155, Jan. 1998.

- [46] Y. Liang, J. W. Lou, J. K. Andersen, J. C. Stoker, O. Boyraz, M. N. Islam, and D. A. Nolan, "Polarization-insensitive nonlinear optical loop mirror demultiplexer with twisted fiber," *Opt. Lett.*, vol. 24, pp. 726–728, June 1999.
- [47] J. P. Sokoloff, P. R. Prucnal, I. Glesk, and M. Kane, "A terahertz optical asymmetric demultiplexer (TOAD)," *IEEE Photon. Technol. Lett.*, vol. 5, pp. 787–190, July 1993.
- [48] K.-L. Deng, I. Glesk, K. I. Kang, and P. R. Prucnal, "Unbalanced TOAD for optical data and clock separation in self-clocked transparent OTDM networks," *IEEE Photon. Technol. Lett.*, vol. 9, pp. 830–832, June 1997.
- [49] J. M. Tang, P. S. Spencer, and K. A. Shore, "Influence of fast gain depletion on the dynamic response of TOAD's," *J. Lightwave Technol.*, vol. 16, pp. 86–91, Jan. 1998.
- [50] D. Zhou, K. I. Kang, I. Glesk, and P. R. Prucnal, "An analysis of signal-to-noise ratio and design parameters of a terahertz optical asymmetric demultiplexer," *J. Lightwave Technol.*, vol. 17, pp. 298–307, Feb. 1999.
- [51] T. Morioka, H. Takara, S. Kawanishi, and M. Saruwatari, "Polarisation-independent all-optical demultiplexing up to 200 Gbit/s using four-wave mixing in a semiconductor laser amplifier," *Electron. Lett.*, vol. 32, pp. 840–841, Apr. 1996.
- [52] T. J. Morgan, R. S. Tucker, and J. P. R. Lacey, "All-optical wavelength translation over 80 nm at 2.5 Gb/s using four-wave mixing in a semiconductor optical amplifier," *IEEE Photon. Technol. Lett.*, vol. 11, pp. 982–984, Aug. 1999.
- [53] R. Calvani, F. Cisternino, R. Girardi, and D. Riccardi, "Polarisation independent all-optical demultiplexing using four-wave mixing in dispersion shifted fibre," *Electron. Lett.*, vol. 35, pp. 72–73, Jan. 1999.
- [54] S. Kawanishi, "Ultrahigh-speed optical time-division-multiplexed transmission technology based on optical signal processing," *IEEE J. Quantum Electron.*, vol. 34, pp. 2064–2079, Nov. 1998.
- [55] A. Hasegawa and M. Matsumoto, *Optical Solitons in Fibers*, 3rd ed. Berlin: Springer-Verlag, 2003.
- [56] *A Guide to Understanding and Characterizing Timing Jitter*, Tektronix, Inc., Beaverton, Or, 2002. [Online]. Available: http://www.tek.com/Masurement/scopes/jitter/55W_16146_0.pdf
- [57] S. E. Ralph, Georgia Institute of Technology, Atlanta, GA (personal communication), 2003.

- [58] D. J. Derickson, A. Mar, and J. E. Bowers, "Residual and absolute timing jitter in actively mode-locked semiconductor lasers," *Electron. Lett.*, vol. 26, pp. 2026–2028, Nov. 1990.
- [59] T. Yilmaz, C. M. DePriest, P. J. Delfyett, Jr., J. H. Abeles, and A. Braun, "Measurement of residual phase noise in 10 GHz pulsetrain using modified Michelson optical frequency discriminator," in *Proc. UEO 2001*, 2001, pp. 52–54.
- [60] T. Yilmaz, C. M. DePriest, P. J. Delfyett, Jr., A. Braun, and J. Abeles, "Timing restoration dynamics in an actively mode-locked fiber ring laser," *Opt. Lett.*, vol. 27, pp. 872–874, May 2002.
- [61] J. B. Schlager, B. E. Callicoatt, R. P. Mirin, and N. A. Sanford, "Passively mode-locked waveguide laser with low residual jitter," *IEEE J. Sel. Top. Quantum Electron.*, vol. 7, pp. 641–655, Jul./Aug. 2001.
- [62] A. Shen, S. Bouchoule, P. Crozat, D. Mathoorasing, and J. M. L. C. Kazmierski, "Low timing jitter of gain- and Q-switched laser diodes for high bit rate OTDM applications," *Electron. Lett.*, vol. 33, pp. 1875–1877, Oct. 1992.
- [63] M. E. Grein, L. A. Jiang, Y. Chen, H. A. Haus, and E. P. Ippen, "Timing restoration dynamics in an actively mode-locked fiber ring laser," *Opt. Lett.*, vol. 24, pp. 1687–1689, Dec. 1999.
- [64] L. A. Jiang, M. E. Grein, H. A. Haus, and E. P. Ippen, "Noise of modelocked laser diodes," in *Proc. LEOS 2000*, 2000, pp. 149–150.
- [65] J. P. Gordon and H. A. Haus, "Random walk of coherently amplified solitons in optical fiber transmission," *Opt. Lett.*, vol. 11, pp. 665–667, Oct. 1986.
- [66] K. Tamura and M. Nakazawa, "Timing jitter of solitons compressed in dispersion-decreasing fiber," *Opt. Lett.*, vol. 23, pp. 1360–1362, Sept. 1998.
- [67] D. Marcuse, "An alternative derivation of the Gordon-Haus effect," *J. Lightwave Technol.*, vol. 10, pp. 273–278, Feb. 1992.
- [68] K. Iwatsuki, S. Kawai, S. Nishi, and M. Saruwatari, "Timing jitter due to carrier linewidth of laser-diode pulse sources in ultra-high speed soliton transmission," *J. Lightwave Technol.*, vol. 13, pp. 639–649, Apr. 1995.
- [69] V. S. Grigoryan, C. R. Menyuk, and R.-M. Mu, "Calculation of timing and amplitude jitter in dispersion-managed optical fiber communications using linearization," *J. Lightwave Technol.*, vol. 17, pp. 1347–1356, Aug. 1999.

- [70] P. V. Mamyshev and N. A. Mamysheva, "Pulse-overlapped dispersion-managed data transmission and intrachannel four-wave mixing," *Opt. Lett.*, vol. 24, pp. 1454–1456, Nov. 1999.
- [71] J. Martensson, A. Berntson, M. Westlund, A. Danielsson, P. Johannisson, D. Anderson, and M. Lisak, "Timing jitter owing to intrachannel pulse interactions in dispersion-managed transmission systems," *Opt. Lett.*, vol. 26, pp. 55–57, Jan. 2001.
- [72] H. A. Haus, "Theory of mode locking with a slow saturable absorber," *IEEE J. Quantum Electron.*, vol. QE-11, pp. 736–746, Sept. 1975.
- [73] H. A. Haus and A. Mecozzi, "Noise of mode-locked lasers," *IEEE J. Quantum Electron.*, vol. 29, pp. 983–996, Mar. 1993.
- [74] E. P. Ippen, "Principles of passive mode-locking," *Appl. Phys. B*, vol. 58, pp. 159–170, Mar. 1994.
- [75] C.-J. Chen, P. K. A. Wai, and C. . R. Menyuk, "Self-starting of passively mode-locked laser with fast saturable absorbers," *IEEE J. Quantum Electron.*, vol. 20, pp. 350–352, Feb. 1995.
- [76] F. X. Kartner, J. Aus der Au, and U. Keller, "Mode-locking with slow and fast saturable absorbers—What's the difference?" *IEEE J. Sel. Top. Quantum Electron.*, vol. 4, pp. 159–168, Mar./Apr. 1998.
- [77] H. A. Haus, "Mode-locking of lasers," *IEEE J. Quantum Electron.*, vol. 6, pp. 1173–1185, Nov./Dec. 2000.
- [78] D. J. Richardson, R. I. Laming, and D. N. Payne, "Switching and passive mode-locking of fibre lasers using nonlinear loop mirrors," in *Proc. SPIE*, vol. 1581, 1991, pp. 26–39.
- [79] M. Hofer, M. H. Ober, F. Haberl, and M. E. Fermann, "Characterization of ultrashort pulse formation in passively mode-locked fiber lasers," *IEEE J. Quantum Electron.*, vol. 28, pp. 720–728, Mar. 1992.
- [80] M. J. Guy, D. U. Noske, and J. R. Taylor, "Generation of femtosecond soliton pulses by passive mode locking of an ytterbium-erbium figure-of-eight fiber laser," *Opt. Lett.*, vol. 18, pp. 1447–1449, Sept. 1993.
- [81] V. Tzelepis, S. Markatos, S. Kalpogiannis, T. Sphicopoulos, and C. Caroubalos, "Analysis of a passively mode-locked self-starting all-fiber soliton laser," *J. Lightwave Technol.*, vol. 11, pp. 1729–1735, Nov. 1993.
- [82] H. A. Haus, E. P. Ippen, and K. Tamura, "Additive-pulse mode-locking in fiber lasers," *IEEE J. Quantum Electron.*, vol. 30, pp. 200–208, Jan. 1994.

- [83] B. B. *et al.*, "High-power erbium-doped fiber laser mode-locked by a semiconductor saturable absorber," *Opt. Lett.*, vol. 20, pp. 471–473, Mar. 1995.
- [84] H. A. Haus, K. Tamura, L. E. Nelson, and E. P. Ippen, "Stretched-pulse additive pulse mode-locking in fiber ring lasers," *IEEE J. Quantum Electron.*, vol. 31, pp. 591–598, Mar. 1995.
- [85] S. Namiki and H. A. Haus, "Noise of the stretched-pulse fiber laser: Part I—experiments," *IEEE J. Quantum Electron.*, vol. 33, pp. 649–659, May 1997.
- [86] C. X. Yu, S. Namiki, and H. A. Haus, "Noise of the stretched-pulse fiber laser: Part II—experiments," *IEEE J. Quantum Electron.*, vol. 33, pp. 660–668, May 1997.
- [87] I. N. Duling III and R. D. Esman, "Single-polarisation fibre amplifier," *Electron. Lett.*, vol. 28, pp. 1126–1128, June 1992.
- [88] T. F. Carruthers and I. N. Duling III, "An actively mode-locked, 10-GHz, single-polarization, picosecond erbium fiber laser," in *Proc. CLEO '96*, 1996, p. 526.
- [89] —, "10-GHz 1.3-ps erbium fiber laser employing soliton pulse shortening," *Opt. Lett.*, vol. 21, pp. 1927–1929, Dec. 1996.
- [90] K. S. Abedin, N. Onodera, and M. Hyodo, "Higher order FM mode locking for pulse-repetition-rate enhancement in actively mode-locked lasers: Theory and experiment," *IEEE J. Quantum Electron.*, vol. 35, pp. 875–890, June 1999.
- [91] T. R. Clark, T. F. Carruthers, P. J. Matthews, and I. N. Duling III, "Phase noise measurements of ultrastable 10GHz harmonically modelocked fibre laser," *Electron. Lett.*, vol. 35, pp. 720–721, Apr. 1999.
- [92] T. R. Clark, T. F. Carruthers, and I. N. P. J. M. Duling III, "Sub-10 femtosecond timing jitter of a 10-GHz harmonically modelocked fiber laser," in *Proc. OFC '99*, 1999, pp. PD24–1–PD24–2.
- [93] M. E. Grein, L. A. Jiang, H. A. Haus, and E. P. Ippen, "A study of the dynamics governing timing restoration in the actively modelocked soliton laser," in *Proc. CLEO 1999*, 1999, p. 100.
- [94] T. F. Carruthers, I. N. Duling III, M. Horowitz, and C. R. Menyuk, "Dispersion management in a harmonically mode-locked fiber soliton laser," *Opt. Lett.*, vol. 25, pp. 153–155, Feb. 2000.
- [95] M. Horowitz, C. R. Menyuk, T. F. Carruthers, and I. N. Duling III, "Theoretical and experimental study of harmonically modelocked fiber lasers for optical communication systems," *J. Lightwave Technol.*, vol. 18, pp. 1565–1574, Nov. 2000.

- [96] M. E. Grein, H. A. Haus, E. P. Ippen, and Y. Chen, "The quantum limit of timing jitter in actively mode-locked soliton fiber lasers," in *Proc. CLEO 2001*, 2001, pp. 243–244.
- [97] L. Yuhua, L. Caiyun, W. Jian, W. Boyu, and G. Yizhi, "Novel method to simultaneously compress pulses and suppresses supermode noise in actively mode-locked fiber ring laser," *IEEE Photon. Technol. Lett.*, vol. 10, pp. 1250–1252, Sept. 1998.
- [98] Y. Silberberg, P. W. Smith, D. J. Eilenberger, D. A. B. Miller, A. C. Gossard, and W. Wiegmann, "Passive mode locking of a semiconductor diode laser," *Opt. Lett.*, vol. 9, pp. 507–508, Nov. 1984.
- [99] P. W. Smith, Y. Silberberg, and D. A. B. Miller, "Mode locking of semiconductor diode lasers using saturable excitonic nonlinearities," *J. Opt. Soc. Am. B*, vol. 2, pp. 1228–1235, July 1985.
- [100] S. Arahira and Y. Ogawa, "Repetition-frequency tuning of monolithic passively mode-locked semiconductor lasers with integrated extended cavities," *IEEE J. Quantum Electron.*, vol. 33, pp. 255–264, Feb. 1997.
- [101] I. Kim and P. D. Dapkus, "Passively mode-locked semiconductor laser under self phase modulation," in *Proc. LEOS '99*, vol. 2, 1999, pp. 707–708.
- [102] D. A. Yanson, M. W. Street, E. A. Avrutin, S. D. McDougall, I. G. Thayne, and J. H. Marsh, "Near-terahertz passive harmonic modelocking in monolithic compound-cavity laser diodes," in *Proc. LEOS 2000*, vol. 2, 2000, pp. 438–439.
- [103] D. A. Yanson, M. W. Street, S. D. McDougall, I. G. Thayne, J. H. Marsh, and E. A. Avrutin, "Terahertz repetition frequencies from harmonic mode-locked monolithic compound-cavity laser diodes," *Appl. Phys. Lett.*, vol. 78, pp. 3571–3573, June 2001.
- [104] F. Rana and R. Ram, "Noise and timing jitter in active and hybrid mode-locked semiconductor lasers," in *Proc. CLEO 2001*, 2001, pp. 6–7.
- [105] J. E. Bowers, P. A. Morton, A. Mar, and S. W. Corzine, "Actively mode-locked semiconductor lasers," *IEEE J. Quantum Electron.*, vol. 25, pp. 1426–1439, June 1989.
- [106] Z. Ahmed, L. Zhai, A. J. Loweery, N. Onodera, and R. S. Tucker, "Locking bandwidth of actively mode-locked semiconductor lasers," *IEEE J. Quantum Electron.*, vol. 29, pp. 1714–1721, June 1994.
- [107] L. Zheng, C. R. Menyuk, and G. M. Carter, "A realistic model for actively modelocked semiconductor lasers," *IEEE Photon. Technol. Lett.*, vol. 6, pp. 167–169, Feb. 1994.

- [108] P. W. Smith, Y. Silberberg, and D. A. B. Miller, "High-frequency and low-jitter optical pulse generation using semiconductor mode-locked lasers," *IEEE Trans. Microwave Theory Techniques*, vol. 47, pp. 1251–1256, July 1999.
- [109] S. Arahira, Y. Katoh, D. Kunimatsu, S. Kutsuzawa, and Y. Ogawa, "160 GHz mode-locked laser diode stabilized by subharmonic-frequency optical pulse injection," in *Proc. LEOS '99*, vol. 2, 1999, pp. 836–837.
- [110] M. Shirane, Y. Hashimoto, H. Yamada, and H. Yokyama, "A compact optical sampling measurement system using mode-locked laser-diode modules," *IEEE Photon. Technol. Lett.*, vol. 12, pp. 1537–1539, Feb. 2000.
- [111] C. M. DePriest, T. Yilmaz, P. J. Delfyett, S. Etemad, A. Braun, and J. H. Abeles, "Ultralow noise and supermode suppression in an actively mode-locked external cavity semiconductor diode ring laser," *Opt. Lett.*, vol. 27, pp. 719–721, May 2002.
- [112] L. A. Jiang, M. E. Grein, H. A. Haus, and E. P. Ippen, "Noise of modelocked semiconductor lasers," *IEEE J. Sel. Top. Quantum Electron.*, vol. 7, pp. 159–167, Mar./Apr. 2001.
- [113] L. A. Jiang, K. S. Abedin, M. E. Grein, and E. P. Ippen, "Timing jitter reduction in modelocked semiconductor lasers with photon seeding," *Appl. Phys. Lett.*, vol. 80, pp. 1707–1709, Mar. 2002.
- [114] D. M. Hughes, D. Burns, W. Sibbet, K. A. Williams, and I. H. White, "Ultra-short pulse semiconductor lasers with improved timing jitter," in *Proc. CLEO '94*, 1994, pp. 255–256.
- [115] A. Shen, S. Bouchoule, C. Cuisin, P. Crozat, and J. M. Lourtioz, "Reduced timing jitter of two-section 1.55- μm laser diodes under gain-/loss-switching regime at multigigahertz rates," *IEEE Photon. Technol. Lett.*, vol. 10, pp. 1694–1696, Dec. 1998.
- [116] K. A. Williams, I. H. White, D. Burns, and W. Sibbett, "Jitter reduction through feedback for picosecond pulsed InGaAsP lasers," *IEEE J. Quantum Electron.*, vol. 32, pp. 1988–1994, Nov. 1996.
- [117] P. Vasil'ev, *Ultrafast Diode Lasers: Fundamentals and Applications*. Norwood, MA: Artech House, 1995.
- [118] L. A. Coldren and S. W. Corzine, *Diode Lasers and Photonic Integrated Circuits*. New York: John Wiley & Sons, 1995.

- [119] C. T. Chang, C. K. Sun, D. J. Albares, and E. W. Jacobs, "High-energy (59-pJ) and low-jitter (250 fs) picosecond pulses from gain-switching of a tapered-stripe laser diode via resonant driving," *IEEE Photon. Technol. Lett.*, vol. 8, pp. 1157–1159, Sept. 1996.
- [120] Y. M. M. D. Pelusi and A. Suzuki, "Generation of 20-fs optical pulses from a gain-switched laser diode by a four-stage soliton compression technique," *IEEE Photon. Technol. Lett.*, vol. 11, pp. 1217–1219, Oct. 1999.
- [121] K. A. Ahmed, K. C. Chan, and H. Liu, "Femtosecond pulse generation from semiconductor lasers using the soliton-effect compression technique," *IEEE J. Sel. Top. Quantum Electron.*, vol. 1, pp. 592–600, June 1995.
- [122] M. D. Pelusi, Y. Matsui, and A. Suzuki, "Pedestal suppression from compressed femtosecond pulses using a nonlinear fiber loop mirror," *IEEE J. Quantum Electron.*, vol. 35, pp. 867–874, June 1999.
- [123] C. K. Sun, C. T. Chang, G. A. Massey, T. Y. Lee, R. Yu, and D. J. Albares, "High energy and low jitter picosecond optical pulser for sample-and-hold," in *Proc. SPIE*, vol. 3463, 1998, pp. 212–218.
- [124] P. Pepeljugoski, J. Lin, J. Gamelin, M. Hong, and K. Y. Lau, "Ultralow timing jitter in electrically gain-switched vertical cavity surface emitting lasers," *Appl. Phys. Lett.*, vol. 62, pp. 1588–1590, Apr. 1993.
- [125] E. Goobar, H. Lee, R. J. Ram, and K. D. Choquette, "Reduced timing jitter in surface emitting lasers," in *Proc. CLEO '99*, 1999, pp. 174–175.
- [126] J. T. Ong, R. Takahashi, M. Tsuchiya, S.-H. Wong, R. T. Sahara, Y. Ogawa, and T. Kamiya, "Subpicosecond soliton compression of gain switched diode laser pulses using an erbium-doped fiber amplifier," *IEEE J. Quantum Electron.*, vol. 29, pp. 1701–1707, June 1993.
- [127] K. R. Tamura and M. Nakazawa, "Spectral smoothing and pedestal reduction of wavelength tunable quasi-adiabatically compressed femtosecond solitons using a dispersion-flattened dispersion-imbalanced loop mirror," *IEEE Photon. Technol. Lett.*, vol. 11, pp. 230–232, Feb. 1999.
- [128] M. D. Pelusi, Y. Matsui, and A. Suzuki, "High-quality sub-100-fs optical pulse generation by fiber-optic soliton compression of gain-switched distributed feedback laser-diode pulses in conjunction with nonlinear optical fiber loops," *Opt. Lett.*, vol. 24, pp. 1172–1174, Aug. 1999.
- [129] M. Nakazawa, T. Yamamoto, and K. R. Tamura, "1.28Tbit/s-70km OTDM transmission using third- and fourth-order simultaneous dispersion compensation with a phase modulator," *Electron. Lett.*, vol. 36, pp. 2027–2029, Nov. 2000.

- [130] E. Yamada and M. Nakazawa, "Reduction of amplified spontaneous emission from a transmitted soliton signal using a nonlinear amplifying loop mirror and a nonlinear optical loop mirror," *IEEE J. Quantum Electron.*, vol. 30, pp. 1842–1850, Aug. 1994.
- [131] A. Takada and M. Saruwatari, "100 Gbit/s optical signal generation by time-division multiplication of modulated and compressed pulses from gain-switched distributed feedback (DFB) laser diode," *Electron. Lett.*, vol. 24, pp. 1406–1408, Nov. 1998.
- [132] M. Cavelier, N. Stelmakh, J. Xie, L. Chusseau, J.-M. Lourtioz, C. Kazmierski, and N. Bouadma, "Picosecond (<2.5 ps) wavelength-tunable (~ 20 nm) semiconductor laser pulses with repetition rates up to 12 GHz," *Electron. Lett.*, vol. 28, pp. 224–226, Jan. 1992.
- [133] K. Iwatsuki, K. Suzuki, and S. Nishi, "Generation of transform limited gain-switched DFB-LD pulses < 6 ps with linear fibre compression and spectral window," *IEEE J. Quantum Electron.*, vol. 30, pp. 2842–2853, Dec. 1994.
- [134] L. Chusseau and C. Kazmierski, "Optimum linear pulse compression of a gain-switched $1.5 \mu\text{m}$ DFB laser," *IEEE Photon. Technol. Lett.*, vol. 6, pp. 24–26, Jan. 1994.
- [135] G. P. Agrawal, *Nonlinear Fiber Optics*, 2nd ed. San Diego: Academic Press, 1995.
- [136] K.-I. Suzuki, K. Iwatsuki, S. Nishi, M. Saruwatari, and T. Kitoh, "160 Gb/s sub-picosecond transform-limited pulse signal generation utilizing adiabatic soliton compression and optical time-division multiplexing," *IEEE Photon. Technol. Lett.*, vol. 6, pp. 352–355, Mar. 1994.
- [137] M. Horowitz and Y. Silberberg, "Nonlinear filtering by use of intensity-dependent polarization rotation in birefringent fibers," *Opt. Lett.*, vol. 22, pp. 1760–1762, Dec. 1997.
- [138] P. Pepeljugoski, D. M. Cutrer, and K. Y. Lau, "Parametric dependence of timing jitter in gain-switched semiconductor lasers," *Appl. Phys. Lett.*, vol. 63, pp. 3556–3558, Dec. 1993.
- [139] L. N. Langley and K. A. Shore, "The effect of external optical feedback on timing jitter in modulated laser diodes," *J. Lightwave Technol.*, vol. 11, pp. 434–439, Mar. 1993.
- [140] M. Schell, W. Utz, D. Huhse, J. Kassner, and D. Bimberg, "Low jitter single-mode pulse generation by a self-seeded, gain-switched Fabry-Pérot semiconductor laser," *Appl. Phys. Lett.*, vol. 65, pp. 3045–3047, Dec. 1994.

- [141] M. Schell, D. Huhse, W. Utz, J. Kassner, D. Bimberg, and I. S. Tarasov, "Jitter and dynamics of self-seeded Fabry-Perot laser diodes," *IEEE J. Sel. Top. Quantum Electron.*, vol. 1, pp. 528–534, June 1995.
- [142] P. A. Andrekson, N. A. Olsson, J. R. Simpson, T. Tanbun-Ek, R. A. Logan, and M. Haner, "Characterization of 1.55- μm pulses from a self-seeded gain-switched Fabry-Perot laser diode using frequency-resolved optical gating," *IEEE Photon. Technol. Lett.*, vol. 10, pp. 935–957, July 1998.
- [143] M. Yao, L. Xu, J. Zhang, M. Chen, J. Wu, C. Lou, and Y. Gao, "A novel self-seeding technique for timing jitter reduction in gain switched DFB laser," in *Proc. CLEO Pacific Rim '99*, 1999, pp. 2.38–2.39.
- [144] M. R. H. Daza and C. A. Saloma, "Jitter dynamics of a gain-switched semiconductor laser under self-feedback and external optical injection," *IEEE J. Quantum Electron.*, vol. 37, pp. 254–264, Feb. 2001.
- [145] I. N. Duling III, R. P. Moeller, and T. R. Clark, "Active filtering of the amplitude noise of a mode-locked fiber laser," in *Proc. CLEO 2000*, 2000, p. 26.
- [146] L. A. Jiang, M. E. Grein, B. R. Robinson, E. P. Ippen, and H. A. Haus, "Experimental demonstration of a timing jitter eater," in *Proc. CLEO 2002*, 2002, pp. 164–65.
- [147] J. W. Lou, T. F. Carruthers, and M. Currie, "Mode-locked multiple-wavelength erbium-doped fiber laser in a sigma configuration," *IEEE Photon. Technol. Lett.*, vol. 14, pp. 281–283, Mar. 2002.
- [148] D.-S. Seo, H.-F. Liu, D. Y. Kim, and D. D. Sampson, "Injection power and wavelength dependence of an external-seeded gain-switched Fabry-Perot laser," *Appl. Phys. Lett.*, vol. 67, pp. 1503–1505, Sept. 1995.
- [149] J. Dellunde, M. C. Torrent, J. M. Sancho, and M. San Miguel, "Frequency dynamics of gain-switched injection-locked semiconductor lasers," *IEEE J. Quantum Electron.*, vol. 33, pp. 1537–1542, Sept. 1997.
- [150] P. Spano, A. d'Ottavi, A. Mecozzi, B. Daino, and S. Piazzolla, "Experiment and theory of first passage time in pulse-modulated semiconductor lasers," *IEEE J. Quantum Electron.*, vol. 25, pp. 1440–1449, June 1989.
- [151] A. Valle and L. Pesquera, "Relative intensity noise of multitransvers mode vertical cavity surface emitting lasers," in *Proc. CLEO '99*, 1999, pp. 175–176.
- [152] S. E. Ralph, Georgia Institute of Technology, Atlanta, GA (personal communication), 2002.

- [153] G.-R. Lin and C.-R. Lee, "The power/frequency-dependent pulse width and jitter of a 1.55 μm Fabry-Perot laser diode transmitter," *Microwave Opt. Tech. Lett.*, vol. 30, pp. 232–234, Aug. 2001.
- [154] M. Nakazawa, T. Yamamoto, and K. R. Tamura, "Femtosecond optical pulse generation using a distributed-feedback laser diode," *Electron. Lett.*, vol. 26, pp. 2038–2040, Nov. 1990.
- [155] D. Cutrer, P. Pepeljugoski, and K. Lau, "Noise properties of electrically gain-switched 1.5 μm DFB lasers after spectral filtering," *Electron. Lett.*, vol. 30, pp. 1418–1419, Aug. 1994.
- [156] T. E. Murphy, "10-GHz 1.3-ps pulse generation using chirped soliton compression in a raman gain medium," *IEEE Photon. Technol. Lett.*, vol. 14, pp. 1424–1426, Oct. 2002.
- [157] K. R. Tamura and K. Sato, "50-GHz repetition-rate. 280-fs pulse generation at 100-mw average power from a mode-locked laser diode externally compressed in a pedestal-free pulse compressor," *Opt. Lett.*, vol. 27, pp. 1268–1270, July 2002.
- [158] H. Okamura, "Automatic optical-loss compensation with Er-doped fibre amplifier," *Electron. Lett.*, vol. 27, pp. 2155–2156, Nov. 1991.
- [159] —, "Automatic optical loss compensation with erbium-doped fiber amplifier," *J. Lightwave Technol.*, vol. 10, pp. 1110–1116, Aug. 1992.
- [160] A. F. Evans, "Dispersion-tapered fiber in nonlinear loop mirrors for intensity and pulse width switching," in *Proc. ECOC '96*, 1996, pp. 4.27–4.30.
- [161] H. A. Haus, J. G. Fujimota, and E. P. Ippen, "Analytic theory of additive pulse and Kerr lens mode locking," *IEEE J. Quantum Electron.*, vol. 28, pp. 2086–2096, Oct. 1992.
- [162] R. P. Davey, K. Smith, R. L. Williams, M. J. Holms, D. M. Pataca, M. L. Rocha, and R. Gunning, "Subpicosecond pulse generation from a 1.3 μm DFB laser gain-switched at 1 GHz," *Electron. Lett.*, vol. 32, pp. 34–36, Feb. 1996.
- [163] H. Stark and J. W. Woods, *Probability, Random Processes, and Estimation Theory for Engineers*, 2nd ed. Englewood Cliffs, NJ: Prentice Hall, 1994.
- [164] J. G. Proakis, *Digital Communications*, 3rd ed. New York: McGraw-Hill, 1995.
- [165] D. von der Linde, "Characterization of the noise in continuously operating mode-locked lasers," *Appl. Phys. B*, vol. 39, pp. 201–217, Apr. 1986.

- [166] E. H. Botcher and D. Bimberg, "Detection of pulse-to-pulse timing jitter in periodically gain-switched semiconductor lasers," *Appl. Phys. Lett.*, vol. 54, pp. 1971–1973, May 1989.
- [167] P. J. Delfyett, D. H. Hartman, and S. Z. Ahmad, "Optical clock distribution using a mode-locked semiconductor laser diode system," *J. Lightwave Technol.*, vol. 9, pp. 1646–1649, Dec. 1991.
- [168] C. R. Mirasso, L. Pesquera, and A. Mecozzi, "Pulse-to-pulse frequency jitter in diode lasers and soliton transmission," *IEEE Photon. Technol. Lett.*, vol. 5, pp. 1455–1458, Dec. 1993.
- [169] E. Yoshida and M. Nakazawa, "Measurement of the timing jitter and pulse energy fluctuation of a PLL regeneratively mode-locked fiber laser," *IEEE Photon. Technol. Lett.*, vol. 11, pp. 548–550, May 1999.
- [170] A. J. Taylor, J. M. Wiesenfeld, G. Eisenstein, and R. S. Tucker, "Timing jitter in mode-locked and gain-switched InGaAsP injection lasers," *Appl. Phys. Lett.*, vol. 49, pp. 681–683, Sept. 1986.
- [171] U. Keller, K. D. Li, M. Rodwell, and D. M. Bloom, "Noise characterization of femtosecond fiber raman soliton lasers," *IEEE J. Quantum Electron.*, vol. 25, pp. 280–288, Feb. 1989.
- [172] M. Jinno, "Correlated and uncorrelated timing jitter in gain-switched laser diodes," *IEEE Photon. Technol. Lett.*, vol. 5, pp. 1140–1142, Oct. 1993.
- [173] —, "Effects of crosstalk and timing jitter on all-optical time-division demultiplexing using a nonlinear fiber sagnac interferometer switch," *IEEE J. Quantum Electron.*, vol. 30, pp. 2842–2853, Dec. 1994.
- [174] T. Stoppard, *Rosencrantz and Guildenstern are Dead*. New York: Grove Press, 1967.
- [175] (2003) Mathworld. [Online]. Available: <http://mathworld.wolfram.com/>
- [176] R. P. Scott, C. Langrock, and B. H. Kolner, "High-dynamic-range laser amplitude and phase noise measurement techniques," *IEEE J. Sel. Top. Quantum Electron.*, vol. 7, pp. 641–655, Jul./Aug. 2001.
- [177] R. Yuan and H. F. Taylor, "Noise characteristics in repetitively pulsed semiconductor lasers," *IEEE J. Quantum Electron.*, vol. 22, pp. 109–117, Jan. 1992.
- [178] B. Zhu, I. H. White, R. V. Penty, A. Wonfor, E. Lach, and H. D. Summers, "Theoretical analysis of timing jitter in monolithic mode-locked DBR laser diodes," *IEEE J. Quantum Electron.*, vol. 33, pp. 1216–1220, July 1997.

- [179] R. Ludwig, S. Diez, A. Ehrhardt, L. Kuller, W. Pieper, and H. G. Weber, "A tunable femtosecond modelocked semiconductor laser for applications in OTDM-systems," *IEICE Trans. Electron.*, vol. E81-C, pp. 140–145, Feb. 1998.
- [180] S. Verghese, S. D. Parker, and E. R. Brown, "Phase noise of a resonant-tunneling relaxation oscillator," *Appl. Phys. Lett.*, vol. 72, pp. 2550–2552, May 1998.
- [181] L. A. Jiang, M. E. Grein, E. P. Ippen, C. McNeilage, J. Searls, and H. Yokoyama, "Quantum-limited noise performance of a mode-locked laser diode," *Opt. Lett.*, vol. 27, pp. 49–51, Jan. 2002.
- [182] H. Tsuchida, "Time-domain measurement of pulse-timing fluctuations in a mode-locked laser diode," *IEEE Photon. Technol. Lett.*, vol. 14, pp. 513–515, Apr. 2002.
- [183] M. E. Grein, Massachusetts Institute of Technology, Cambridge, MA (personal communication), 2002.
- [184] M. Ridley, *The Red Queen: Sex and the Evolution of Human Nature*. New York: HarperCollins, 1993.

Vita

Michael Charles Gross received the Bachelor of Science degree in electrical engineering from Rice University and was awarded the Master of Science degree in electrical engineering from the Georgia Institute of Technology. Mr. Gross is currently working toward the Doctor of Philosophy degree, again in electrical engineering, at Georgia Tech. After completing his doctorate, he will begin a postdoctoral fellowship at the Naval Research Laboratory. His research interests include short-pulse lasers, noise measurements, optical communications, and optical metrology. He is a recipient of the Shackelford Research Fellowship and the National Academies Postdoctoral Research Fellowship.